Experimental Investigation of Fluorescence Resonance Energy Transfer Using Quantum Dots

By Ee Zhuan Chong

Ph.D. Thesis

School of Physics and Astronomy
Cardiff University

November 2007

ProQuest LLC
789 East Eisenhower Parkway
P.O. Box 1346
Ann Arbor, MI 48106-1346

Abstract

Quantum dots (QDs) are light emitting nanoscale semiconductor crystals with novel optical properties that are markedly different from the conventional organic dyes. Their size tunable emission, broad absorption and resistance to photo- and chemical degradation have afforded a new route to biomolecular studies, especially in long term live cell imaging that is hardly feasible with the utility of organic dyes. With the advent of highly luminescent core-shell QDs with quantum yields over 0.5, sensitive and robust optical sensing assays can be realised in which organic dyes rarely have much success. In this research, I incorporated these core-shell QDs of variable core compositions that are tailored to emit in the visible and the far-red spectral regimes into the development of multiplexed QD-dye assays via a ligand-receptor binding scheme. The close proximity of QDs to energetically resonant dyes is commensurate to Förster/fluorescence resonance energy transfer (FRET) from which course we set to evaluate the potential of QDs as energy donors through the use of the steady state and the time-resolved spectroscopic techniques. Both approaches not only complement each other but also can provide substantive evidence in verifying the suitability of QDs in the design of FRET based assays where the efficiency of energy transfer is generally governed by the donor-acceptor separation and in turn, the size of QDs. Henceforth from that notion, the relevance of FRET efficiency to the proximity relationships in QD-dye self-assemblies are examined theoretically as a function of acceptor-to-donor ratio. Besides the experimental studies of QDs in proximity-induced energy coupling, I take the initiative to develop a theoretical treatment of the multilayer structure of QDs based on the parabolic band approximation to offer a simple analytical route to investigate the size dependency of energy gap and the localisation of carriers which in essence underpin the QD optical behaviour. The analyses are further extended to the type-II QDs with a slight different band profile in which the conduction and the valence band extrema centre on different regions of the heterostructure leading to the separation of carriers and thus, contributing to the distinctive optical characteristics that strongly depart from typical type-I QDs.

Acknowledgements

I would like express my appreciation to Dr. Huw Summers and Prof. Peter Blood for their critical advices, ingenious suggestions and relentless encouragement in the course of my project. I would also like to thank Dr. Daniel Matthews, Dr. Pierpaolo Porta and Dr. John Thomson for helping me in the experimental setups. Of course, my project will not have progressed as smoothly as planned without the assistance from Glynn Summers and Jeff Trivett in building mechanical devices, Malcolm Anderson in 'reviving' my computer and Rob Tucker in circuitry design of pulse picker. The help from Ian Robinson and Louis Winter cannot be dismissed as well. I am also grateful to Dr. Clarence Matthai, Prof. John Inglesfield and Prof. Alex Ivanov for their great efforts in helping me to solve mathematical problems. I would like to pay special thanks to Dr. Angelo Amoroso from School of Chemistry and School of Biosciences for giving me the permission to use their instrumentation. Special thanks also go to Prof. David Lloyd for the use of his laboratory space. I am truly grateful for the financial support from Engineering and Physical Sciences Research Council (EPSRC) and GlaxoSmithKline (GSK) in sponsoring my 3-year postgraduate course. Last but not least, I would like to express my utmost appreciation to my family for their continuous support.

CONTENTS

CHAPTER 1:

NANOCRYSTALS AND THEIR APPLICATIONS IN FRET

CONTENTS:

Abstract: In this chapter, I briefly describe the chemical routes to synthesise colloidal nanoparticles, the various techniques to stabilise them in aqueous media and the bioconjugation schemes to afford targeting abilities. This is followed by an overall description of quantum dot optical characteristics and a concise review of the recent advances of quantum dots in the development of FRET assays. I also elucidate the motivations and rationales behind the project I have undertaken which relates to the application of quantum dots in the far-red spectral regime. Following that, I provide a quick account of the thesis outline.

CHAPTER 1:

NANOCRYSTALS AND THEIR APPLICATIONS IN FRET

1.1 A Perspective on Cadmium Chalcogenide Quantum Dots: Chemical Synthesis, Solubilisation and Bioconjugation

Quantum dot (QD), nanocrystal (NC) and nanoparticle (NP) are the common synonyms referring to a semiconductor crystallite with its size in the order of few nanometers. These tiny light emitting particles are well known for their size tunable optical properties arising from the size quantum confinement effect [1]. Due to the limitation of lithography and etching, the synthesis of new classes of material in the range of 2-5 nm diameters has resorted to other alternative methods which are essentially relying on the wet chemical routes. The study of colloidal nanoscale crystallites can be considered to be instigated by Brus's group upon the successful reversed micelle mediated synthesis of II-VI binary semiconductor QDs that contained primarily cadmium (Cd) element in 1980s [2-4]. Via the inverse micelle synthetic route, they were among the first few chemists to report the size dependent bandgap of colloidal semiconductor nanocrystal as indicated by the substantial blue shift in the ensemble absorption onset compared to that of the bulk phase [2, 3, 5, 6]. However, the quality of the dots was substandard considering the pronounced red tail in the emission spectrum which is often associated with radiative recombination from surface states (or deep traps) and the broad emission bandwidth that stretched beyond 100 nm which reflects the high polydisparity in the size distribution of the ensemble. No values for quantum yield were reported [2, 3]. Despite the poor crystallinity, the demonstration of the size dependent quantum confinement effect has generated a rippling effect among the research community with an ever growing interest in QDs. Since then, the search for a better chemical recipe was the top priority in hope of attaining good quality QDs. In the early 1990s, Bawendi's group has published a ground breaking achievement in the field of QD synthesis [7]. They demonstrated that a range of high quality cadmium based II-VI QDs could be grown using organometallic synthetic procedures by injecting the element reagents (precursors) at the correct stoichiometry into the organic surfactant medium (i.e. trioctylphosphine oxide, TOPO) which was heated over hundreds of degree Celsius (typically > 200 °C). At high temperature, the oppositely charged cadmium and chalcogen ions in the coordinating medium would react and began to nucleate. The nucleation of semiconductor seeds grew in the controlled heated reaction flask and eventually the process yielded an ensemble of surface passivated semiconductor nanocrystallites suspended in the organic solvent, hence in turn, this led to the creation of semiconductor colloids. With their refined comprehensive organometallic chemical route followed by a size selective precipitation, they have successfully produced a variation of QD species from CdS to CdTe that were nearly monodisperse (< 5 % rms in diameter) and have no detectable deep trap emission yet the quantum yield was ~10 %. The lattice structures of the cadmium chalcogenide QDs were predominately wurzite with a bond length similar to the bulk crystal. Besides that, they also reported the observations of sharp discrete features in the optical density of smaller QDs and concomitantly a systematic blue shift in the band edge absorption with reducing QD size.

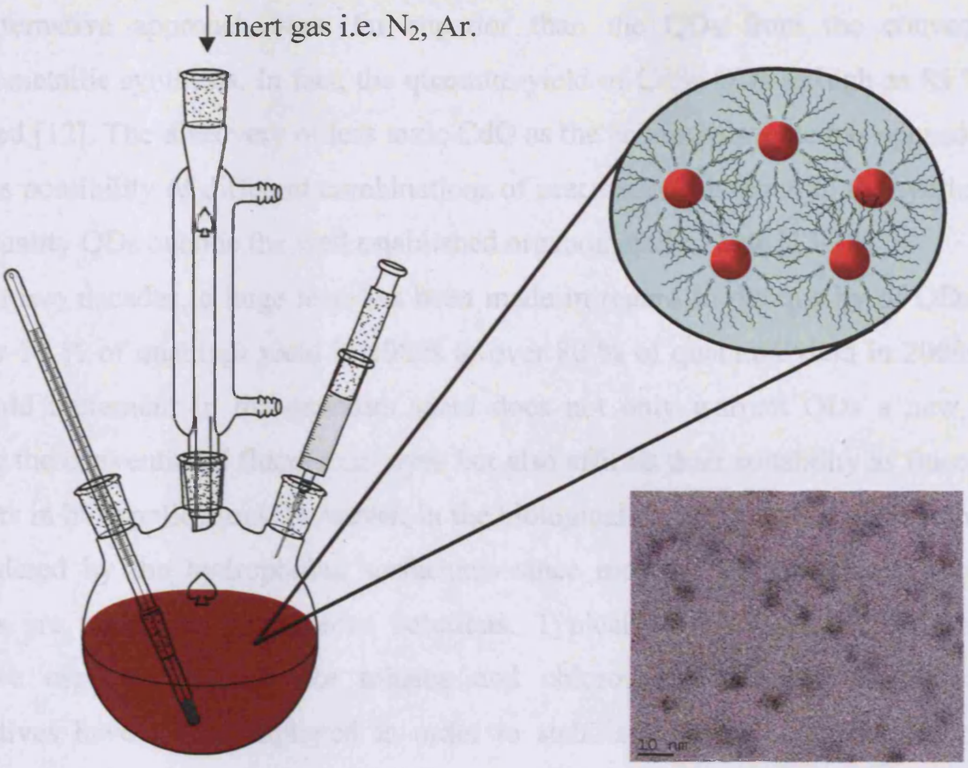

Figure 1.1: Cartoon of a typical experimental setup for QD synthesis with the mixture of injected precursors and surfactant medium in the three neck flask heated above 200 °C in an inert atmosphere. A transmission electron microscopy (TEM) image of QDs is shown at the right hand corner (Courtesy of Christy Cooper, Purdue University).

Since the discovery of quality quasi-single QDs by the orgnanometallic synthetic method, cadmium based II-VI QDs began to proliferate. In mid 1990s, high luminescent wide bandgap capped core-shell CdSe/ZnS and CdSe/CdS QDs were introduced by Guyot-Sionnest's, Bawendi's and Alivisatos's teams [8-10]. Dependent on the shell thickness, the quantum yield as high as 50 % was reported. This corroborates the effective suppression of carrier traps by surface passivation with inorganic materials. The growth of the outer wide bandgap shell was epitaxial. The unprecedented quantum efficiency was the highlight in the venture of promoting QD as the new class of luminescent material. However, dimethyl cadmium ($CdMe_2$ or $Cd(CH_3)_2$) in the original organometallic route is highly toxic and expensive reagent to be used as the cadmium precursor. Furthermore, it can be unstable and explosive at elevated temperatures due to the liberation of large volume of gas. Therefore, in concern with the toxicity level in the QD production, in the early 2000s, Peng's team has taken a 'greener' approach in the synthesis of QDs by proposing the substitution of $CdMe_2$ with less toxic CdO without compromising the quantum yield [11, 12]. It was surprisingly found that the QDs from the alternative approach were far superior than the QDs from the conventional organometallic synthesis. In fact, the quantum yield of CdSe QDs as high as 85 % was reported [12]. The discovery of less toxic CdO as the cadmium source has opened up an endless possibility of different combinations of precursors/surfactant in the synthesis of high quality QDs outside the well established organometallic route [13-18].

Within two decades, a huge leap has been made in regard to the quality of QDs from merely 10 % of quantum yield in 1980s to over 80 % of quantum yield in 2000s. The eightfold increment in the quantum yield does not only warrant QDs a new status among the conventional fluorescent dyes but also affirms their suitability as fluorescent markers in bio-applications. However, in the biological perspective, the viability of QDs is hindered by the hydrophobic surfactants since most of the molecular or cellular studies are conducted in aqueous solutions. Typical TOPO capped QDs can only dissolve organic solvents like toluene and chloroform. Hence, different surface derivatives have to be employed in order to stabilise QDs in aqueous solutions. A varying strategy to solubilise QDs in aqueous solutions has been proposed from comprehensive surface exchange with bifunctional molecules such mercaptoacetic acid (MAA) [19] and dihydrolipoic acid (DHLA) [20] which contain the thiol group (-SH) that adsorbs onto the QD surface and the hydrophilic carboxyl group (-COOH) that protrudes into the water based medium to a more laborious encapsulation method using amine cross-linked amphiphilic polymer [21, 22] which contains the hydrophobic alkyl chains that intercalate with the alkyl chains of TOPO surfactants and the carboxyl group upon the hydrolysation of anhydride ring that renders the water solubility of QD.

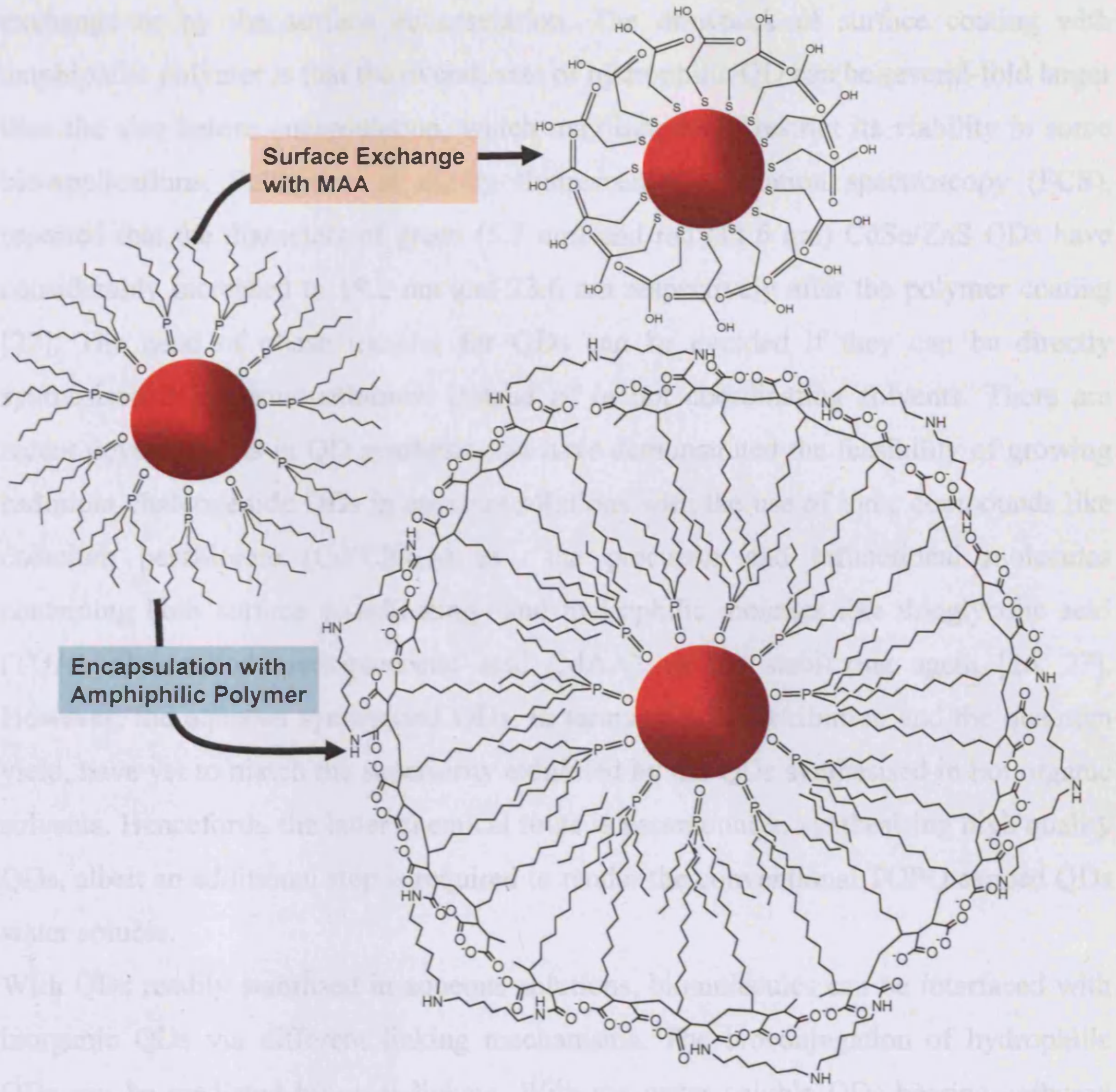

Figure 1.2: Diagram depicts two alternative schemes of converting hydrophobic TOPO capped QD into water soluble QD by: i) surface exchange with mercaptoacetic acid (MAA), ii) encapsulation with amphiphilic polymer cross-linked with amine molecules. Adapted from [22, 23].

Between the two techniques, the thiol capped QDs by ligand exchange are less stable and tend to precipitate in water if kept over a long period of time. The precipitation of thiolated QDs is primarily linked to the weak surface adsorption of -SH [13, 24, 25]. The dynamics of Cd-S or Zn-S bonds are dictated by the local environment. Conversely, no hindrance in the water solubility of the polymer coated QDs is reported [22]. Despite that, no organic material can sustain forever without chemical degradation. Hence, there will be a limitation in the shelf life of QDs that are solubilised either by the surface exchange or by the surface encapsulation. The drawback of surface coating with amphiphilic polymer is that the overall size of hydrophilic QD can be several-fold larger than the size before encapsulation, which may inherently restrict its viability in some bio-applications. Pellegrino et al, by fluorescence correlation spectroscopy (FCS), reported that the diameters of green (5.7 nm) and red (11.6 nm) CdSe/ZnS QDs have considerably increased to 19.2 nm and 23.6 nm respectively after the polymer coating [22]. The need of phase transfer for QDs can be avoided if they can be directly synthesised in aqueous solutions instead of in hot coordinating solvents. There are recent developments in QD synthesis that have demonstrated the feasibility of growing cadmium chalcogenide QDs in aqueous solutions with the use of ionic compounds like cadmium perchlorate ($Cd(ClO_4)_2$) as the precursor and bifunctional molecules containing both surface coordinating and hydrophilic moieties like thioglycolic acid (TGA), also called mercaptoacetic acid (MAA), as the stabilizing agent [26, 27]. However, the aqueous synthesised QDs, in terms of size distribution and the quantum yield, have yet to match the superiority exhibited by the QDs synthesised in hot organic solvents. Henceforth, the latter chemical route is paramount in synthesising high quality QDs, albeit an additional step is required to render the conventional TOPO capped QDs water soluble.

With QDs readily stabilised in aqueous solutions, biomolecules can be interfaced with inorganic QDs via different linking mechanisms. The bioconjugation of hydrophilic QDs can be mediated by cross-linkers. With the water soluble QDs bearing carboxyl group, biomolecules with reactive amine group can be covalently attached to the QDs by zero-length cross-linkage in the presence of carbodiimide [28]. The carbodiimide compound commonly used to facilitate the cross-linking reaction (condensation) between -COOH and $-NH_2$ is EDC (1-ethyl-3-(3-dimethylamino propyl)carbodiimide), as has been widely applied in the streptavidin (STV) conjugation of commercial Qdots [21]. By surface engineering with different molecules, a variety of bio-targeting abilities can be achieved in QDs. Bruchez et al and Chan et al are the first to explore the feasibility of bioconjugated QDs in cell staining [19, 29]. They covalently attached a range of molecules from glycoprotein, antibody to biotin onto the surface of QDs with the manipulation of cross-linkers and further induced by ligand-receptor bindings, some success was attained in a novel QD mediated in-vitro imaging. No substantial interference in the cellular activities was reported. Furthermore, they both confirmed that QDs are exceptionally photostable over extended excitation period in comparison to standard dye molecules that can be quite easily photobleached. From a microscopic imaging perspective, the superior resistance of QD to photobleaching can have remarkable impact on a real time biomolecular tracking in live cells which has been long proven problematic or occasionally impossible if dye molecules are used as the fluorescent probes.

1.2 Optical Properties of Cadmium Chalcogenide Quantum Dots

Quantum dots are generally known for their size tunable emission/absorption. Cadmium chalcogenides are direct bandgap II-VI semiconductors and QDs of these compositions can be tailored to have emissions that cover the visible and the near infra red spectra [30, 31]. Although the core material coarsely dictates the QD emission, its wavelength can be fine tuned from blue to red by decreasing or increasing the dot size accordingly. This is attributed to the size dependent quantum confinement effect of excitons. When the radius of QD is comparable to the bulk exciton Bohr radius, the photoinduced exciton experiences strong spatial confinement in all dimensions which subsequently leads to the quantization of electronic states [1, 5, 32]. In conformity with the quantum mechanics prediction, the continuum in the density of states of a three dimensional bulk phase will reduce to the discrete states of an ideal zero dimensional QD. The band edge will be appreciably separated from the upper ladder of energy levels. Therefore, the absorption profile of pseudo-zero dimensional QD exhibits several discrete features with well resolved band edge state [7]. In the strong confinement regime, the dependence of energy shift on dot size is elementarily analogous to the particle in one dimensional well model. As the size of QD is reduced, the band edge shifts to higher energy level which results in the blue shift of the absorption and in turn, the emission. With the simple effective mass approximated energy band structure of bulk material, the excitonic shift of QD scales as $1/r^2$, where r is the dot radius [33, 34]. However, there is a substantial discrepancy between the experimental data and the theoretical prediction based on the parabolic band assumption [7, 34]. A more rigorous approach is needed to precisely model the size correlation of QD band edge.

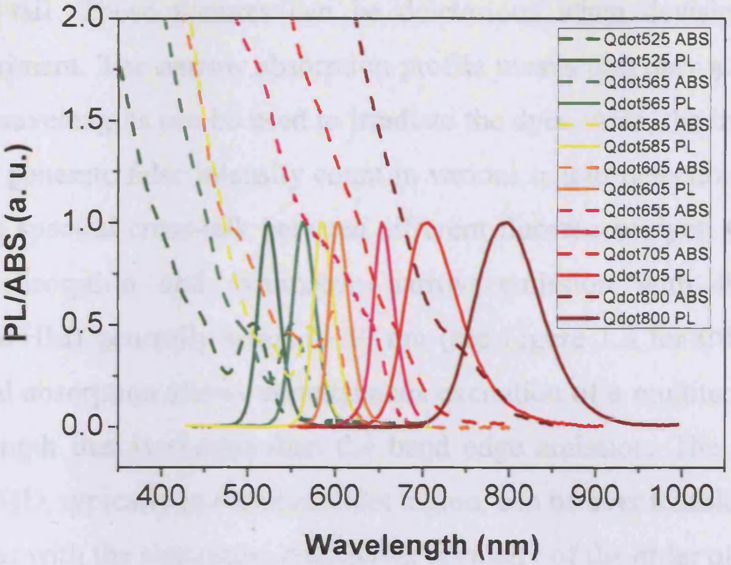

Figure 1.3: Photoluminescence and absorption spectra of commercial Invitrogen Qdot series. From Qdot525 to Qdot655 are CdSe/ZnS core-shell QDs and from Qdot705 to Qdot800 are CdTe/ZnS core-shell QDs. Data is acquired from Ref. [35], courtesy of Invitrogen.

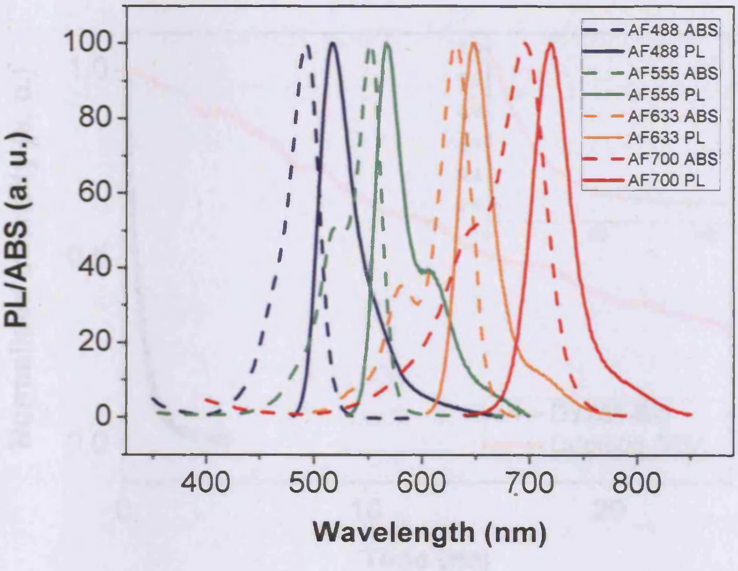

Figure 1.4: Photoluminescence and absorption spectra of Alexa Fluor (AF) dye series. Data is acquired from Ref. [35], courtesy of Invitrogen.

As exemplified in Figure 1.3 and 1.4, there are contrasting differences in the emission and the absorption lineshapes between semiconductor QDs and molecular dyes. In general, organic dyes have narrow absorption and asymmetric broad emission with extended red tail. These features can be deleterious when devising a multicolour imaging experiment. The narrow absorption profile means that only a limited selection of excitation wavelengths can be used to irradiate the dyes. Also, the intrinsic red tail of emission may generate false intensity count in various colour detection channels due to a considerable spectral cross-talk between different fluorescent dyes. Conversely, QDs have broad absorption and symmetric narrow emission with full-width-at-half-maximum (FWHM) generally around ~30 nm (see Figure 1.3 for CdSe Qdots) [8, 9, 29]. The broad absorption allows simultaneous excitation of a multitude of QDs with a single wavelength that is shorter than the band edge emission. The molar extinction coefficient of QD, typically in the ultraviolet region, can be over tenfold higher than that of organic dyes with the absorption coefficient normally of the order of 100 000 $M^{-1}cm^{-1}$ [29, 36]. Moreover, less constraint is placed on the multiplexing of QDs owing to the narrow fluorescence linewidth that the signal overlap is minimal. In concert with the fact that QDs are remarkably photostable [19, 21, 29], these favourable spectroscopic features invariably makes QDs the ideal fluorescent labels in bio-applications especially in a long term multicolour imaging.

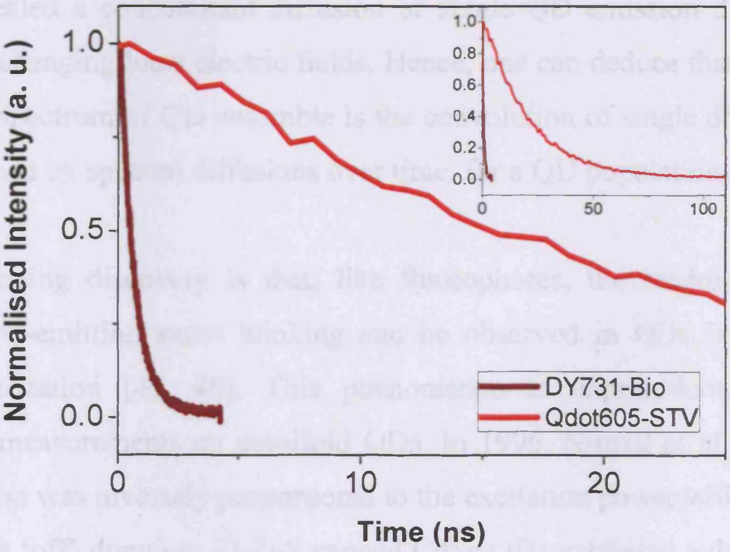

Figure 1.5: Comparison of fluorescence decays between DY731-Bio molecular dye and Qdot605-STV semiconductor QD ensemble. The inset shows the full decay of Qdot605-STV.

Neglecting the heterogeneity of QD fluorescence decay temporarily, as depicted in Figure 1.5, the time for dye photoluminescence to decay to 1/e of its initial intensity is distinctively shorter than that of inorganic QDs. The fluorescence lifetimes of conventional organic dyes are typically in the order of few nanoseconds [37, 38] but contrarily the lifetimes of QDs can approach to 20 ns or beyond that [39-41]. In a time-gated detection system equipped with pulsed excitation source, the long fluorescence decay of QDs can be exploited in suppressing the background noise from short lived autofluorescence by carefully tuning the photon detection time window after every laser pulse [29, 42, 43]. The merit is that the complete removal of autofluorescence signal is possible without losing important spectral information. Therefore, a greater contrast between QD labelled biomolecules and unlabelled background can be attained in a cell imaging.

With the recent development of single dot spectroscopy, some interesting characteristics of single QD which are previously obscured by the inhomogeneities of QD ensemble can now be observed. Following that, new frontiers of QD photophysics have been unravelled since. One, the emission linewidth of single QD was found to be several-fold narrower than QD ensemble [44]. At cryogenic temperatures, the linewidth of single QD emission as narrow as 120 μeV was resolved [44]. In the same context, Empedocles et al also revealed a concomitant diffusion of single QD emission that was possibly caused by the changing local electric fields. Hence, one can deduce that the steady state luminescence spectrum of QD ensemble is the convolution of single dot spectra, which can be broadened by spectral diffusions over time, for a QD population with a finite size variation.

A more interesting discovery is that, like fluorophores, the random 'on' (emitting state)/'off' (non-emitting state) blinking can be observed in QDs in close-up under continuous excitation [45, 46]. This phenomenon is unprecedented in ensemble spectroscopic measurements on manifold QDs. In 1996, Nirmal et al first reported: i) the 'on' duration was inversely proportional to the excitation power while no correlation was seen in the 'off' duration; ii) ZnS capped CdSe QDs exhibited a drastic increase in 'on' and 'off' periods as compared to TOPO capped CdSe QDs [45]. Based on the experimental findings, they arrived at a postulation that the fluorescence intermittence was attributed to the photoionisation of single QD leading to the localisation of one carrier (electron or hole) outside the core. The hypothesis is implicitly supported by the evidence of photoinduced positive charge of single CdSe QDs upon continuous illumination as revealed by means of electrostatic force microscopic measurement, albeit it lacks the direct link between dark state and charged QD that might have been hindered by the difficulty of devising a simultaneous detection of surface charge and fluorescence signal [47]. Therefore, ultrafast nonradiative Auger recombination in the order of picoseconds is usually used to rationalise the non-emissive state of ionised QD since it can be an efficient relaxation channel in a three-carrier system [48, 49]. When a neutral ground state QD is initially photoexcited, electron or hole can be localised outside the core via carrier trapping by surface states or tunnelling to external traps primarily leaving a lone core residing carrier [50, 51]. This process results in a charged QD (presumably also refers to the core of a core-shell QD). Upon further excitation, the new photoinduced electron-hole pair can relax to ground state via Auger recombination in the presence of the proximal lone carrier. The Auger relaxation can involve exciton-electron or exciton-hole interactions. The QD restores to charge neutrality, hence, the emissive state once the ejected carrier is recovered. In the light of the strong dependence on the ejection/recovery of charge to/from exterior, surface morphology and local environment must play an important role in governing the dynamics of 'on'/'off' blinking [52-54].

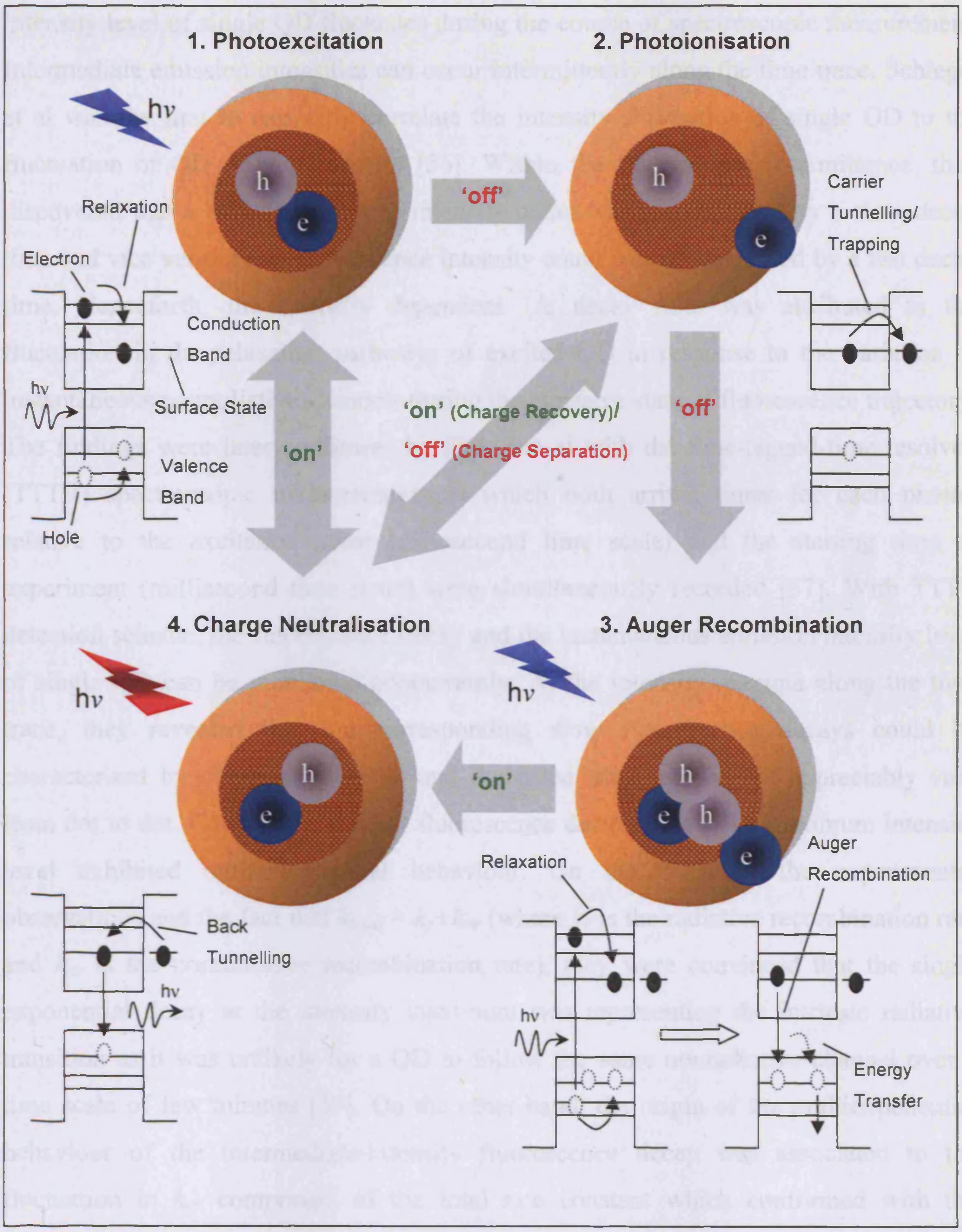

Figure 1.6: Diagram of an exemplary model based on the concept of three-particle Auger relaxation mechanism to corroborate the observation of dark ('off') state in single QD. The illustration further delineates the postulated ionisation (charging) cycle of a QD which results in the binary like 'on'/'off' photoluminescence trajectory. Adapted from Ref. [55].

Although the phenomenon of single dot blinking in various conditions has been extensively studied, a perfect binary photoluminescence trajectory with a constant intensity level during 'on' times is rarely found. Instead, most often, the recorded 'on' intensity level of single QD fluctuates during the course of spectroscopic measurement. Intermediate emission intensities can occur intermittently along the time trace. Schlegel et al was the first to explicitly correlate the intensity fluctuation of single QD to the fluctuation of QD decay dynamics [56]. Within the fluorescence intermittence, they discovered that a high fluorescence intensity count was accompanied by a slow decay time and vice versa a low fluorescence intensity count was accompanied by a fast decay time. Henceforth, the intensity dependent 1/e decay time was attributed to the fluctuation in the relaxation pathways of excited QD in response to the variation of instantaneous nonradiative channels during the emissive state of fluorescence trajectory. The findings were later confirmed by Fisher et al with the time-tagged-time-resolved (TTTR) spectroscopic measurements in which both arrival times for each photon relative to the excitation pulse (nanosecond time scale) and the starting time of experiment (millisecond time scale) were simultaneously recorded [57]. With TTTR detection scheme, the fluorescence decay and the instantaneous emission intensity level of single QD can be monitored concurrently. At the intensity maxima along the time trace, they revealed that the corresponding slow fluorescence decays could be characterised by single exponential and the fitted lifetimes did not appreciably vary from dot to dot. Conversely, the fast fluorescence decays below the maximum intensity level exhibited multiexponential behaviour. On the basis of the experimental observations and the fact that $k_{total} = k_r + k_{nr}$ (where k_r is the radiative recombination rate and k_{nr} is the nonradiative recombination rate), they were convinced that the single exponential decay at the intensity maximum was representing the intrinsic radiative transition as it was unlikely for a QD to follow the same nonradiative channel over a time scale of few minutes [57]. On the other hand, the origin of the multiexponential behaviour of the intermediate-intensity fluorescence decay was associated to the fluctuation in k_{nr} component of the total rate constant which conformed with the Schlegel et al hypothesis. Hereby, the variation of relaxation processes over time as highlighted by the inconsistency of intensity dependent 1/e decay time underpins the non-single exponential characteristic observed in time averaged ensemble and even single dot fluorescence decays.

1.3 Quantum Dots in FRET

FRET, the acronym for fluorescence (Förster) resonance energy transfer is a near field dipole-dipole interaction that involves the radiationless energy transfer from an excited molecule (donor) to a proximal resonant molecule in a relaxed state (acceptor) [58]. Due to its sensitivity in the nanometer range (typically below 100 Å) and its practicability in spectroscopic measurements, FRET has been widely applied in the studies of biomolecular conformations and dynamics [37, 58, 59]. However, the majority of FRET studies only concern organic matter. In 1996, Kagan and coworkers were the first to incorporate FRET concepts in the investigation of dot-to-dot interaction [60, 61]. Luminescence quenching of smaller dots (38.5 Å) along with luminescence enhancement of larger dots (62 Å) in a closely packed mixed CdSe QD solid were detected. The intensity changes in the mixed QD solid film were consistent with FRET process that nonradiative energy transfer from small QD donors to large QD acceptors in the vicinity was feasible upon photoexcitation due to the exceptional spectral overlap between 38.5 Å QD emission and 62 Å QD absorption. The FRET interpretation of interdot interactions was further warranted by the independent time domain spectroscopic measurements in which a decrease in the fluorescence decay time of large QDs and an increase in the fluorescence decay time of small QDs for the close-packed mixed QD solid were recorded [60, 61]. Besides that, they also noticed a perceptible spectral red shift and linewidth narrowing in single QD solids relative to the control QD solutions which arisen from the size disparity within the single QD ensembles. Due to the considerable inhomogeneity of QD population, the proximity between neighbouring QDs in close-packed solid favoured the nonradiative energy migration from smaller QDs to larger QDs subsequently contributing to the quenching of the blue side and the enhancement of the red side of QD ensemble emission. The observation of FRET signatures in single QD solids was consistent with the time-resolved studies performed by Crooker et al [62]. A systematic increase in the fluorescence lifetime with increasing wavelength (increasing dot size) i.e. from 1.9 ns time constant at high energy end to 22 ns time constant at low energy end was extracted from single CdSe/ZnS QD close-packed solid. By contrast, no discernible variation of lifetime as a function of energy was predicated for the same QDs dispersed in solution. This again elucidates the efficient energy coupling from smaller QDs to proximal resonant larger QDs within a densely packed monodisperse QD population. Although the effectiveness of interdot energy coupling has been verified, the compatibility of QDs as FRET donors in biological applications remains to be identified.

In 2001, Willard et al demonstrated the use of core-shell QDs as FRET donors in a streptavidin-biotin binding assay [63]. CdSe/ZnS QDs covalently attached to biotinyated bovine serum albumin (bBSA) functioned as the energy donors while streptavidin labelled tetramethylrhodamine fluorophores (STV-TMR) acted as the energy acceptors. Via the ligand-receptor binding scheme, the spatial distance between QDs and TMR were minimised for efficient donor-to-acceptor energy transfer upon the photoexcitation of QDs. In the titration of QD with TMR, a dramatic reduction of QD emission intensity was observed with increasing concentration of TMR. In parallel, a FRET induced enhancement of TMR luminescence was measured. However, the report lacked the concrete lifetime data to support the FRET interpretation. A more extensive study of QD in biological FRET context was later led by Mattoussi and coworkers. In 2003, Medintz et al took an alternative approach in the surface modification of CdSe/ZnS core-shell QDs with histidine terminated maltose-binding protein (MBP-his) [64]. The adopted binding scheme allowed the self-coordination of liganded QSY9 dark quenchers (non-fluorescent light absorbing moiety) around MBP tagged QDs. Upon the formation of QD-MBP-QSY9 assays, a pronounced reduction in the QD fluorescence intensity and the QD fluorescence decay time were detected. On further elaboration, the initial QD dynamics were recovered once the donor-acceptor interaction was inhibited by the displacement of QSY9 with maltose (MBP's preferred binding moiety). The results were essential proofs of QD as a competent energy donor that could be exploited in building FRET nanosensing precursors. Hence, more explicit FRET studies on QDs in a range of diverse assay configurations were conducted by the same research team.

For instance, three different size groups of QDs emitting at 510 nm, 530 nm and 555 nm were used as FRET donors that chemically coupled to multiple Cy3 fluorescent molecules in similar MBP binding route [65]. By carefully size-tuning the emission peak of QDs, the magnitude of spectral overlap integral, hence, the FRET interaction between QDs and proximal Cy3 was optimized. This was reflected by the trend in FRET efficiency based on steady state measurements where 555 nm and 530 nm emitting QDs which strongly resonant with Cy3 displayed a greater luminescence quenching effect with increasing labelling ratio comparatively to 510 nm emitting QDs. FRET efficiency around 0.8 was reported for respective 530 nm and 550 nm QDs at a ratio of 10 Cy3 per QD. On the contrary, at the same Cy3 loading, 510 nm QDs contributed an overall efficiency of merely ~0.6. The steady state FRET analysis was further complemented with time-resolved measurements showing a systematic increase of decay rate with increasing number of immobilised Cy3. Besides revealing the suitability of QD as efficient energy donor, the article also highlighted the advantage of size tunable QD emission in maximising the energy coupling between inorganic QDs and organic dyes under the condition that the size of QD is not excessively larger than R_0 (the donor-acceptor separation at which the efficiency is 0.5). Other examples of successful profiling of QDs as FRET donors in bioassay prototyping have been indicated in numerous studies performed by Mattoussi and coworkers [66-68].

Having experimentally justified the feasibility of QDs as energy donors, they assessed the future exploitation of QDs as FRET acceptors [69]. In the FRET experiment, three variant QD-MBP-dye self-assemblies were investigated: i) 555 nm emitting QD as acceptor and AF488 dye as donor, ii) 570 nm emitting QD as acceptor and AF488 as donor and iii) 590 nm emitting QD as acceptor and Cy3 as donor. However, no apparent FRET manifestations i.e. luminescence quenching of dyes (donors) and luminescence enhancement of QDs (acceptors) were detected in all combinations of FRET assays, albeit there was a substantial spectral overlap between QD absorption and dye emission. The negative outcome was attributed to the undesirable decay rates of fluorescent dyes which were typically several-fold greater than that of QDs along with the high absorption coefficient of QDs at the excitation wavelength which unavoidably caused a pronounced direct excitation of QDs. To prove the point, they labelled 610 nm QDs with ruthenium fluorophores that have long lifetime of the order of 400 ns. In this configuration, a significant drop in the decay time of ruthenium from 419 ns to 160 ns was deduced from time-resolved measurements. The observation was consistent with their explanations and hence this underlines the important fact that QDs can be used as viable FRET acceptors only if long lived fluorescent donors are selected.

In a recent QD FRET study, Levy et al reported on the use of commercial Invitrogen Qdot525 as energy coupler in FRET assemblies via streptavidin-biotin binding approach [70]. Qdot525 was surface functionalised with streptavidin to specifically target biotinylated oligonucleotide that bound to single/double Eclipse dark quenchers. In a titration experiment, a systematic loss of Qdot525 emission intensity was observed at rising number of singly/doubly labelled oligonucleotides. FRET responded exceptionally well with doubly labelled oligonucleotide complex showing near 100 % quenching efficiency. Despite that, the merits of such bioassay prototype were yet to be warranted by additional lifetime data. Along with Levy et al, Grecco et al also incorporated commercial streptavidin functionalised Qdot585 in a series of titrations with biotinylated AF594 [71]. Because of the strong affinity of streptavidin for biotin, AF594 acceptors were brought in the close vicinity of Qdot585 which could facilitate FRET interaction between resonant analytes. Hence, a progressive increment in FRET efficiency with increasing concentration of AF594 was reported. In addition, they claimed a quenching efficiency of 0.85 was attained at ~1 acceptor-to-QD ratio. This, however, remains controversial considering the physical size of Qdot585 and the calculated R_0 of 64 Å. Oh and coworkers utilised streptavidin modified Invitrogen Qdot (though not specified) as energy donor in a FRET inhibition study [72]. Upon conjugation with biotinylated gold nanoparticles (AuNP), over 80 % of Qdot luminescence was quenched. However, the photoluminescence of Qdot was quickly restored to the initial intensity by the displacement of AuNPs with avidin substrates since avidin has far superior affinity for biotin relatively to streptavidin. The luminescence recovery in retrospect indicated the specific binding of AuNPs on Qdot which in turn favoured the photoinduced energy migration from Qdot to proximal energetically resonant AuNP that subsequently contributed to the substantial quenching of Qdot photoluminescence. Probably because of the physical dimension of QDs, it seems apparent that all of the QD FRET investigations performed so far assert a crucial criterion that QDs must be attached to multiple acceptors for devising an efficient dipole-dipole interaction.

1.4 Project Motivation

Semiconductor QDs are attractive fluorescent particles in a sense that they are exceptionally photo- and chemically stable together with other unique photophysical properties i.e. high quantum yield, broad absorption and symmetric narrow emission. QD can be an ideal tool in building a robust FRET based bioassays. Although the application of QD as FRET donor in a variety of conjugation strategies has been widely examined, the majority of QD emission spectra were mainly centred on the visible spectral region, typically within 500 nm to 600 nm wavelength range. So far, no FRET assays entailing QDs in the far-red spectrum have been reported. Hence, it will be beneficial to investigate the FRET interaction explicitly tailored in the far-red spectral region. From a biological perspective, there are merits in extending fluorescence sensing applications into the far-red regime: i) less absorption by biological tissues occurs in far-red, thus, more fluorescence signal is transmitted, ii) biomolecular autofluorescence in the visible region is avoided, thus, the sensitivity of fluorescence over background is enhanced [37]. In the preliminary development of far-red FRET bioassays, we have selected commercial streptavidin functionalised Qdot705-STV (Invitrogen) that emits at ~700 nm as the energy donor and biotinylated DY731-Bio (MoBiTec) molecular dye that is strongly resonant with Qdot705-STV as the energy acceptor. Via streptavidin-biotin association, multiple DY731-Bio molecules can self-coordinate around a Qdot705-STV which may eventually induce dipole-dipole interactions between QD and proximal fluorophores given the donor-acceptor distance is succinctly conducive to FRET. Along with that, we have also devised FRET pairs in the visible region constituted of streptavidin functionalised Qdot585-STV (Invitrogen) and biotinylated AF594-Bio dye (Invitrogen). This approach is taken in view of the fact that Qdot705-STV and Qdot585-STV are distinctively different in composition as well as in physical geometry [31, 73]. Comparative studies on the photophysical properties of Qdot585-STV and Qdot705-STV and the implications of that on the efficiency of nonradiative transfer in a donor-acceptor configuration are therefore necessary. To evaluate the QD-dye FRET interaction, we utilise both steady state and temporal spectroscopic techniques. Lifetime measurements not only complement but also warrant the FRET analysis based on steady state fluorescence. Henceforth, a more reliable conclusion can be predicated from the experimental data.

1.5 Thesis Overview

In general, the thesis describes the investigations of semiconductor nanocrystals as energy donors in FRET interactions in the visible spectrum and this extends to the far-red spectral region, based on the commercial Qdot585-STV and Qdot705-STV. Following this chapter, Chapter 2 proceeds with a brief outline on the principles of FRET and the basic structural and optical characteristics of Qdot nanoparticles i.e. Qdot585-STV and Qdot705-STV. Then, Chapter 3 moves on to elaborating the details of experimental procedures employed in the preparation of QD-dye conjugated samples and the experimental setups used in the steady state and time-resolved spectroscopic characterisations of analytes i.e. Qdot585-STV, Qdot705-STV, AF594-Bio, DY731-Bio, AF594-Bio-STV and DY731-Bio-STV and donor-acceptor FRET pairs. On the basis of steady state and lifetime data, Chapter 4 presents the qualitative and quantitative analyses of FRET interactions between Qdot585-STV and AF594-Bio in a titration experiment and after size exclusion purification. Next, Chapter 5 reports on the FRET coupling between Qdot705-STV and DY731-Bio in a titration and after centrifugation with filter devices. Following that, some computational work, within the framework of 2-step finite spherical well model, to gain some insights into the photophysics of Qdot585-STV and Qdot705-STV are described in Chapter 6. The thesis ends with some conclusions highlighting the experimental findings elicited and the complicated issues arising from Qdot585-STV-AF594-Bio and Qdot705-STV-DY731-Bio FRET assay development and this is followed by some suggestions in regard to the future work of FRET research on QDs.

1.6 References

1. Alivisatos AP. Semiconductor Clusters, Nanocrystals, and Quantum Dots. *Science* 1996, **271**(5251):933-937.

2. Steigerwald ML, Alivisatos AP, Gibson JM, Harris TD, Kortan R, Muller AJ, Thayer AM, Duncan TM, Douglass DC, Brus LE. Surface Derivatization and Isolation of Semiconductor Cluster Molecules. *J Am Chem Soc* 1988, **110**(10):3046-3050.

3. Kortan AR, Hull R, Opila RL, Bawendi MG, Steigerwald ML, Carroll PJ, Brus LE. Nucleation and Growth of CdSe on ZnS Quantum Crystallite Seeds, and Vice Versa, in Inverse Micelle Media. *J Am Chem Soc* 1990, **112**(4):1327-1332.

4. Rossetti R, Nakahara S, Brus LE. Quantum Size Effects in the Redox Potentials, Resonance Raman-Spectra, and Electronic-Spectra of CdS Crystallites in Aqueous Solution. *J Chem Phys* 1983, **79**(2):1086-1088.

5. Brus L. Zero-Dimensional Excitons in Semiconductor Clusters. *IEEE J Quantum Electron* 1986, **22**(9):1909-1914.

6. Brus L. Electronic Wave-Functions in Semiconductor Clusters - Experiment and Theory. *J Phys Chem* 1986, **90**(12):2555-2560.

7. Murray CB, Norris DJ, Bawendi MG. Synthesis and Characterization of Nearly Monodisperse CdE (E = S, Se, Te) Semiconductor Nanocrystallites. *J Am Chem Soc* 1993, **115**(19):8706-8715.

8. Hines MA, Guyot-Sionnest P. Synthesis and Characterization of Strongly Luminescencing ZnS-Capped CdSe Nanocrystals. *J Phys Chem* 1996, **100**(2):468-471.

9. Dabbousi BO, RodriguezViejo J, Mikulec FV, Heine JR, Mattoussi H, Ober R, Jensen KF, Bawendi MG. (CdSe)ZnS Core-Shell Quantum Dots: Synthesis and Characterization of a Size Series of Highly Luminescent Nanocrystallites. *Journal of Physical Chemistry B* 1997, **101**(46):9463-9475.

10. Peng XG, Schlamp MC, Kadavanich AV, Alivisatos AP. Epitaxial Growth of Highly Luminescent CdSe/CdS Core/Shell Nanocrystals with Photostability and Electronic Accessibility. *J Am Chem Soc* 1997, **119**(30):7019-7029.

11. Peng ZA, Peng XG. Formation of High-Quality CdTe, CdSe, and CdS Nanocrystals Using CdO as Precursor. *J Am Chem Soc* 2001, **123**(1):183-184.

12. Peng XG. Green Chemical Approaches toward High-Quality Semiconductor Nanocrystals. *Chemistry-a European Journal* 2002, **8**(2):335-339.

13. Aldana J, Wang YA, Peng XG. Photochemical Instability of CdSe Nanocrystals Coated by Hydrophilic Thiols. *J Am Chem Soc* 2001, **123**(36):8844-8850.

14. Donega CD, Hickey SG, Wuister SF, Vanmaekelbergh D, Meijerink A. Single-Step Synthesis to Control the Photoluminescence Quantum Yield and Size Dispersion of CdSe Nanocrystals. *Journal of Physical Chemistry B* 2003, **107**(2):489-496.

15. Qu LH, Peng ZA, Peng XG. Alternative Routes toward High Quality CdSe Nanocrystals. *Nano Letters* 2001, **1**(6):333-337.

16. Wuister SF, van Driel F, Meijerink A. Luminescence and Growth of CdTe Quantum Dots and Clusters. *Physical Chemistry Chemical Physics* 2003, **5**(6):1253-1258.

17. Talapin DV, Rogach AL, Kornowski A, Haase M, Weller H. Highly Luminescent Monodisperse CdSe and CdSe/ZnS Nanocrystals Synthesized in a Hexadecylamine-Trioctylphosphine Oxide-Trioctylphospine Mixture. *Nano Letters* 2001, **1**(4):207-211.

18. Talapin DV, Haubold S, Rogach AL, Kornowski A, Haase M, Weller H. A Novel Organometallic Synthesis of Highly Luminescent CdTe Nanocrystals. *Journal of Physical Chemistry B* 2001, **105**(12):2260-2263.

19. Chan WCW, Nie SM. Quantum Dot Bioconjugates for Ultrasensitive Nonisotopic Detection. *Science* 1998, **281**(5385):2016-2018.

20. Mattoussi H, Mauro JM, Goldman ER, Anderson GP, Sundar VC, Mikulec FV, Bawendi MG. Self-Assembly of CdSe-ZnS Quantum Dot Bioconjugates Using an Engineered Recombinant Protein. *J Am Chem Soc* 2000, **122**(49):12142-12150.

21. Wu XY, Liu HJ, Liu JQ, Haley KN, Treadway JA, Larson JP, Ge NF, Peale F, Bruchez MP. Immunofluorescent Labeling of Cancer Marker Her2 and Other Cellular Targets with Semiconductor Quantum Dots. *Nature Biotechnology* 2003, **21**(1):41-46.

22. Pellegrino T, Manna L, Kudera S, Liedl T, Koktysh D, Rogach AL, Keller S, Radler J, Natile G, Parak WJ. Hydrophobic Nanocrystals Coated with an Amphiphilic Polymer Shell: A General Route to Water Soluble Nanocrystals. *Nano Letters* 2004, **4**(4):703-707.

23. Michalet X, Pinaud FF, Bentolila LA, Tsay JM, Doose S, Li JJ, Sundaresan G, Wu AM, Gambhir SS, Weiss S. Quantum Dots for Live Cells, In Vivo Imaging, and Diagnostics. *Science* 2005, **307**(5709):538-544.

24. Kloepfer JA, Bradforth SE, Nadeau JL. Photophysical Properties of Biologically Compatible CdSe Quantum Dot Structures. *Journal of Physical Chemistry B* 2005, **109**(20):9996-10003.

25. Dollefeld H, Hoppe K, Kolny J, Schilling K, Weller H, Eychmuller A. Investigations on the Stability of Thiol Stabilized Semiconductor Nanoparticles. *Physical Chemistry Chemical Physics* 2002, **4**(19):4747-4753.

26. Eychmuller A, Rogach AL. Chemistry and Photophysics of Thiol-Stabilized II-VI Semiconductor Nanocrystals. *Pure and Applied Chemistry* 2000, **72**(1-2):179-188.

27. Gaponik N, Talapin DV, Rogach AL, Hoppe K, Shevchenko EV, Kornowski A, Eychmuller A, Weller H. Thiol-Capping of CdTe Nanocrystals: An Alternative to Organometallic Synthetic Routes. *Journal of Physical Chemistry B* 2002, **106**(29):7177-7185.

28. Parak WJ, Pellegrino T, Plank C. Labelling of Cells with Quantum Dots. *Nanotechnology* 2005, **16**(2):R9-R25.

29. Bruchez M, Moronne M, Gin P, Weiss S, Alivisatos AP. Semiconductor Nanocrystals as Fluorescent Biological Labels. *Science* 1998, **281**(5385):2013-2016.

30. EviDots and EviComposites: Commercially Available Quantum Dots for Wide Range of Novel Semiconductor Applications. Evident Technologies, 2005.

31. Qdot Streptavidin Conjugates User Manual. Invitrogen, 2006.

32. Alivisatos AP. Perspectives on the Physical Chemistry of Semiconductor Nanocrystals. *J Phys Chem* 1996, **100**(31):13226-13239.

33. Brus LE. Electron-Electron and Electron-Hole Interactions in Small Semiconductor Crystallites - The Size Dependence of the Lowest Excited Electronic State. *J Chem Phys* 1984, **80**(9):4403-4409.

34. Wang Y, Herron N. Nanometer-Sized Semiconductor Clusters - Materials Synthesis, Quantum Size Effects, and Photophysical Properties. *J Phys Chem* 1991, **95**(2):525-532.

35. http://probes.invitrogen.com/servlets/spectra/

36. http://probes.invitrogen.com/servlets/datatable?id=38089

37. Lakowicz J. Principles of Fluorescence Spectroscopy. 3rd Edition. Springer, 2006.

38. Strickler SJ, Berg RA. Relationship between Absorption Intensity and Fluorescence Lifetime of Molecules. *Journal Chemical Physics* 1962, **37**(4):814-822.

39. Kapitonov AM, Stupak AP, Gaponenko SV, Petrov EP, Rogach AL, Eychmuller A. Luminescence Properties of Thiol-Stabilized CdTe Nanocrystals. *Journal of Physical Chemistry B* 1999, **103**(46):10109-10113.

40. Nirmal M, Norris DJ, Kuno M, Bawendi MG, Efros AL, Rosen M. Observation of the Dark Exciton in CdSe Quantum Dots. *Phys Rev Lett* 1995, **75**(20):3728-3731.

41. Javier A, Magana D, Jennings T, Strouse GF. Nanosecond Exciton Recombination Dynamics in Colloidal CdSe Quantum Dots under Ambient Conditions. *Applied Physics Letters* 2003, **83**(7):1423-1425.

42. Dahan M, Laurence T, Pinaud F, Chemla DS, Alivisatos AP, Sauer M, Weiss S. Time-Gated Biological Imaging by Use of Colloidal Quantum Dots. *Optics Letters* 2001, **26**(11):825-827.

43. Michalet X, Pinaud F, Lacoste TD, Dahan M, Bruchez MP, Alivisatos AP, Weiss S. Properties of Fluorescent Semiconductor Nanocrystals and Their Application to Biological Labeling. *Single Molecules* 2001, **2**(4):261-276.

44. Empedocles SA, Norris DJ, Bawendi MG. Photoluminescence Spectroscopy of Single CdSe Nanocrystallite Quantum Dots. *Phys Rev Lett* 1996, **77**(18):3873-3876.

45. Nirmal M, Dabbousi BO, Bawendi MG, Macklin JJ, Trautman JK, Harris TD, Brus LE. Fluorescence Intermittency in Single Cadmium Selenide Nanocrystals. *Nature* 1996, **383**(6603):802-804.

46. Nirmal M, Brus L. Luminescence Photophysics in Semiconductor Nanocrystals. *Accounts Chem Res* 1999, **32**(5):407-414.

47. Krauss TD, Brus LE. Charge, Polarizability, and Photoionization of Single Semiconductor Nanocrystals. *Phys Rev Lett* 1999, **83**(23):4840-4843.

48. Efros AL, Rosen M. Random Telegraph Signal in the Photoluminescence Intensity of a Single Quantum Dot. *Phys Rev Lett* 1997, **78**(6):1110-1113.

49. Klimov VI, McBranch DW, Leatherdale CA, Bawendi MG. Electron and Hole Relaxation Pathways in Semiconductor Quantum Dots. *Phys Rev B* 1999, **60**(19):13740-13749.

50. Verberk R, van Oijen AM, Orrit M. Simple Model for The Power-Law Blinking of Single Semiconductor Nanocrystals. *Phys Rev B* 2002, **66**(23).

51. Gomez DE, van Embden J, Jasieniak J, Smith TA, Mulvaney P. Blinking and Surface Chemistry of Single CdSe Nanocrystals. *Small* 2006, **2**(2):204-208.

52. Issac A, von Borczyskowski C, Cichos F. Correlation between Photoluminescence Intermittency of CdSe Quantum Dots and Self-Trapped States in Dielectric Media. *Phys Rev B* 2005, **71**(16).

53. Hohng S, Ha T. Near-Complete Suppression of Quantum Dot Blinking in Ambient Conditions. *J Am Chem Soc* 2004, **126**(5):1324-1325.

54. Koberling F, Mews A, Basche T. Oxygen-Induced Blinking of Single CdSe Nanocrystals. *Adv Mater* 2001, **13**(9):672-676.

55. Shimizu K. Spectroscopy and External Control of Optical Dynamics in Single Semiconductor Nanocrystals. Massachusetts Institute of Technology, 2002.

56. Schlegel G, Bohnenberger J, Potapova I, Mews A. Fluorescence Decay Time of Single Semiconductor Nanocrystals. *Phys Rev Lett* 2002, **88**(13).

57. Fisher BR, Eisler HJ, Stott NE, Bawendi MG. Emission Intensity Dependence and Single-Exponential Behavior in Single Colloidal Quantum Dot Fluorescence Lifetimes. *Journal of Physical Chemistry B* 2004, **108**(1):143-148.

58. Stryer L. Fluorescence Energy-Transfer as a Spectroscopic Ruler. *Annu Rev Biochem* 1978, **47**:819-846.

59. Steinberg IZ. Long-Range Nonradiative Transfer of Electronic Excitation Energy in Proteins and Polypeptides. *Annu Rev Biochem* 1971, **40**:83-114.

60. Kagan CR, Murray CB, Nirmal M, Bawendi MG. Electronic Energy Transfer in CdSe Quantum Dot Solids. *Phys Rev Lett* 1996, **76**(9):1517-1520.

61. Kagan CR, Murray CB, Bawendi MG. Long-Range Resonance Transfer of Electronic Excitations in Close-Packed CdSe Quantum-Dot Solids. *Phys Rev B* 1996, **54**(12):8633-8643.

62. Crooker SA, Hollingsworth JA, Tretiak S, Klimov VI. Spectrally Resolved Dynamics of Energy Transfer in Quantum-Dot Assemblies: Towards Engineered Energy Flows in Artificial Materials. *Phys Rev Lett* 2002, **89**(18).

63. Willard DM, Carillo LL, Jung J, Van Orden A. CdSe-ZnS Quantum Dots as Resonance Energy Transfer Donors in a Model Protein-Protein Binding Assay. *Nano Letters* 2001, **1**(9):469-474.

64. Medintz IL, Clapp AR, Mattoussi H, Goldman ER, Fisher B, Mauro JM. Self-Assembled Nanoscale Biosensors Based on Quantum Dot FRET Donors. *Nature Materials* 2003, **2**(9):630-638.

65. Clapp AR, Medintz IL, Mauro JM, Fisher BR, Bawendi MG, Mattoussi H. Fluorescence Resonance Energy Transfer between Quantum Dot Donors and Dye-Labeled Protein Acceptors. *J Am Chem Soc* 2004, **126**(1):301-310.

66. Goldman ER, Medintz IL, Whitley JL, Hayhurst A, Clapp AR, Uyeda HT, Deschamps JR, Lassman ME, Mattoussi H. A Hybrid Quantum Dot-Antibody Fragment Fluorescence Resonance Energy Transfer-Based TNT Sensor. *J Am Chem Soc* 2005, **127**(18):6744-6751.

67. Clapp AR, Medintz IL, Uyeda HT, Fisher BR, Goldman ER, Bawendi MG, Mattoussi H. Quantum Dot-Based Multiplexed Fluorescence Resonance Energy Transfer. *J Am Chem Soc* 2005, **127**(51):18212-18221.

68. Medintz IL, Sapsford KE, Clapp AR, Pons T, Higashiya S, Welch JT, Mattoussi H. Designer Variable Repeat Length Polypeptides as Scaffolds for Surface Immobilization of Quantum Dots. *Journal of Physical Chemistry B* 2006, **110**(22):10683-10690.

69. Clapp AR, Medintz IL, Fisher BR, Anderson GP, Mattoussi H. Can Luminescent Quantum Dots Be Efficient Energy Acceptors with Organic Dye Donors? *J Am Chem Soc* 2005, **127**(4):1242-1250.

70. Levy M, Cater SF, Ellington AD. Quantum-Dot Aptamer Beacons for The Detection of Proteins. *Chembiochem* 2005, **6**(12):2163-2166.

71. Grecco HE, Lidke KA, Heintzmann R, Lidke DS, Spagnuolo C, Martinez OE, Jares-Erijman EA, Jovin TM. Ensemble and Single Particle Photophysical Properties (Two-Photon Excitation, Anisotropy, FRET, Lifetime, Spectral Conversion) of Commercial Quantum Dots in Solution and in Live Cells. *Microscopy Research and Technique* 2004, **65**(4-5):169-179.

72. Oh E, Hong MY, Lee D, Nam SH, Yoon HC, Kim HS. Inhibition Assay of Biomolecules Based on Fluorescence Resonance Energy Transfer (FRET) between Quantum Dots and Gold Nanoparticles. *J Am Chem Soc* 2005, **127**(10):3270-3271.

73. Giepmans BNG, Deerinck TJ, Smarr BL, Jones YZ, Ellisman MH. Correlated Light and Electron Microscopic Imaging of Multiple Endogenous Proteins Using Quantum Dots. *Nature Methods* 2005, **2**(10):743-749.

CHAPTER 2:

FRET PRINCIPLES AND INTRODUCTION TO QDOT NANOPARTICLES

CONTENTS:

Abstract: This chapter highlights the important aspects of FRET theory and introduces the concept of dipolar energy coupling into the analyses of quantum dot based multiplexes. This is then followed by a brief overview of Qdot585-STV and Qdot705-STV as regards the optical and structural characteristics in which they are markedly different from one to another.

CHAPTER 2:

FRET PRINCIPLES AND INTRODUCTION TO QDOT NANOPARTICLES

2.1 Principles of FRET

Nonradiative energy transfer can be generalised as a dynamic process that involves the radiationless migration of energy from excited molecule/atom (serves as donor) to neighbouring energetically resonant molecule/atom (serves as acceptor). The manifestation of nonradiative energy transfer was first observed in the early 1920s with the demonstration of indirect excitation of thallium atoms in a vapour mixture of mercury and thallium irradiated at 253.6 nm wavelength that could only excite mercury atoms [1]. However, the famous FRET (Förster/Fluorescence Resonance Energy Transfer) formalism in relation to biological processes only came to light two decades later. In 1948, Theodor Förster first proposed the inverse sixth power law dependence of the radiationless energy transfer rate on the intermolecular donor-acceptor separation in a mathematical treatment using quantum mechanical theory [1]. Later, in 1951, Förster proved that the $1/r^6$ dependence of transfer rate could also be derived from the classical model of an oscillating dipole [2]. In the classical approach, the spatial distance of two approaching dipoles (molecules) is treated to be larger than the charge distribution of individual dipole (molecular size) but appreciably smaller than the wavelength of emission [2]. Following that, the rate of nonradiative energy migration can be expressed as

$$k_T(r) = \left(\frac{9000(\ln 10)}{128\pi^5 N_{AV} n^4} \right) \frac{Q_D \kappa^2}{\tau_D r^6} \int_0^\infty f_D(\lambda)\varepsilon(\lambda)\lambda^4 d\lambda \tag{2.1}$$

where N_{AV} is the Avogadro's number, n is the refractive index of the medium, Q_D is the quantum yield of the donor in the absence of acceptor, κ^2 is the orientation factor describing the angle between the donor and the acceptor dipole moments, τ_D is the fluorescence decay lifetime of the donor in the absence of acceptor, r is the donor-acceptor separation, $f_D(\lambda)$ is the normalised fluorescence intensity of the donor in the absence of acceptor and $\varepsilon(\lambda)$ is the molar extinction coefficient of the acceptor [2-4]. As the underlying derivation of FRET theory can be rather complex to apprehend, we focus on the pertinent aspects of the FRET concept without involving too much of the mathematical rationalisation. The full derivation of Equation 2.1 can, however, be referred to Ref. [2]. We can alternatively rewrite Equation 2.1 as

$$k_T(r) = \frac{1}{\tau_D}\left(\frac{R_0}{r}\right)^6 \tag{2.2}$$

with R_0 absorbing all the constants and the variable parameters except τ_D and r,

$$R_0{}^6 = \left(\frac{9000(\ln 10)}{128\pi^5 N_{AV} n^4}\right) Q_D \kappa^2 \int_0^\infty f_D(\lambda)\varepsilon(\lambda)\lambda^4 d\lambda \tag{2.3}$$

With reference to Equation 2.2, R_0 can be defined as the distance between the donor and acceptor transition dipoles at which the FRET energy transfer rate equals the total intrinsic decay rate (the radiative and nonradiative decay rates in the absence of FRET) of the donor i.e. $k_T(R_0) = 1/\tau_D$. Intuitively, it also means that at the distance equals to R_0, half of the excitation energy of the donor is lost through FRET and the remaining half is lost through the intrinsic radiative and other nonradiative channels. Therefore, R_0 is customarily described as the Förster distance. Besides that, it is usual to assign the integral term in Equation 2.3 to $J(\lambda)$. $J(\lambda)$ denotes the degree of spectral overlap between the donor emission and the acceptor absorption.

$$J(\lambda) = \int_0^\infty f_D(\lambda)\varepsilon(\lambda)\lambda^4 d\lambda \qquad \text{in M}^{-1}\text{cm}^3 \tag{2.4}$$

with λ in cm, $f_D(\lambda)$ in cm^{-1} and $\varepsilon(\lambda)$ in M^{-1}cm^{-1}. The unit cm^{-1} in $f_D(\lambda)$ is attributed to the statistical normalisation of the area under the intensity curve of the donor such that,

$$f_D(\lambda) = \frac{F_D(\lambda)}{\int_0^\infty F_D(\lambda)d\lambda} \tag{2.5}$$

where $F_D(\lambda)$ is the dimensionless fluorescence intensity of the donor at λ (It is practically the measured donor emission lineshape). R_0 can then be further reduced to

$$R_0{}^6 = \left(\frac{9000(\ln 10)}{128\pi^5 N_{AV} n^4}\right) Q_D \kappa^2 J(\lambda) \tag{2.6}$$

but $N_{AV} = 6.02 \times 10^{23}$ M^{-1}, hence

$$R_0{}^6 = 8.79 \cdot 10^{-25} n^{-4} Q_D \kappa^2 J(\lambda) \qquad \text{in cm}^6 \tag{2.7}$$

$$R_0^{\,6} = 8.79 \cdot 10^{23} n^{-4} Q_D \kappa^2 J(\lambda) \quad \text{in Å}^6 \tag{2.8}$$

Finally,

$$R_0 = 9.79 \cdot 10^{3} \left(n^{-4} Q_D \kappa^2 J(\lambda)\right)^{1/6} \quad \text{in Å} \tag{2.9}$$

As elucidated by Equation 2.2 and 2.9, the magnitude of R_0, in turn, the transfer rate is critically bound by four parameters namely n, Q_D, κ^2 and $J(\lambda)$. In practise, n is typically within the range from 1.3 to 1.4 of refractive index since most of the intermolecular interactions occur in water based media [3]. In conformity with the definition,

$$\kappa^2 = (\cos\theta_T - 3\cos\theta_D \cos\theta_A)^2 \tag{2.10}$$

with θ_T representing the angle between the donor transition dipole and the acceptor transition dipole and θ_D (θ_A) representing the angle between the donor (acceptor) dipole and the separation vector connecting the donor and the acceptor centres, the value of κ^2 factor can vary from 0 to 4 in dependence on the relative orientation of the transition dipoles of the donor and the acceptor [2, 3].

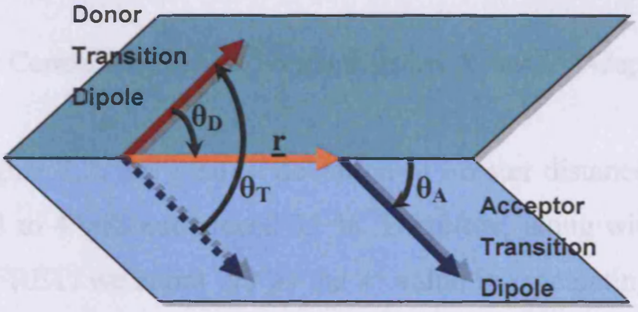

Figure 2.1: Schematic diagram of exemplary orientations of donor transition dipole and acceptor transition dipole defining θ_D, θ_A and θ_T in κ^2 factor.

Although the possible orientations are manifold, the values of κ^2 at 0, 1 and 4 are distinct. As depicted in Figure 2.1, κ^2 has the highest value of 4 only when both transition dipoles align along with the separation vector. On the contrary, κ^2 is 0 when both dipoles are perpendicular to each other in such a way that the angle between one of the dipole moments and the separation vector i.e. θ_D or θ_A is 90°. At fixed $\theta_D = 90°$, κ^2 becomes 1 when the acceptor transition dipole is orientated in parallel with the donor transition dipole and vice versa for $\theta_A = 90°$. Due to the difficulty in predicating the precise value of κ^2 experimentally, it is general to assume κ^2 as dynamically averaged 2/3 where fast rotational mobility of dipoles is allowed during the decay time of an excited donor [3, 5]. As long as the mutual dipole-dipole orientation does not fall into the disastrous $\kappa^2 = 0$ regime, the uncertainty in R_0 contributed by κ^2 factor is usually small [2, 3, 5].

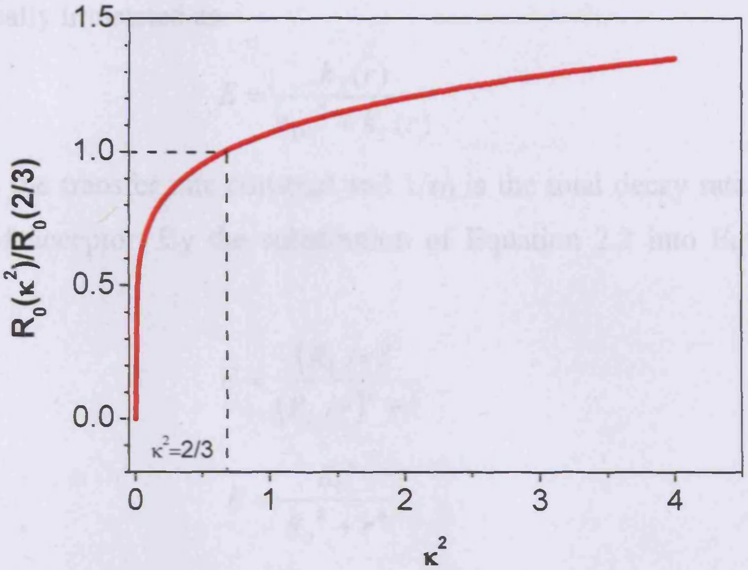

Figure 2.2: Correlation between Förster distance, R_0 and κ^2. Adapted from [2].

As depicted in Figure 2.2, the greatest deviation of Förster distance, R_0 in the range of κ^2 values from 2/3 to 4 will not exceed 35 %. Therefore, along with other literature in relevance to QD FRET, we adopt 2/3 as the κ^2 value in calculating R_0 presuming that the coordination of acceptors onto a QD surface via non-covalent ligand-receptor binding is randomized [6-8]. The error in R_0 introduced by $\kappa^2 = 2/3$ may be further vitiated by the non-rigidity of binding moieties whereby segmental mobility of acceptors is highly probable especially in solutions of low viscosity. As the values of n and κ^2 are reasonably restricted to 1.3-1.4 and 2/3 respectively, the spatial extension of R_0 at the condition $k_T = 1/\tau_D$ can be improved by optimizing the quantum yield of the donor, Q_D and the spectral overlap between the donor emission and the acceptor absorption, $J(\lambda)$. In practise, this can be achieved, if possible, by choosing only those highly fluorescent dyes with Q_D above 0.5 as donors and those highly light harvesting dyes with ε_A above 100 000 $M^{-1}cm^{-1}$ at donor emission wavelength as acceptors. So far, R_0 ranging from as small as ~10 Å to as large as ~80 Å have been reported for a variety of donor-acceptor combinations in organic dye-dye FRET systems [9]. As for QD-dye

FRET complexes, Mattoussi and coworkers elicited R_0 to be around 40-60 Å from their work in prototyping FRET based biosensors [6, 7].

FRET efficiency, E is defined as the fraction of photons absorbed by the donor that are transferred through the nonradiative channel to the acceptor in resonance. The meaning can be generically translated as

$$E = \frac{k_T(r)}{\tau_D^{-1} + k_T(r)} \tag{2.11}$$

where $k_T(r)$ is the transfer rate constant and $1/\tau_D$ is the total decay rate of the donor in the absence of acceptor. By the substitution of Equation 2.2 into Equation 2.11, we arrive at

$$E = \frac{(R_0/r)^6}{(R_0/r)^6 + 1} \tag{2.12}$$

$$E = \frac{R_0^{\ 6}}{R_0^{\ 6} + r^6} \tag{2.13}$$

Therefore, due to the sixth power relationship in Equation 2.12, it is apparent that FRET efficiency is highly dependent on the donor-acceptor separation, r. In fact, E varies rapidly when r approaches R_0. On the basis of Equation 2.12, one can easily define R_0 as the distance between the donor and acceptor dipoles at which the efficiency of energy transfer is 0.5. The theoretical prediction of $1/r^6$ dependence in FRET derived by Förster has been verified by numerous experimental studies which can go back as far as 1960s led by Stryer et al in the investigation of FRET between α-naphthyl energy donor moiety and dansyl energy acceptor moiety covalently attached to both ends of a polypeptide chain that served as a spacer of variable length ranging from 12-46 Å [10]. However, it should be noted that Equation 2.12 is only applicable to single donor-acceptor pairs in which the transition dipoles are separated by a uniform distance r. Hence, the FRET efficiency formula has to be modified to account for the multivalency of QD-dye conjugations where multiple acceptors can be arrayed around a single QD through different binding strategies. Presuming that the probability of energy transfer per unit time is linearly increased by the number of available acceptors bound to the donor at a constant distance r, we can redefine Equation 2.2 as

$$k_T(r) = \frac{n}{\tau_D}\left(\frac{R_0}{r}\right)^6 \tag{2.14}$$

where n denotes the number of acceptors attached onto a single donor. On the same definition of FRET efficiency as described by Equation 2.11, it gives

$$E = \frac{n(R_0 / r)^6}{n(R_0 / r)^6 + 1} \tag{2.15}$$

$$E = \frac{nR_0^{\ 6}}{nR_0^{\ 6} + r^6} \tag{2.16}$$

As shown by Equation 2.15, at a fixed donor-acceptor distance, the efficiency of nonradiative energy transfer can increase by several factors depending on the degree of multivalency. This is illustrated in Figure 2.3.

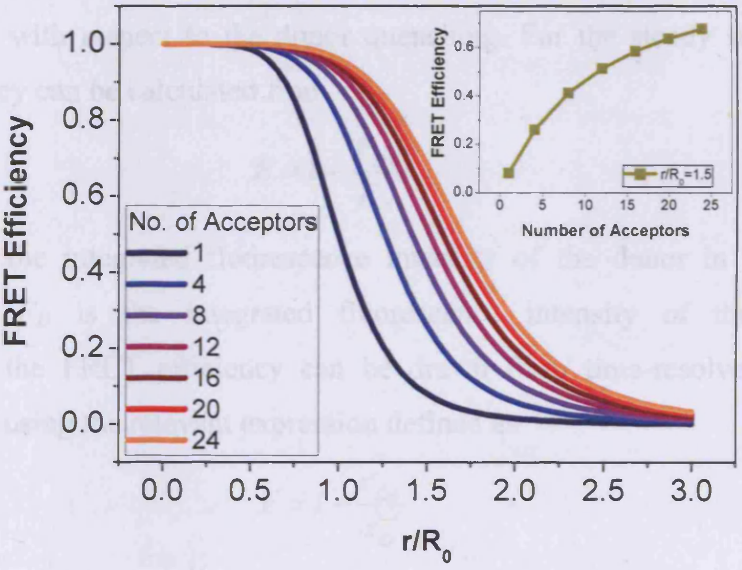

Figure 2.3: Plot of FRET efficiency against r/R_0 ratio in correspondence with the number of bound acceptors per donor. R_0 is the Förster distance. The inset depicts the efficiency as a function of acceptor number at fixed $r = 1.5R_0$.

Because of its $1/r^6$ dependence, Equation 2.16 is utilised in the estimation of QD-dye separation, neglecting the complication that the acceptors may not be entirely centro-symmetric around the donor [6-8]. The non-spherical shape of QD and the non-rigid structure of binding moieties can ultimately contribute to the heterogeneity in the spatial distribution of acceptors. Therefore, a more rigorous mathematical treatment of FRET efficiency may be required by taking into account the non-uniformity in the spatial distribution of acceptors in QD-dye FRET system. However, since the simple n-acceptor FRET efficiency expression conforms reasonably well with the empirical data as unequivocally reported by Mattoussi's research group [6, 7], it will be adequate for us to pursue the same approach in our QD FRET analysis, primarily in the determination of donor-acceptor separation. As indicated by Stryer, FRET can be an effective tool as a nanoscale spectroscopic ruler with the capability of discriminating between the donor-acceptor distances of 60 Å and 30 Å, for example, but not between the distances of 30 Å and 35 Å [5]. Due to the extent of uncertainties i.e. the orientation factor and the distance distribution of acceptors, we expect the proximity relationships in QD-dye assays drawn from idealised FRET formula will be merely a rough estimation.

The efficiency of energy coupling between donor and proximal acceptor can be determined experimentally by steady state and time-resolved fluorescence measurements with respect to the donor quenching. For the steady state method, the FRET efficiency can be calculated from

$$E = 1 - \frac{F_{DA}}{F_D} \tag{2.17}$$

where F_{DA} is the integrated fluorescence intensity of the donor in the presence of acceptor and F_D is the integrated fluorescence intensity of the donor alone. Alternatively, the FRET efficiency can be drawn from time-resolved spectroscopic measurements using the relevant expression defined as

$$E = 1 - \frac{\tau_{DA}}{\tau_D} \tag{2.18}$$

where τ_{DA} denotes the fluorescence lifetime of the donor in the presence of the acceptor and τ_D denotes the fluorescence lifetime of the donor alone. There are, of course, advantages and disadvantages in each method of detecting the manifestation of dipolar energy coupling. The appealing side of FRET characterisation by steady state measurements is the simplicity of data acquisition without the need of sophisticated instrumentation. However, there is always the tendency of overestimation of donor quenching due to the reabsorption by acceptors which can appreciably affect the accountability of calculated FRET efficiency based on Equation 2.17. The overestimation of FRET efficiency can be eliminated by shifting to the utilisation of temporal spectroscopy since indirect energy coupling via photon reabsorption by acceptor does not account for the reduction of donor fluorescence decay lifetime. Therefore, lifetime measurement inherently appears to be a more robust way in quantifying FRET efficiency. The major drawback of eliciting FRET efficiency from a temporal approach is the difficulty of interpreting non-exponential kinetics of the donor. Well behaved single exponential decays are rare in reality. Hence, the source of lifetime data to be substituted into Equation 2.18 can sometimes be controversial. These nontrivial problems can, however, be reliably minimised if both methods are employed to complement each other.

2.2 Introduction to Qdot585-STV: Optical and Structural Characteristics

Qdot585-STV is a commercial QD from Invitrogen. It is a CdSe/ZnS core-shell QD which is surface derivatised with amphiphilic polymer to render it water soluble and followed by additional surface functionalisation with streptavidin to afford labelling specificity [11]. Streptavidin is an avidin analogue derived from bacterium *Streptomyces avidinii* that is universally known to have high affinity for biotin (K_a = 10^{15} M^{-1}) [12]. Via the utility of the streptavidin-biotin binding scheme, Qdot585-STV can target a variety of liganded molecules. The only drawback is that streptavidin is a relatively large tetrameric protein with a molecular size of ~5 nm and a molecular weight (MW) of ~60 kDa [13, 14]. This will unambiguously increase the overall size of QD and thus, can be deleterious to FRET applications where donor-acceptor separation is a requisite factor in determining the efficacy of energy transfer.

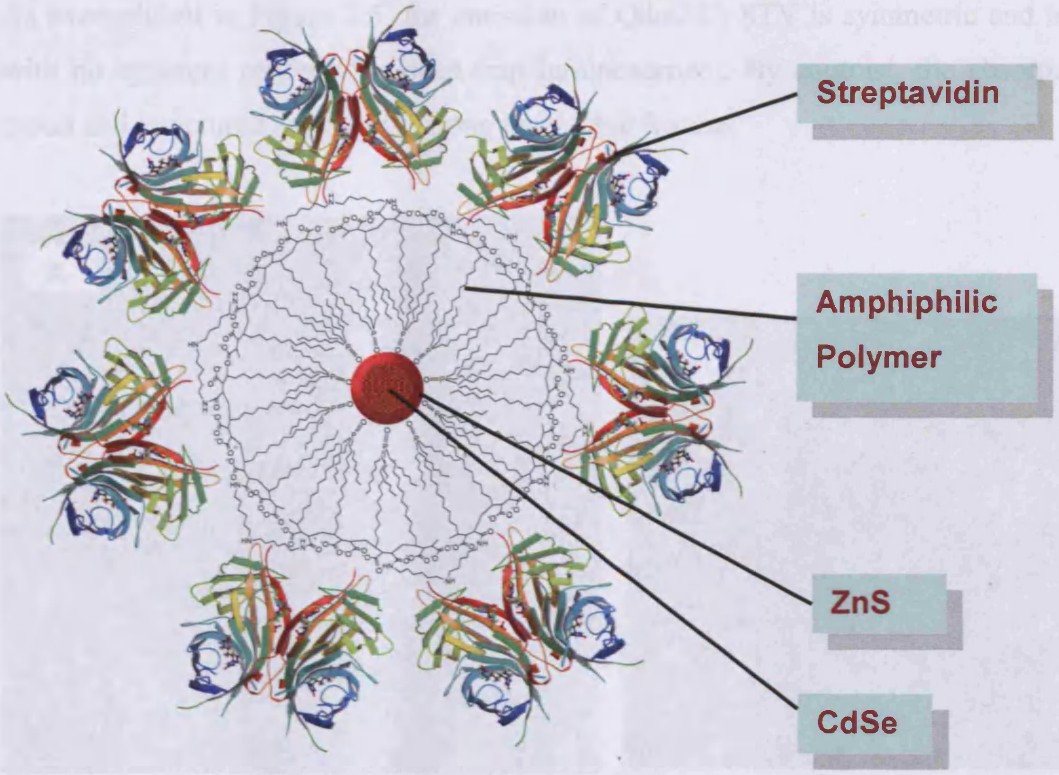

Figure 2.4: Cartoon delineating the overall structure of Qdot585-STV that is conjugated to streptavidin. Note: the diagram is not drawn to scale and the chemical structure of amphiphilic polymer may not represent the real chemical compound used by the manufacturer. The ribbon diagram of streptavidin is acquired from [15].

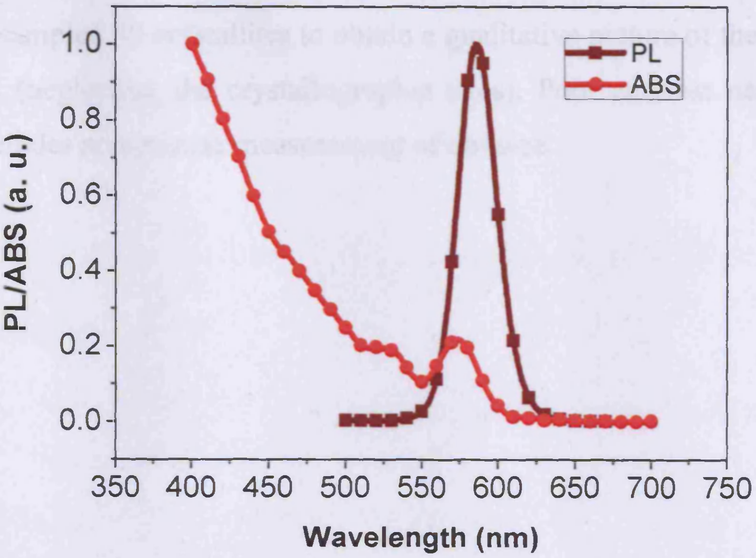

Figure 2.5: Absorption and photoluminescence profiles of Qdot585-STV.

As exemplified in Figure 2.5, the emission of Qdot585-STV is symmetric and narrow with no apparent red tail (no deep trap luminescence). By contrast, the absorption is broad and structured displaying strong band edge feature.

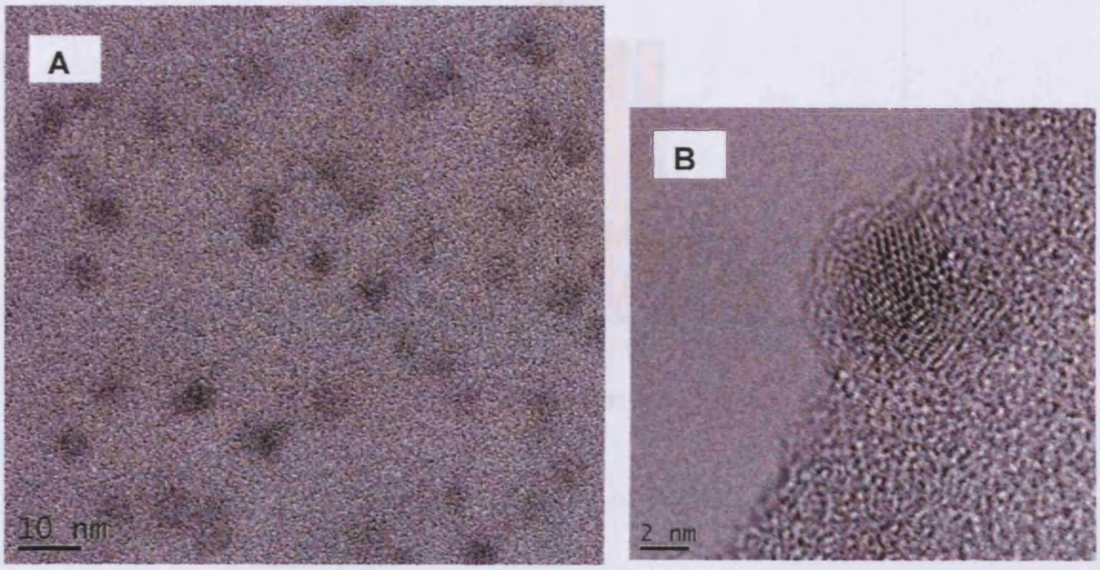

Figure 2.6: TEM images of Qdot585 (without the conjugation of streptavidin) taken at low (A) and high (B) resolutions. (Courtesy of Christy Cooper, Purdue University)

The wide-field micrograph in Figure 2.6(A) shows that core-shell Qdot585 nanoparticles are typically near spherical. Upon close-up inspection, the fringe contrast in Figure 2.6(B) reveals that Qdot585 crystallite adopts a wurzite (hexagonal) crystal structure. We sampled 40 crystallites to obtain a qualitative picture of the distribution of Qdot585 radii (neglecting the crystallographic axes). Poor contrast near the edge of crystallite precludes an accurate measurement of dot size.

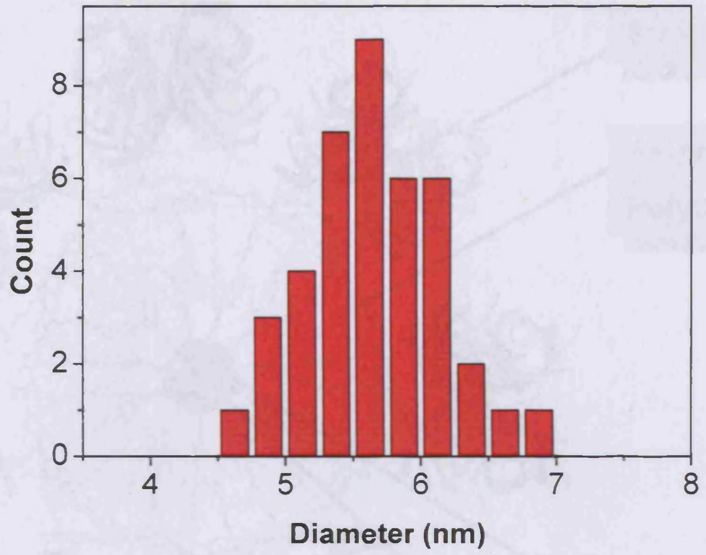

Figure 2.7: Histogram of Qdot585 size.

The size histogram in Figure 2.7 reveals that Qdot585 ensemble is near monodisperse from which the size variation is reasonably small with the dot diameter ranging from 5 to 7 nm. As the band edge emission is strongly correlated with the size of crystallite due to the confinement effect of exciton, the size histogram is essential evidence in support of the narrow emission lineshape of Qdot585-STV that displays a full-width-at-half-maximum of ~30 nm (see Figure 2.5). From 40 crystallites, we statistically elicited a mean radius of 5.66 ± 0.08 nm. Nonetheless, it should not be perceived as the definite value primarily due to the lack of contrast in the image.

2.3 Introduction to Qdot705-STV: Optical and Structural Characteristics

Except for the core, Qdot705-STV has a similar structural construction to that of Qdot585-STV. Instead of CdSe, CdTe constitutes the core material. The overall composition of Qdot705-STV is depicted in Figure 2.8.

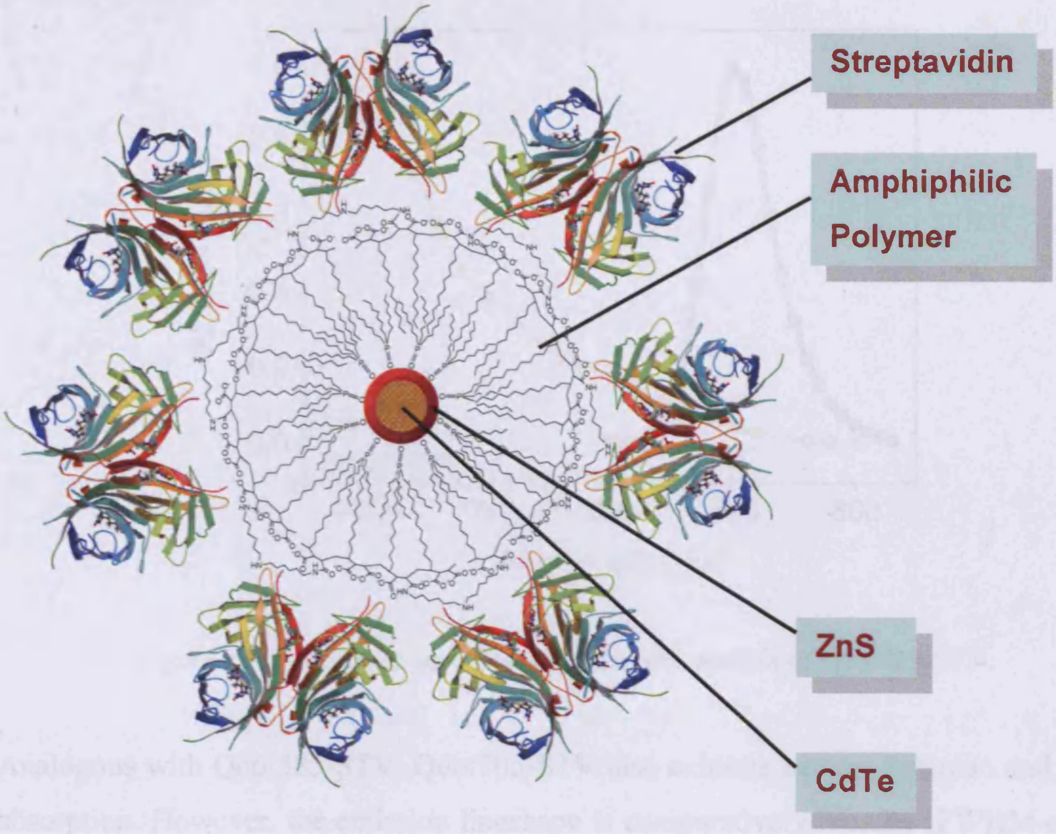

Figure 2.8: Cartoon delineating the overall structure of streptavidin conjugated Qdot705-STV. The illustration is not drawn to scale and the chemical structure of amphiphilic polymer as depicted here is only exemplary and may not represent the exact chemical compound used by the manufacturer in the synthesis of Qdot705-STV. The ribbon diagram of streptavidin is obtained from [15].

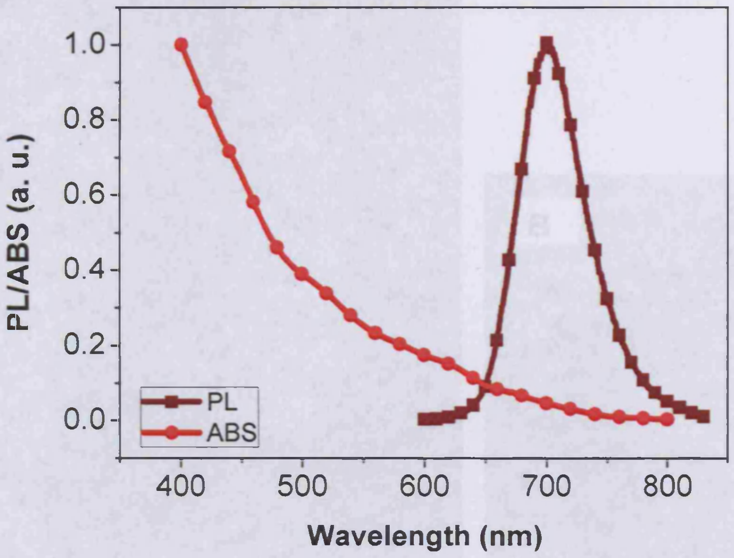

Figure 2.9: Absorption and photoluminescence spectra of Qdot705-STV.

Analogous with Qdot585-STV, Qdot705-STV also exhibits narrow emission and broad absorption. However, the emission lineshape is comparatively broader (FWHM of ~70 nm) and less symmetric than Qdot585-STV. Furthermore, no apparent band edge feature is resolved in the absorption curve. The inhomogeneous distribution of sizes can be one of the cofactors to the observations. In light of that, we conducted a preliminary structural characterisation of Qdot705 to have qualitative information on the QD sizes within the population.

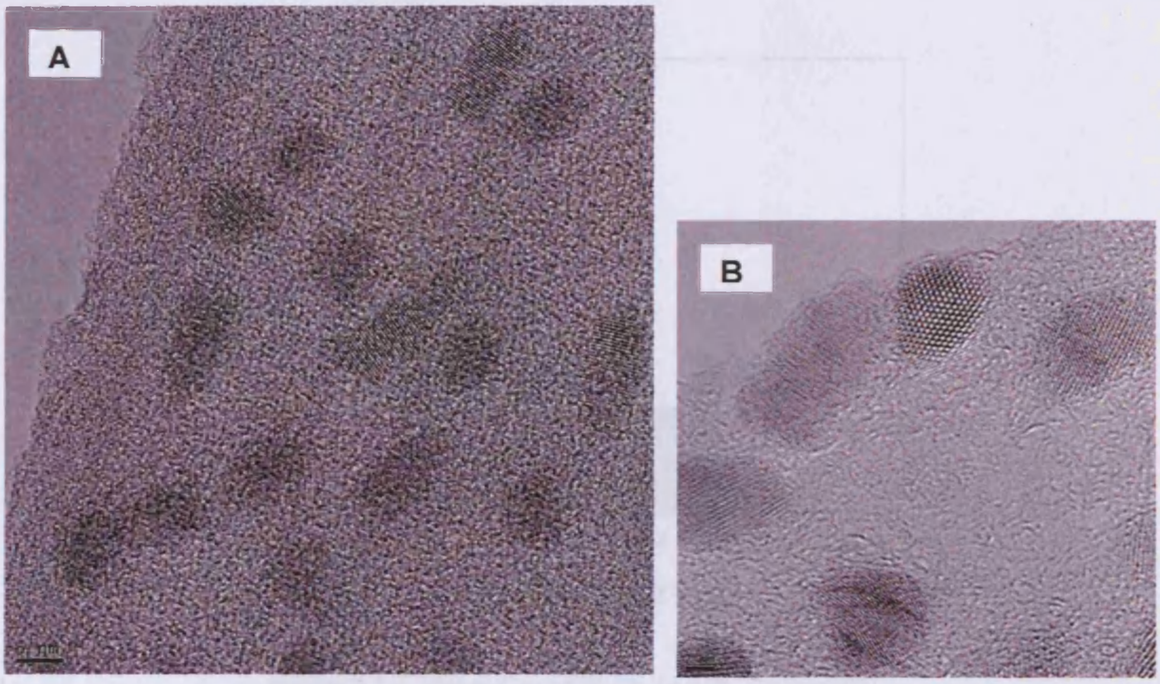

Figure 2.10: TEM images of Qdot705 (without the conjugation of streptavidin) taken at low (A) and high (B) resolutions. The length markers of 5 nm and 2 nm are indicated at the left corners. (Courtesy of Christy Cooper, Purdue University)

Figure 2.10(A) showcases a surprisingly large variation of Qdot705 sizes and shapes. Some are elongated while others are spherical in shape. Upon higher magnification, the lattice fringes in Figure 2.10(B) depict a close match of wurzite crystal structure. We sampled 40 crystallites of Qdot705 to investigate the distribution of lengths along major/minor axes and the aspect ratio. However, the significant drop-off of lattice contrast near the edge of crystallite is a hindrance to precise measurement of length. Hence, it is worth mentioning that the measured values are merely rough estimations of lengths in accordance to the provided calibration bars.

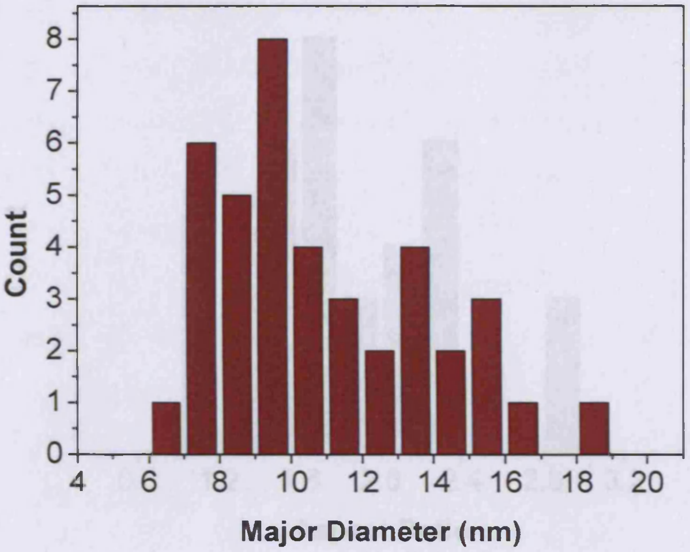

Figure 2.11: Histogram of major length of Qdot705.

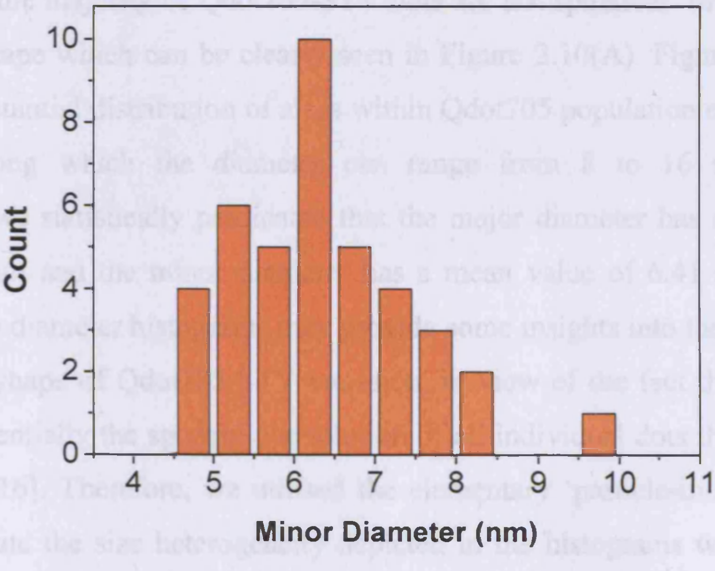

Figure 2.12: Histogram of minor length of Qdot705.

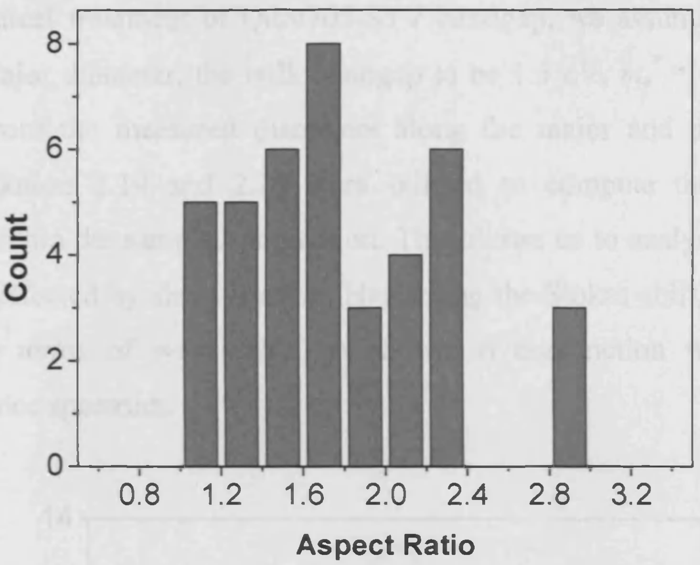

Figure 2.13 Histogram of aspect ratio of Qdot705.

The significant deviation of the aspect ratio from unity as shown in Figure 2.13 is indicative that the majority of Qdot705-STV dots are not spherical. In reality, they are elongated in shape which can be clearly seen in Figure 2.10(A). Figure 2.11 and 2.12 illustrate a substantial distribution of sizes within Qdot705 population especially for the major axis along which the diameter can range from 8 to 16 nm. Out of 40 nanoparticles, we statistically predicated that the major diameter has a mean value of 11.05 ± 0.46 nm and the minor diameter has a mean value of 6.41 ± 0.17 nm. The skewness in the diameter histograms may provide some insights into the broad and non-symmetric lineshape of Qdot705-STV emission, in view of the fact that the ensemble emission is essentially the spectral convolution of all individual dots that constitute the bulk solution [16]. Therefore, we utilised the elementary 'particle-in-a-box' model in effort to correlate the size heterogeneity depicted in the histograms with the emission lineshape of Qdot705-STV. The lowest excited state energy eigenvalue of electron/hole can be calculated from

$$E_{e,h}(x,y,z)=\frac{\hbar^2\pi^2}{2m_{e,h}*}\left(\frac{1}{x^2}+\frac{1}{y^2}+\frac{1}{z^2}\right) \tag{2.19}$$

with $m_{e,h}^*$ denotes the bulk effective masses for electron and hole and x, y, z represent the dimensions of QD [17]. With that, the energy gap of a particular size QD can be expressed as

$$E_g(QD) = E_g(bulk) + E_e + E_h \tag{2.20}$$

In the mathematical treatment of Qdot705-STV bandgap, we assumed $x = y =$ minor diameter, $z =$ major diameter, the bulk bandgap to be 1.5 eV, $m_e^* = 0.11m_e$ and $m_h^* = 0.35m_e$ [18]. From the measured diameters along the major and minor axes of 40 crystallites, Equation 2.19 and 2.20 were utilised to compute the energy gap of individual dot within the sampled population. This allows us to analyse the distribution of energy gaps effected by size variation. Neglecting the Stokes shift, the histogram of energy gap (in terms of wavelength) is shown in conjunction with the Qdot705 photoluminescence spectrum.

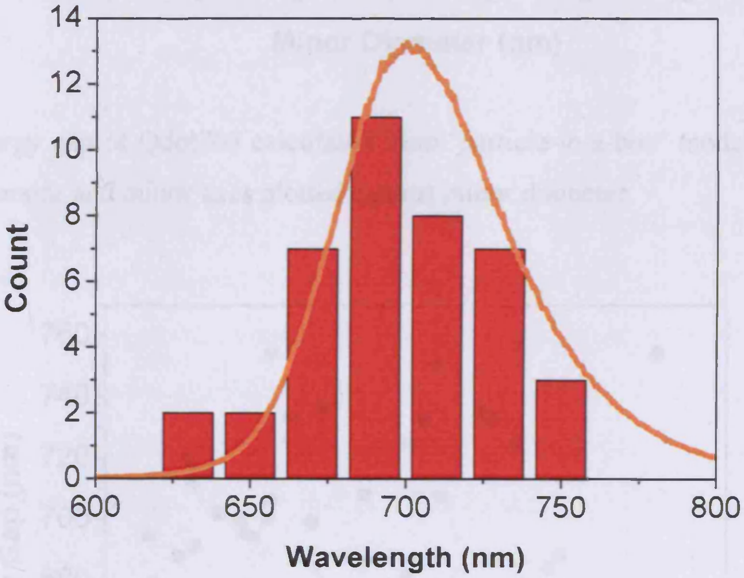

Figure 2.14: Histogram of Qdot705 bandgap along with the ensemble luminescence spectrum.

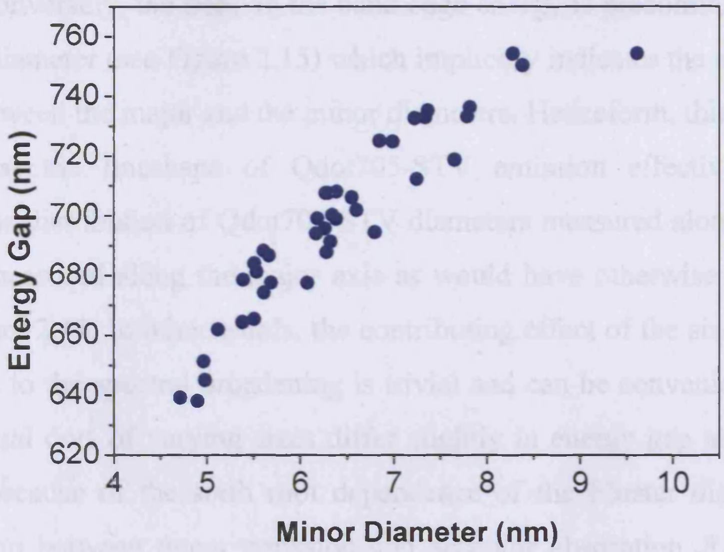

Figure 2.15: Energy gap of Qdot705 calculated from 'particle-in-a-box' model using diameters measured along major and minor axes plotted against minor diameter.

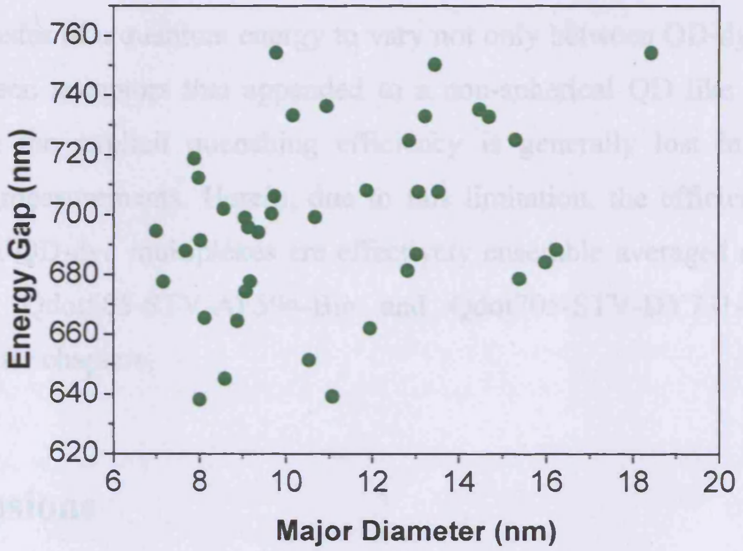

Figure 2.16: Energy gap of Qdot705 calculated from 'particle-in-a-box' model using diameters measured along major and minor axes plotted against major diameter.

Despite the crude theoretical modelling of Qdot705 energy bandgap, the statistical prediction produces a bandgap histogram that reasonably parallels the lineshape of Qdot705-STV emission. In essence of that, the skewness of Qdot705-STV emission is largely attributed to the substantial distribution of dot sizes. However, on close inspection, Figure 2.16 shows weak correlation between the major diameter and the energy gap. Conversely, the trend in the band edge energy is predominantly determined by the minor diameter (see Figure 2.15) which implicitly indicates the absence of strong correlation between the major and the minor diameters. Henceforth, this further adds the conclusion that the lineshape of Qdot705-STV emission effectively reflects the inhomogeneous distribution of Qdot705-STV diameters measured along the minor axis and not that measured along the major axis as would have otherwise expected at first glance of Figure 2.11. In other words, the contributing effect of the size disparity along the major axis to the spectral broadening is trivial and can be conveniently discounted. While individual dots of varying sizes differ slightly in energy gap and thus emission wavelength, because of the sixth root dependence of the Förster distance R_0 on the spectral overlap between donor emission and acceptor absorption $J(\lambda)$ (see Equation 2.9), the spectral variation has minor effect on the efficacies of near field dipole-dipole interactions between these dots and energetically resonant energy acceptors in the vicinity. It could, however, be affected by the extent of the separation between the QD and the interacting acceptor due to the $1/r^6$ relation and for this reason we anticipate that the rate of transfer of a quantum energy to vary not only between QD-dye conjugations but also between acceptors that appended to a non-spherical QD like Qdot705-STV. Unfortunately, the explicit quenching efficiency is generally lost in the ensemble spectroscopic measurements. Herein, due to this limitation, the efficiencies of FRET extracted from QD-dye multiplexes are effectively ensemble averaged and there is no exception for Qdot585-STV-AF594-Bio and Qdot705-STV-DY731-Bio bioassays discussed in later chapters.

2.4 Conclusions

In this chapter, I have covered the fundamentals of FRET through a brief account on the theoretical derivation of pertinent expressions as regards Förster distance, R_0 and FRET efficiency, E. In addition, I have also highlighted the importance of physical parameters, especially the orientation factor, κ^2, the donor quantum efficiency, Q_D and the spectral overlap between the donor emission and the acceptor absorption, $J(\lambda)$, in the determination of R_0 on which criterion the theoretical efficiency of energy transfer is strongly dependent. Apart from FRET theory, short descriptions on the optical properties of Qdot585-STV and Qdot705-STV were presented and these were then followed by the preliminary structural characterisations of the respective dot systems revealing that core-shell Qdot585 is near spherical and almost monodisperse but core-shell Qdot705 behaves contrariwise i.e. highly non-spherical and extremely disparate in shapes, to the extent that the photoemission of Qdot705-STV is markedly broadened relative to that of Qdot585-STV. However, I later showed, by simple quantum mechanics, that the spectral broadening in Qdot705-STV is primarily correlated with the variation of the minor lengths.

2.5 References

1. Clegg R. The History of FRET : From Conception through the Labors of Birth. *Reviews in Fluorescence 2006.* Edited by Lakowicz J, Geddes C. Springer, 2006.

2. Van Der Meer BW, Coker G, Simon Chen SY. Resonance Energy Transfer. John Wiley and Sons, 1994.

3. Lakowicz J. Principles of Fluorescence Spectroscopy. 3rd edn. Springer, 2006.

4. Steinberg IZ. Long-Range Nonradiative Transfer of Electronic Excitation Energy in Proteins and Polypeptides. *Annu Rev Biochem* 1971, **40**:83-114.

5. Stryer L. Fluorescence Energy-Transfer as a Spectroscopic Ruler. *Annu Rev Biochem* 1978, **47**:819-846.

6. Clapp AR, Medintz IL, Mauro JM, Fisher BR, Bawendi MG, Mattoussi H. Fluorescence Resonance Energy Transfer between Quantum Dot Donors and Dye-Labeled Protein Acceptors. *J Am Chem Soc* 2004, **126**(1):301-310.

7. Medintz IL, Clapp AR, Mattoussi H, Goldman ER, Fisher B, Mauro JM. Self-Assembled Nanoscale Biosensors Based on Quantum Dot FRET Donors. *Nature Materials* 2003, **2**(9):630-638.

8. Goldman ER, Medintz IL, Whitley JL, Hayhurst A, Clapp AR, Uyeda HT, Deschamps JR, Lassman ME, Mattoussi H. A Hybrid Quantum Dot-Antibody Fragment Fluorescence Resonance Energy Transfer-Based TNT Sensor. *J Am Chem Soc* 2005, **127**(18):6744-6751.

9. Wu PG, Brand L. Resonance Energy-Transfer - Methods and Applications. *Analytical Biochemistry* 1994, **218**(1):1-13.

10. Stryer L, Haugland RP. Energy Transfer: A Spectroscopic Ruler. *Proceedings of the National Academy of Sciences of the United States of America* 1967, **58**(2):719-726.

11. Qdot Streptavidin Conjugates User Manual. Invitrogen, 2006.

12. Livnah O, Bayer EA, Wilchek M, Sussman JL. 3-Dimensional Structures of Avidin and the Avidin-Biotin Complex. *Proceedings of the National Academy of Sciences of the United States of America* 1993, **90**(11):5076-5080.

13. Bayer EA, Wilchek M. Application of Avidin-Biotin Technology to Affinity-Based Separations. *Journal of Chromatography* 1990, **510**:3-11.

14. Arakaki A, Hideshima S, Nakagawa T, Niwa D, Tanaka T, Matsunaga T, Osaka T. Detection of Biomolecular Interaction between Biotin and Streptavidin on a Self-Assembled Monolayer Using Magnetic Nanoparticles. *Biotechnology and Bioengineering* 2004, **88**(4):543-546.

15. Katz BA. Streptavidin-Biotin Complex. 1998.
http://www.rcsb.org/pdb/explore.do?structureId=2RTF

16. Empedocles SA, Norris DJ, Bawendi MG. Photoluminescence Spectroscopy of Single CdSe Nanocrystallite Quantum Dots. *Phys Rev Lett* 1996, **77**(18):3873-3876.

17. French AP, Taylor EF. An Introduction to Quantum Physics. Stanley Thornes, 1998.

18. Pellegrini G, Mattei G, Mazzoldi P. Finite Depth Square Well Model: Applicability and Limitations. *J Appl Phys* 2005, **97**(7).

CHAPTER 3:

RESEARCH METHODS

CONTENTS:

Abstract: Qdot nanoparticles, Qdot585-STV and Qdot705-STV, and organic dyes, AF594-Bio and DY731-Bio, were the building blocks for developing FRET based assays in the visible and the far-red spectral regimes in which the efficiencies of the dipolar resonance interactions were probed using the steady state and the time-resolved spectroscopic techniques. This chapter describes the detailed protocols of the preparations and the optical characterisations of these self-assemblies in the titration experiments and after ultrafiltration, aside from the fundamental optical characterisations of Qdot585-STV, Qdot705-STV, AF594-Bio, DY731-Bio, AF594-Bio-STV and DY731-Bio-STV. All experiments were done at ambient conditions.

CHAPTER 3:

RESEARCH METHODS

3.1 Qdot585-STV and AF594-Bio

3.1.1 Optical Characterisations of Qdot585-STV and AF594-Bio

20 μL of 1 μM Qdot585-STV (Invitrogen, CA, USA) was dispersed in 400 μL of 10 mM, pH 7.4 phosphate buffered saline (PBS) before transferred to a 10 mm optical path fluorimeter cell. The absorption and the fluorescence spectra of Qdot585-STV were respectively recorded using a UV/Vis/NIR Jasco spectrometer (Tokyo, Japan) and a Varian Cary Eclipse fluorimeter (Palo Alto, CA, USA) with the excitation wavelength tuned to 425 nm. From the measured absorbance, the molar extinction coefficient of Qdot585-STV was determined in conformity with the Beer-Lambert law expressed as

$$A = \log_{10} \frac{I_0}{I} = \varepsilon c l \tag{3.1}$$

where A denotes the absorbance, I_0 denotes the intensity of incident light, I denotes the intensity of transmitted light, ε denotes the molar extinction coefficient (in $M^{-1}cm^{-1}$), c denotes the solution concentration (in M) and l denotes the optical path length (in cm) [1].

40 μL of 23 μM AF594-Bio (Invitrogen, CA, USA) was diluted with 400 μL PBS (pH 7.4) before dispensed in a 10 mm optical path cuvette. The absorption and the emission spectra of AF594-Bio were measured with the UV/Vis/NIR Jasco spectrometer and the Varian Cary Eclipse fluorimeter with the excitation wavelength set at 540 nm. Apart from that, photoluminescence excitation (PLE) measurements, with the utility of the Varian Cary Eclipse fluorimeter, were performed on the AF594-Bio solution by monitoring the emission intensity at 650 nm whilst scanning the excitation wavelength from 400 nm to 640 nm.

3.1.2 Characterisation of AF594-Bio-STV by Absorption Measurements

~17 μM of streptavidin solution was produced by dissolving 1 mg of dessicated streptavidin powder (Sigma-Aldrich, Dorset, UK) in 1 mL of 10 mM PBS (pH 7.4) assuming the molecular weight (MW) of streptavidin is 60 kDa (Dalton = gram per mole) [2]. 14 μL of 23 μM AF594-Bio and 16 μL of 17 μM streptavidin were both dispersed in 400 μL PBS (pH 7.4) giving a stoichiometry of ~1:1. Since streptavidin is a tetrameric protein, the total binding pockets should be fourfold greater than the number of biotinylated AF594-Bio, thereby populating the solution with conjugated complexes formed via streptavidin-biotin linkage. The mixture was shaken and allowed to sit in the dark for 2-3 minutes before transferred to a 10 mm optical path cuvette and have the absorption measured using a UV/Vis/NIR Jasco V570 spectrometer from which the molar extinction coefficient of AF594-Bio-STV complex was calculated.

3.1.3 FRET Investigation by Steady State Spectroscopy

10 μL of 1 μM Qdot585-STV was dispensed into 400 μL of 10 mM PBS (pH 7.4) in a 10 mm optical path fluorimeter cell. A titration of Qdot585-STV was performed by sequentially adding 2 μL of 23 μM AF594-Bio aliquots until a total volume of 26 μL has been dispensed into the Qdot585-STV solution. In the course of titration, the fluorescence intensity of the mixture was measured using a Varian Cary Eclipse fluorimeter with the excitation wavelength tuned to 425 nm keeping the direct excitation of AF594-Bio minimal. For comparison, a control experiment was carried out following the same protocols with the exception that the 10 μL Qdot585-STV solution was replaced with 10 μL PBS solution.

3.1.4 FRET Investigation by Time-Resolved Spectroscopy

4 separate samples of various Qdot585-STV-to-AF594-Bio molar ratios were produced by dispensing 2-100 μL of 23 μM AF594-Bio into 20 μL of 1 μM Qdot585-STV which were later diluted with 200 μL of 10 mM PBS (pH 7.4). These samples were let to rest at room temperature in the dark for 15-20 minutes to allow the binding between Qdot585-STV and AF594-Bio before purification using Microcon YM50 spin column

(Millipore, Billerica, MA, USA) with a cut-off molecular weight of 50 kDa. The samples were spun 3 times at 2000 x g (6000 rpm) for 20 minutes per wash. The unbound AF594-Bio (a MW of ~1 kDa) was filtered out of the mixture leaving only conjugated complexes. The final product of Qdot585-STV-AF594-Bio self-assemblies was transferred to a 10 mm optical path cell and diluted with 100 μL PBS. In addition, a pure Qdot585-STV solution was made by dispersing 10 μL of 1μM Qdot585-STV stock in 100 μL PBS.

Pure Qdot585-STV and filtered Qdot585-STV-AF594-Bio solutions were optically pumped with a ~160 fs [3] Ti:Sapphire pulsed laser (Coherent, Santa Clara, USA) that has the central wavelength tuned from 850 nm to 425 nm by a frequency-doubler to achieve minimal excitation of AF594-Bio and the repetition rate reduced from 76 MHz to 1.1 MHz by a pulse-picker to allow complete transient of Qdot585-STV fluorescence. Because of the spectral cross-talk between Qdot585-STV and AF594-Bio emissions, a 600 nm short pass filter was used to cut-off unwanted AF594-Bio emission. An additional 450 nm long pass filter was utilised to cut-off any scattered laser. The time-resolved measurements were conducted using a Hamamatsu streak camera Model C5680 (Japan) with a temporal resolution of ~2.5 ns for 500 ns time range [4]. Following that, each sample was further diluted with 300 μL PBS to have the absorption measured with a UV/Vis/NIR Jasco V570 spectrometer from which the Qdot585-STV:AF594-Bio stoichiometry was derived using the molar extinction coefficient of Qdot585-STV at 450 nm ($\varepsilon = 870\,000\ \mathrm{M^{-1}cm^{-1}}$) and the molar extinction coefficient of AF594-Bio at 590 nm ($\varepsilon = 65\,000\ \mathrm{M^{-1}cm^{-1}}$) after spectral deconvolution in view of the strong band edge resonance of Qdot585-STV.

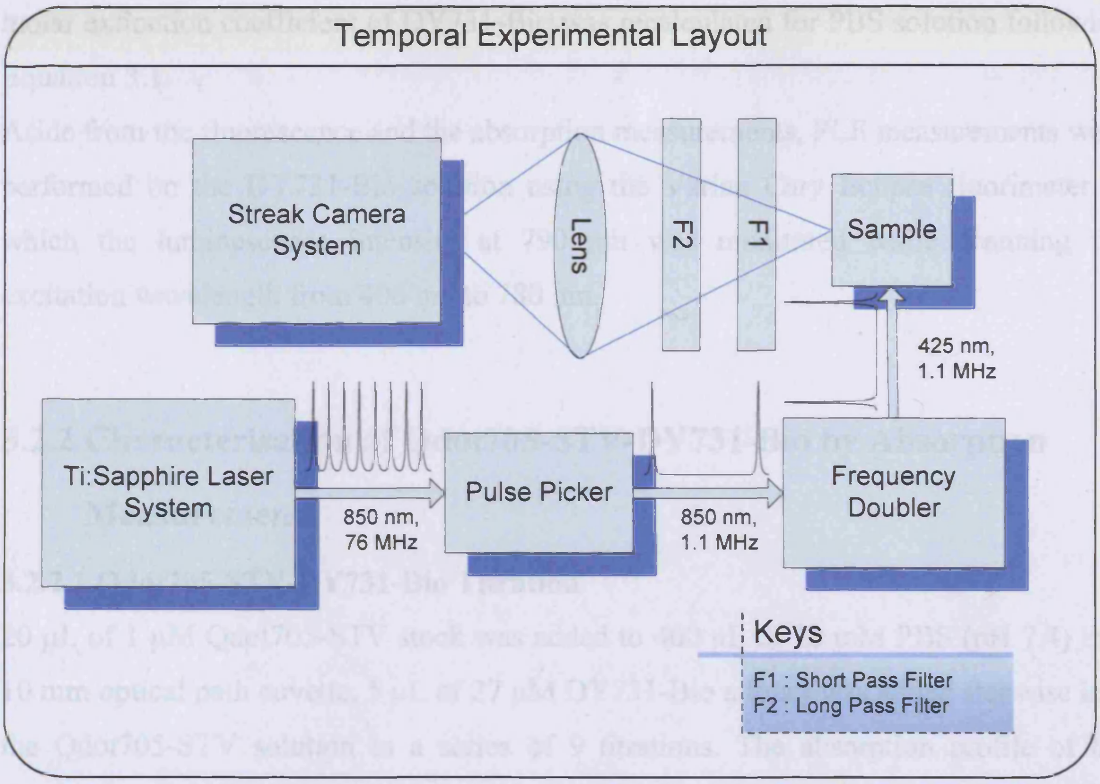

Figure 3.1 Schematic diagram of the experimental setup for the time-resolved photoluminescence measurements.

3.2 Qdot705-STV and DY731-Bio

3.2.1 Optical Characterisations of Qdot705-STV and DY731-Bio

20 µL of 1 µM Qdot705-STV (Invitrogen, CA, USA) was added to 400 µL of 10 mM PBS (pH 7.4) and the solution was later transferred to a 10 mm optical path cuvette. The steady state absorption and photoluminescence spectra of Qdot705-STV were recorded with a UV/Vis/NIR Jasco V570 spectrometer and a Varian Cary Eclipse fluorimeter with the excitation wavelength set at 425 nm. From the measured absorbance, the molar extinction coefficient of Qdot705-STV was determined following Equation 3.1.

10 µL of 30 µM DY731-Bio was dispersed in 400 µL PBS in a 10 mm optical path cell. The absorption and emission profiles of DY731-Bio (MoBiTec, Göttingen, Germany) were recorded using the UV/Vis/NIR Jasco V570 spectrometer and the Varian Cary Eclipse fluorimeter with the excitation wavelength tuned to 670 nm. Since the optical properties of dyes are highly dependent on the local environment and the manufacturer's molar extinction coefficient of DY731-Bio was given in ethanol, the

molar extinction coefficient of DY731-Bio was recalculated for PBS solution following Equation 3.1.

Aside from the fluorescence and the absorption measurements, PLE measurements were performed on the DY731-Bio solution using the Varian Cary Eclipse fluorimeter in which the luminescence intensity at 790 nm was monitored while scanning the excitation wavelength from 400 nm to 780 nm.

3.2.2 Characterisation of Qdot705-STV-DY731-Bio by Absorption Measurements

3.2.2.1 Qdot705-STV-DY731-Bio Titration

20 μL of 1 μM Qdot705-STV stock was added to 400 μL of 10 mM PBS (pH 7.4) in a 10 mm optical path cuvette. 5 μL of 27 μM DY731-Bio aliquot was added stepwise into the Qdot705-STV solution in a series of 9 titrations. The absorption profile of the solution in the course of titration was recorded using a UV/Vis/NIR Jasco V570 spectrometer. For comparison, pure DY731-Bio solution in the absence of Qdot705-STV was made as the control sample by replacing 20 μL Qdot705-STV solution with 20 μL PBS solution and the same protocols were repeated.

3.2.2.2 Qdot705-STV-DY731-Bio Reverse Titration

15 μL of 27 μM DY731-Bio and 5 μL of 1 μM Qdot705-STV were both dispersed in 400 μL of 10 mM PBS (pH 7.4) in a 10 mm optical path cuvette. This was followed by a titration with 5 μL Qdot705-STV aliquot until a total volume of 25 μL of 1 μM Qdot705-STV was dispensed into the mixture. For each Qdot705-STV addition, the absorption of the mixture was recorded using a UV/Vis/NIR Jasco V570 spectrometer.

3.2.3 Characterisation of DY731-Bio-STV by Absorption Measurements

1 mg of dessicated streptavidin powder was dissolved in 100 μL of 10 mM PBS (pH 7.4) to make up ~170 μM of streptavidin solution assuming the molecular weight is 60 kDa. 5 μL of 170 μM streptavidin aliquot was dispersed in 400 μL of 2.5 μM DY731-Bio solution to ensure the stoichiometry was ~1:1. Because streptavidin is a tetrameric

protein, the biotinylated DY731-Bio should be outnumbered by the binding pockets, thereby populating the solution with DY731-Bio-STV complexes formed via streptavidin-biotin linkage. The mixture was shaken and allowed to sit in the dark for 2-3 minutes before being transferred to 10 mm optical path cell to have the absorption measured using a UV/Vis/NIR Jasco V570 spectrometer from which the molar extinction coefficient was deduced.

3.2.4 FRET Investigation by Steady State Spectroscopy

10 μL of 1 μM Qdot705-STV was dispersed in 400 μL of 10 mM PBS (pH 7.4) in a 10 mm optical path fluorimeter cell. 2 μL of 30 μM DY731-Bio aliquot was first added to the Qdot705-STV solution and this was followed by further 9 successive titrations with 4 μL DY731 aliquot. The fluorescence intensity of the mixture in the course of titration was recorded using a Varian Cary Eclipse fluorimeter with the excitation wavelength set at 425 nm keeping the direct excitation of DY731-Bio minimal. For comparison, a control experiment was created in which the concentration of DY731-Bio in the control solution was maintained as that in the titration of Qdot705-STV with DY731-Bio by substituting 10 μL Qdot705-STV solution with 10 μL PBS solution. Apart from that, the same protocols were followed.

3.2.5 FRET Investigation by Time-Resolved Spectroscopy

5 diluted Qdot705-STV solutions were prepared by respectively dispersing 20 μL of 1 μM Qdot705-STV stock in 200 μL of 10 mM PBS (pH 7.4). 4-200 μL of 30 μM DY731-Bio was added to the solutions whereby varying the molar ratios. The mixtures were left to sit at room temperature in the dark for 15-20 minutes to allow streptavidin-biotin binding. By ultrafiltration with Microcon YM50 filter devices, the unbound DY731-Bio molecules were separated and removed from the solutions producing only conjugated complexes in that the molecular weight of DY731-Bio is ~1 kDa, which is well below the filter's cut-off molecular weight of 50 kDa. The samples were spun at 2000 x g (6000 rpm) three times for 20 minutes per wash. Each purified solution was collected and diluted with 100 μL PBS before being transferred to a 10 mm path length cell. In addition, a pure Qdot705-STV solution was prepared by dispersing 20 μL of Qdot705-STV stock in 100 μL PBS. Pure Qdot705-STV and filtered Qdot705-STV-

DY731-Bio solutions were optically pumped with a ~160 fs Ti:Sapphire pulsed laser that has the central wavelength tuned from 850 nm to 425 nm by a frequency-doubler to achieve minimal excitation of DY731-Bio and the repetition rate reduced from 76 MHz to 1.1 MHz by a pulse-picker to detect the rather long lived Qdot705-STV fluorescence decay. Due to the spectral overlap between Qdot705-STV and DY731-Bio emissions, a 700 nm short pass filter was used to attenuate DY731-Bio fluorescence. A 630 nm long pass filter was utilised to cut-off any scattered laser. The time-resolved measurements were conducted on a Hamamatsu streak camera Model C5680 with a temporal resolution of ~0.5 ns for 100 ns time range [4]. Then, each centrifuged sample was further diluted with 300 μL PBS to have the absorption measured with a UV/Vis/NIR Jasco V570 spectrometer which allowed the determination of the Qdot705-STV:DY731-Bio stoichiometry using the molar extinction coefficient of Qdot705-STV at 405 nm (ε = 6 800 000 $M^{-1}cm^{-1}$) and the molar extinction coefficient of DY731-Bio at 664 nm (ε = 103 000 $M^{-1}cm^{-1}$) without involving spectral deconvolution in view of the fact that Qdot705-STV lacks the strong band edge resonance and the absorption of DY731-Bio near UV regime is insignificant.

3.3 References

1. Skoog DA, West DM, Holler FJ. Fundamentals of Analytical Chemistry. 7th edn. Saunders College, 1996.

2. Bayer EA, Wilchek M. Application of Avidin-Biotin Technology to Affinity-Based Separations. *Journal of Chromatography* 1990, **510**:3-11.

3. Coherent. *Personal Communication.* 2006.

4. Hamamatsu. *Personal Communication.* 2007.

CHAPTER 4:

FRET INVESTIGATION USING CDSE/ZNS QUANTUM DOTS

CONTENTS:

Abstract: Here, we report on the use of Qdot585-STV as an energy donor and AF594-Bio as an energy acceptor in the design of ligand-binding mediated QD-dye self-assemblies in the visible spectral regime. We measure and evaluate the quenching efficiency of that with the utility of two independent spectroscopic techniques: i) the steady state fluorescence measurements and ii) the time-resolved fluorescence measurements in which the results are analysed qualitatively and quantitatively based on FRET formulae. In light of the $1/r^6$ dependence of FRET, we then proceed to the use of these data to provide the pertinent spatial information of QD-dye assays using theoretical FRET efficiency model that incorporates the idea of multiplexing whereby multiple resonant acceptors are self-adsorbed to a single donor.

CHAPTER 4:

FRET INVESTIGATIONS USING CDSE/ZNS QUANTUM DOTS

4.1 Optical Properties of Qdot585-STV

Qdot585-STV are core-shell QDs with II-VI semiconductor CdSe of bulk bandgap 1.74 eV as the inner core material, each of which exhibits spectral profiles that lie within the visible spectral region [1]. The core-shell QDs are size-tuned such that the emission peaks at a 585 nm wavelength. The narrow emission and the broad absorption of Qdot585-STV are shown below.

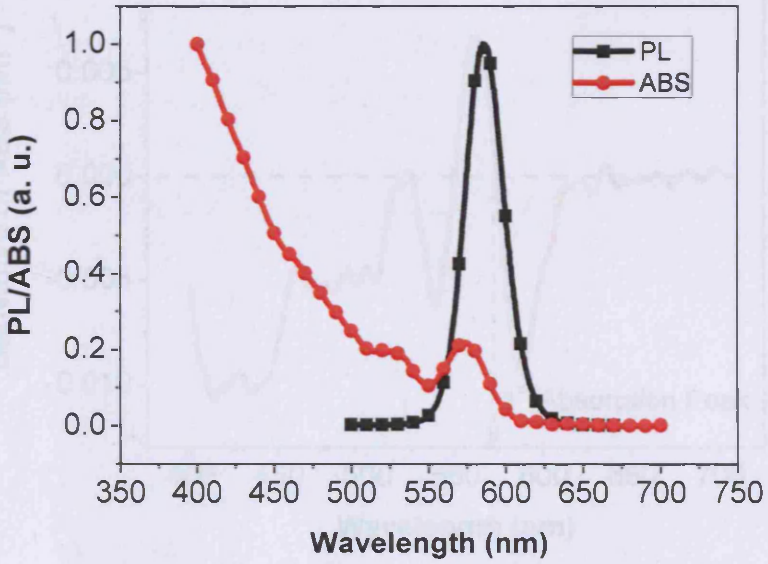

Figure 4.1: Photoluminescence and absorption spectra of Qdot585-STV.

As clearly illustrated in Figure 4.1, the absorption lineshape is continuous into the UV region and structured displaying several discrete features which provide the evidence of strong quantum confinement effect in pseudo-zero dimensional Qdot585-STV crystallites. The confinement effect arises when the QD radius becomes smaller than the bulk exciton Bohr radius, a_B [2]. For bulk CdSe, a_B is 56 Å. The same principle applies to Qdot585-STVwith the inner core composed of CdSe. Our TEM images (see Figure 2.6 in Chapter 2) show that the diameter of Qdot585-STV with ZnS coverage is typically around 5-6 nm. When pushing into the $R < a_B$ region (where R denotes the core radius), the energy states become quantised, in turn, giving rise to strong resonance at the absorption onset [3]. Hereby, because of the substantial changes in the electronic states, the lowest excited state of QD can be usually resolved with the utility of various spectroscopic techniques despite the linewidth broadening due to the inhomogeneous size distribution of QDs.

The first absorption peak is often ascribed to 1S-1S excitonic state, synonymously, the band edge state. At first glance of Figure 4.1, the band edge of Qdot585-STV appears to have dramatically blue shifted when compared to the bulk bandgap of CdSe that corresponds to a wavelength of 713 nm. To accurately identify the absorption maximum, we resorted to the first derivative of the absorption spectrum with respect to wavelength as depicted in Figure 4.2.

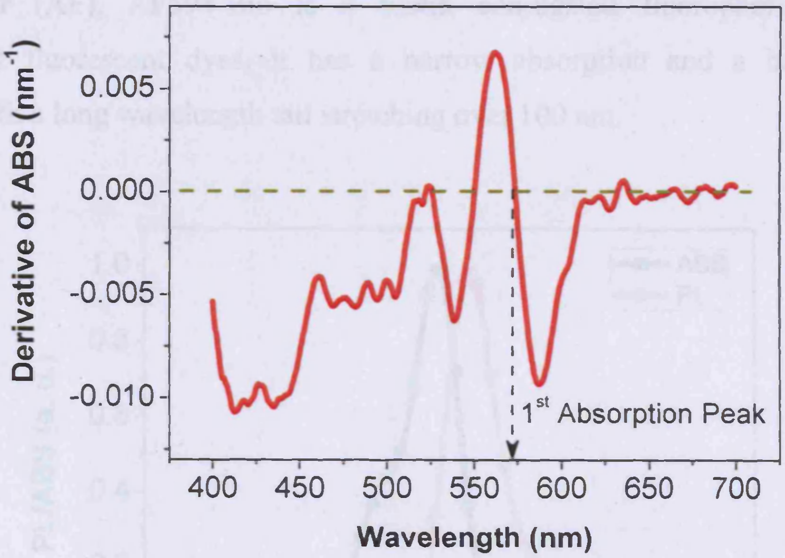

Figure 4.2: Derivative of Qdot585-STV absorption.

The gradient in Figure 4.2 indicates that the energy of 1S-1S excitonic state is 2.16 eV with an apparent 0.42 eV of magnitude higher than the bulk bandgap of CdSe. This demonstrates the exploitation of size correlated quantum confinement effect in QDs whereby the transitions of core-shell QD excited states can be tuned simply by the variation of core sizes to produce a range of QDs with photoemissions covering the whole visible spectrum.

The commercial Qdot585-STV shown here emit at a peak wavelength of 585 nm when photoexcited at a wavelength shorter than the absorption onset. The QDs are nearly monodisperse as reflected by the narrow linewidth of the emission spectrum. This is unequivocally supported by the evidence of small distribution in the Qdot585 size histogram (see Figure 2.7 in Chapter 2). As depicted in Figure 4.1, Qdot585-STV photoluminescence is symmetric and narrow with a full-width-at-half-maximum (FWHM) of about 30 nm. The narrow emission lineshape can be advantageous in the context of minimising the spectral cross-talk between fluorescent markers in a multiplex labelling and coupled with the broad absorption profile, Qdot585-STV are highly suitable to many bio-applications especially FRET based sensing [4].

4.2 Optical Properties of AF594-Bio

Alexa Fluor (AF), AF594-Bio is a biotin conjugated fluorophore. Like other conventional fluorescent dyes, it has a narrow absorption and a broad emission spectrum with a long wavelength tail stretching over 100 nm.

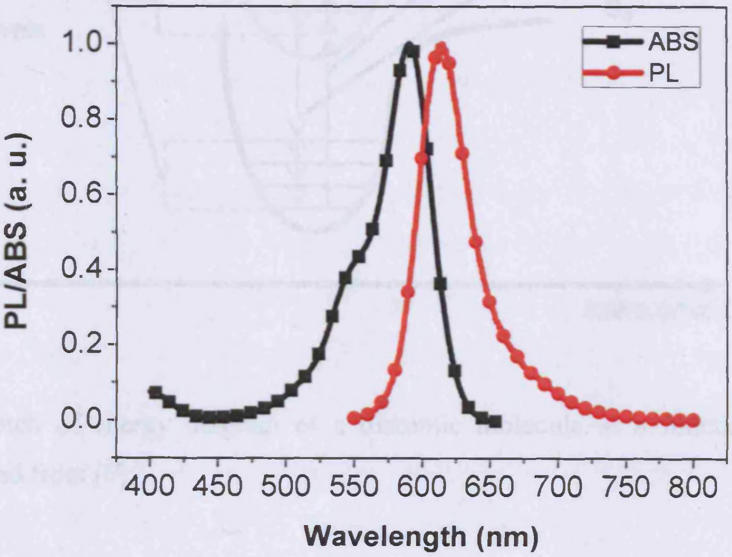

Figure 4.3: Absorption and emission spectra of AF594-Bio.

As shown in Figure 4.3, the absorption of AF594-Bio resonates at 590 nm. The 590 nm principal absorption is accompanied by a secondary absorbance centres round 550 nm. Generally, the absorption shoulder is ascribed to the excitation of electron to higher electronic state S_2 in a Jablonski diagram [5]. The photoinduced electron can later fall to ground state via a radiative or nonradiative decay pathway. The emission and absorption maxima are spectrally separated by a Stokes shift of ~20 nm. Although AF594-Bio is a homogeneous system, its fluorescence FWHM is rather broad in the order of 44 nm, which is comparatively greater than that of the inhomogeneous Qdot585-STV emission by a factor of 1.5. The linewidth broadening is attributed to the vibrational modes of AF594-Bio molecule that primarily define its energy states (vibrational levels). The underlying electronic transitions of AF594-Bio can be explained pictorially with the energy diagram of a simple diatomic molecule as delineated in Figure 4.3.

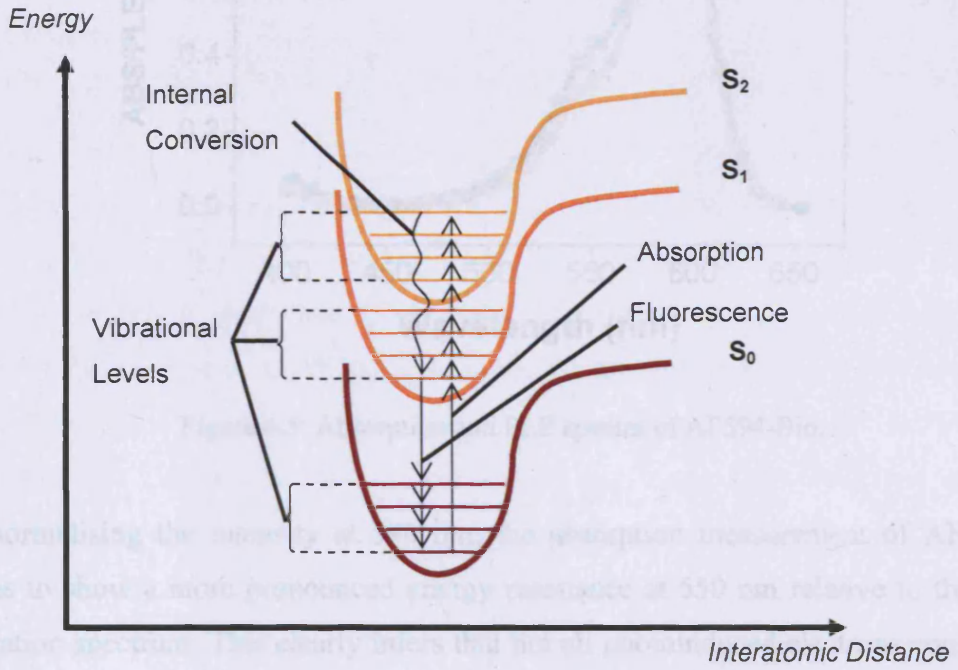

Figure 4.4: Sketch of energy diagram of a diatomic molecule as a function of interatomic distance. Adapted from [6].

From a multicolour imaging perspective, the broad photoemission profile of AF594-Bio is unfavourable where the presence of red tail is likely to render false signal count in various detection channels if it is utilised alongside other long wavelength emitting labels.

Besides having the ability to resolve the excited states of fluorescent dyes, when compared with the absorption spectrum, the measurement of photoluminescence excitation (PLE) spectroscopy can reveal the relative efficiency of the absorbed photon energy in converting to radiation. PLE spectroscopic technique works by monitoring the intensity of fluorescence when the excitation wavelength is scanned across the absorption band of molecular dye. Here, the fluorescence intensity at a wavelength of 650 nm was measured during the course of PLE measurement. The absorption of AF594-Bio is shown along with the PLE spectrum in Figure 4.5.

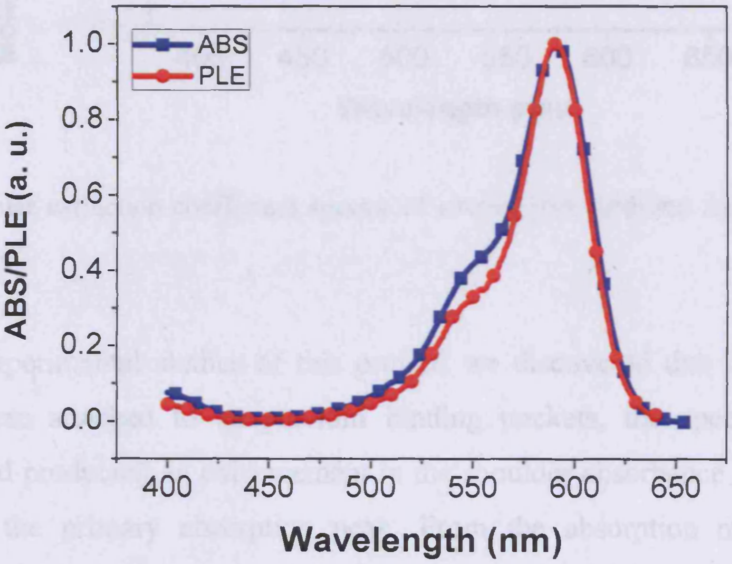

Figure 4.5: Absorption and PLE spectra of AF594-Bio.

By normalising the intensity at 590 nm, the absorption measurement of AF594-Bio seems to show a more pronounced energy resonance at 550 nm relative to that of the excitation spectrum. This clearly infers that not all photoinduced electrons constitute to spontaneous radiation. Some excited electrons may lose energy through nonradiative channels. In addition, the possibility of AF594-Bio having non-emitting moiety that absorbs at 550 nm but does not fluoresce can also provide a plausible explanation to the unparallel intensities observed between the absorption and PLE measurements at 550 nm [7].

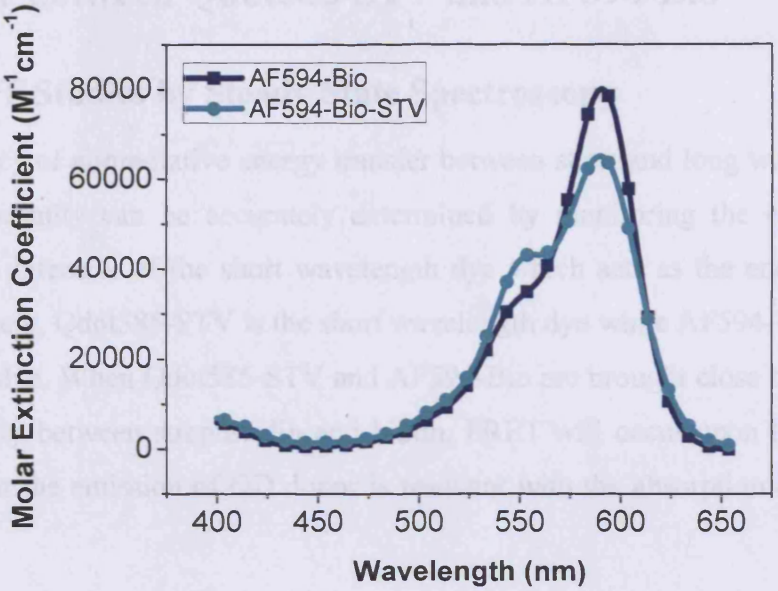

Figure 4.6: Molar extinction coefficient spectra of streptavidin modified AF594-Bio-STV and pure AF594-Bio.

During the experimental studies of this project, we discovered that when AF594-Bio molecules were attached to streptavidin binding pockets, the spectral profile was slightly altered producing an enhancement in the shoulder absorbance and a concurrent reduction in the primary absorption peak. From the absorption measurement, we predicate the maximum molar extinction coefficient of conjugated AF594-Bio-STV to be 65 000 $M^{-1}cm^{-1}$ which is ~19 % lower than the reported value for AF594-Bio by Invitrogen (i.e. 80 000 $M^{-1}cm^{-1}$ at pH 7) [8]. Following that, the latter extinction coefficient was utilised to quantitate the stoichiometry of AF594-Bio in FRET based assays. No spectral shift was detected in either of the absorption curves before and after the dispersion of streptavidin into the AF594-Bio solution. This provides the evidence that the electronic transitions in streptavidin bound/unbound AF594-Bio species remain unchanged. We attribute the changes in the absorptivity of conjugated AF594-Bio-STV complex to the structural modifications of AF594-Bio molecule upon streptavidin binding. To cooperate into the binding pocket of streptavidin, AF594-Bio may have modified its molecular conformation during the association of streptavidin-biotin. The speculation is supported by the report of structural cooperativity changes (protein tightness) in liganded streptavidin that induced by biotin binding [9].

4.3 FRET between Qdot585-STV and AF594-Bio

4.3.1 FRET Studies by Steady State Spectroscopy

The efficiency of nonradiative energy transfer between short and long wavelength dyes in close proximity can be accurately determined by monitoring the changes in the fluorescence intensity of the short wavelength dye which acts as the energy donor. In this experiment, Qdot585-STV is the short wavelength dye while AF594-Bio is the long wavelength dye. When Qdot585-STV and AF594-Bio are brought close together by the strong affinity between streptavidin and biotin, FRET will occur upon blue excitation provided that the emission of QD donor is resonant with the absorption of fluorophore acceptor.

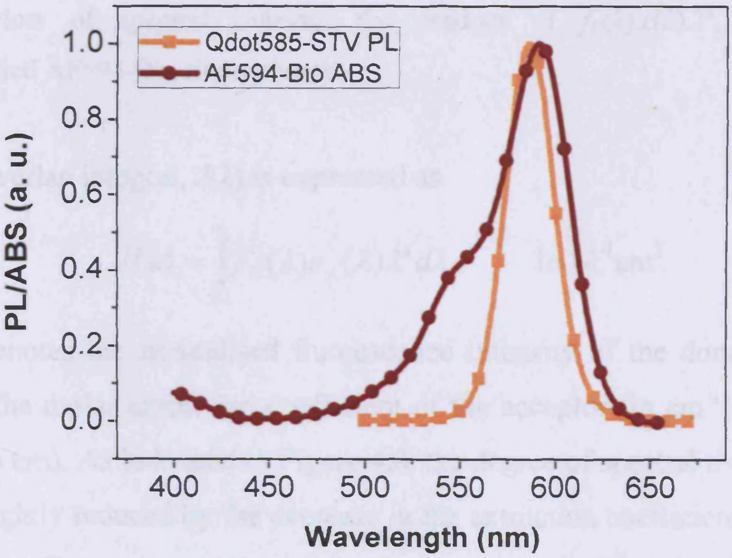

Figure 4.7: Qdot585-STV emission and AF594-Bio absorption spectra.

In view of the spectroscopic profiles of Qdot585-STV and pure AF594-Bio in Figure 4.7, they should be ideal FRET pairs assuming other criteria i.e. high quantum yield of the donor, Q_D and effective dipole-dipole orientation, κ^2 are satisfied. The spectral overlap between QD luminescence and dye absorption is exceptionally good with both maxima virtually coincident. However, since there are discernible differences between the optical densities of streptavidin bound AF594-Bio-STV and unbound AF594-Bio as shown previously (see Figure 4.6), we plot out the respective spectral overlaps as a function of wavelength prior to comparative studies of Förster distance, R_0.

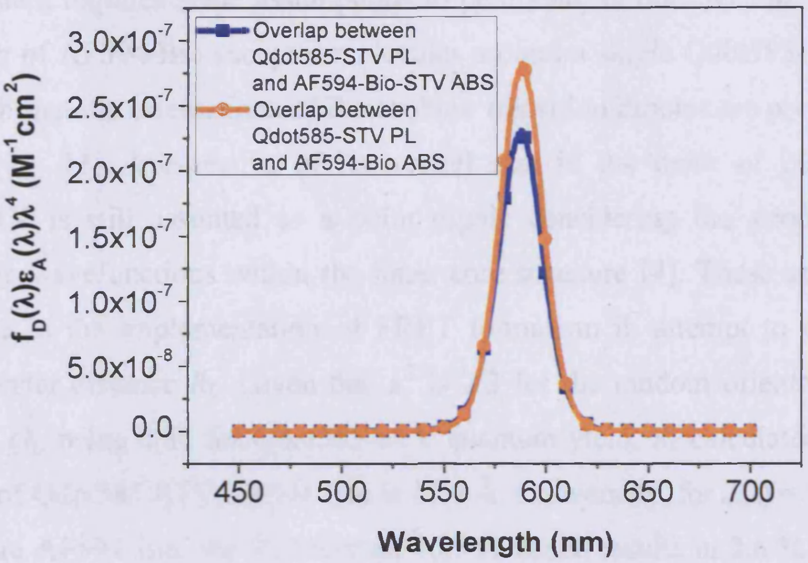

Figure 4.8: Plots of spectral overlap, the product of $f_D(\lambda).\varepsilon(\lambda).\lambda^4$, for streptavidin labelled/unlabelled AF594-Bio fluorophores.

The spectral overlap integral, $J(\lambda)$ is expressed as

$$J(\lambda) = \int_0^\infty f_D(\lambda)\varepsilon_A(\lambda)\lambda^4 d\lambda \qquad \text{in } M^{-1}cm^3 \qquad (4.1)$$

where $f_D(\lambda)$ denotes the normalised fluorescence intensity of the donor (in cm^{-1}) and $\varepsilon_A(\lambda)$ denotes the molar extinction coefficient of the acceptor (in cm^{-1}M^{-1}) and λ is the wavelength (in cm). As indicated in Figure 4.8, the degree of spectral overlap in AF594-Bio-STV is slightly reduced by the decrease in the extinction coefficient at the principal S_0-S_1 transition. The corresponding theoretical calculated $J(\lambda)$ value is 6.42x10^{-13} M^{-1}cm^3, which accounts for 14 % change in magnitude in comparison with 7.50x10^{-13} M^{-1}cm^3 for pure AF594-Bio. It seems apparent that there is a possibility that the impact on the accuracy of Förster distance, R_0 calculation can be significant if the former overlap integral is not applied. The extent of these implications on the predication of R_0 was investigated and the results are described in the following paragraph.

The Förster distance, R_0 of donor-acceptor conjugation is defined as

$$R_0 = 9.79 \cdot 10^3 \left(n^{-4} Q_D \kappa^2 J(\lambda)\right)^{1/6} \qquad \text{in Å} \qquad (4.2)$$

with n is the refractive index of the medium in which the conjugated assays are embedded, Q_D is the quantum efficiency of the donor, κ^2 is the orientation factor of donor-acceptor transition dipoles and $J(\lambda)$ is the spectral overlap integral. Since FRET

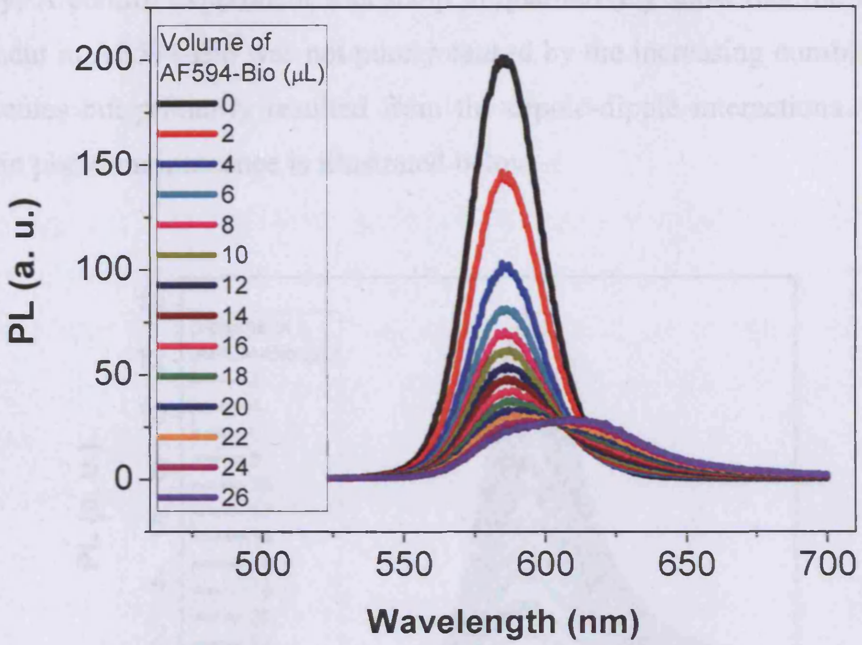

Figure 4.9: Spectral evolution of Qdot585-STV-AF594-Bio photoluminescence in a titration experiment.

Figure 4.9 shows a drastic fall in the intensity of Qdot585-STV luminescence when 2 μL of AF594-Bio solution was initially dispensed into the QD solution. Herein, we attribute the quenching effect to FRET process since the optical density of AF594-Bio was well below 0.01. The trivial photon reabsorption by AF594-Bio should be negligible here. The quenching effect of Qdot585-STV fluorescence can be rationalised by the fact that when Qdot585-STV and AF594-Bio are brought closer by the binding moieties, a new nonradiative relaxation pathway is introduced to the photoexcited carriers in QDs, which in turn, depopulates the band edge level. Thus, the lesser the electrons recombine radiatively, the weaker the donor fluorescence signal becomes. However, the quenching effect gradually levelled off as more acceptors were added indicating that the saturation point has been reached and further onset of titration would not contribute to FRET quenching. In that situation, the QD surface would have probably packed with AF594-Bio molecules and the close packing of acceptors might be a hindrance to further dipole-dipole interactions with more acceptors.

Besides the quenching effect of Qdot585-STV donor emission, the enhancement of AF594-Bio emission was also triggered by FRET. Energy transferred from Qdot585-

STV can excite ground state AF594-Bio fluorophores which subsequently relax radiatively. A control experiment was setup to qualitatively show that the fluorescence enhancement in AF594-Bio was not purely caused by the increasing number of AF594-Bio molecules but primarily resulted from the dipole-dipole interactions. The control AF594-Bio photoluminescence is illustrated below.

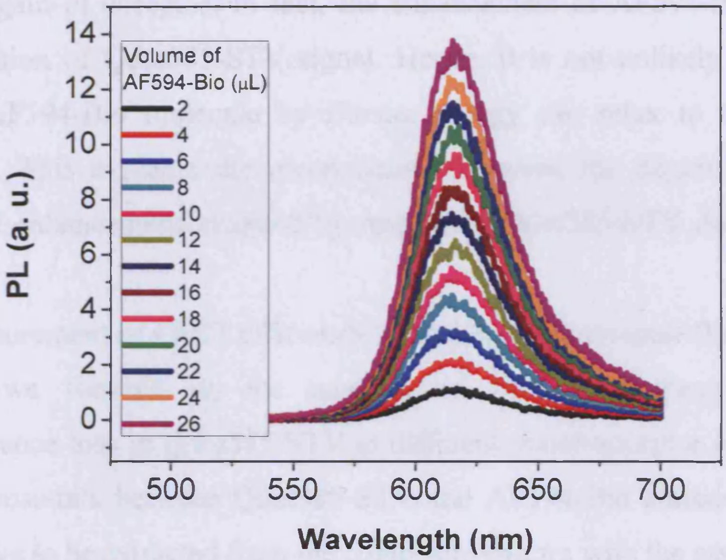

Figure 4.10: Control photoluminescence of AF594-Bio in a series of titrations.

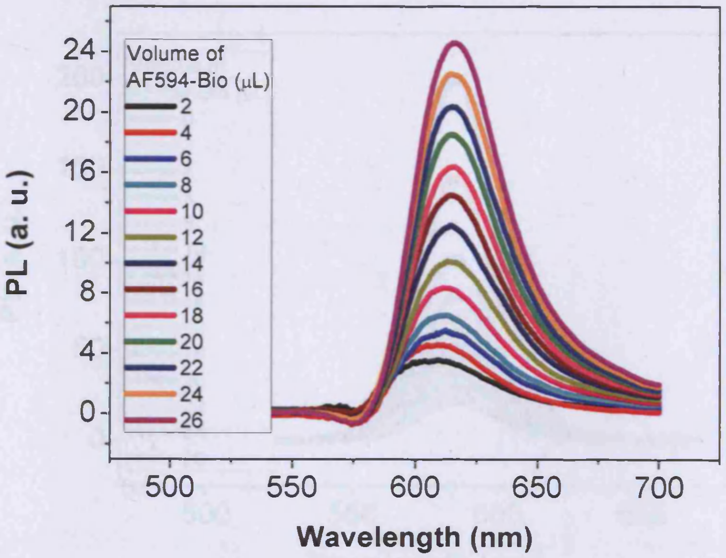

Figure 4.11: Photoluminescence of AF594-Bio extracted from the composite spectra in Figure 4.9.

The intensities of the control spectra from 425 nm direct excitation in Figure 4.10 are typically below that of the extracted spectra in Figure 4.11. The systematic enhancement of AF594-Bio fluorescence is the resultant of FRET as the radiation by reabsorption of QD photons is trivial for the first few titrations. However, from the qualitative comparisons between the spectral intensities in Figure 4.9, Figure 4.10 and Figure 4.11, the percentage drop in the donor emission does not translate completely into the luminescence gain of acceptor. In fact, the enhancement of AF594-Bio signal is less than the reduction of Qdot585-STV signal. Hence, it is not unlikely that the excited electrons in AF594-Bio molecule by Förster energy can relax to the ground state nonradiatively. This explains the inconsistency between the degree of fluorescence quenching and enhancement incurred by respective Qdot585-STV donor and AF594-Bio acceptor.

Since the measurement of FRET efficiency from enhanced acceptor fluorescence is less reliable [5], we focused on the analysis of FRET efficiency based on the photoluminescence loss in Qdot585-STV at different donor-acceptor molar ratios. Due to the small cross-talk between Qdot585-STV and AF594-Bio emissions, the relevant QD spectra have to be extracted from the composite spectra with the assumption that the respective optical profiles remained unchanged throughout the titrations. The extracted Qdot585-STV spectra in a series of titrations are compiled in Figure 4.12.

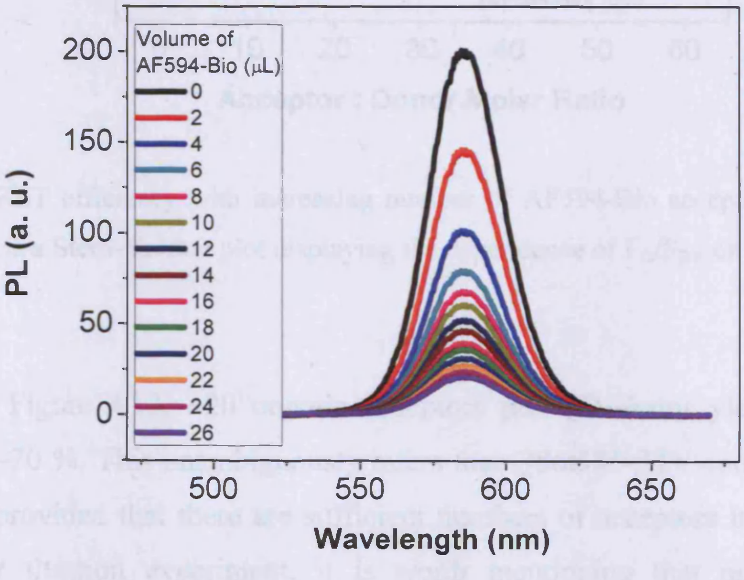

Figure 4.12: Evolution of extracted Qdot585-STV photoluminescence with increasing concentration of AF594-Bio.

Figure 4.12 depicts a systematic loss of Qdot585-STV fluorescence intensity upon stepwise titration with AF594-Bio. With the integration of individual Qdot585-STV photoemission intensity spectrum at each donor/acceptor stoichiometry, the corresponding efficacy of direct energy coupling between Qdot585-STV and AF594-Bio can be determined from

$$E = 1 - \frac{F_{DA}}{F_D} \qquad (4.3)$$

where F_{DA} is the integrated fluorescence intensity of the donor in the presence of the acceptor and F_D is the integrated fluorescence intensity of the donor alone. Hereby, we express the FRET efficiency as a function of acceptor-donor molar ratio in Figure 4.13 calculated from the integrated Qdot585-STV intensity spectra.

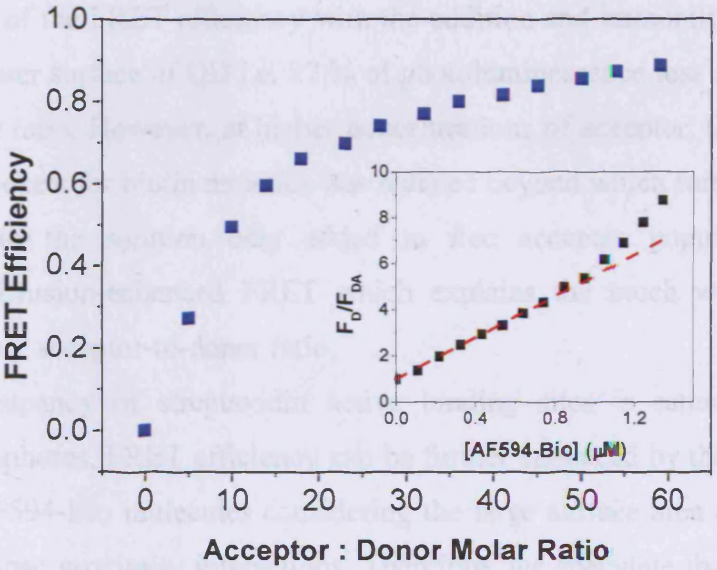

Figure 4.13: FRET efficiency with increasing number of AF594-Bio acceptors per Qdot585-STV. The inset is a Stern-Volmer plot displaying the dependence of F_D/F_{DA} on the concentration of acceptor.

As shown in Figure 4.13, ~20 organic acceptors per QD donor yield a quenching efficiency of ~70 %. This unambiguously infers that Qdot585-STV can be an effective FRET donor provided that there are sufficient numbers of acceptors in its vicinity. In this particular titration experiment, it is worth mentioning that no filtration was performed on the mixed solution. Therefore, fast diffusing unbound AF594-Bio molecules in non-viscous PBS are likely to compete for FRET, if they enter the Förster zone of Qdot585-STV through viable translational motion, to the extent that its significance can no longer be discounted [10]. This is substantiated by the upward curvature of the Stern-Volmer plot shown in the inset of Figure 4.13 in which the characteristic feature is only observable when there is more than one quenching process responsible for the reduction of donor fluorescence. Hence, other than the static FRET between bound donor-acceptor, the occurrence of diffusion-mediated FRET is not unlikely for a non-filtered mixture of Qdot585-STV and AF594-Bio.

By estimation, around 5-10 streptavidin are chemically coupled to a Qdot585-STV [12]. Bearing in mind that streptavidin is a tetrameric protein, one Qdot585-STV, hypothetically, will have the potential to bind with 20-40 biotin molecules. Hence, for the first few titrations with AF594-Bio, the number of binding pockets per QD should be in excess as compared to the number of biotinylated acceptors. This correlates to the initial increase of the FRET efficiency with the addition and immobilisation of AF594-Bio onto the outer surface of QD i.e. 27 % of photoluminescence loss at a 5:1 acceptor-to-donor molar ratio. However, at higher concentrations of acceptor, the availability of free binding pockets for biotin moieties was reduced beyond which further dispersion of AF594-Bio into the solution only added to free acceptor population ultimately mediating a diffusion-enhanced FRET which explains the much weaker quenching effect after ~20:1 acceptor-to-donor ratio.

When the occupancy of streptavidin active binding sites is saturated with biotin liganded fluorophores, FRET efficiency can be further enhanced by the diffusion effect of unbound AF594-Bio molecules considering the large surface area of Qdot585-STV available for close proximity interactions. Therefore, we speculate that the increase in FRET efficiency after 20-40:1 molar ratio is attributed to the diffusion-induced dipole-dipole interactions between Qdot585-STV and free AF584-Bio presuming that the translational motion of AF594-Bio is fast comparative to the rate of decay of excited Qdot585-STV. If otherwise, no further static FRET, thus, no further reduction in the donor intensity should be detected as all possible binding sites were liganded. Since the diffusion-induced FRET between Qdot585-STV and unlinked AF594-Bio is a much weaker quenching process than that of static bound pairs, the degree of photoluminescence loss in the donor should be less dramatic as suggested by the subtle differences in the quenching efficiencies within the range from 20 to 60 acceptor-to-donor molar ratios. As the optical density of AF594-Bio at the final titration was kept below 0.1, the linearity expressed in the Beer-Lambert law is still applied to the experiment. The inner filter effect by radiative reabsorption is less likely accountable for the non-linear reduction in Qdot585-STV emission intensities at increasing molar ratios particularly above 20:1. Therefore, FRET mediation by lateral translation of free AF594-Bio molecules should be a more effective donor quenching mechanism in a non-viscous medium like PBS solution. However, it is only by temporal measurement that the hypothesis of diffusion-enhanced FRET can be verified.

Due to the spatial sensitivity of FRET in nanometer range, we fitted the experimental data with theoretical FRET efficiency formula in order to obtain an estimate for the centre-to-centre separation between Qdot585-STV and AF594-Bio. Assuming that the acceptors are homogeneously distributed over the surface of QD at a constant distance, the FRET efficiency can be expressed as

$$E = \frac{nR_0^{\ 6}}{nR_0^{\ 6} + r^6} \tag{4.4}$$

where n represents the valency of QD (the number of acceptors per QD), R_0 represents the Förster distance and r represents the donor-acceptor distance.

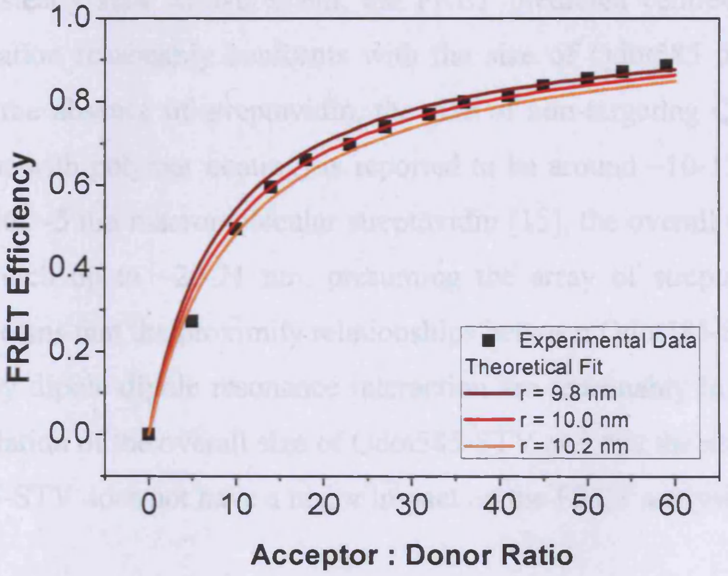

Figure 4.14: The experimental data points (■) are fitted using *n*-acceptor FRET efficiency formula with *r* set as adjustable parameter (represented by solid lines) to elicit the optimum donor-acceptor distance. $R_0 = 68.7$ Å was used in the calculation.

It seems apparent that, from Figure 4.14, the FRET model with $r = 10.0$ nm produces the best fit which inherently suggests that the centre-to-centre distance between

Qdot585-STV and AF594-Bio could be 10.0 nm. However, the interpretation of the donor-acceptor spatial information based on the steady state donor quenching data is hardly straightforward due to the geometrical nature of Qdot585-STV. Not all of the dots in the Qdot585-STV ensemble are perfectly spherical. Some resemble more of a prolate shape (see Figure 2.6 in Chapter 2) [13]. The structural heterogeneity of Qdot585-STV is further exacerbated by the inhomogeneous distribution of sizes. In the preceding chapter, we have shown that there are dots with different diameters ranging from 5 to 7 nm in Qdot585-STV ensemble (see Figure 2.7 in Chapter 2). With the heterogeneities of size and shape, Qdot585-STV is readily ramified into subpopulations of crystallites displaying slight dissimilarities in structure. Hereby, the real separation between Qdot585-STV and AF594-Bio is effectively distributed across a finite range. Furthermore, streptavidin and biotin are not completely rigid binding moieties. The vibrational and rotational motions of these bio-linkers will broaden the distance distribution that cannot be revealed by steady state photoluminescence measurement [5]. Hence, the numerical r value elicited from steady state measurements should be seen as an approximation and not the absolute donor-acceptor distance. Despite the limitations of steady state measurement, the FRET predicted centre-to-centre donor-acceptor separation reasonably conforms with the size of Qdot585 that estimated by Invitrogen. In the absence of streptavidin, the size of non-targeting Qdot585 (without streptavidin but with polymer coating) is reported to be around ~10-11 nm [14]. Upon conjugation with ~5 nm macromolecular streptavidin [15], the overall size of Qdot585-STV could stretch up to ~20-21 nm, presuming the array of streptavidin is centro-symmetric. It seems that the proximity relationships between Qdot585-STV and AF594-Bio revealed by dipole-dipole resonance interaction are reasonably in good agreement with our postulation of the overall size of Qdot585-STV and that the structural disparity of the Qdot585-STV does not have a major impact on the FRET analysis.

4.3.2 FRET Studies by Time-Resolved Spectroscopy

Temporal measurement is a more robust method for studying the efficiency of FRET between Qdot585-STV and AF594-Bio as it is not susceptible to the inner filter effect caused by high acceptor concentration. The trivial radiative reabsorption does not affect the dynamics of excited carriers in QD. Hence, any change in the decay profile of QD can be reliably related to FRET process.

In this experiment, we examined the intermolecular interaction between Qdot585-STV and AF594-Bio in an assay configuration. Unbound impurities were removed by centrifugations prior to temporal measurements. Therefore, along with the assessment of Qdot585-STV functionality as energy donor in bioassays, we estimated the greatest number of AF594-Bio that could possibly self-assemble around a single Qdot585-STV from steady state absorption measurements. The measured absorbance of each purified Qdot585-STV-AF594-Bio sample is plotted in Figure 4.14.

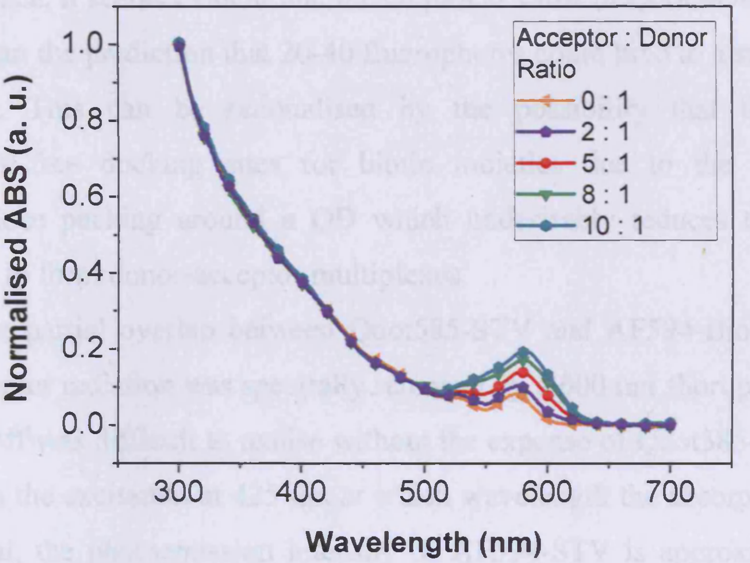

Figure 4.15: Absorption spectra of Qdot585-STV-AF594-Bio assays at various loading ratios.

To achieve an accurate numeration of *n*-acceptors per QD in self-assemblies can be a challenge as the exact number of streptavidin per Qdot585-STV is usually unknown. The range can be distributed across 5 to 10 streptavidin per QD and the matter is further exacerbated by the tetrameric nature of streptavidin. In view of the heterogeneity of the streptavidin coupling, the number of bound fluorophores could vary from dot to dot in an ensemble solution. Nonetheless, absorption measurements can be used to determine the effective AF594-Bio-to-Qdot585-STV loading ratio which primarily indicates the average valency of Qdot585-STV. Based on the measured absorbance, we deduced the average number of labelled AF594-Bio per QD from the molar extinction coefficient of Qdot585-STV at 450 nm (ε = 870 000 $M^{-1}cm^{-1}$) and the molar extinction coefficient of AF594-Bio-STV at 590 nm (ε = 65 000 $M^{-1}cm^{-1}$). Bearing in mind that since bound and unbound AF594-Bio molecules have been previously shown to exhibit slightly dissimilar absorption property (see Figure 4.6), the extinction coefficient of AF594-Bio-STV has to be utilised in the calculation of the molar concentration of fluorophores in self-assemblies. Prior to the determination of molar concentrations, the composite absorption spectra in Figure 4.15 were separated into individual donor and acceptor spectral components. The molar ratio of AF594-Bio to Qdot585-STV was rounded to the nearest integer which can be perceived as the average number of labelled AF594-Bio per Qdot585-STV in self-assemblies. The absorption measurements revealed that a single Qdot585-STV could target up to ~10 free biotinylated biomolecules in a volatile dispersion. Hence, it seems evident that the empirical value of Qdot585-STV valency is much lower than the prediction that 20-40 fluorophores could bind to a surface modified Qdot585-STV. This can be rationalised by the possibility that there could be obscuration of free docking sites for biotin moieties due to the orientations of streptavidin close packing around a QD which undesirably reduces the potential of Qdot585-STV to form donor-acceptor multiplexes.

Because of the partial overlap between Qdot585-STV and AF594-Bio emissions, the irrelevant acceptor radiation was spectrally removed by a 600 nm short pass filter, albeit complete cut-off was difficult to realise without the expense of Qdot585-STV radiation. However, with the excitation at 425 nm at which wavelength the absorption of AF594-Bio is minimal, the photoemission intensity of AF594-STV is approximately tenfold weaker than that of Qdot585-STV (see Figure 4.9), not to mention the differences below 600 nm. Moreover, organic luminescent molecules have typical short lifetimes of the order of few nanoseconds [5, 16]. On the basis of that, we can reliably deduce that only the time response of the transmitted Qdot585-STV photoluminescence was monitored by a streak camera. The spectrally filtered and unfiltered luminescence spectra of Qdot585-STV ensemble are shown alongside AF594-Bio fluorescence in Figure 4.16 for comparison.

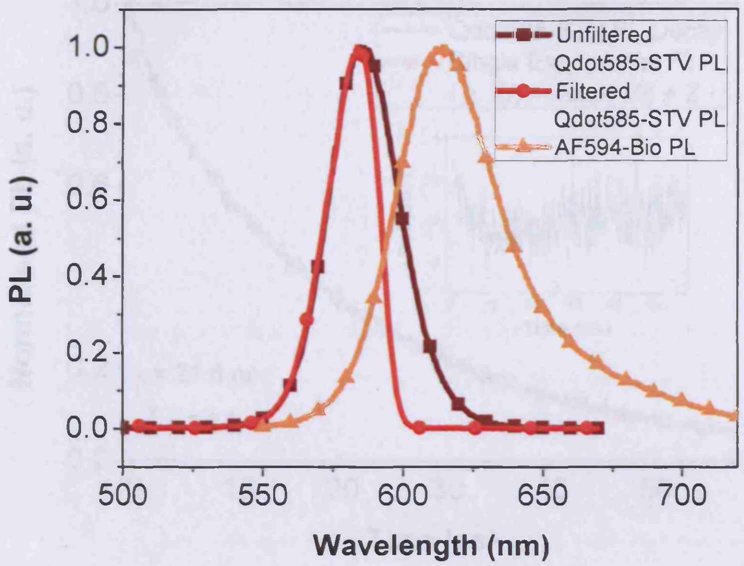

Figure 4.16: Spectrally filtered and unfiltered photoluminescence spectra of Qdot585-STV along with AF594-Bio photoluminescence spectrum.

FRET efficiency between Qdot585-STV donors and bound AF594-Bio acceptors can be unravelled by the dynamical studies of Qdot585-Bio excitons upon femtosecond pulsed excitation. Within a finite time scale, the photoinduced excitons will eventually recombine to the ground state radiatively or nonradiatively. Since the time response of QD photoluminescence is a measurable quantity that relates to the depopulation rate of the band edge state, by tracing the changes in the photoluminescence decays of Qdot585-STV in the presence/absence of immobilised AF594-Bio, the efficacy of nonradiative energy transfer within the donor-acceptor self-assemblies can be evaluated. We discretely prepared Qdot585-STV-AF594-Bio assays in a series of increasing stoichiometric ratio from 0 to 10 of AF594-Bio per Qdot585-STV. For each sample, the fluorescence decay of QD ensemble was recorded and compared. In the context of recombination kinetics, QDs are widely known to deviate from well-behaved single exponential [11, 17, 18]. This is clearly shown in Figure 4.17 where a single exponential function fail to provide a reasonable fit to a typical PL decay of Qdot585-STV (in the absence of AF594-Bio) giving a χ^2 value close to 1.3.

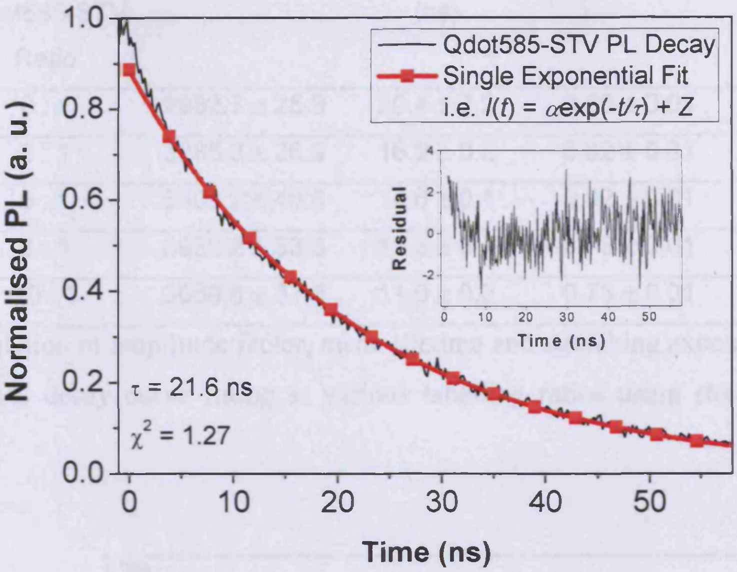

Figure 4.17: Photoluminescence decay of Qdot585-STV without AF594-Bio.

In view of the poor statistical fit of Qdot585-STV luminescence decay using the single lifetime model, a biexponential decay model was later utilised to extract the lifetimes of Qdot585-STV at various conjugation ratios. The biexponential function is defined as

$$I(t) = \alpha_1 \exp(-\frac{t}{\tau_1}) + \alpha_2 \exp(-\frac{t}{\tau_2}) + Z \tag{4.5}$$

with α_1 (α_2) are the amplitude factors, τ_1 (τ_2) are the time constants and Z is the baseline. From the data fitting, the biexponential model was found to have sufficient lifetime parameters, within reasonable goodness-of-fit as indicated by the chi-squared χ^2, to describe the dynamic behaviour of the QD photoemission following an instantaneous excitation pulse (refer Table 4.3). While other alternative decay model like a stretched exponential function

$$I(t) = \alpha \exp\left[-\left(\frac{t}{\tau}\right)^{\beta}\right] + Z \tag{4.6}$$

where α is the amplitude factor, τ is the mean lifetime, β is the stretching exponent ($0 < \beta \leq 1$) and Z is the baseline, can afford a reasonable good fit to the experimental data as shown in Table 4.2, the double exponential model is a preferred fitting scheme because it allows the interpretation of results with reference to QD kinetics.

AF594-Bio : Qdot585-STV Ratio	$\alpha \pm \Delta\alpha$	$\tau \pm \Delta\tau$ (ns)	$\beta \pm \Delta\beta$	χ^2
0 : 1	2982.7 ± 25.3	20.4 ± 0.2	0.86 ± 0.01	1.05
2 : 1	3285.3 ± 26.9	16.9 ± 0.2	0.82 ± 0.01	0.97
5 : 1	5509.2 ± 48.5	14.6 ± 0.1	0.82 ± 0.01	1.10
8 : 1	3932.2 ± 33.3	12.3 ± 0.1	0.78 ± 0.01	0.96
10 : 1	3089.8 ± 37.8	11.0 ± 0.2	0.75 ± 0.01	1.11

Table 4.2: Tabulation of amplitude factor, mean lifetime and stretching exponent obtained from Qdot585-STV PL decay curve fitting at various labelling ratios using stretched exponential function.

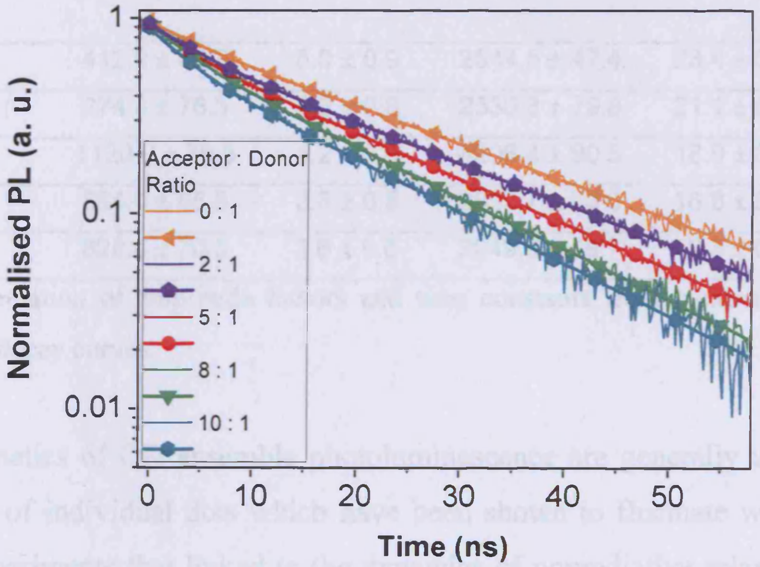

Figure 4.18: Qdot585-STV photoluminescence decay profiles and the corresponding two-lifetime fits at various labelling ratios where the number of conjugated AF594-Bio increases from 0 to 10.

When the acceptor loading was systematically increased, a progressive reduction in the photoemission decay time of Qdot585-STV was detected as illustrated in Figure 4.18. The substantial rise in the decay rate provides the essential evidence of dipole-dipole resonance interactions between Qdot585-STV energy donors and adjacent AF594-Bio energy acceptors. Within the Förster zone, the immobilised AF594-Bio molecules via ligand-receptor binding could afford an additional de-excitation pathway to QD excitons. This further adds to the native nonradiative channels in Qdot585-STV. As the rate of band edge photoluminescence decay is the sum of radiative and nonradiative recombination rates, the presence of bound acceptors, which only affects the nonradiative component of the total decay rate, will invariably reduce the overall time scale of Qdot585-STV fluorescence decay.

At various conjugation configurations, it seems apparent that the adopted fitting scheme is sufficient to recover the photoemission decay profiles of Qdot585-STV ensembles as indicated by the fact that for every exponential fit, the chi-squared χ^2 is well below 1.1. The numerical values of amplitude factors and decay lifetimes extracted from two-lifetime fits are compiled and tabulated in Table 4.3.

AF594-Bio : Qdot585-STV Ratio	$\alpha_1 \pm \Delta\alpha_1$	$\tau_1 \pm \Delta\tau_1$ (ns)	$\alpha_2 \pm \Delta\alpha_2$	$\tau_2 \pm \Delta\tau_2$ (ns)	χ^2
0 : 1	412.9 ± 46.6	5.0 ± 0.9	2544.5 ± 47.4	23.4 ± 0.4	1.04
2 : 1	674.8 ± 76.3	4.6 ± 0.8	2536.8 ± 79.8	21.1 ± 0.8	0.90
5 : 1	1120.9 ± 79.8	4.2 ± 0.6	4206.4 ± 90.5	18.9 ± 0.4	0.99
8 : 1	864.0 ± 65.5	3.8 ± 0.5	2837.7 ± 73.6	16.8 ± 0.4	0.93
10 : 1	828.4 ± 70.5	3.6 ± 0.6	2049.9 ± 79.7	16.3 ± 0.6	1.01

Table 4.3: Tabulation of amplitude factors and time constants from biexponential fitting of Qdot585-STV decay curves.

The decay kinetics of QD ensemble photoluminescence are generally underpinned by the dynamics of individual dots which have been shown to fluctuate with intensity in single dot experiments that linked to the dynamics of nonradiative relaxation channels [18, 19]. Moreover, the evidence of unparallel behaviour of decay dynamics across the photoluminescence spectrum of CdSe QDs in close packed solid implicitly infers that dots of various sizes within an ensemble are not only energetically but also dynamically distinct [20]. These findings highlight the heterogeneous effects perceived in most photoluminescence measurements of QD solution. Therein, the discreteness of single dot properties is often indecipherable in bulk solution due to ensemble averaging effect. It is no exception for the time resolved spectroscopic measurements of Qdot585-STV whereby the statistical exponential fits of the fluorescence decays only generate ensemble averaged lifetimes. By no means are the deduced lifetimes explicitly representative of single dot dynamics.

Two distinct lifetime components were resolved from the measured photoemission intensity decays as noted in Table 4.3. The short component was within 5 ns time scale and the long component was within 23 ns time scale. For pure Qdot585-STV solution, the long lifetime component of the order of 23 ns is typically ascribed to the intrinsic radiative lifetime of excitons in QDs as in [20], whilst the short lifetime component can be associated to fast nonradiative relaxations since the decay rates are usually several fold shorter than the radiative rate. However, the underlying physical process is unclear. Primarily, within the framework of QD FRET studies, we are interested in the magnitude change of the long lifetime component in the presence of proximal AF594-Bio molecules. Based on the empirical lifetime data, there is a marked reduction in the long decay lifetime component of Qdot585-STV with the elevation of acceptors bound onto QD surface. The average decay rate increases from 1/23 ns^{-1} to 1/16 ns^{-1} at the maximum labelling ratio. This and the results from steady state measurements unequivocally confirm the nonradiative FRET interactions in energetically resonant Qdot585-STV-AF594-Bio self-assemblies.

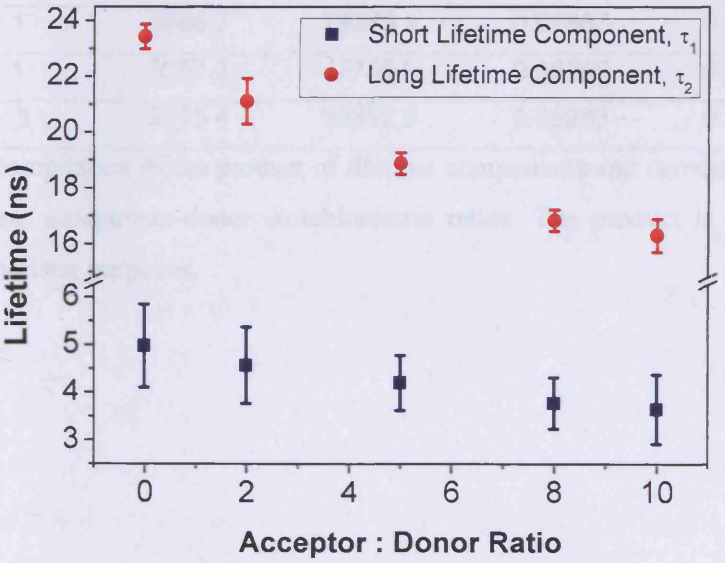

Figure 4.19: Short and long lifetime components as a function of increasing energy acceptors per QD energy donor.

From Figure 4.19, it seems apparent that the magnitude of reduction in the short lifetime component was less convincing than that of long lifetime. Due to the large error bar, one can argue that the short lifetime stays appreciably constant across the variation of Qdot585-STV valencies. Since the short lifetime parameter is insensitive to FRET, the study of the dipole-dipole resonance interactions between Qdot585-STV and immobilised AF594-Bio is based solely on the quantitative analysis of long lifetime component. To justify the approach, we calculated and compared the product of α_i and τ_i which is fundamentally proportional to the time integrated steady state fluorescence intensity [5]. The relation is described as follows,

$$\int_0^\infty I(t) = \sum_i \alpha_i \tau_i \tag{4.7}$$

where α_i is the amplitude factor, τ_i is the associated lifetime component and i is the number of lifetime parameters. In relevance to Equation 4.7, the explicit contribution of each decay time to steady state photoluminescence can be inferred.

AF594-Bio : Qdot585-STV Ratio	$\alpha_1\tau_1$ (ns)	$\alpha_2\tau_2$ (ns)	$\alpha_1\tau_1/\Sigma\alpha_i\tau_i$	$\alpha_2\tau_2/\Sigma\alpha_i\tau_i$
0 : 1	2052.2	59592.9	0.03329	0.96671
2 : 1	3077.3	53526.1	0.05437	0.94563
5 : 1	4696.7	79375.1	0.05587	0.94413
8 : 1	3257.3	47759.0	0.06385	0.93615
10 : 1	3015.4	33392.9	0.08282	0.91718

Table 4.4: Data compilation of the product of lifetime components and corresponding amplitude factors at different acceptor-to-donor stoichiometric ratios. The product is also expressed in fraction for comparison purposes.

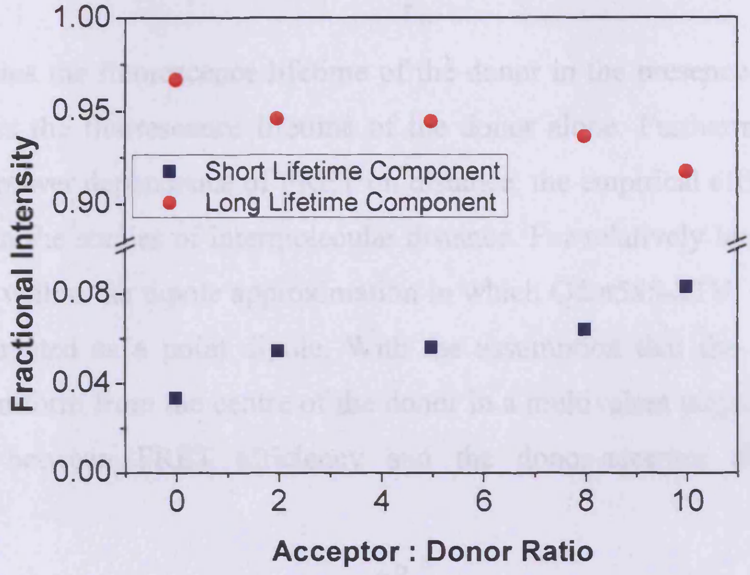

Figure 4.20: Fractional intensities of short and long lifetime components versus number of labelled AF594-Bio acceptors per Qdot585-STV.

As depicted by Figure 4.20, the overwhelming percentage of contribution to time integrated photoemission is from the 23 ns lifetime component showing a typical value of 0.9. There are only nuances in the fractional intensities of long lifetime component with steady increment of labelled acceptors per dot from 0 to 10. Hereby, with the assignment of the long lifetime component to the intrinsic radiative recombination process, it is intuitive to say that Qdot585-STV is a highly efficient luminescent crystallite. This is further supported by the high quantum yield of ~0.87 recorded by Invitrogen with reference to rhodamine. On the contrary, the radiative contribution from the short lifetime component was remote. In view of that, we approached FRET analysis discretely from the aspect of time fluctuation perceived in the dominant long lifetime component. The scale of reduction in the long lifetime component in the presence of proximal acceptors would afford some useful information on the potential of Qdot585-STV as energy donor in energetically resonant Qdot585-STV-AF594-Bio self-assemblies. With the lifetimes readily deduced from the statistical biexponential fits of Qdot585-STV fluorescence decays, the efficiency of nonradiative energy migration from Qdot585-STV donor at increasing acceptor-to-donor ratios can be quantified in accordance to the time-domain FRET efficiency formula as defined below,

$$E = 1 - \frac{\tau_{DA}}{\tau_D} \qquad (4.8)$$

with τ_{DA} denotes the fluorescence lifetime of the donor in the presence of the acceptor and τ_D denotes the fluorescence lifetime of the donor alone. Furthermore, due to the inverse sixth power dependence of FRET on distance, the empirical efficiency data can be exploited in the studies of intermolecular distance. For relatively large QD, this can be proceeded within the dipole approximation in which Qdot585-STV, besides AF594-Bio, is also treated as a point dipole. With the assumption that the coordination of acceptors is uniform from the centre of the donor in a multivalent targeting scheme, the relationships between FRET efficiency and the donor-acceptor distance can be expressed as

$$E = \frac{nR_0^{\,6}}{nR_0^{\,6} + r^6} \qquad (4.9)$$

where n represents the number of bound energy acceptors per donor and R_0 represents the Förster distance and r represents the centre-to-centre donor-acceptor distance. Though, in reality, QDs are inhomogeneous in size, we applied Equation 4.9 to our Qdot585-STV-AF594-Bio FRET system to acquire some forms of spatial information on the donor-acceptor proximity relationships. This theoretical approach to QD FRET analysis has been performed by a number of researchers and it has been shown to be useful in QD structural studies [10, 11, 21]. However, the extent of the size disparity in Qdot585-STV ensemble could be a source of hindrance to accurate prediction of radial distance between dot and dye centres. Henceforth, it is worth mentioning that the r value deduced from the theoretical treatment of FRET efficiency should be perceived as the ensemble averaged donor centre-to-acceptor centre separation, effectively, the average radius of Qdot585-STV (including streptavidin). Prior to the theoretical efficiency calculation, the spectral overlap integral, $J(\lambda)$, and the donor quantum yield, Q_D have to be predefined while keeping the values of other physical parameters i.e. $\kappa^2 = 2/3$ and $n = 1.33$ (refractive index) generally intact as in Section 4.3.1. The overlap integral between the spectrally filtered Qdot585-STV photoemission and AF594-Bio absorption was found to be $6.50\text{x}10^{-13}$ $M^{-1}cm^3$ and Q_D was assumed to be unity for the radiative lifetime, thereby generating R_0 of 70.4 Å. The experimental FRET efficiencies and several close fits are displayed in Figure 4.21.

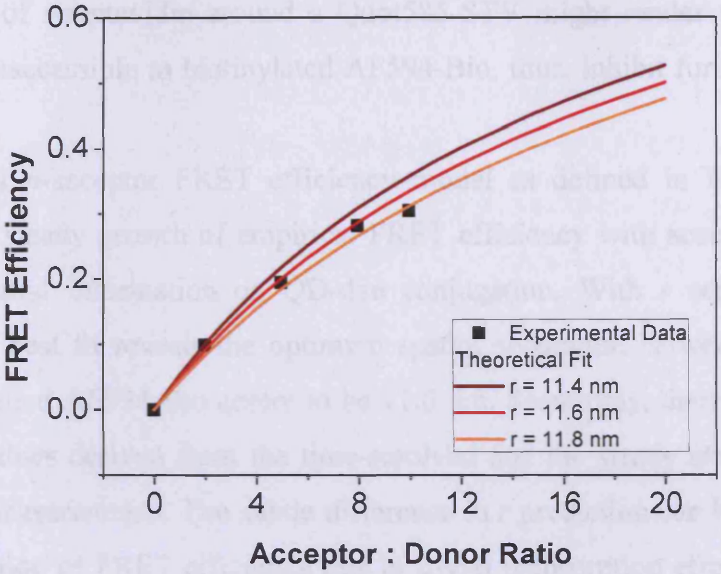

Figure 4.21: Plot of FRET efficiency versus acceptor-to-donor ratio. The experimental FRET efficiency data (■) is fitted with *r* adjustable *n*-acceptor FRET efficiency model (represented by solid lines).

The elevation of nonradiative energy transfer efficacy in QD-dye bioconjugates, before reaching the saturation level, is primarily restricted by the targeting ability/valency of biofunctionalised QD. This limitation is exemplified in Figure 4.21 whereby only a modest efficiency of ~0.3 was measurable when an estimate of maximum 10 biotinylated AF594-Bio molecules were appended to Qdot585-STV surface via streptavidin-biotin linkage. From direct comparison with the FRET efficiencies attained from the steady state photoluminescence measurements (see Figure 4.13), it seems likely that further dipole-dipole resonance interactions are viable if only the present valency of Qdot585-STV could be raised. Because of the large surface to volume ratio of QDs, the number of AF594-Bio molecules that could possibly interact with a Qdot585-STV should be greater than 10 leading to an extended loss of donor luminescence as depicted in Figure 4.13. Therefore, in the context of bioassay development, the potential of Qdot585-STV as effectual energy donor is basically bound by the number of accessible binding sites for biotin ligands. In other words, the FRET efficiency with reference to Qdot585-STV should improve if the maximum labelling ratio is not limited to 10 acceptors per QD. Since the number of free binding pockets is predicted to be around 20-40 per Qdot585-STV for which 5-10 tetrameric streptavidin are covalently appended onto the dot surface [12], we postulate that the close packing of streptavidin around a Qdot585-STV might render some of the free binding sites inaccessible to biotinylated AF594-Bio, thus, inhibit further direct energy coupling.

The theoretical n-acceptor FRET efficiency model as defined in Equation 4.9 was adapted to the steady growth of empirical FRET efficiency with acceptors in effort to extract the spatial information on QD-dye conjugation. With r set as the variable parameter, the best fit reveals the optimum spatial separation between Qdot585-STV centre and labelled AF594-Bio centre to be 11.6 nm. Seemingly, there is a discrepancy between the values derived from the time-resolved and the steady state (r = 10.0 nm) fluorescence measurements. The subtle difference in r prediction can be rationalised by the overestimation of FRET efficiency due to trivial reabsorption effect in steady state measurements (which is absent in temporal measurements) invariably causing the underestimation of donor-acceptor distance. Whilst that could be a plausible explanation for the discrepancy, the possibility of overestimation of the number of immobilisation AF594-Bio per Qdot585-STV cannot be discounted as well and thus leads to the overestimation of distance based on the lifetime data. Nonetheless, taking account of the uncertainty in Qdot585-STV physical dimension, the radial distances elicited from two independent spectroscopic measurements appear to conform with the postulated Qdot585-STV radius with reference to the structural information given by Invitrogen. The size of Qdot585 with polymer coating is estimated to be ~10-11 nm [14]. Presuming that Qdot585-STV is centro-symmetric, the size could be expanded to ~20-21 nm after surface functionalisation with ~5 nm streptavidin proteins to provide specificity [15]. Hence, the spacer between Qdot585-STV and AF594-Bio point dipoles is approximated to be ~10-11 nm. The extracted r values are appreciably consistent with the hypothetical dipole-dipole distance despite the heterogeneity in the QD-dye system i.e. the size distribution of QDs and the non-rigidity of streptavidin structure. This reassuringly verifies FRET as a viable spectroscopic technique in the studies of molecular conformation and the concept can be even extended to large semiconductor QDs with multiple valency.

4.4 Conclusions

In this chapter, I have shown that Qdot585-STV can serve as efficient energy donor in FRET assays given the criterion that there are considerable numbers of energetically resonant acceptors in the vicinity. The efficiency can elevate to ~0.7 for ~20:1 acceptor-to-donor stoichiometry as indicated by the steady state measurements. However, I later reported that the highest valency of Qdot585-STV after centrifugation is ~10 which ultimately impairs its performance in becoming efficacious in direct energy coupling. From the lifetime measurements, the corresponding FRET efficiency is merely ~0.3. Henceforth, in the development of QD-dye FRET based assays of increased sensitivity, it would be desirable to improve the present specificity of Qdot585-STV if it is to be utilised as the donor precursor. Alongside the experimental assessment of resonance interactions between Qdot585-STV and AF594-Bio, I have also revealed the practical aspect of theoretical FRET efficiency formulism in obtaining the spatial information on the QD-dye configuration that was later found to be reasonably consistent with the anticipated Qdot585-STV size.

4.5 References

1. CRC Handbook of Chemistry and Physics: A Ready-Reference Book of Chemical and Physical Data. 82th edn. Edited by Lide DR. CRC Press, 2001.

2. Wang Y, Herron N. Nanometer-Sized Semiconductor Clusters - Materials Synthesis, Quantum Size Effects, and Photophysical Properties. *J Phys Chem* 1991, **95**(2):525-532.

3. Alivisatos AP. Semiconductor Clusters, Nanocrystals, and Quantum Dots. *Science* 1996, **271**(5251):933-937.

4. Clapp AR, Medintz IL, Mattoussi H. Forster Resonance Energy Transfer Investigations Using Quantum-Dot Fluorophores. *Chemphyschem* 2006, **7**(1):47-57.

5. Lakowicz J. Principles of Fluorescence Spectroscopy. 3rd edn. Springer, 2006.

6. UV Spectroscopy Techniques, Instrumentation, Data Handling. vol. 4. Edited by Clark BJ, Frost T, Russell MA. Chapman and Hall, 1993.

7. Berlier JE, Rothe A, Buller G, Bradford J, Gray DR, Filanoski BJ, Telford WG, Yue S, Liu JX, Cheung CY *et al.* Quantitative Comparison of Long-Wavelength Alexa Fluor Dyes to Cy Dyes: Fluorescence of the Dyes and their

Bioconjugates. *Journal of Histochemistry & Cytochemistry* 2003, **51**(12):1699-1712.

8. http://probes.invitrogen.com/servlets/spectra/

9. Gonzalez M, Bagatolli LA, Echabe I, Arrondo JLR, Argarana CE, Cantor CR, Fidelio GD. Interaction of Biotin with Streptavidin - Thermostability and Conformational Changes upon Binding. *Journal of Biological Chemistry* 1997, **272**(17):11288-11294.

10. Goldman ER, Medintz IL, Whitley JL, Hayhurst A, Clapp AR, Uyeda HT, Deschamps JR, Lassman ME, Mattoussi H. A Hybrid Quantum Dot-Antibody Fragment Fluorescence Resonance Energy Transfer-Based TNT Sensor. *J Am Chem Soc* 2005, **127**(18):6744-6751.

11. Clapp AR, Medintz IL, Mauro JM, Fisher BR, Bawendi MG, Mattoussi H. Fluorescence Resonance Energy Transfer between Quantum Dot Donors and Dye-Labeled Protein Acceptors. *J Am Chem Soc* 2004, **126**(1):301-310.

12. Qdot Streptavidin Conjugates User Manual. Invitrogen, 2006.

13. Giepmans BNG, Deerinck TJ, Smarr BL, Jones YZ, Ellisman MH. Correlated Light and Electron Microscopic Imaging of Multiple Endogenous Proteins Using Quantum Dots. *Nature Methods* 2005, **2**(10):743-749.

14. Invitrogen. *Personal Communication.* 2006.

15. Arakaki A, Hideshima S, Nakagawa T, Niwa D, Tanaka T, Matsunaga T, Osaka T. Detection of Biomolecular Interaction between Biotin and Streptavidin on a Self-Assembled Monolayer Using Magnetic Nanoparticles. *Biotechnology and Bioengineering* 2004, **88**(4):543-546.

16. Strickler SJ, Berg RA. Relationship between Absorption Intensity and Fluorescence Lifetime of Molecules. *Journal Chemical Physics* 1962, **37**(4):814-822.

17. Empedocles SA, Neuhauser R, Shimizu K, Bawendi MG. Photoluminescence from Single Semiconductor Nanostructures. *Adv Mater* 1999, **11**(15):1243-1256.

18. Fisher BR, Eisler HJ, Stott NE, Bawendi MG. Emission Intensity Dependence and Single-Exponential Behavior in Single Colloidal Quantum Dot Fluorescence Lifetimes. *Journal of Physical Chemistry B* 2004, **108**(1):143-148.

19. Schlegel G, Bohnenberger J, Potapova I, Mews A. Fluorescence Decay Time of Single Semiconductor Nanocrystals. *Phys Rev Lett* 2002, **88**(13).

20. Crooker SA, Hollingsworth JA, Tretiak S, Klimov VI. Spectrally Resolved Dynamics of Energy Transfer in Quantum-Dot Assemblies: Towards Engineered Energy Flows in Artificial Materials. *Phys Rev Lett* 2002, **89**(18).

21. Medintz IL, Clapp AR, Mattoussi H, Goldman ER, Fisher B, Mauro JM. Self-Assembled Nanoscale Biosensors Based on Quantum Dot FRET Donors. *Nature Materials* 2003, **2**(9):630-638.

CHAPTER 5:

FRET INVESTIGATION USING CDTE/ZNS QUANTUM DOTS

CONTENTS:

Abstract: In this chapter, I report on the utilisation of Qdot705-STV as an energy donor and DY731-Bio as an energy acceptor in developing far-red QD-dye self-assemblies from which approach there are several benefits over prototyping bioassays in the visible spectral range, particularly in regard to the avoidance of cell autofluorescence. The excitation energy transfer from Qdot705-STV to proximal DY731-Bio is characterised using two independent spectroscopic techniques: i) the steady state fluorescence measurements and ii) the time-resolved fluorescence measurements. The experimental results are analysed qualitatively and quantitatively based on FRET formulae. Because of the sensitivity of FRET in nanometer range, we attempt to provide some spatial information of QD-dye self-assemblies using the theoretical FRET efficiency model modified for multiple acceptor interactions.

CHAPTER 5:

FRET INVESTIGATION USING CDTE/ZNS QUANTUM DOTS

5.1 Optical Properties of Qdot705-STV

Qdot705-STV is structurally analogous to Qdot585-STV but with a different core composition. Instead of CdSe, a smaller bandgap semiconductor CdTe is used as the core material. Like Qdot585-STV, the CdTe core is encapsulated by monolayers of wide bandgap ZnS to suppress the formation of deep traps that could severely cripple the quantum efficiency. Since biological cells generally survive in aqueous media, further surface derivatisation is needed to stabilize QDs in aqueous solution for the application as bio-reporting agents in in vivo imaging. The solubilisation of Qdot705-STV is achieved by the adsorption of thick amphiphilic polymer layer onto the ZnS outer surface with hydrophilic chains protruding outwards into the aqueous solution. The water soluble QDs then undergo final surface modification by direct coupling with streptavidin proteins which render the inorganic Qdot705-STV end product biocompatible with an exceptional ligand binding ability. Because of the smaller bulk bandgap of CdTe (1.56 eV at 300 K [1]) relative to that of CdSe, Qdot705-STV is size-tuned to emit in the far red spectral region [1]. The long wavelength spectral feature is beneficial in bioimaging applications allowing deep tissue labelling and avoidance of cellular autofluorescence. Therefore, the potential of Qdot705-STV as ideal luminescent material within the framework of FRET studies was explored. The steady state optical properties of Qdot705-STV are shown in Figure 5.1.

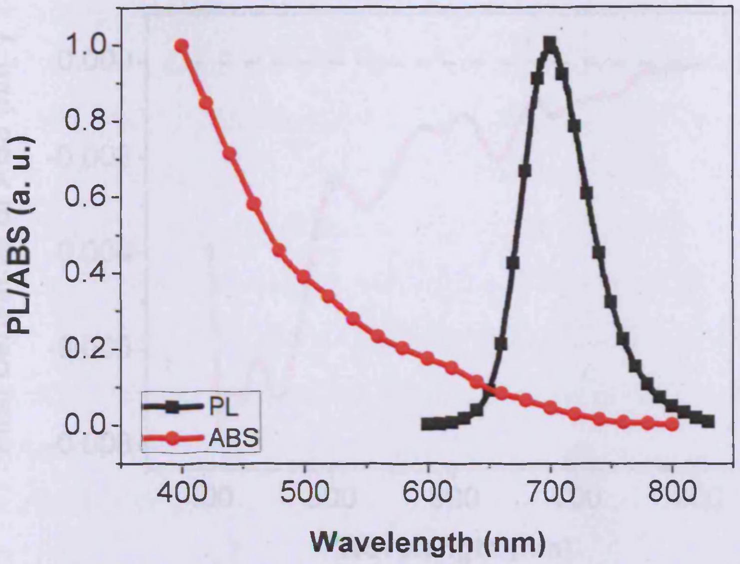

Figure 5.1: Steady state photoluminescence and absorption spectra of Qdot705-STV.

As depicted in Figure 5.1, the emission of Qdot705-STV centres round 700 nm while exhibiting rather broad linewidth. The full-width-at-half-maximum (FWHM) measured is ~70 nm, roughly twofold that of Qdot585-STV. With reference to the discreteness of single dot photoemission [2, 3], it seems likely that the extent of the size disparity in Qdot705-STV ensemble is the justification for its broad spectral linewidth. This has been corroborated with the Qdot705 TEM images and the size histograms measured along major/minor axes in the foregoing chapter (see Figure 2.10, 2.11 and 2.12 in Chapter 2) showing a wide variation of sizes and shapes of dots within Qdot705 population. We then further demonstrated that, by simple mathematical treatment of energy gap using 'particle-in-a-box' as the basis of three dimensional quantum confinement model, the distribution of predicted size dependent bandgaps, discounting the effect of Stokes shift, reasonably conforms with the lineshape of Qdot705-STV emission (refer to Figure 2.14).

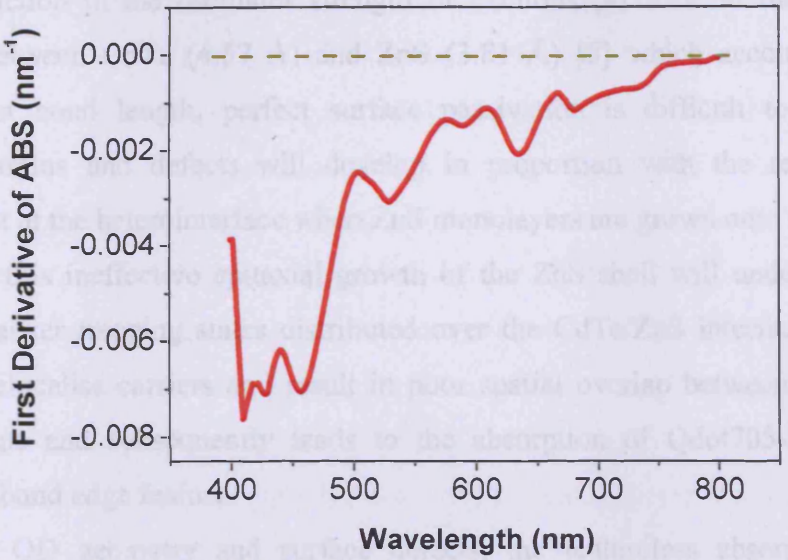

Figure 5.2: Plot of the derivative of Qdot705-STV absorption as a function of wavelength.

No discrete feature is resolved from the absorption measurement of Qdot705-STV as revealed in Figure 5.2. Without the discrete band edge feature, the absorbance profile of Qdot705-STV bears resemblance to the structureless absorption characteristic of CdTe in bulk phase. The diminishing of apparent band edge resonance in Qdot705-STV absorption, in contrast to Qdot585-STV absorption, can be attributed to the geometrical dimensions of Qdot705-STV crystallites which have shown in the preceding chapter to be markedly different from Qdot585-STV whereby Qdot705-STV nanoclusters are typically non-spherical and larger in comparison to Qdot585-STV and this can be elucidated on the basis of quantum physics. The size dependent quantum confinement effect in large QDs is usually less pronounced than smaller counterparts due to a greater spatial extension of electron-hole wavefunctions that in turn contributes to the decline in the energy separation between nearby transition states. The effect could be aggravated by the substantial breadth of size disparity within the population inducing a broad distribution of energy bandgaps which ultimately weaken the effective band edge resonance of QD ensemble. Therefore, the bulk-like resemblance in Qdot705-STV absorption is not unlikely and we substantiate the speculation with the TEM images of Qdot705-STV (see Figure 2.10) showcasing a large variation of dot sizes ranging from 8 to 16 nm (the lengths measured along the major axis, see Figure 2.11).

In addition, the formation of surface traps at CdTe/ZnS interface can also be a cofactor for the reduction in the oscillator strength of excitons [4]. Due to the large lattice mismatch between CdTe (4.57 Å) and ZnS (3.81 Å) [5] which accounts for 17 % difference in bond length, perfect surface passivation is difficult to achieve [6]. Structural strains and defects will develop in proportion with the relative atomic displacement at the heterointerface when ZnS monolayers are grown onto the CdTe core surface and this ineffective epitaxial growth of the ZnS shell will undesirably create some fast carrier trapping states distributed over the CdTe/ZnS interface. This must, therefore, delocalise carriers and result in poor spatial overlap between electron-hole wavefunctions and subsequently leads to the absorption of Qdot705-STV with no pronounced band edge feature.

Apart from QD geometry and surface defects, the featureless absorption may be indicative of Qdot705-STV being intrinsically type-II QDs. Type-II QDs are a new class of core-shell QDs, by the manipulation of the interfacial band offsets, with the extrema of conduction and valence bands located at different regions of the heterostructure. QDs of type-II band structures have been successfully synthesised and optically characterised by several leading researchers like Bawendi's and Klimov's groups [7-9]. They have been shown to exhibit several interesting optical properties that deviate markedly from typical core-shell QDs (type-I QDs), particularly with regard to the featureless bulk-like absorption spectra and the relatively long decay lifetimes in which aspects Qdot705-STV have some similarities. These phenomena observed in type-II QDs are driven by the event of charge separation of exciton after photoexcitation. When the QD is excited, either electron or hole is confined within the shell layer while the other carrier remains localised within the inner core in relevance to the specific conduction and valence band alignments. The significant spatial separation between electron and hole will weaken the oscillator strength of the exciton and this explains the loss of the excitonic feature in the absorption and the long luminescence decay of CdTe/CdSe type-II QDs [7]. Qdot705-STV of CdTe/ZnS core-shell is unquestionably type-I QD if the heterojunction is dislocation-free for the bulk bandgap of ZnS is greater than that of CdTe by a factor of 2. Nevertheless, because of the differences in the lattice parameters, alloying may occur at the interface between CdTe core and ZnS shell during the process of surface passivation. In hot coordinating solvent, there is likelihood that elemental ions used for surface coverage may diffuse into the CdTe core and thus induces Qdot705-STV to deviate from typical type-I band structures. The occurrence of band restructuring leading to hypothetical type-II band lineups in Qdot705-STV is possible if only the interfacial alloy has conduction band (valence band) much lower (much higher) than that of CdTe core together with the right thickness in order to localise electron (hole) in the potential well between CdTe/ZnS heterojunction giving rise to the separation of charges, in turn, the featureless absorption profile and the long fluorescence decay perceived in Qdot705-STV. Extensive studies of crystalline morphology and chemical composition of Qdot705-STV are, of course, essential to verify our preliminary ratiocination of Qdot705-STV being type-II QDs. Nonetheless, we assessed the possibility of that with the utility of 3-dimensional finite spherical potential model specifically adapted to treat layered QDs. The relevant theoretical computations and findings are deferred to a later chapter – Chapter 6.

5.2 Optical Properties of DY731-Bio

DY731-Bio are biotinylated luminescent molecules which are chemically designed to bind with streptavidin modified biomolecules to form biological assays. DY731-Bio was carefully selected for our FRET assay prototyping development in the far-red spectral region. The optical properties of DY731-Bio are shown in Figure 5.3.

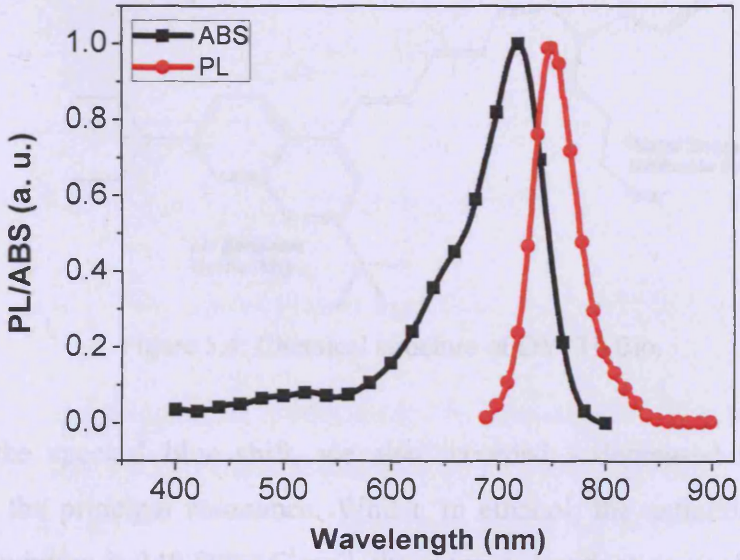

Figure 5.3: Absorption and photoluminescence spectra of DY731-Bio.

In contrast to Qdot705-STV (see Figure 5.1), DY731-Bio exhibits narrow absorption and broad photoluminescence with a long tail at red wavelengths. The FWHM of DY731-Bio photoemission is approximately 47 nm. DY731-Bio has a principal absorption peak at 720 nm when dispersed in pH 7.4 stabilised solutions. Direct comparison with the manufacturer's absorption data, performed in ethanol, reveals that there is a decipherable blue shift in the absorptivity of aqueous solubilised DY731-Bio. Instead of 720 nm, it is reported that the absorption maximum in ethanol is 736 nm. We attribute the observed spectral shift to the solvent effects [10]. Since DY731-Bio is overall a negatively charged molecule, it is anticipated to be highly sensitive to the ionicity of its local environment. With reference to the DY731-Bio chemical structure, the SO_3^- sulfonate groups are responsible for the water solubility [10]. Therefore, the remaining positively charged oxygen in the heterocyclic ring should contribute to the pH sensitivity of DY731-Bio.

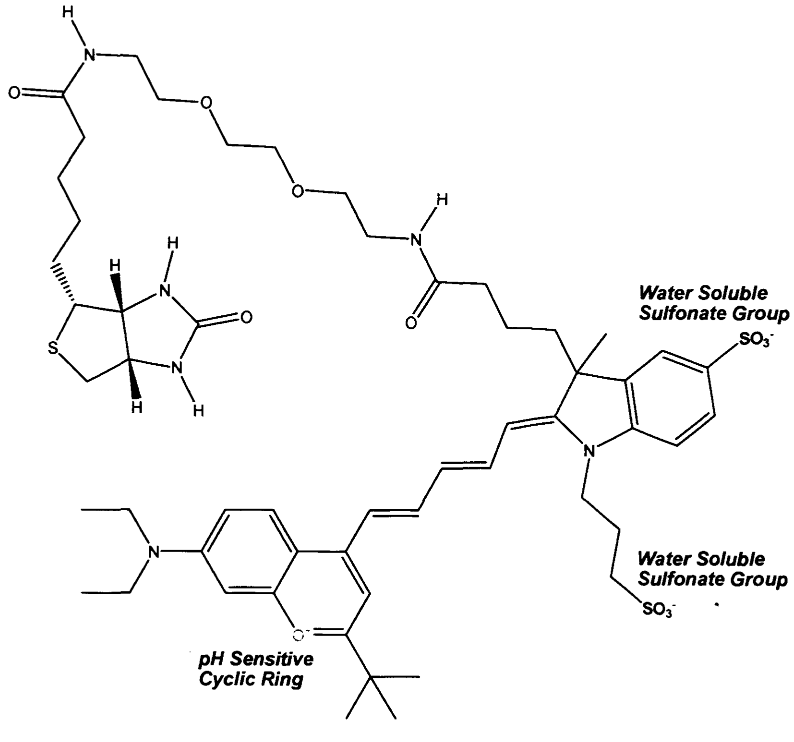

Figure 5.4: Chemical structure of DY731-Bio.

Along with the spectral blue shift, we also recorded a decreased molar extinction coefficient at the principal resonance. Whilst, in ethanol, the extinction coefficient at absorption maximum is 240 000 $M^{-1}cm^{-1}$, the measured extinction coefficient in pH 7.4 stabilised solution is 117 000 $M^{-1}cm^{-1}$, a 50 % reduction in the absorption strength. The empirical extinction coefficient is further substantiated with the data from Dyomics, i.e.

120 000 $M^{-1}cm^{-1}$ [11]. Besides the absorption shift, a concomitant blue shift in the emission spectrum of DY731-Bio was detected with the maximum intensity centres round ~750 nm. Subsequently, these spectral shifts yield a considerable Stokes shift of 30 nm which can be beneficial in minimizing the cross-talk between QD and fluorophore emissions during the development of QD-fluorophore hybrid assays.

Photoluminescence excitation (PLE), an alternative to absorption technique, can be used to reveal the S_0-S_1 transition in DY731-Bio. However, in contrast to the latter spectroscopic method, only radiative transitions are detectable in PLE and this difference can be exploited to uncover the non-emissive photon absorbing state/moiety hidden in DY731-Bio. We monitored the fluorescence intensity of DY731-Bio at 790 nm in the variation of excitation wavelengths from 400 nm to 780 nm. The recorded excitation spectrum is shown alongside the absorption spectrum in Figure 5.5 for comparisons.

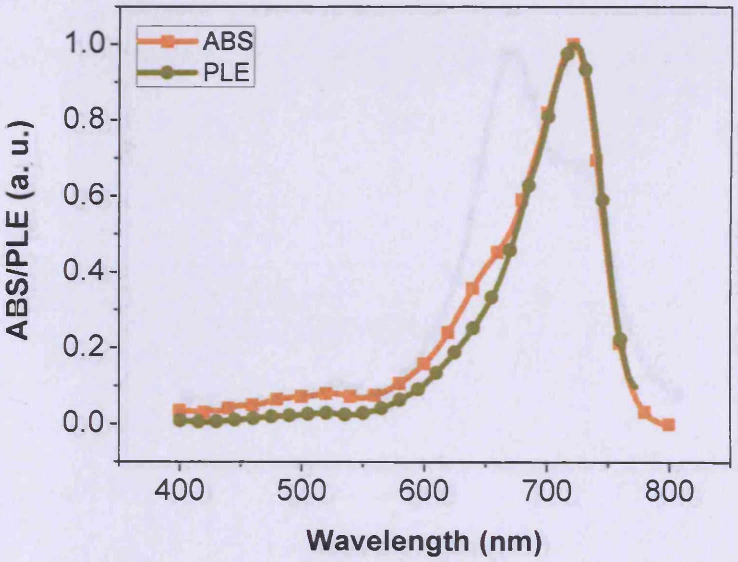

Figure 5.5: Normalised PLE and absorption spectra of DY731-Bio.

In parallel with the absorption measurement, PLE is capable of retrieving the same principal S_0-S_1 transition that resonates at 720 nm. However, it seems apparent that the excitation intensity lineshape of DY731-Bio lacks the pronounced secondary resonance at 650 nm as revealed by the absorbance spectrum. The relative shoulder intensities between the normalised excitation and optical density spectra implicitly infer that the photoexcitation of electrons to higher vibrational states does not necessarily lead to the eventual radiative relaxation of electrons. Some electrons could recombine to the ground state through viable nonradiative relaxation channels. Furthermore, we cannot rule out the possibility of nonfluorescent light absorbing moiety in DY731-Bio which contributes to the ensemble absorption but remains undetectable in the PLE measurement [12]. This explains the manifestation of strong resonance at 650 nm in the absorption but not in the excitation intensity spectrum.

Dramatic changes in the absorption lineshape of DY731-Bio were detected when the fluorescent molecules were dispersed in a solution of abundant streptavidin proteins. The molar ratio of DY731-Bio to streptavidin was maintained at 1:1 such that the number of free anchoring sites for biotin was in excess and thus we presume the conversion of DY731-Bio to DY731-Bio-STV complex via exceptional streptavidin-biotin binding affinity i.e. 10^{15} M^{-1} was complete [13]. The absorption of the final conjugated complex is depicted in Figure 5.6.

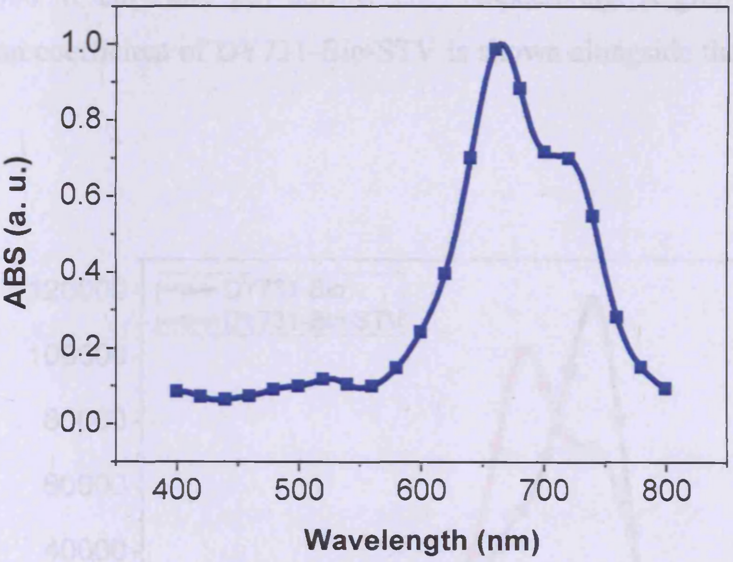

Figure 5.6: Normalised absorbance of DY731-Bio-STV.

As shown in Figure 5.6, streptavidin derivatised DY731-Bio-STV displays an unusual structured optical density profile with the reversal of the intensity ratio of principal to secondary maxima. After the conjugation, DY731-Bio-STV exhibits a strong absorption at 664 nm but a weaker end at 720 nm. In retrospect, this is in contradistinction to the earlier DY731-Bio absorption spectrum and the distinguishable spectral differences afford a unique optical signature to the presence of DY731-Bio-STV compounds. We speculate that the modification of DY731-Bio structural conformation following streptavidin-biotin interaction could be accounted for the foregoing spectral changes observed in DY731-Bio. Since DY731-Bio molecule is not entirely rigid, it could structurally reorganise to fit inside the deep pocket of streptavidin. Whilst precise structural implications on DY731-Bio by the protein-ligand binding process is unclear and requires extensive crystallographic research to unfold the underlying structural transformation, the speculation is supported by a report on the elevation of structural cooperativity (protein tightness) of streptavidin after biotin binding [14].

As attested in Figure 5.6, the conformational changes during the formation of DY731-Bio-STV complex are not optically silent. In fact, the conjugation has drastically affected the absorbance intensity across the spectrum. Therefore, in the context of FRET assay development, the characterisation of DY731-Bio-STV molar extinction coefficient is critical for later determination of Qdot705-STV valency. We found the extinction coefficient of streptavidin conjugated DY731-Bio-STV at 720 nm and 664 nm to be 72 000 $M^{-1}cm^{-1}$ and 103 000 $M^{-1}cm^{-1}$ respectively. A graphical plot of the molar extinction coefficient of DY731-Bio-STV is shown alongside that of DY731-Bio in Figure 5.7.

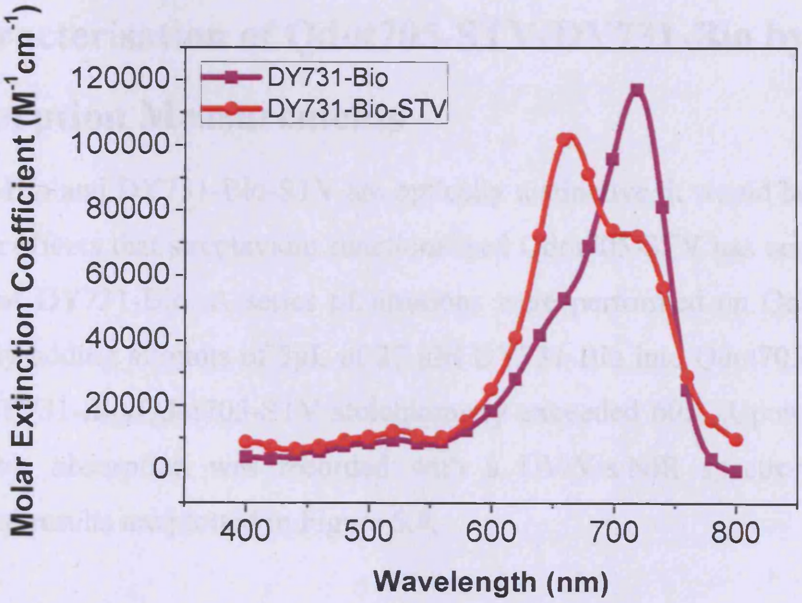

Figure 5.7: Molar extinction coefficients of pure DY731-Bio and streptavidin bound DY731-Bio-STV.

Figure 5.7 depicts a discernible reduction in the extinction coefficient of DY731-Bio at the principal resonance by a fraction of 0.4 after the conjugation with streptavidin. On the contrary, the extinction coefficient at a shorter wavelength, the secondary absorbance, almost double that of DY731-Bio to 103 000 $M^{-1}cm^{-1}$. The unexpected optical fluctuations could be deleterious to the spectral overlap between donor emission and acceptor absorption which primarily governs the effectiveness of transfer of an energy quantum from donor to acceptor. The extent of the effects will be analysed quantitatively.

Compounds	Molar Extinction Coefficient at 664 nm, ε ($M^{-1}cm^{-1}$)	Percentage Change (%)	Molar Extinction Coefficient at 720 nm, ε ($M^{-1}cm^{-1}$)	Percentage Change (%)
DY731-Bio	55 000	n/a	117 000	n/a
DY731-Bio-STV	103 000	87.3	72 000	38.5

Table 5.1: Data compilation of the molar extinction coefficients and the corresponding percentage changes at respective 664 nm and 720 nm wavelengths for DY731-Bio and DY731-Bio-STV compounds.

5.3 Characterisation of Qdot705-STV-DY731-Bio by Absorption Measurements

As DY731-Bio and DY731-Bio-STV are optically distinctive, it would be interesting to monitor the effects that streptavidin functionalised Qdot705-STV has on the absorption behaviour of DY731-Bio. A series of titrations were performed on Qdot705-STV by continuously adding aliquots of 5μL of 27 μM DY731-Bio into Qdot705-STV solution until the DY731-Bio/Qdot705-STV stoichiometry exceeded 60:1. Upon each titration, the ensemble absorption was recorded with a UV/Vis/NIR spectrometer and the experimental results are plotted in Figure 5.8.

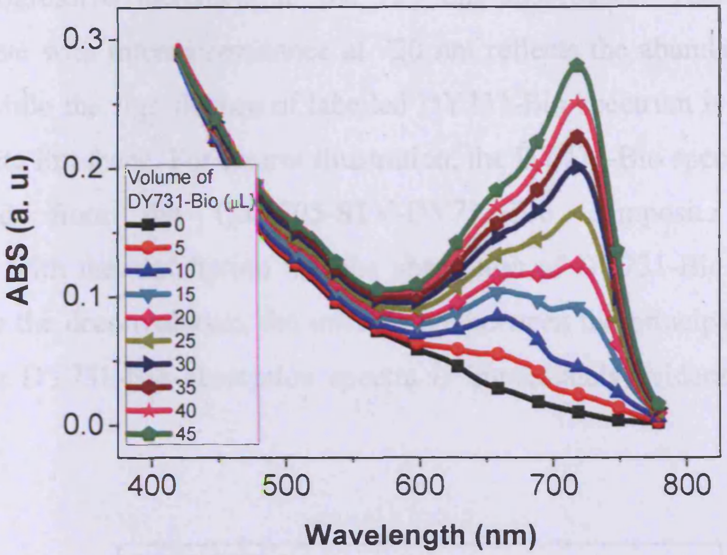

Figure 5.8: Composite absorption spectra of Qdot705-STV-DY731-Bio mixture in a series of titrations with DY731-Bio.

Figure 5.8 delineates a systematic evolution in the composite absorption in the course of titration. Prior to titration with DY731-Bio, the absorbance of Qdot705-STV was seen as broad and featureless lineshape with no pronounced band edge resonance near the far red spectral region. When DY731-Bio aliquot was first added, a slight protuberance was seen at around 660 nm and this was followed by much weaker absorption at lower energies. It seems obvious that the optical densities at 720 nm and 660 nm are reversed if compared to that of non-interacting Qdot705-STV and DY731-Bio. In this instance, the DY731-Bio/Qdot705-STV molar ratio is ~7:1. As QDs are singly coupled to 5-10 streptavidin, the number of binding pockets should suffice for complete labelling [15]. Therefore, the reversal of absorbance occurs within the absorption band of DY731-Bio signifies the presence of streptavidin conjugated DY731-Bio in the solution and this corroborates the compatibility of Qdot705-STV and DY731-Bio to form bioassays.

With the continuance of DY731-Bio dissolution in small quantity, the optical density at 720 nm was gradually increased until the principal S_0-S_1 absorption maximum was recovered. The spectral restoration is attributed to the free unbound DY731-Bio. When more DY731-Bio molecules were added to fixed molar Qdot705-STV, the competition for free binding sites was elevated until a saturation point was reached when all possible sites were liganded and further titrations only contaminated the solution with unbound

DY731-Bio species. The unlabelled DY731-Bio populating the bulk solution effectively led to the progressive increment in the 720 nm absorbance. Therefore, the final absorption curve with intense resonance at 720 nm reflects the abundance of unbound DY731-Bio, while the significance of labelled DY731-Bio spectrum is virtually buried in the composite lineshape. For clearer illustration, the DY731-Bio spectral contribution was extracted from the Qdot705-STV-DY731-Bio composite spectrum by deconvolution with the assumption that the absorption of DY731-Bio at 420 nm was minimal. After the deconvolution, the interchange between the principal and secondary maxima in the DY731-Bio absorption spectra is immediately evident, as depicted in Figure 5.9.

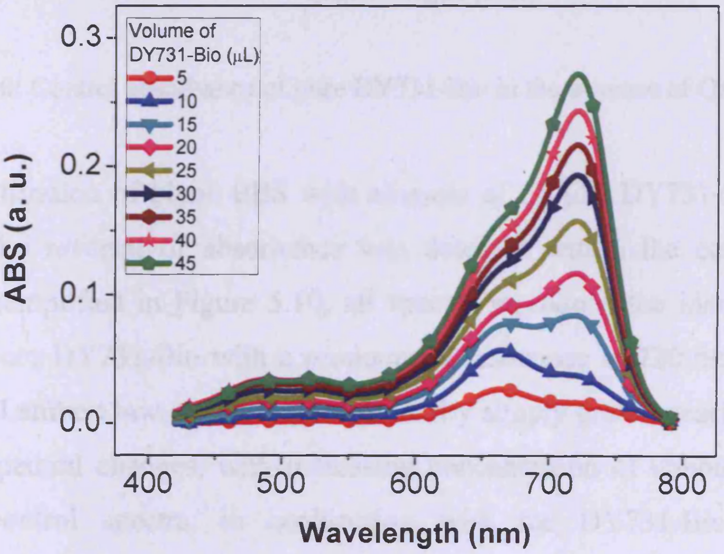

Figure 5.9: Evolution of DY731-Bio absorption extracted from the composite spectra in Figure 5.8.

To assure that the spectral changes in DY731-Bio were genuinely from the conjugation of Qdot705-STV-DY731-Bio and not from the artefacts contributed by light harvesting chemical impurities, a control experiment was constructed using the same DY731-Bio stock solution and the protocols were similar to the titration of Qdot705-STV with the exception that the Qdot705-STV solution was replaced by PBS in order to simulate the same concentration of DY731-Bio as that in the preceding experiment. The recorded control absorption spectra are shown in Figure 5.10.

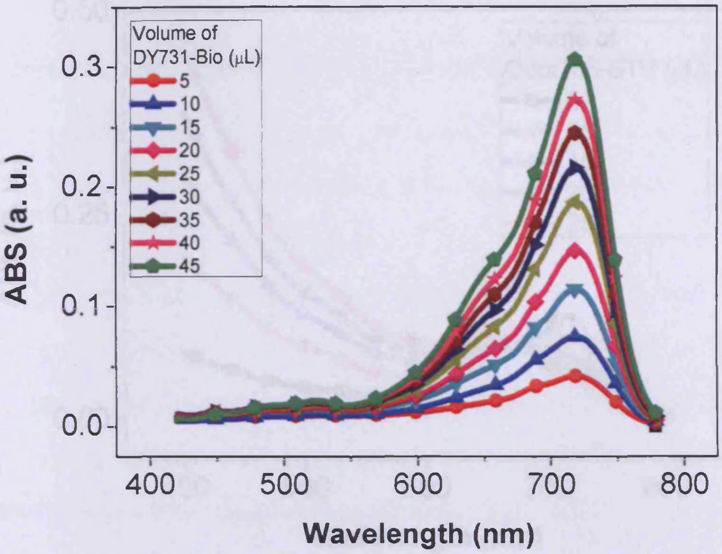

Figure 5.10: Control absorbance of pure DY731-Bio in the absence of Qdot705-STV.

In systematic titration of blank PBS with aliquots of 27 μM DY731-Bio solution, no signature of the reversal of absorbance was detected within the control absorption spectra. As exemplified in Figure 5.10, all spectra reproduce the identical absorption lineshape of pure DY731-Bio with a pronounced resonance at 720 nm. In conformity with the Beer-Lambert law, the absorption intensity simply grew linearly, without other concomitant spectral changes, with increasing concentration of unbound DY731-Bio. Hence, the control spectra, in conjunction with the DY731-Bio-STV optically characterised spectrum, unequivocally confirm that the unusual protuberance in the composite absorption (see Figure 5.8) is truly the contribution of Qdot705-STV-DY731-Bio multiplexes and this is consistent with the experimental observations attained in a reversed titration of Qdot705-STV.

In the reversed titration of Qdot705-STV, the number of DY731-Bio was held constant whilst 5 μL of 1 μM Qdot705-STV aliquot was continuously added to the DY731-Bio solution. The conjoint absorption spectra of Qdot705-STV and DY731-Bio for respective QD/fluorophore stoichiometries were recorded and these are plotted in Figure 5.11.

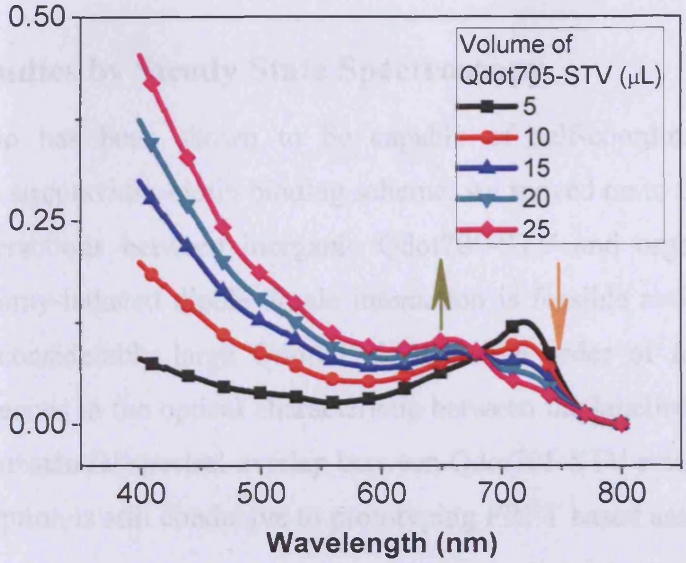

Figure 5.11: Evolution of absorption spectra for Qdot705-STV-DY731-Bio solution at variable stoichiometric ratios.

Figure 5.11 displays some substantial structured changes in the composite spectra of Qdot705-STV and DY731-Bio. In the elevation of Qdot705-STV concentration, a progressive diminution of the optical density at 720 nm, which is predominantly constituted of DY731-Bio absorbance, was detected. The Qdot705-STV-to-DY731-Bio molar ratio was initially ~1:80 in which only a fraction of fluorophores were appended to Qdot705-STV leaving the majority of free DY731-Bio dominating the absorption at the far red spectral regime. Therein, the S_0-S_1 transition resonance is clearly visible in the first conjoint absorption of Qdot705-STV and DY731-Bio as delineated in Figure 5.11. By varying the Qdot705-STV/DY731-Bio stoichiometry from ~1:80 to ~1:16, the abundance of unbound DY731-Bio was markedly reduced as more deep pockets were available for ligand binding, thus, more QD-fluorophore conjugations ensued. This accounts for the absorption onset at 660 nm which is most pronounced at the final titration. As the absorption profile of Qdot705-STV is lacking in discrete features, the immobilisation of DY731-Bio onto the Qdot705-STV surface via ligand-receptor interaction should be responsible for the 660 nm onset. Therefore, with reference to the experimental findings, we unambiguously believe that Qdot705-STV is commensurate with DY731-Bio to form self-assemblies, albeit the efficiency of FRET induced by the close proximity has yet to be evaluated.

5.4 FRET between Qdot705-STV and DY731-Bio

5.4.1 FRET Studies by Steady State Spectroscopy

While DY731-Bio has been shown to be capable of self-coordination around a Qdot705-STV via streptavidin-biotin binding scheme, we moved on to the investigation of resonance interactions between inorganic Qdot705-STV and organic fluorescent labels. The proximity-induced dipole-dipole interaction is feasible as long as it is not deterred by the considerably large Qdot705-STV of the order of few nanometers. Despite the differences in the optical characteristic between the labelled and unlabelled DY731-Bio, the substantial spectral overlap between Qdot705-STV emission and bound DY731-Bio absorption is still conducive to prototyping FRET based assays as indicated in Figure 5.12.

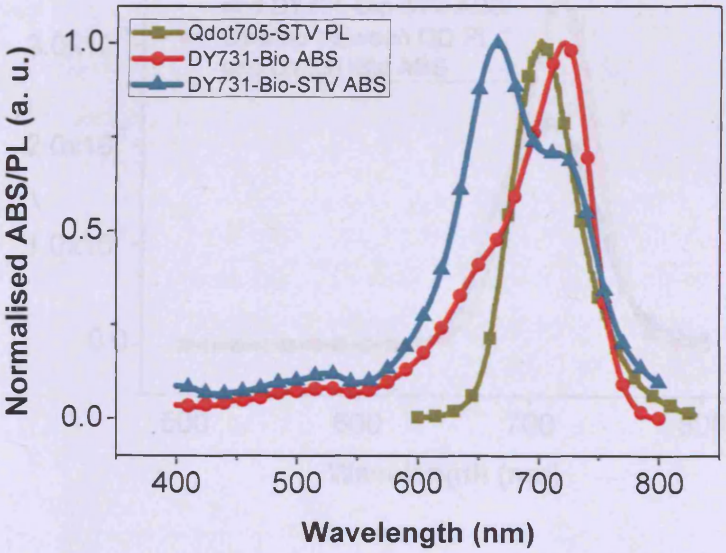

Figure 5.12: Normalised Qdot705-STV emission, DY731-Bio absorption and DY731-Bio-STV absorption.

In view of the fact that no apparent spectral shift in DY731-Bio is induced upon streptavidin binding and Qdot705-STV fluorescence remains largely within the absorption band of DY731-Bio-STV, bound fluorophores are in essence energetically resonant with excited QD. Nonetheless, the minor suppression of the absorption strength at 720 nm could affect the spectral overlap, *J*(λ) and thus the Förster distance, R_0. Henceforth, we performed comparative studies of *J*(λ) and R_0 based on two different molar extinction coefficients of DY731-Bio and DY731-Bio-STV in order that the extent of the effect can be understood. The spectral overlap integral, $J(\lambda)$, is defined as

$$J(\lambda) = \int_0^\infty f_D(\lambda)\varepsilon_A(\lambda)\lambda^4 d\lambda \qquad \text{in M}^{-1}\text{cm}^3 \qquad (5.1)$$

with $f_D(\lambda)$ denotes the normalised fluorescence intensity of the donor, (in cm^{-1}) and $\varepsilon_A(\lambda)$ denotes the molar extinction coefficient of the acceptor (in $\text{cm}^{-1}\text{M}^{-1}$) and λ is the wavelength (in cm). With Equation 5.1, we can quantify the spectral overlap between DY731-Bio (DY731-Bio-STV) absorption and Qdot705-STV photoemission. The spectral overlaps, in terms of $f_D(\lambda).\varepsilon(\lambda).\lambda^4$, for DY731-Bio and DY731-Bio-STV are plotted against wavelength as shown in Figure 5.13.

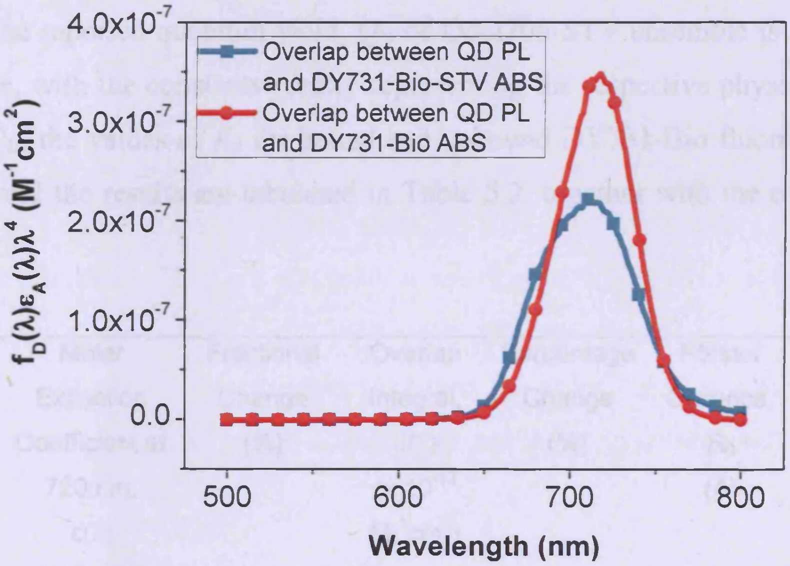

Figure 5.13: Plots of spectral overlap function, $f_D(\lambda).\varepsilon(\lambda).\lambda^4$, versus wavelength for DY731-Bio and DY731-Bio-STV instances.

A substantial impairment of the spectral overlap evoked by the spectral changes in the absorption of DY731-Bio upon streptavidin binding is evident in Figure 5.13, otherwise the spectral overlap should be reasonably high with a peak value of $3.5\text{x}10^{-7}$ M^{-1}cm^2 at 717 nm (-●- in Figure 5.13) if the conformational changes induced by the ligand-receptor interaction are optically silent. By contrast, we predicated the actual spectral overlap for Qdot705-STV-DY731-Bio assays to be much lower with a peak value of $2.2\text{x}10^{-7}$ M^{-1}cm^2 at 711 nm. Nevertheless, the broad linewidth of the latter overlap function should compensate for the diminishing effect. We calculated the overlap integral, $J(\lambda)$, and the associated Förster distance, R_0, for the respective DY731-Bio and DY731-Bio-STV compounds in effort to quantitatively analyse the ramification of the spectral changes in FRET based assays. R_0 is expressed as

$$R_0 = 9.79 \cdot 10^3 \left(n^{-4} Q_D \kappa^2 J(\lambda)\right)^{1/6} \quad \text{in Å} \tag{5.2}$$

where n is the refractive index of the solvent, Q_D is the quantum efficiency of the donor, κ^2 is the orientation factor of donor-acceptor transition dipoles and $J(\lambda)$ is the spectral overlap integral. In the evaluation of R_0, several physical parameters have to be defined in antecedence. Along with other published QD FRET analyses, we assigned κ^2 to 2/3 [16-19]. We presumed that the notion of random coordination of DY731-Bio molecules onto the QD surface is reasonably well characterised by κ^2 = 2/3. Besides that, the refractive index, n, was assumed to be 1.33 for PBS is fundamentally a water based medium. The reported quantum yield, Q_D of Qdot705-STV ensemble is approximately 0.68. Hence, with the constants readily representing the respective physical parameters n, κ^2 and Q_D, the values of R_0 for bound and unbound DY731-Bio fluorophores can be calculated and the results are tabulated in Table 5.2, together with the overlap integral $J(\lambda)$.

Donor-Acceptor Pair	Molar Extinction Coefficient at 720 nm, $\varepsilon(\lambda)$ ($M^{-1}cm^{-1}$)	Fractional Change (%)	Overlap Integral, $J(\lambda)$ ($\times 10^{-12}$ $M^{-1}cm^3$)	Percentage Change (%)	Förster Distance, R_0 (Å)	Fractional Change (%)
Qdot705-STV and unbound DY731-Bio	117 000	n/a	1.92	n/a	79.1	n/a
Qdot705-STV and bound DY731-Bio	72 000	38.5	1.58	17.7	76.6	3.2

Table 5.2: Tabulation of extinction coefficients, overlap integrals, Förster distances (where n = 1.33, κ^2 = 2/3 and Q_D = 0.68) and the corresponding fractional changes for bound and unbound DY731-Bio.

The dramatic spectral changes of DY731-Bio in QD-fluorophore hybrid assays were initially surmised to render DY731-Bio ineffective as energy acceptor. However, following further quantitative analysis, the difference of R_0 between DY731-Bio and DY731-Bio-STV seems to be trivial. The overlap integral for DY731-Bio in conjugated format decreases by ~18 % compared to the unbound donor-acceptor overlap integral which in turn remotely causes a reduction in R_0 i.e. 3.2 % change as shown in Table 5.2 primarily due to its sixth root dependence on $J(\lambda)$. This infers that the value of R_0 is not very sensitive to the changes in $J(\lambda)$ and therefore dipole-dipole resonance interactions are still viable in Qdot705-STV-DY731-Bio self-assemblies provided the condition that the donor-acceptor separation is favourable.

The distinctive signatures of FRET in a donor-acceptor conjugated configuration can be easily picked up by steady state photoluminescence spectroscopy. If an energetically resonant acceptor is in the vicinity of a donor, excitation energy can migrate from the photoexcited donor to the adjacent acceptor resulting in a quenching effect of the donor fluorescence and, if the acceptor is also emissive, an enhancement in the acceptor radiation. In the evaluation of FRET between Qdot705-STV and DY731-Bio, we conducted an experimental titration of Qdot705-STV with DY731-Bio. 2 μL of 30 μM DY731-Bio was first added into the pH 7.4 stabilised Qdot705-STV solution and from which successive addition of 4 μL DY731-Bio aliquots ensued until a total volume of 38 μL DY731-Bio solution was dispersed into the Qdot705-STV solution. For each titration, the corresponding photoluminescence spectrum was recorded as depicted in Figure 5.14.

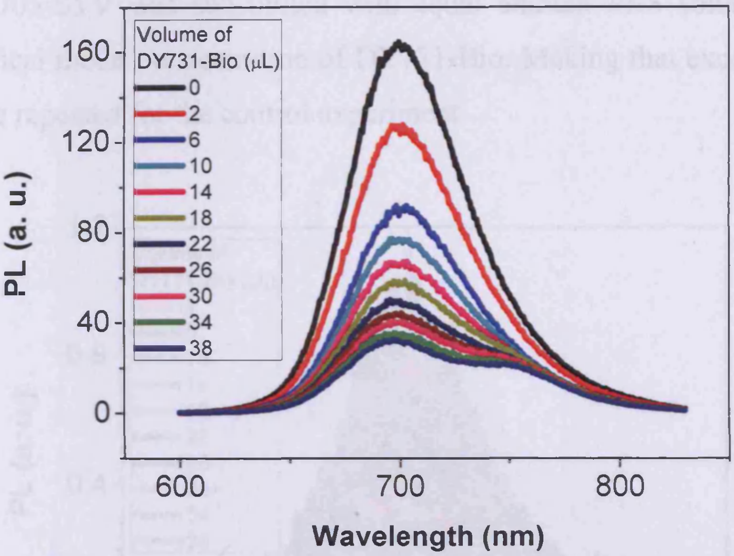

Figure 5.14: Photoluminescence spectra from stepwise titration of Qdot705-STV with DY731-Bio.

With dropwise dispersals of DY731-Bio solution, a systematic quenching of the Qdot705-STV fluorescence was detected in which, for first few titrations, the reduction in the QD intensity is more intense. A gradual subsidence in the quenching effect was perceived after a total of ~20 μL DY731-Bio solution was added. Since DY731-Bio absorbance was kept below 0.1 (2 μL to 14 μL of DY731-Bio), the trivial inner filter effect by photon reabsorption should not be accountable for the significant loss of Qdot705-STV photoluminescence. With the substantial spectral overlap between Qdot705-STV emission and DY731-Bio absorption, a proximal resonant DY731-Bio acceptor can afford an alternative nonradiative relaxation pathway to QD exciton depopulating the lowest excited state and thus inducing the quenching of donor fluorescence. In other words, the nonradiative de-excitation dynamics converge at the loss of steady state Qdot705-STV photoluminescence and therefore, the quenching effect is imperatively correlated to FRET between Qdot705-STV and DY731-Bio. Alongside the systematic decrement of Qdot705-STV fluorescence intensity, we also noticed a concomitant enhancement in the DY731-Bio photoemission when the mixture was excited at 425 nm at which wavelength the absorption of DY731-Bio was minimal implicating its contribution to DY731-Bio fluorescence enhancement was remotely small. A control experiment on DY731-Bio was performed and compared, the spectral data, with the preceding titration of Qdot705-STV with DY731-Bio. In the control sample, Qdot705-STV was substituted with equal amount PBS solution in order to preserve identical molar concentration of DY731-Bio. Making that exception, the same protocols were repeated for the control experiment.

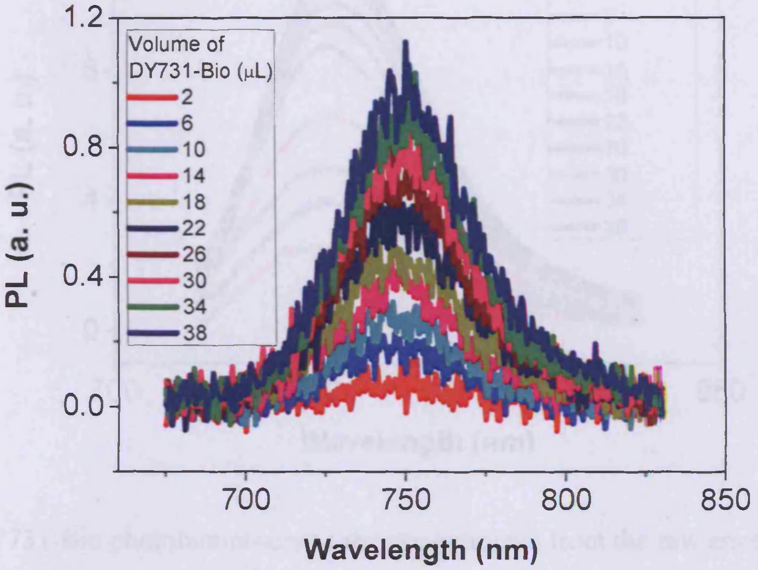

Figure 5.15: Control DY731-Bio photoluminescence spectra excited at 425 nm.

Direct comparison between Figure 5.14 and Figure 5.15 provides the evidence that the direct excitation of DY731-Bio at 425 nm is minimal. In fact, the intensity maxima are well below the nominal value of 2. With reference to the absorption profile, DY731-Bio is almost optically transparent across the blue wavelengths of the visible spectrum and therefore, a large fraction of DY731-Bio molecules in the control sample remained grounded upon 425 nm excitation. The superficial DY731-Bio radiation shown in Figure 5.15 is a direct indication that the enhancement of DY731-Bio photoemission depicted in Figure 5.14 was attributed to the nonradiative transfer of energy from photoexcited Qdot705-STV to proximal DY731-Bio considering no other energy coupling source was present in the mixture. Since there is a partial overlap between QD and fluorophore emissions, we subtracted the intensity contribution of Qdot705-STV from the composite spectrum in Figure 5.14 in order that the enhanced DY731-Bio spectral lineshape can be elicited. With the acquired DY731-Bio spectra, a more definitive comparison can be made between the luminescence gain by direct excitation and that by FRET enhancement. The deconvoluted DY731-Bio emission lineshapes from the composite spectra are shown in Figure 5.16.

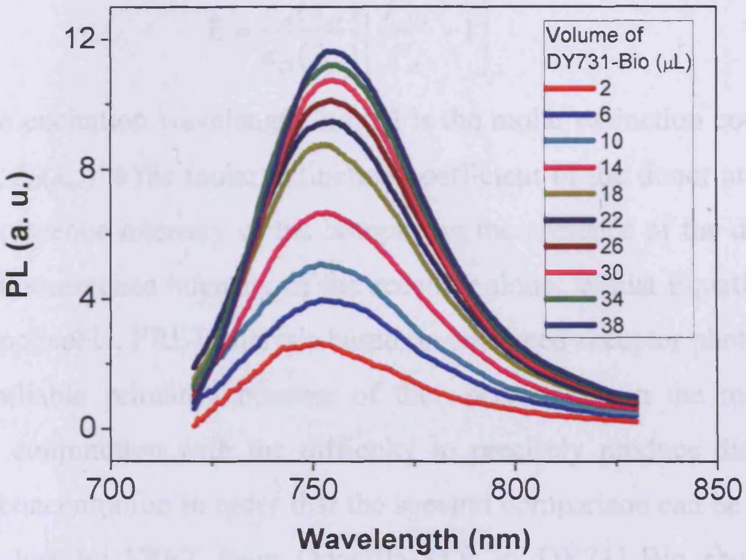

Figure 5.16: DY731-Bio photoluminescence spectra extracted from the raw ensemble spectra in Figure 5.14.

Figure 5.16 depicts a steady enhancement of DY731-Bio photoemission with increasing DY731-Bio/Qdot705-STV stoichiometry. While the excitation occurred outside the principal DY731-Bio absorption regime, a marked intensity gain in DY731-Bio luminescence was attained in the presence of Qdot705-STV as compared to the superficial control DY731-Bio luminescence whereby the integrated DY731-Bio intensity for the final titration of Qdot705-STV was almost tenfold that of the control experiment. The exceptional gain in the DY731-Bio (acceptor) luminescence and the pronounced loss in the Qdot705-STV (donor) luminescence unequivocally corroborate the occurrence of FRET phenomenon in the mixture upon 425 nm irradiation. We can therefore analyse FRET quantitatively based on either the donor fluorescence quenching or the acceptor fluorescence enhancement. In relation to the donor quenching, FRET efficiency is expressed as

$$E = 1 - \frac{F_{DA}}{F_D} \tag{5.3}$$

with F_{DA} is the integrated fluorescence intensity of the donor in the presence of the acceptor and F_D is the integrated fluorescence intensity of the donor alone. On the other hand, in relation to the acceptor enhancement, FRET efficiency is expressed as

$$E = \frac{\varepsilon_A(\lambda_{ex})}{\varepsilon_D(\lambda_{ex})}\left[\frac{F_{AD}}{F_A} - 1\right] \tag{5.4}$$

where λ_{ex} is the excitation wavelength, $\varepsilon_A(\lambda_{ex})$ is the molar extinction coefficient of the acceptor at λ_{ex}, $\varepsilon_D(\lambda_{ex})$ is the molar extinction coefficient of the donor at λ_{ex}, F_{AD} is the integrated fluorescence intensity of the acceptor in the presence of the donor and F_A is the integrated fluorescence intensity of the acceptor alone. Whilst Equation 5.3 and 5.4 are generally applicable, FRET analysis based on enhanced acceptor photoluminescence is often less reliable primarily because of the uncertainties in the molar extinction coefficients in conjunction with the difficulty to precisely produce distinct solutions with the same concentration in order that the spectral comparison can be made [10, 17]. Every exciton lost by FRET from Qdot705-STV to DY731-Bio should be ideally recovered as the luminescence gain in DY731-Bio but contrarily, in addition to the emissive relaxations from S_1 vibrational levels, the excited fluorophores by resonance interactions could, in reality, relax to the ground state nonradiatively. In essence of that, the efficiency of energy transfer in the donor-acceptor system will be underestimated if enhanced acceptor fluorescence is utilised in the evaluation of FRET. This underpins our approach to understanding QD FRET from the donor quenching effect. To quantitatively measure the FRET efficiency, Qdot705-STV spectral contribution was extracted from the composite emission with the assumption that the integrity of its spectral profile was not disturbed by FRET process.

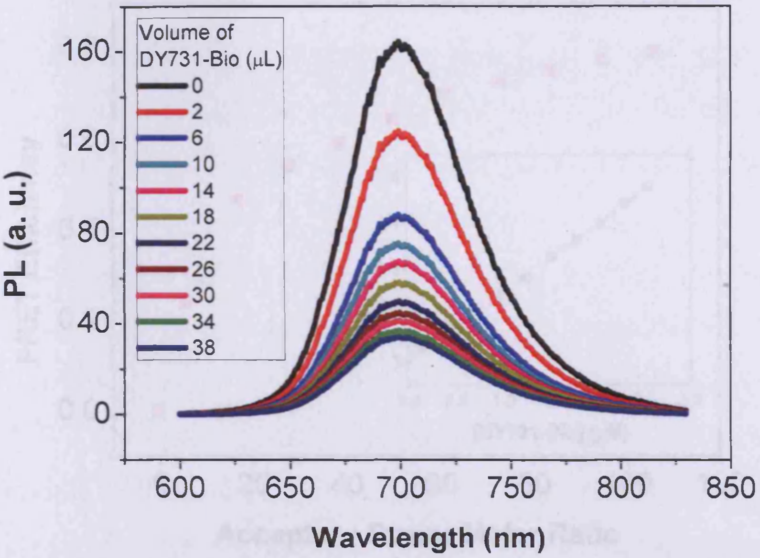

Figure 5.17: Evolution of Qdot705-STV photoluminescence spectra subtracted from the composite spectra in Figure 5.14.

Figure 5.17 shows, initially, a rapid drop in Qdot705-STV intensity followed by a steady decrease in the quenching effect with extended titrations. To quantitate the FRET performance in the experimental titration of Qdot705-STV with DY731-Bio, we integrated the donor fluorescence intensity in Figure 5.17 and applied that to the calculation of FRET efficiency utilising Equation 5.3. At each donor/acceptor molar ratio, the corresponding energy transfer efficiency was determined and shown in Figure 5.18.

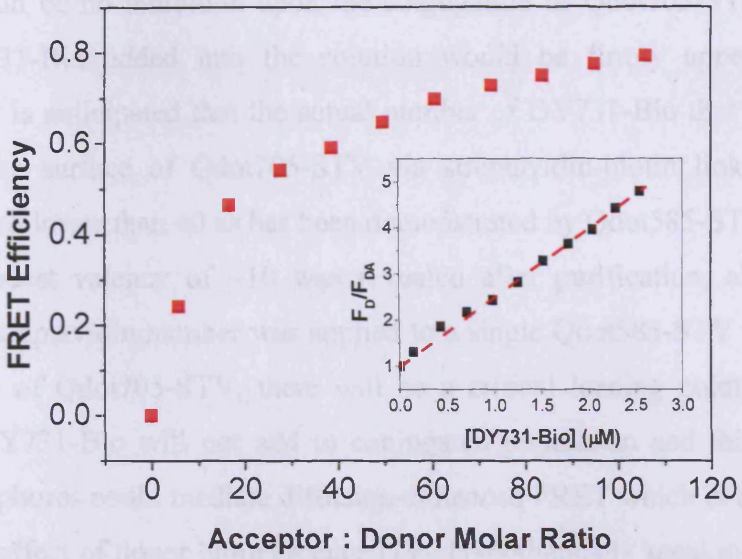

Figure 5.18: Plot of FRET efficiency as a function of acceptor/donor stoichiometry based on the integrated QD (donor) photoluminescence in Figure 5.17. The inset is a Stern-Volmer plot depicting the dependence of F_D/F_{DA}, where F_D and F_{DA} denoting the integrated fluorescence intensities of donor in the absence and presence of acceptor, on DY731-Bio concentration.

Figure 5.18 shows a systematic rise in the FRET efficiency with incremental increase in the acceptor concentration. Despite the unfavourable physical size of Qdot705-STV after streptavidin conjugation, a reasonably high quenching efficiency was acquired in the titration experiment i.e. a ~60 % of efficiency was achieved at 40:1 acceptor-to-donor stoichiometric ratio. Presuming that no other non-FRET excitonic quenching mechanism was present in the system, the pronounced photoluminescence loss in Qdot705-STV, on which parameter FRET efficiency was predicated, warrants the feasibility of Qdot705-STV as energy donor in devising FRET based assays. The remarkable achievement demonstrated by Qdot705-STV is attributed to its large surface area available for interdipole resonance interactions. In Chapter 2, we have shown that Qdot705-STV is typically elongated and quite large exhibiting a range of sizes from 8 to 16 nm if measured along the major axis (see Figure 2.10 and 2.11) and hence, multiple energetically resonant acceptors are able to crowd around a single QD to compete for FRET interactions. In view of the fact that a single Qdot705-STV is chemically coupled to 5-10 streptavidin [15] and a streptavidin has four binding pockets, static FRET mechanism should account for the initial rise of FRET efficiency at increasing acceptor-to-donor molar ratio in which free binding sites were abundant and there should be no inhibition upon the conjugation of Qdot705-STV-DY731-Bio. All free DY731-Bio added into the solution would be firmly appended to QDs. Nonetheless, it is anticipated that the actual number of DY731-Bio that could possibly anchor onto the surface of Qdot705-STV via streptavidin-biotin linking scheme is effectively much lower than 40 as has been demonstrated by Qdot585-STV in Chapter 4 whereby a modest valency of ~10 was revealed after purification, albeit the same estimation of streptavidin number was applied to a single Qdot585-STV dot. Therefore, in the titration of Qdot705-STV, there will be a critical loading point where further dispersal of DY731-Bio will not add to conjugated population and this is when free agitated fluorophores could mediate diffusion-enhanced FRET which is likely to extend the quenching effect of donor luminescence [19]. Hypothetically speaking, if 30:1 is the critical acceptor-to-donor loading point, the solution-induced FRET, assuming no other non-FRET quenching effect, could contribute to the gain in the quenching efficiency above the critical point. Since the solution-induced FRET, essentially a collisional quenching process, is primarily governed by the translational motion of unbound DY731-Bio and the Qdot705-STV decay lifetime, the effectiveness of dynamical quenching mechanism is generally much weaker comparatively to that of the static FRET induced by specific ligand binding. This elucidates the reduced quenching effect of Qdot705-STV fluorescence beyond ~30:1 acceptor-to-donor ratio, whilst the overall Stern-Volmer plot (inset of Figure 5.18) appears to be linear which is imperatively underpinned by the limited range of DY731-Bio concentrations [10]. By comparison with Qdot585-STV, the slow onset of the positive deviation (upward curvature) from linear Stern-Volmer plot reflects the size of Qdot705-STV which is considerably larger than Qdot585-STV making it less sensitive to both static and dynamic FRET quenching. Because of the inverse sixth power dependence of energy transfer on distance, the spatial extension from Qdot705-STV to DY731-Bio, within the dipole approximation, can be deduced from the correlation between the FRET efficiency and the acceptor/donor stoichiometry. We, therefore, attempted to fit the experimental data points in Figure 5.18 with theoretical FRET efficiency model to uncover the spatial relationship of Qdot705-STV to DY731-Bio in multiplexes. The FRET efficiency with respect to multiple-acceptor-to-single-donor configuration, presuming the distribution of acceptors is concentrically uniform, is defined as follows,

$$E = \frac{nR_0^{\ 6}}{nR_0^{\ 6} + r^6} \qquad (5.5)$$

where n is the number of acceptors per donor, R_0 is the Förster distance and r is the centre-to-centre donor-acceptor separation in a centro-symmetric system. In our pursuit to estimate the separation between Qdot705-STV and DY731-Bio, a number of theoretical efficiency fits in the variation of r values were plotted alongside the empirical FRET efficiencies as exemplified in Figure 5.19. The distance of closest approach between Qdot705-STV and bound DY731-Bio was derived from the best fit.

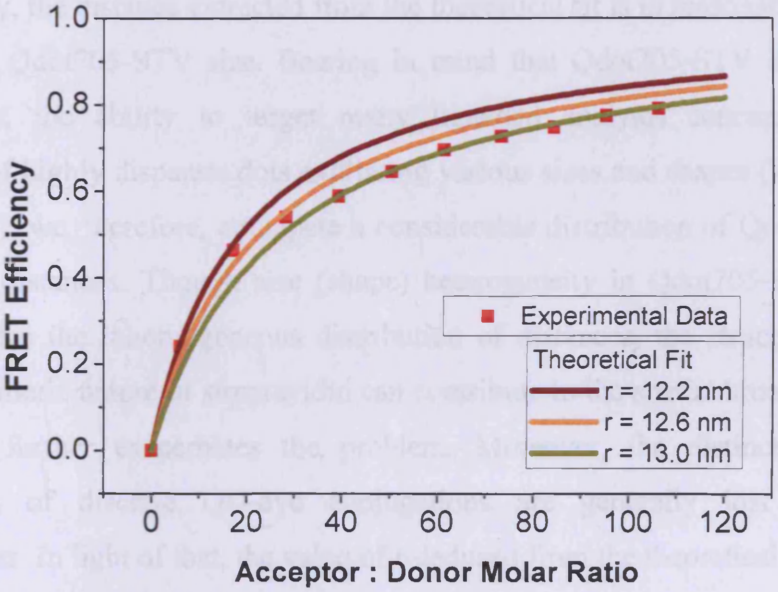

Figure 5.19: Plots of the empirical FRET efficiency data (■) derived from the quenching effect of Qdot705-STV in the titration with DY731-Bio (see Figure 5.17) and the predicted efficiency-stoichiometry curves for r = 12.2 nm, r = 12.6 nm and r = 13.0 nm.

From Figure 5.19, it seems apparent that there are some discrepancies between theoretical and experimental efficiencies as no single prediction curve derived from the idealised Equation 5.5 can satisfactorily fit the experimental data for the entire acceptor-to-donor stoichiometries ranging from ~10:1 to ~110:1. Henceforth, we arrived at a resolution that the theoretical fit closely matched the experimental data points for the acceptor-to-donor ratio under ~30:1 should provide the best estimation of donor-acceptor spatial separation. Since Equation 5.5 was customarily modified to treat donor-acceptor multiplexes, the empirical efficiencies below the appointed fractional limit, in which case DY731-Bio were mostly self-assembled onto QDs, should be better described by the theoretical model and thus, from which fitting scheme an approximated value of 12.6 nm for the Qdot705-STV-to-DY731-Bio distance was deduced. A non-targeting Qdot705 is estimated to be around 18.5 nm in diameter taking account of the thickness of polymer coating [20]. If large streptavidin proteins (~5 nm in size [21]) are concentrically cross-linked to the surface at a fixed distance to offer targeting ability, the overall size of Qdot705-STV can, conceivably, expand to ~28.5 nm. While the value of r is principally the donor-acceptor separation, it can be alternatively perceived as the effective radius of biofunctionalised QD. Hence, the numerical comparison between the FRET deduced and the postulated values yield ~12 % difference. Despite the inconsistency, the distance extracted from the theoretical fit is in reasonable accord with the scale of Qdot705-STV size. Bearing in mind that Qdot705-STV dot system has multivalency, the ability to target many liganded analytes concurrently, and is constituted of highly disparate dots exhibiting various sizes and shapes (see Figure 2.10 in Chapter 2), we, therefore, anticipate a considerable distribution of Qdot705-STV-to-DY731-Bio distances. Though size (shape) heterogeneity in Qdot705-STV is mainly responsible for the inhomogeneous distribution of distances, the structural flexibility and the tetrameric nature of streptavidin can contribute to the spatial broadening as well and hence, further exacerbates the problem. Moreover, the distinctive proximity relationships of discrete QD-dye conjugations are generally lost in ensemble measurements. In light of that, the value of r deduced from the theoretical fit is regarded as the ensemble averaged and not the absolute donor-acceptor separation in Qdot705-STV-DY731-Bio system. Attributed to the disparity in QD size (shape) and the structural and binding nature of streptavidin, the definition of r derived the simple mathematical treatment of FRET efficiency in a multivalent configuration is less clear cut and therefore, the detailed analysis of the spatial dependence of FRET in inhomogeneous systems such as QD-fluorophore assays will require advanced theoretical model that have sufficient number of parameters to absorb some if not all the heterogeneous characteristics mentioned. Nonetheless, despite the limitations, the value of 12.6 nm elicited from the simple theoretical fit using Equation 5.5 was not exceedingly far away from the postulated distance.

5.4.2 FRET Studies by Time-Resolved Spectroscopy

With energetically resonant acceptors in the close vicinity of photoexcited donor, the occurrence of FRET, through which relaxation channel the exciton could recombine nonradiatively to the ground state, can be instigated and in turn, alters the donor exciton decay dynamics. Therefore, the information on the efficiency of resonance interaction can be drawn from the temporal response of the donor in the presence of acceptors. Since photoluminescence is a measurable quantity and its intensity decay rate correlates with the excitonic depopulation rate, we explicitly monitored the change of Qdot705-STV luminescence decay and thus the FRET efficiency in a range of acceptor-to-donor labelling ratios. Variable conjugations were achieved by mixing the Qdot705-STV solutions with increasing concentration of DY731-Bio until the quantity of fluorophore was hundredfold more than that of QD in the mixture at which instance the saturation point was most probably reached if not exceeded. The large proportion of acceptors to donors in the solution was to assure all possible free binding sites were liganded. The unbound DY731-Bio molecules were later removed by size exclusion centrifugations with Microcon YM-50 spin columns. To characterise the acceptor/donor stoichiometry after the centrifugation, we measured the ensemble absorption of individual solution in order that the corresponding molar concentrations of Qdot705-STV and DY731-Bio could be determined. The Qdot705-STV and appended DY731-Bio concentrations were calculated from known molar extinction coefficients at 405 nm ($\varepsilon_{Qdot705\text{-}STV} = 6\ 800\ 000$ $M^{-1}cm^{-1}$) and 664 nm ($\varepsilon_{DY731\text{-}Bio\text{-}STV} = 103\ 000\ M^{-1}cm^{-1}$) with the assumption that the absorptivity of Qdot705-STV at 664 nm and the absorptivity of DY731-Bio-STV at 405 nm are trivial. Moreover, Qdot705-STV does not exhibit strong excitonic resonance like Qdot585-STV. In view of that, no deconvolution of the composite absorbance was necessary to generate the respective QD and dye spectral components for the foregoing molar calculations. The acceptor/donor fractions, attained by dividing DY731-Bio molar concentration with that of Qdot705-STV, were rounded to the nearest integer. The normalised absorption spectra of various DY731-Bio-to-Qdot705-STV conjugation ratios are illustrated in Figure 5.20.

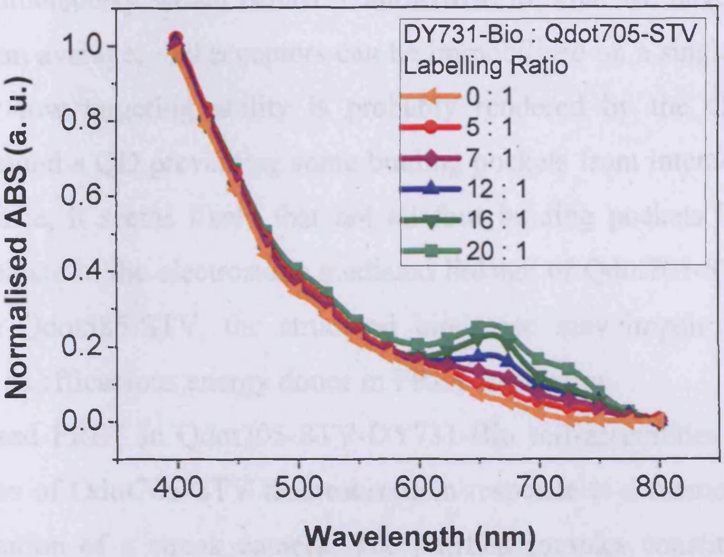

Figure 5.20: Normalised absorption spectra of Qdot705-STV-DY731-Bio assays at increasing acceptor-to-donor ratio.

A structured evolution of composite absorption was observed with the incremental increase in the acceptor-to-donor ratio from 0:1 to 20:1. The acceptor-to-donor stoichiometry of 20:1 was calculated from the measured absorbance of a filtered Qdot705-STV-DY731-Bio mixture which prior to centrifugation was made up of ~300 DY731-Bio per Qdot705-STV molar ratio in which case there should be sufficient fluorophores to filled all accessible binding pockets creating a critical loading point where no further conjugation of Qdot705-STV-DY731-Bio was feasible. By the centrifugations with Microcon filter devices, free DY731-Bio were precluded from contributing to the ensemble absorption and this is verified by the inverted feature observed in the red spectral regime of the measured absorbance for the 20:1 stoichiometry showing a strong resemblance to the optical behaviour of DY731-Bio-STV. Therein, the molar ratio of 20:1 derived from the absorption of the centrifuged solution should represent the maximum valency of a Qdot705-STV. However, it is worth mentioning that the predicated valency is subjected to some uncertainties primarily arises from the surface functionalisation of Qdot705-STV where accurate control of the chemical coupling of streptavidin onto a single dot is lacking. This is corroborated by the report that a single Qdot705-STV is cross-linked to 5-10 streptavidin proteins [15]. On pure conjecture, if all binding pockets in the tetrameric proteins are accessible to biotin, a Qdot705-STV could target up to 40 DY731-Bio acceptors simultaneously which behave contrariwise to what we have experimentally revealed that, on average, ~20 acceptors can be immobilised on a single Qdot705-STV. The relatively low targeting ability is probably rendered by the close packing of streptavidin around a QD preventing some binding pockets from interacting with biotin molecules. Hence, it seems likely that not all four binding pockets in a streptavidin tetramer participate in the electrostatic mediated linkage of Qdot705-STV and DY731-Bio. Likewise Qdot585-STV, the structural hindrance may impair the potential of Qdot705-STV as efficacious energy donor in FRET interaction.

We characterised FRET in Qdot705-STV-DY731-Bio self-assemblies by studying the decay dynamics of Qdot705-STV fluorescence in response to a momentary irradiation with the utilisation of a streak camera. The purified samples constituted of variable labelling ratios were optically pumped with 425 nm, ~1 MHz pulsed laser. The low repetition rate was to enable a near complete decay of Qdot705-STV fluorescence after an instantaneous femtosecond excitation. Since there was a partial overlap between Qdot705-STV and DY731-Bio emissions, a 700 nm short pass filter was added to the experimental setup in effort to optically isolate the unwanted DY731-Bio fluorescence, though a complete attenuation of that was difficult to obtain without the expense of Qdot705-STV luminescence. The optically filtered Qdot705-STV fluorescence spectrum is shown together with the complete Qdot705-STV ensemble and DY731-Bio fluorescence spectra in Figure 5.21.

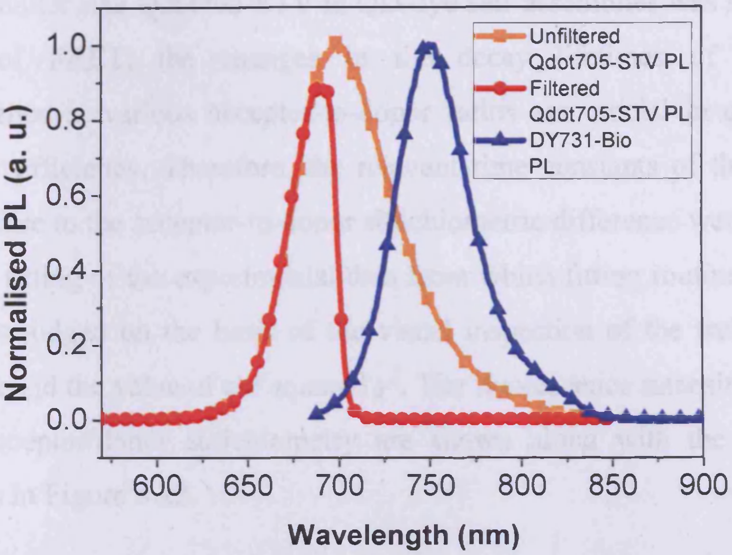

Figure 5.21: Optically filtered and complete Qdot705-STV photoemission spectra along with DY731-Bio photoemission spectrum.

The partial crosstalk between Qdot705-STV and DY731-Bio fluorescence spectra obviate the sampling of the whole Qdot705-STV population. As clearly indicated in Figure 5.21, we only sampled a fraction of the dot population by spectrally selecting those emit in the blue regime of the ensemble radiation using a 700 nm short pass filter. Even though the core material generally dictates the feasible range of QD emissions, the characteristic emission of QD is essentially governed by the core size due to the quantum confinement effect and thus, the higher photon energies in ensemble photoluminescence should represent the subpopulation of smaller dots in the Qdot705-STV ensemble. The apprehension that the red wavelengths of Qdot705-STV emission correspond to the larger dots in Qdot705-STV ensemble and vice versa conforms with the plot of theoretical bandgap-size dependency based on a simple 'particle-in-a-box' model (refer to Figure 2.15 in Chapter 2) displaying a strong correlation between the minor diameter and the energy gap, in turn, the emission wavelength. Conversely, no such relation is perceived in the diameter measured along the major axis as indicated in Figure 2.16. This directly implies that the optically studied Qdot705-STV subpopulation was composed of dots that were not only relatively smaller in size but were very much disparate in shapes from which circumstance the intricacy of FRET analysis began to arise.

By monitoring the intensity decay of the transmitted fluorescence, the dynamic behaviour of smaller size Qdot705-STV in QD-dye self-assemblies was investigated. In the analysis of FRET, the changes in the decay lifetimes of Qdot705-STV photoluminescence at various acceptor-to-donor ratios are crucial in quantifying the energy transfer efficiency. Therefore, the relevant time constants of the fluorescence decays in response to the acceptor-to-donor stoichiometric difference were derived from an exponential fitting of the experimental data from which fitting routine the quality of a decay fit was judged on the basis of the visual inspection of the weighted residual (deviation) plot and the value of chi squared χ^2. The fluorescence intensity decays in the variation of acceptor/donor stoichiometry are shown along with the corresponding exponential fits in Figure 5.22.

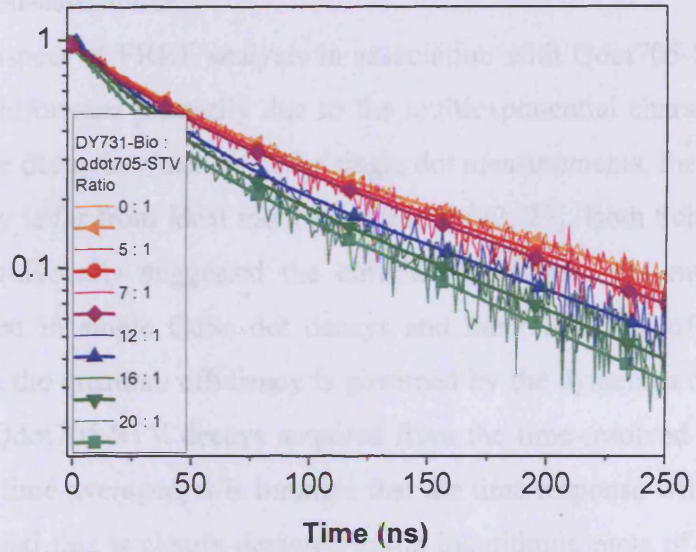

Figure 5.22: Logarithmic plots of time-resolved Qdot705-STV photoluminescence and corresponding exponential fits at various acceptor-to-donor stoichiometries for Qdot705-STV-DY731-Bio self-assemblies. The experimental data are represented by the solid lines and the exponential fits are represented by the composite line symbols.

The intensity decay of Qdot705-STV photoemission was steadily shortened with the rising number of labelled acceptors per QD from 0 to 20. Since the inner filter effects by trivial photon reabsorption do not contribute to the acceleration of decay time, FRET should be the sole quenching mechanism responsible for the rapid decay, particularly at the maximal acceptor/donor loading ratio of 20:1 where the decrease in the fluorescence decay time is most pronounced. The perceptible changes in the fluorescence dynamics with and without DY731-Bio unambiguously corroborate the presence of direct energy coupling between Qdot705-STV and energetically resonant DY731-Bio in QD-dye bioassay configuration. With the substantial spectral overlap integral, DY731-Bio appended to the binding pocket of streptavidin could afford additional nonradiative channel to QD excitons. This exciton loss to DY731-Bio will result in the increment of nonradiative rate in Qdot705-STV and in turn, the effective band edge depopulation rate i.e. the sum of radiative and nonradiative recombination rates that is physically perceived as a reduction in the overall decay of Qdot705-STV fluorescence. Presuming that no other energy coupling mechanism was present during the temporal measurements, the discernible reduction in Qdot705-STV intensity decay warrants the feasibility of Qdot705-STV, regardless of its size, as FRET energy donor in multivalent QD-fluorophore self-assemblies.

The quantitative aspect of FRET analysis in association with Qdot705-STV system is not entirely straightforward primarily due to the multiexponential characteristic of the photoluminescence decay in which even for single dot measurements, the time averaged fluorescence decay is far from ideal monoexponential [22, 23]. Both Schlegel et al and Fisher et al unequivocally suggested the correlation between the multiexponential behaviour observed in single CdSe dot decays and the fluctuation of instantaneous emission in which the quantum efficiency is governed by the dynamics of nonradiative pathways. Since Qdot705-STV decays acquired from the time-resolved measurements are ensemble and time averaged, it is intuitive that the time response will be inherently multiexponential and this is clearly depicted in the logarithmic plots of Qdot705-STV fluorescence decays at varied labelling ratios (see Figure 5.22) where no single straight line was attainable. For instance, at the maximal acceptor-to-donor loading point of 20:1, there is a decipherable fast decay component within first 50 ns time and this is ensued by a comparatively slow decay component. The typical multiexponential behaviour of QDs is further corroborated by the poor statistical fit of Qdot705-STV luminescence decay curve using a single exponential function as shown in Figure 5.23.

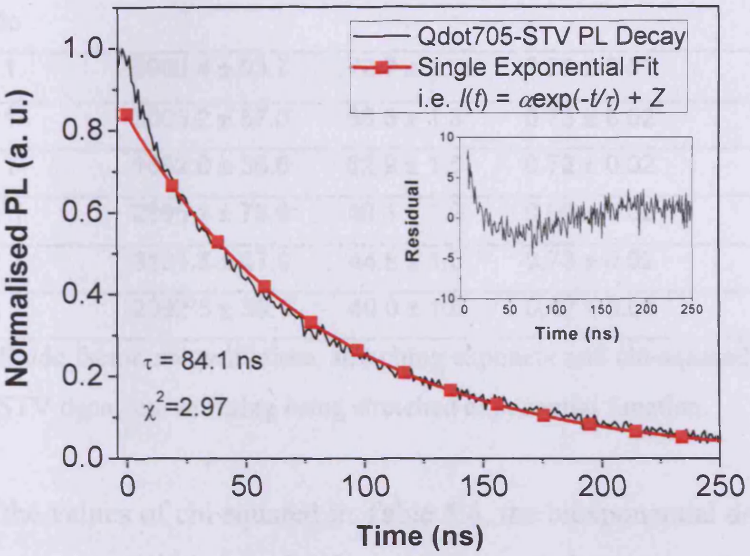

Figure 5.23: Photoluminescence decay of Qdot705-STV without DY731-Bio.

Therefore, a discrete double-exponential function was used as the decay model to extract lifetimes that have relevance to the physical relaxation processes of QDs, albeit other data fitting schemes like a stretched exponential function, which might not be physically meaningful, is also applicable as indicated in Table 5.3 showing a good range of χ^2 values that fall below 1.2. The stretched exponential function is expressed as

$$I(t) = \alpha \exp\left[-\left(\frac{t}{\tau}\right)^{\beta}\right] + Z \tag{5.6}$$

with α denoting the amplitude factor, τ denoting the mean lifetime, β denoting the stretching exponent ($0 < \beta \leq 1$) and Z denoting the baseline.

DY731-Bio : Qdot705-STV Ratio	$\alpha \pm \Delta\alpha$	$\tau \pm \Delta\tau$ (ns)	$\beta \pm \Delta\beta$	χ^2
0 : 1	5906.4 ± 93.7	72.7 ± 1.3	0.78 ± 0.01	1.18
5 : 1	3005.2 ± 57.0	66.5 ± 1.3	0.73 ± 0.02	1.17
7 : 1	1682.0 ± 36.6	62.9 ± 1.5	0.72 ± 0.02	1.07
12 : 1	2896.4 ± 75.6	50.1 ± 1.9	0.69 ± 0.02	1.18
16 : 1	3131.8 ± 57.9	44.8 ± 1.0	0.73 ± 0.02	1.13
20 : 1	2382.5 ± 39.1	40.0 ± 1.0	0.67 ± 0.01	1.08

Table 5.3 Amplitude factor, mean lifetime, stretching exponent and chi-squared values obtained from Qdot705-STV decay curve fitting using stretched exponential function.

Judging from the values of chi squared in Table 5.4, the biexponential decay model can afford a better description of the dynamic behaviour of Qdot705-STV photoluminescence than that of single lifetime model. The biexponential function is expressed as follows,

$$I(t) = \alpha_1 \exp(-\frac{t}{\tau_1}) + \alpha_2 \exp(-\frac{t}{\tau_2}) + Z \tag{5.7}$$

where α_1, α_2 are the amplitude factors and τ_1, τ_2 are the time constants and Z is the baseline.

Two distinct lifetime components were derived from fitting the experimental intensity decay profiles with Equation 5.7. In general, the short lifetime component was within 30 ns time range whilst the long lifetime component was within 100 ns time range. The values of respective fitting parameters i.e. α_1, α_2, τ_1, τ_2 drawn from the Qdot705-STV fluorescence decays at various acceptor/donor loading ratios are compiled in Table 5.4.

DY731-Bio : Qdot705-STV Ratio	Amplitude Factors		Lifetimes (ns)		χ^2
	$\alpha_1 \pm \Delta\alpha_1$	$\alpha_2 \pm \Delta\alpha_2$	$\tau_1 \pm \Delta\tau_1$	$\tau_2 \pm \Delta\tau_2$	
0 : 1	2504.8 ± 83.4	3195.9 ± 108.9	37.2 ± 2.0	130.0 ± 2.4	1.14
5 : 1	1190.8 ± 70.3	1590.4 ± 97.6	31.9 ± 3.6	122.9 ± 4.5	1.08
7 : 1	624.9 ± 42.2	920.6 ± 42.7	29.3 ± 3.8	118.7 ± 3.0	1.18
12 : 1	1429.0 ± 84.8	1318.9 ± 106.2	25.1 ± 3.1	109.0 ± 8.8	1.06
16 : 1	1569.7 ± 107.7	1479.0 ± 90.9	22.3 ± 2.7	97.0 ± 4.7	1.06
20 : 1	1231.9 ± 67.2	1045.3 ± 47.3	20.2 ± 1.8	94.3 ± 2.6	1.14

Table 5.4: Tabular form of parameters, which include the lifetime components, the amplitude factors and the chi-squared values, derived from biexponential fitting of the experimental data.

Based on the χ^2 values in Table 5.4, it is self-explanatory that the dynamics of Qdot705-STV upon femtosecond excitation are well described by an exponential function with two adjustable time constants. As the DY731-Bio-to-Qdot705-STV ratio was methodically increased, some decreases were seen in both extracted lifetime component yet the rate of reduction in correlation with the stoichiometry appears to vary between the short and the long lifetime components. The long lifetime component declines from initial 130 ns to final 94 ns at the maximum labelling ratio which accounts for 28 % change. By contrast, the short lifetime component declines markedly from initial 37 ns to final 20 ns at the maximum labelling ratio which accounts for 46 % change. To provide an overview of the acceptor/donor stoichiometric dependence of QD time response, the short and long lifetime components are plotted against the number of DY731-Bio per Qdot705-STV as exemplified in Figure 5.24.

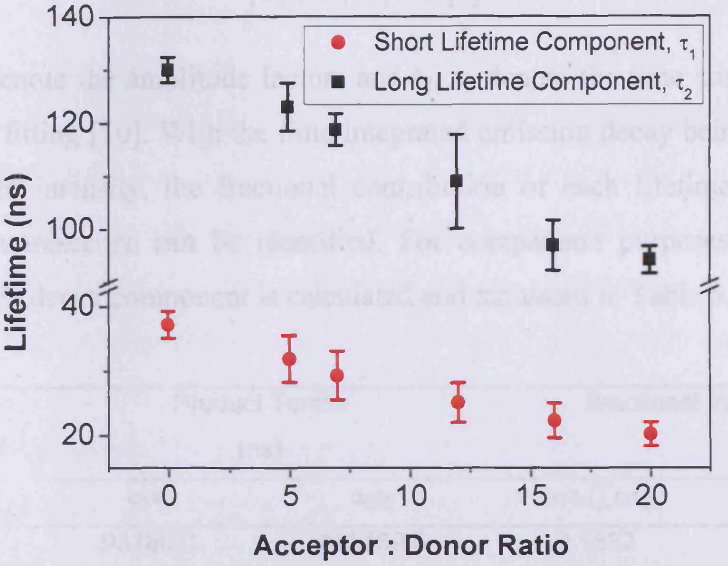

Figure 5.24: Short and long lifetime components versus acceptor-to-donor loading ratio.

Figure 5.24 depicts a clear descending trend in the Qdot705-STV donor decay lifetimes with increasing immobilisation of DY731-Bio acceptors. In that FRET is the pertinent quenching mechanism responsible for the systematic reduction in the donor luminescence decays, the differences in the predicated time constants would provide some useful information as regards the effectiveness of the direct energy coupling between Qdot705-STV and multitude of viable DY731-Bio acceptors. We approach FRET analysis discretely from two separable lifetime components derived from the two-lifetime fitting of the time-resolved spectroscopic data on account of the notion that both decay components behave differently towards the variation of DY731-Bio labelling. Moreover, in contradistinction to the decay fits of Qdot585-STV fluorescence dynamics, Qdot705-STV exhibits two decay components with amplitude factors of similar magnitude (see Table 5.4). In light of that, both lifetime components could probably bear the same weight in the FRET analysis of QD-dye assays and hence, this underpins our attempt to understand the dipolar coupling in Qdot705-STV-DY731-Bio self-assemblies explicitly on the basis of short and long lifetime components.

As the product of amplitude factor, α, and lifetime, τ, is proportional to the area under the fluorescence decay curve, the time integrated luminescence intensity, $I(t)$, can be expressed as

$$\int_0^\infty I(t) = \alpha_1\tau_1 + \alpha_2\tau_2 \tag{5.8}$$

where α_1, α_2 denote the amplitude factors and τ_1, τ_2 denote the time constants for two-lifetime decay fitting [10]. With the time integrated emission decay being equivalent to the steady state intensity, the fractional contribution of each lifetime component to steady state fluorescence can be identified. For comparison purposes, the fractional intensity of each decay component is calculated and tabulated in Table 5.5.

DY731-Bio : Qdot705-STV	Product Terms (ns)		Fractional Intensities	
Ratio	$\alpha_1\tau_1$	$\alpha_2\tau_2$	$\alpha_1\tau_1/\sum\alpha_i\tau_i$	$\alpha_2\tau_2/\sum\alpha_i\tau_i$
0 : 1	93180.0	415469.6	0.1832	0.8168
5 : 1	38270.4	195620.4	0.1636	0.8364
7 : 1	18310.4	109274.0	0.1435	0.8566
12 : 1	35868.9	143756.8	0.1997	0.8003
16 : 1	35004.5	143464.9	0.1961	0.8039
20 : 1	24883.6	98568.0	0.2016	0.7984

Table 5.5: Tabulation of the product terms and the corresponding fractional intensities for short (τ_1) and long (τ_2) decay components.

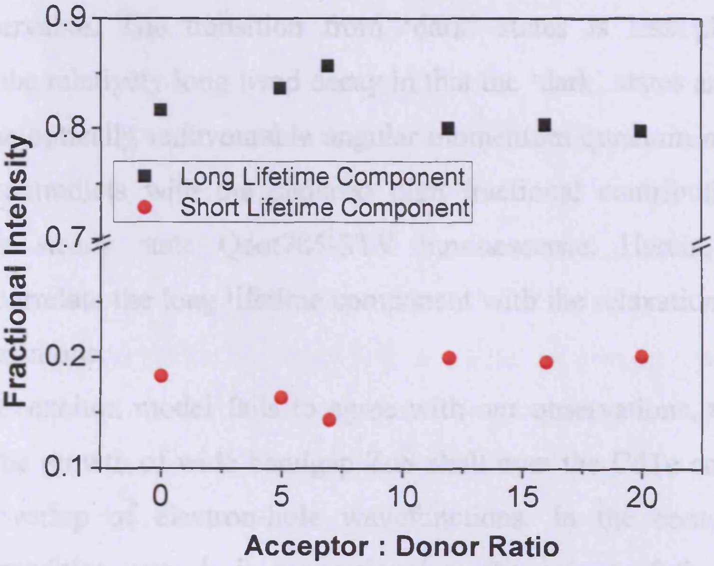

Figure 5.25: Fractional intensities of short (represented by ●) and long (represented by ■) lifetime components as a function of acceptor-to-donor conjugation ratio.

As shown in Figure 5.25, the fractional intensities of the long lifetime component are predominantly above 0.8 inferring that the contribution of the long decay time to steady state emission is approximately fourfold larger than that of the short decay time. Considering the high proportion of the former contribution to the luminescence yield and the fact that we were monitoring the blue spectral region of Qdot705-STV photoemission where the radiation from deep traps is very unlikely, it is justifiable to associate the long lifetime component elicited from the double-exponential fit of Qdot705-STV fluorescence decay in the absence of DY731-Bio to the intrinsic radiative recombination of excitons. In comparison to Qdot585-STV with CdSe as the core material, the ascribed radiative recombination rate of Qdot705-STV electron-hole pairs is relatively slower. In fact, not only the radiative relaxation rate of Qdot585-STV is faster than that of Qdot705-STV by a factor of 5, the extracted long radiative lifetime of Qdot705-STV (without immobilised DY731-Bio) does not exactly conform with the dynamical studies of organic capped CdTe QDs that were published in literature [24-26]. The reported radiative lifetimes of these CdTe QDs were typically of the order of ~20 ns and no longer lifetimes were resolved. Henceforth, we suspect that the poor electronic confinement in Qdot705-STV could be the culprit behind the slow decay rate. The postulation is supported by the weak oscillation strength near the onset of Qdot705-STV ensemble absorption (see Figure 5.1) where essentially no discrete band edge feature is observable. The transition from 'dark' states is less plausible for the explanation of the relatively long lived decay in that the 'dark' states are weak emitting states due to the optically unfavourable angular momentum quantum number of 2 [27, 28] and this contradicts with the deduced high fractional contribution of the long lifetime to the steady state Qdot705-STV luminescence. Herein, it seems less appropriate to correlate the long lifetime component with the relaxation of the optically passive 'dark' excitons.

Since the 'dark' exciton model fails to agree with our observations, this leaves us to speculate that the growth of wide bandgap ZnS shell over the CdTe core might induce weak spatial overlap of electron-hole wavefunctions. In the context of quantum mechanics, a transition rate, k, is proportional to the square of the spatial overlap integral of electron-hole wavefunctions,

$$k \propto \left| \int \psi_e \psi_h dV \right|^2 \tag{5.9}$$

with ψ_e, ψ_h representing the electron and hole wavefunctions and V representing the volume. Therefore, on the basis of Equation 5.9 alone, for the radiative rate to decrease, say, from $k_r = 1/20\ \text{ns}^{-1}$ to $k_r = 1/120\ \text{ns}^{-1}$, the initial electron-hole spatial integral must drop by 60 %. Whilst the potential barrier at CdTe/ZnS interface is finite in Qdot705-STV, the extent of exponential tunnelling of electron wavefunction into ZnS shell will not be sufficient to induce the dramatic 60 % change in the spatial overlap of electron-hole wavefunctions. In view of that, there should be a much greater structural effect, capable of spatially separating the photoexcited electron and hole in Qdot705-STV, undesirably evoked by the inorganic surface passivation. It is not unlikely for the occurrence of alloying between CdTe core and ZnS shell as regards the marked 17 % difference in the lattice constants. The interfacial alloy, dependent on its thickness and bandoffsets, could localise either electron or hole outside the CdTe core. This could substantially reduce the electron-hole overlap, in turn, the recombination rate as observed in type-II CdTe/CdSe QDs exhibiting a decay lifetime of 57 ns [7]. On account of the long radiative lifetime and the unstructured absorption characteristic, we surmise that Qdot705-STV heterostructure could possess the conduction and valence band alignments which render it type-II and this possibility is theoretically assessed, in Chapter 6, using a 2-step finite depth spherical well model.

Due to the large lattice mismatch between CdTe and ZnS, a perfect epitaxial growth of ZnS shell on CdTe surface is difficult to obtain [29, 30]. The irregular lattice reconstruction at the heterojunction could give rise to surface defects providing fast carrier trapping states. The hypothesis is coherent with the lower ensemble quantum yield of Qdot705-STV as compared to that of Qdot585-STV. The quantum yield of Qdot705-STV is reported to be 0.67 while the quantum yield of Qdot585-STV is 0.87. Thus, the relatively low quantum efficiency reveals that electron-hole pairs generated in Qdot705-STV upon photoexcitation could recombine to the ground state through viable nonradiative deactivation channels. Given that a single exponential decay kinetics is principally the sum of radiative and nonradiative relaxation rates i.e. $k = k_r + k_{nr}$ and the carrier trapping to extrinsic surface states usually occurs at much faster time-scale, we could then reliably assume the exciton relaxation is predominantly nonradiative and thus we attribute the fast decay rate to the coupling between the lowest excited state and the trap state.

As the time-resolved measurements were taken over a period of time, it is anticipated that the manifold dynamics of Qdot705-STV in the bulk solution would be detected which imperatively convoluted to a multiexponential decay curve. With a time resolution of 2.5 ns, the distinctive fast and slow time responses of Qdot705-STV alone (without DY731-Bio) was resolved qualitatively by logarithmic plot and quantitatively by discrete multiexponential fit from which we speculate that the fast relaxation to be predominantly nonradiative and the slow relaxation to be predominantly radiative. It is worth noting that the acquired fluorescence decay curves, with and without the presence of DY731-Bio, were time and ensemble averaged and thus it is intuitive that the lifetimes derived from the two-component exponential fit would be subjected to the averaging effects. Nonetheless, in our pursuit to study the dipolar resonance coupling in Qdot705-STV-DY731-Bio assays, we determined the efficiency of that based on the optimal short and long lifetime components deduced from the adopted double-exponential fitting scheme. The FRET efficiency expression in relation to the lifetimes is defined as

$$E = 1 - \frac{\tau_{DA}}{\tau_D} \tag{5.10}$$

where τ_{DA} is the fluorescence lifetime of donor in the presence of the acceptor and τ_D is the fluorescence lifetime of the donor alone. At each DY731-Bio-to-Qdot705-STV stoichiometry, the FRET efficiency formula was applied to the short and long lifetime components in order that the underlying dipole-dipole interactions between Qdot705-STV and immobilised DY731-Bio could be evaluated explicitly. The calculated FRET efficiency with respect to the short and long lifetime components are shown in Figure 5.26.

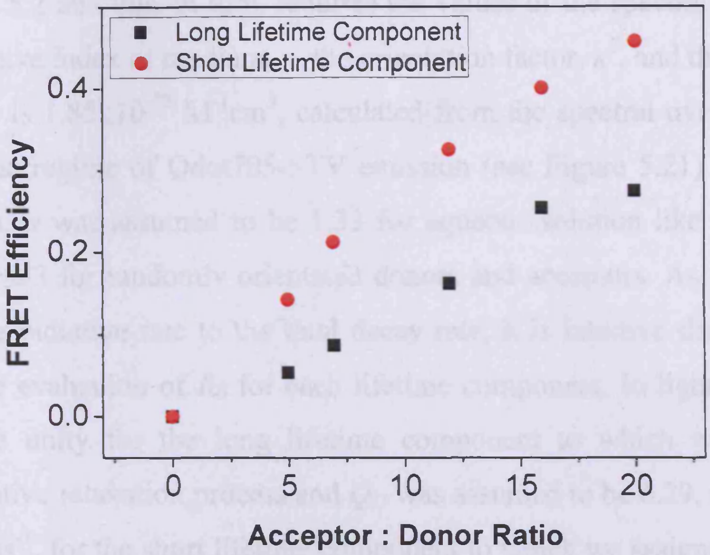

Figure 5.26: FRET efficiencies derived from respective short and long decay components for a range of acceptor-to-donor labelling ratios.

Figure 5.26 displays a discernible difference between the FRET efficiencies determined from the short and the long lifetime components. By contrast with the slow kinetics, the fast kinetics appears to yield greater efficiency in the direct energy coupling between Qdot705-STV and adjacent resonant DY731-Bio. Bound by the limitation of the valency of Qdot705-STV, the highest efficiency achieved so far is ~46 % at 20 DY731-Bio per QD. Conversely, for the long lifetime component, a modest efficiency of ~27 % is acquired at the same acceptor-to-donor stoichiometry. The prevalence of the use of FRET technique in the molecular studies due to its inverse sixth power dependence on the donor-acceptor distance has brought to our attention that it could be also possible to apply the same dipolar concept to extract the proximity relationships in our QD-dye assays, of course, assuming that photoexcited Qdot705-STV behaves like an oscillating point dipole and thereby, the donor-acceptor distance in centro-symmetric QD-dye self-assemblies can be deduced from the FRET efficiency expression defined as

$$E = \frac{nR_0^{\ 6}}{nR_0^{\ 6} + r^6} \tag{5.11}$$

where n denotes the number of bound acceptors per donor and R_0 denotes the Förster distance and r is the centre-to-centre donor-acceptor separation provided that the distribution of acceptors around a single donor is uniform. As indicated in Equation

5.11, prior to the theoretical calculation of FRET efficiency, R_0 has to be predetermined from Equation 5.2 and this, in turn, requires the values of the spectral overlap integral, $J(\lambda)$, the refractive index of medium, n, the orientation factor, κ^2, and the donor quantum yield, Q_D. $J(\lambda)$ is $1.85\text{x}10^{-12}$ $M^{-1}cm^3$, calculated from the spectral overlap between the transmitted blue regime of Qdot705-STV emission (see Figure 5.21) and the DY731-Bio absorption. n was assumed to be 1.33 for aqueous solution like PBS and κ^2 was assumed to be 2/3 for randomly orientated donors and acceptors. As quantum yield is the ratio of the radiative rate to the total decay rate, it is intuitive that Q_D will not be identical in the evaluation of R_0 for each lifetime component. In light of that, Q_D was assumed to be unity for the long lifetime component to which we associated the dominant radiative relaxation process and Q_D was assumed to be 0.29, the ratio of 1/130 ns^{-1} to 1/37.2 ns^{-1}, for the short lifetime component to which we assigned the fast carrier capture. By incorporating all the pertinent values into Equation 5.2, R_0 for the short and the long lifetime components were found to be 83.8 Å and 68.2 Å respectively.

Donor-Acceptor Complex	Donor Lifetime Component, τ (ns)	Overlap Integral, $J(\lambda)$ (x 10^{-12} $M^{-1}cm^3$)	Donor Quantum Yield, Q_D	Förster Distance, R_0 (Å)
Qdot705-STV-DY731-Bio	130.0	1.85	1.00	83.8
	37.2	1.85	0.29	68.2

Table 5.6: Tabulation of short and long lifetime components, spectral overlap integral, donor quantum yield and Förster distance.

With known R_0 for each lifetime component, $1/r^6$ dependence of Equation 5.11 can be exploited to provide the spatial information of Qdot705-STV-DY731-Bio assays. In effort to elicit the distance of closest approach between the donor and the acceptor, several theoretical fits, with reference to Equation 5.11, for a range of r values were plotted alongside the experiment data as indicated in Figure 5.27. The best fit for the experimental FRET efficiency data should, supposedly, reveal the spatial extension from the donor dipole to the interacting acceptor dipole in Qdot705-STV-DY731-Bio self-assemblies.

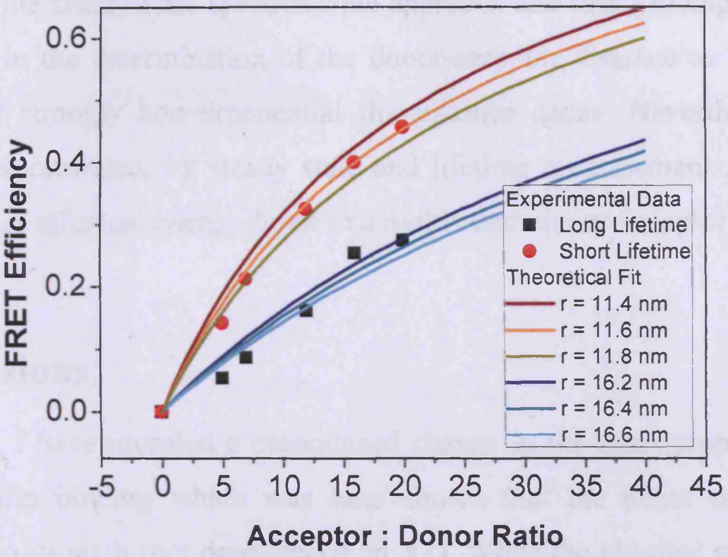

Figure 5.27: Plots of empirical FRET efficiency and theoretical prediction versus acceptor-to-donor labelling ratio.

From Figure 5.27, it seems apparent that the theoretical fits produce two markedly different distances for the respective lifetime components. The fast transient assignable to the carrier trapping affords a smaller donor-acceptor separation (r = 11.6 nm) while, conversely, the slow transient ascribed to the predominant radiative relaxation yields a larger separation (r = 16.4 nm). This spatial difference does not quite accord with our apprehension. Since the donor-acceptor distances in Qdot705-STV-DY731-Bio conjugates are appreciably consistent in the course of two independent transition processes, both predicted values should converge at the same distance by taking account of the change in the quantum efficiency. The contradictory finding is indicative that the idealised point dipole approximation of Qdot705-STV in the FRET efficiency formulation may not be entirely true. For now, we preliminarily speculate that the shape anisotropy and the charging of dot core upon surface trapped carriers could affect the distribution of charges within the inner core of Qdot705-STV and thus, causing it to deviate from point dipole approximation, in turn, the idealised theoretical FRET formulism. However, the underlying mechanism responsible for that and the extent of the deviation are not fully understood and will require rigorous theoretical and experimental studies of inherent Qdot705-STV photophysical behaviours. The explicit quantitative analysis of FRET with reference to the short and the long lifetime components has shown that some hidden characteristics of Qdot705-STV could be overlooked by the steady state spectroscopic approach and thus proving that the use of Equation 5.11 in the determination of the donor-acceptor distance to be less reliable particularly for strongly non-exponential fluorescence decay. Nevertheless, we have successfully demonstrated, by steady state and lifetime measurements, that Qdot705-STV can serve as effectual energy donor in a multivalent donor-acceptor configuration.

5.5 Conclusions

In this chapter, I have revealed a pronounced change in the absorption of DY731-Bio upon streptavidin binding which was later shown that the effect on R_0 was only fractional due to its sixth root dependence on $J(\lambda)$. While the physical size of Qdot705-STV over 100 Å could be perceived as unfavourable to FRET, a considerable high quenching efficiency was attained in the titration experiment with DY731-Bio showing a 60 % drop in the Qdot705-STV luminescence at 40:1 acceptor-to-donor labelling ratio. Only by centrifugation with a filter device, the maximal valency of Qdot705-STV was unravelled where 46 % of FRET efficiency was obtained for the short lifetime component attributed to the fast carrier capture by surface states and 27 % of FRET efficiency for the long lifetime component ascribed to the predominant radiative recombination of band edge exciton. On the basis of that assignment to Qdot705-STV kinetics, our attempt to fit the experimental data with theoretical model failed to generate a satisfactory result as regards the donor-acceptor spatial separation. The inconsistency in the distances extracted from the short and the long lifetime components implicitly showed that the underlying behaviour Qdot705-STV was far more complex than a simple point dipole which was overlooked in the steady state approach.

5.6 References

1. Rajh T, Micic OI, Nozik AJ. Synthesis and Characterization of Surface-Modified Colloidal CdTe Quantum Dots. *J Phys Chem* 1993, **97**(46):11999-12003.

2. Empedocles SA, Norris DJ, Bawendi MG. Photoluminescence Spectroscopy of Single CdSe Nanocrystallite Quantum Dots. *Phys Rev Lett* 1996, **77**(18):3873-3876.

3. Empedocles SA, Neuhauser R, Shimizu K, Bawendi MG. Photoluminescence from Single Semiconductor Nanostructures. *Adv Mater* 1999, **11**(15):1243-1256.

4. Wang Y, Herron N. Nanometer-Sized Semiconductor Clusters - Materials Synthesis, Quantum Size Effects, and Photophysical Properties. *J Phys Chem* 1991, **95**(2):525-532.

5. CRC Handbook of Chemistry and Physics: A Ready-Reference Book of Chemical and Physical Data 82th edn. Edited by Lide DR. CRC Press, 2001.

6. Oladeji IO, Chow L, Ferekides CS, Viswanathan V, Zhao ZY. Metal/CdTe/CdS/$Cd_{1-x}Zn_xS$/TCO/Glass: A New CdTe Thin Film Solar Cell Structure. *Solar Energy Materials and Solar Cells* 2000, **61**(2):203-211.

7. Kim S, Fisher B, Eisler HJ, Bawendi M. Type-II Quantum Dots: CdTe/CdSe(Core/Shell) and CdSe/ZnTe(Core/Shell) Heterostructures. *J Am Chem Soc* 2003, **125**(38):11466-11467.

8. Ivanov SA, Nanda J, Piryatinski A, Achermann M, Balet LP, Bezel IV, Anikeeva PO, Tretiak S, Klimov VI. Light Amplification Using Inverted Core/Shell Nanocrystals: Towards Lasing in the Single-Exciton Regime. *Journal of Physical Chemistry B* 2004, **108**(30):10625-10630.

9. Balet LP, Ivanov SA, Piryatinski A, Achermann M, Klimov VI. Inverted Core/Shell Nanocrystals Continuously Tunable between Type-I and Type-II Localization Regimes. *Nano Letters* 2004, **4**(8):1485-1488.

10. Lakowicz J. Principles of Fluorescence Spectroscopy. 3rd edn. Springer, 2006.

11. Dyomics. *Personal Communication.* 2006.

12. Berlier JE, Rothe A, Buller G, Bradford J, Gray DR, Filanoski BJ, Telford WG, Yue S, Liu JX, Cheung CY *et al.* Quantitative Comparison of Long-Wavelength Alexa Fluor Dyes to Cy Dyes: Fluorescence of the Dyes and their Bioconjugates. *Journal of Histochemistry & Cytochemistry* 2003, **51**(12):1699-1712.

13. Livnah O, Bayer EA, Wilchek M, Sussman JL. 3-Dimensional Structures of Avidin and the Avidin-Biotin Complex. *Proceedings of the National Academy of Sciences of the United States of America* 1993, **90**(11):5076-5080.

14. Gonzalez M, Bagatolli LA, Echabe I, Arrondo JLR, Argarana CE, Cantor CR, Fidelio GD. Interaction of Biotin with Streptavidin - Thermostability and Conformational Changes upon Binding. *Journal of Biological Chemistry* 1997, **272**(17):11288-11294.

15. Qdot Streptavidin Conjugates User Manual. Invitrogen. 2006.

16. Medintz IL, Clapp AR, Mattoussi H, Goldman ER, Fisher B, Mauro JM. Self-Assembled Nanoscale Biosensors Based on Quantum Dot FRET Donors. *Nature Materials* 2003, **2**(9):630-638.

17. Clapp AR, Medintz IL, Mauro JM, Fisher BR, Bawendi MG, Mattoussi H. Fluorescence Resonance Energy Transfer between Quantum Dot Donors and Dye-Labeled Protein Acceptors. *J Am Chem Soc* 2004, **126**(1):301-310.

18. Willard DM, Carillo LL, Jung J, Van Orden A. CdSe-ZnS Quantum Dots as Resonance Energy Transfer Donors in a Model Protein-Protein Binding Assay. *Nano Letters* 2001, **1**(9):469-474.

19. Goldman ER, Medintz IL, Whitley JL, Hayhurst A, Clapp AR, Uyeda HT, Deschamps JR, Lassman ME, Mattoussi H. A Hybrid Quantum Dot-Antibody Fragment Fluorescence Resonance Energy Transfer-Based TNT Sensor. *J Am Chem Soc* 2005, **127**(18):6744-6751.

20. Invitrogen. *Personal Communication.* 2006.

21. Arakaki A, Hideshima S, Nakagawa T, Niwa D, Tanaka T, Matsunaga T, Osaka T. Detection of Biomolecular Interaction between Biotin and Streptavidin on a Self-Assembled Monolayer Using Magnetic Nanoparticles. *Biotechnology and Bioengineering* 2004, **88**(4):543-546.

22. Schlegel G, Bohnenberger J, Potapova I, Mews A. Fluorescence Decay Time of Single Semiconductor Nanocrystals. *Phys Rev Lett* 2002, **88**(13).

23. Fisher BR, Eisler HJ, Stott NE, Bawendi MG. Emission Intensity Dependence and Single-Exponential Behavior in Single Colloidal Quantum Dot Fluorescence Lifetimes. *Journal of Physical Chemistry B* 2004, **108**(1):143-148.

24. Van Driel AF, Allan G, Delerue C, Lodahl P, Vos WL, Vanmaekelbergh D. Frequency-Dependent Spontaneous Emission Rate from CdSe and CdTe Nanocrystals: Influence of Dark States. *Phys Rev Lett* 2005, **95**(23).

25. Wuister SF, Donega CD, Meijerink A. Influence of Thiol Capping on the Exciton Luminescence and Decay Kinetics of CdTe and CdSe Quantum Dots. *Journal of Physical Chemistry B* 2004, **108**(45):17393-17397.

26. Wuister SF, Donega CDM, Meijerink A. Luminescence Temperature Antiquenching of Water-Soluble CdTe Quantum Dots: Role of the Solvent. *J Am Chem Soc* 2004, **126**(33):10397-10402.

27. Norris DJ, Efros AL, Rosen M, Bawendi MG. Size Dependence of Exciton Fine Structure in CdSe Quantum Dots. *Phys Rev B* 1996, **53**(24):16347-16354.

28. Nirmal M, Norris DJ, Kuno M, Bawendi MG, Efros AL, Rosen M. Observation of the Dark Exciton in CdSe Quantum Dots. *Phys Rev Lett* 1995, **75**(20):3728-3731.

29. Dabbousi BO, RodriguezViejo J, Mikulec FV, Heine JR, Mattoussi H, Ober R, Jensen KF, Bawendi MG. (CdSe)ZnS Core-Shell Quantum Dots: Synthesis and Characterization of a Size Series of Highly Luminescent Nanocrystallites. *Journal of Physical Chemistry B* 1997, **101**(46):9463-9475.

30. Hines MA, Guyot-Sionnest P. Synthesis and Characterization of Strongly Luminescencing ZnS-Capped CdSe Nanocrystals. *J Phys Chem* 1996, **100**(2):468-471.

CHAPTER 6:

THEORETICAL MODELLING OF SIZE DEPENDENT ENERGY GAPS AND CARRIER WAVEFUNCTIONS OF QUANTUM DOTS

CONTENTS:

Abstract: In this chapter, I demonstrate the usage of several theoretical approaches, from a simple 'particle-in-a-sphere' model to a more advanced 2-step finite depth spherical well model, to investigate the size dependent bandgaps and the localisation of carriers in typical type-I QDs, within the parabolic band approximation. Then, by a slight modification of the finite well model, I proceed to the theoretical study of type-II QDs wherein the conduction and valence band extrema are spatially separated, in attempt to provide a logical explanation underpinning the rather long fluorescence transient perceived in Qdot705-STV.

CHAPTER 6:

THEORETICAL MODELLING OF SIZE DEPENDENT ENERGY GAPS AND CARRIER WAVEFUNCTIONS OF QUANTUM DOTS

6.1 Absorption Profiles of Quantum Dots

Colloidal QDs fabricated by wet chemical synthesis are well known for their size tunable photoemission. With the same core material, the lowest excited state of QDs can be shifted to higher or lower energy by simply decreasing or increasing the QD size. This phenomenal characteristic is attributed to the quantum confinement effect where the motion of electron-hole is restricted within the bulk exciton Bohr radius, a_B. It is worth mentioning that the a_B for CdSe and CdTe are 56 Å [1] and 73 Å [2] respectively. In the strong confinement regime, with the core radius smaller than a_B, the density of states in the QD becomes discrete. The nearby bound states are split by energy gaps in correlation with the QD dimension. As the size of a QD is reduced, the bound states move to upper energy levels and become more widely spaced. Because of the substantial separation of energy states, the quasi-zero dimensional QD is categorised as an 'artificial atom'. The delta like characteristic in the density of states vividly appears in the absorption profile of a QD ensemble. Owing to the size disparity in the QD ensemble, the absorption lineshape is inhomogeneously broadened by the convolution of individual dot absorption spectra. Nonetheless, in general, the first peak at the absorption onset is termed as the 1S-1S band edge transition. The upward trend in the band edge energy with descending size of commercial Qdot nanoparticle is depicted in Figure 6.1.

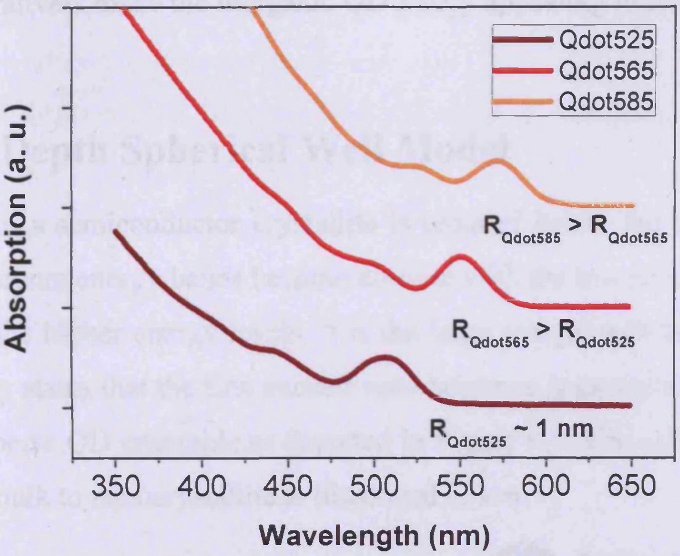

Figure 6.1: Absorption profiles of commercial CdSe/ZnS Qdots. Data obtained from [3]. (Courtesy of Invitrogen)

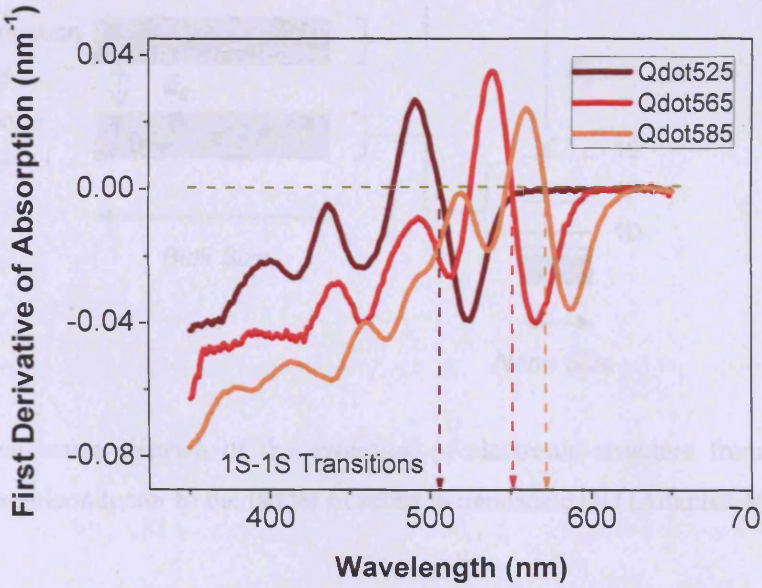

Figure 6.2 First derivatives of absorption spectra of Qdot525, Qdot565 and Qdot585.

A qualitative description of the electronic quantum size effect in QDs is clearly displayed in Figure 6.1. With increasing dot size, the excitonic peak is red shifted. The lowest transition can be easily resolved by taking the first derivative of the absorption as shown in Figure 6.2 that the absorption peaks for Qdot525, Qdot565 and Qdot585 are

506 nm, 550 nm and 572 nm respectively. Henceforth, the size tunable the optical properties imperatively make the inorganic QD a very appealing luminescent label.

6.2 Infinite Depth Spherical Well Model

When the size of a semiconductor crystallite is reduced below the bulk exciton Bohr radius, the continuum energy bands become discrete with the lowest excitonic state well separated from the higher energy levels. It is the large energy split between successive ascending energy states that the first excited state becomes apparent in the absorption of nearly monodisperse QD ensemble as depicted in Figure 6.1. The evolution of the band structures from bulk to nanocrystallite is illustrated below.

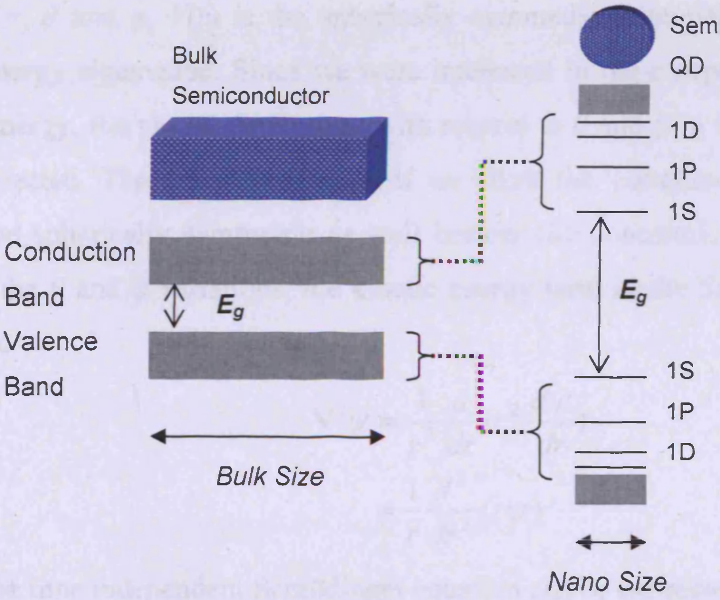

Figure 6.3: Schematic diagram of the evolution of electronic structure from the continuum bands in bulk semiconductor to the ladder of states in nanoscale QD (Adapted from [4]).

The pseudo-zero dimension QD is analogous to an atom with electron and hole occupying the 1S orbitals. If the QD is ideally spherical, the lowest electron and hole with S-like eigenfunction can be elementarily modelled as 'particle-in-a-sphere'. Within the framework of effective mass approximation, we employed a 'particle-in-a-sphere' model to theoretically predict the trend in the energy shift of the lowest excited state with the reducing size of QD. Hereby, on the basis of this simple model, the complexity of band structure is ignored presuming that the lowest conduction band and the highest valence band are parabolic near the origin of k vector. Also, the bulk lattice structure is retained in QD. The latter assumption is generally true as bare CdSe QD has been reported to have a crystalline structure that resembled bulk CdSe [5]. With the assumptions readily made, we derived the eigenenergy of the excitonic state of bare CdSe and CdTe QDs by solving the time independent Schrödinger equation in the spherical polar coordinates r, θ, φ.

$$[-\frac{\hbar^2}{2m^*}\nabla^2 + V(r)]\psi(r,\theta,\varphi) = E\psi(r,\theta,\varphi) \tag{6.1}$$

with
$$\nabla^2 = \frac{1}{r^2}\frac{d}{dr}(r^2\frac{d}{dr}) + \frac{1}{r^2\sin\theta}\frac{d}{d\theta}(\sin\theta\frac{d}{d\theta}) + \frac{1}{r^2\sin^2\theta}\frac{d^2}{d\varphi^2} \tag{6.2}$$

where m^* is the bulk effective mass of electron (hole), ∇^2 is the Laplacian operator in terms of r, θ and φ, $V(r)$ is the spherically symmetric potential energy and E is the lowest energy eigenvalue. Since we were interested in the r dependence of the lowest excited energy, the partial derivatives with respect to θ and φ in the Laplacian operator were neglected. The omission is valid if we allow the wavefunctions of electron and hole to be spherically symmetric as well besides the concentric potential barrier [6]. Without the θ and φ variations, the kinetic energy term in the Schrödinger expression reduces to

$$\begin{aligned}\nabla^2\psi &= \frac{1}{r^2}\frac{d}{dr}(r^2\frac{d\psi}{dr}) \\ &= \frac{1}{r}\frac{d^2}{dr^2}(r\psi)\end{aligned} \tag{6.3}$$

Hence, the time independent Schrödinger equation can be expressed in terms of r only.

$$-\frac{\hbar^2}{2m^*}\frac{d^2}{dr^2}(r\psi(r)) + V(r)(r\psi(r)) = E(r\psi(r)) \tag{6.4}$$

In a simple prediction of the quantum confinement effect on the lowest exciton in QD, the potential at the boundary was taken to be infinite i.e. $V(r) = \infty$ for $r \geq a$, where a representing the QD radius. On the other hand, the inner potential is essentially zero i.e. $V(r) = 0$ for $r < a$. The imposed electronic confinement conditions are illustrated in Figure 6.4.

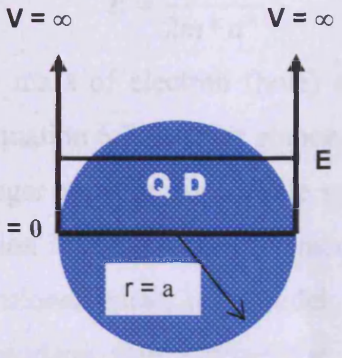

Figure 6.4: Potential energy diagram for infinite depth spherical well model.

The wavefunctions of 1S electron and 1S hole (with angular momentum l = 0) in infinite depth well can be characterised by spherical Bessel function of the first kind of zeroth order [7-10]. As the barrier is perfectly rigid and impenetrable, no carrier wavefunction is allowed outside the bare QD. Therefore, the wavefunctions at $r < a$ region and $r > a$ regions are as follows,

$$\psi(r) = \frac{A\sin(kr)}{r}, \text{ for } r < a \tag{6.5}$$

$$\psi(r) = 0, \qquad \text{for } r \geq a$$

where k is the wavenumber and A is the arbitrary constant.

At the rigid boundary $r = a$, the radial function $r.\psi(r)$ is 0. In such condition, the wavenumber k will be restricted to discrete values.

$$A\sin(ka) = 0$$

$$\therefore ka = n\pi \tag{6.6}$$

$$k = \frac{n\pi}{a}$$

where n = 1, 2, etc.

With $V(r)$ = 0 in the core of QD, the total energy of carrier is entirely kinetic by the definition of radial Schrödinger equation.

$$E = \frac{\hbar^2 k^2}{2m^*} \tag{6.7}$$

As 1S orbital is equivalent to the lowest bound state with n = 1, the eigenenergy for the confined electron or hole becomes

$$E = \frac{\hbar^2 \pi^2}{2m^* a^2} \tag{6.8}$$

where m^* is the effective mass of electron (hole) and a is the crystallite radius, by substituting $k = \pi/a$ into Equation 6.7. At first glance, the final eigenvalue elicited from solving the radial Schrödinger equation for infinite spherical square well in the limit of effective mass approximation is mathematically analogous with 'one-dimensional-box' model. Like the one dimensional square well model, the upward energy shift of bound exciton above the bulk bandgap also follows the $1/a^2$ dependence as indicated in Equation 6.8. By calculating the eigenvalues for the respective electron and hole, the trend of the lowest excited state of QD in response to the variation of the dot radius can be theoretically simulated provided that the QD size is within the strong confinement regime where $a < a_B$. The linear superposition of the bulk bandgap and the energies of the bound states for electron and hole will define the effective bandgap of QD.

$$E_{eff}(QD) = E_g(bulk) + \frac{\hbar^2 \pi^2}{2m_e^* a^2} + \frac{\hbar^2 \pi^2}{2m_h^* a^2} \tag{6.9}$$

where E_g is the bulk bandgap of semiconductor, a is the spherical dot radius and m_e^*, m_h^* are the bulk effective masses of electron and hole. Although the infinite spherical well model does not include the influence of matrix on the bare QD or the confinement effect of inorganic shell on the overcoated QD, we compared and contrasted the theoretical exciton energies of CdSe and CdTe QDs with the empirical values from the literature. It would be interesting to know how well the infinite depth model based on the parabolic band approximation fares with the experimental observations. The predicted bandgap of QD at a particular radius was converted to the relevant wavelength before inclusion in the bandgap-size correlation plot. This permits the direct comparison between the first absorption peak (effective bandgap of QD) and the QD radius. The material parameters i.e. effective masses of electron and hole used to determine the lowest excited state of QD are reported in Table 6.1.

QD Material	Effective Masses		Bulk Bandgap (300 K)
	m_e^*/m_e	m_h^*/m_e	E_g (eV)
CdSe[a]	0.13	0.45	1.74
CdTe[b]	0.11	0.35	1.56

[a] m_e^*, m_h^* from Ref. [11], E_g from Ref. [12].

[b] m_e^*, m_h^* from Ref. [10], E_g from Ref. [13].

Table 6.1: Material parameters used in the infinite spherical well calculations.

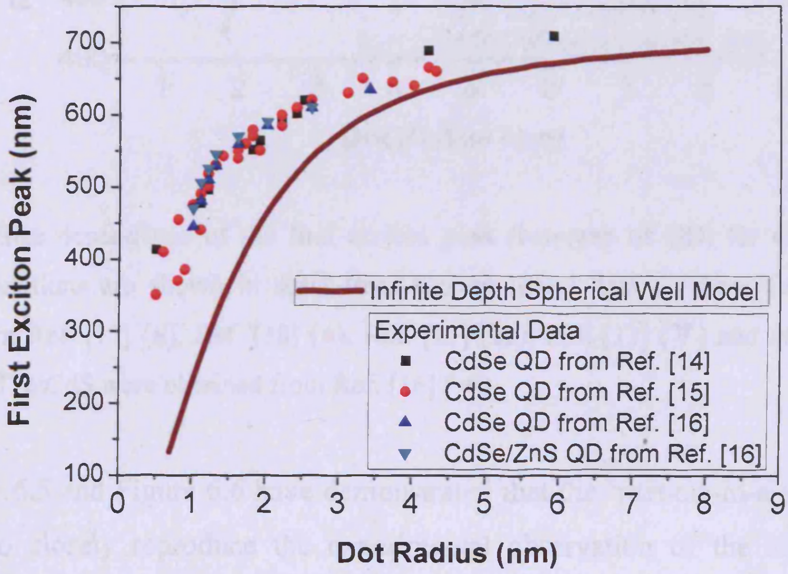

Figure 6.5: Size dependence of the first absorption peak (energy gap of QD) for CdSe QDs. The present theoretical model is shown in solid line. The experimental data for bare CdSe QDs were taken from Ref. [14] (■), Ref. [15] (●), Ref. [16] (▲) and the data for CdSe/ZnS core-shell QDs were taken from Ref. [16] (▼).

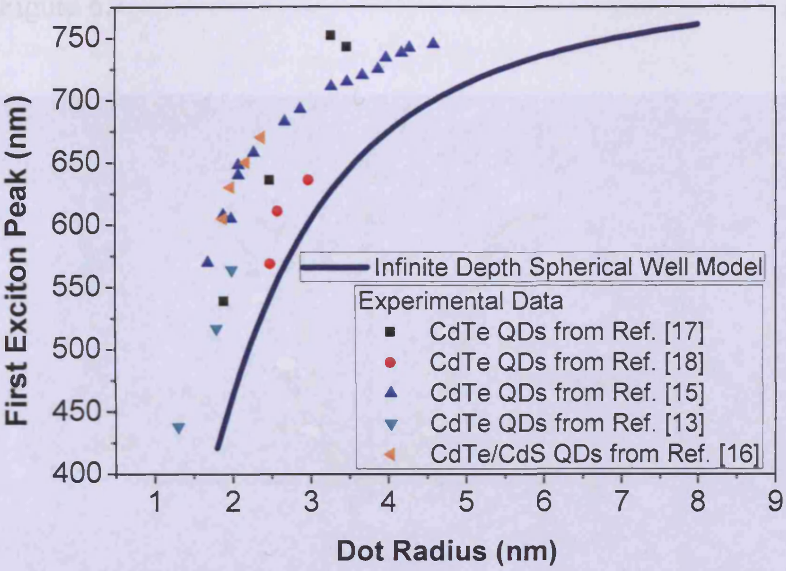

Figure 6.6: Size dependence of the first exciton peak (bandgap of QD) for CdTe QDs. The present calculations are shown in solid line. The empirical data for bare CdTe QDs were obtained from Ref. [17] (■), Ref. [18] (●), Ref. [15] (▲), Ref. [13] (▼) and the experimental values for CdTe/CdS were obtained from Ref. [16] (◀).

Both Figure 6.5 and Figure 6.6 have demonstrated that the 'particle-in-a-sphere' model is unable to closely reproduce the experimental observation of the size dependent exciton energy in semiconductor QDs that are in the form of bare or surface passivated crystallites. Over small radii, the theoretical prediction of the bound state energy is significantly higher than the real energy shift by the size dependent quantum confinement. This can be clearly evident in Figure 6.5 where the calculated absorption peak position at 1 nm of dot radius is approximately twofold the experimental value. The overestimation of the energy shift by the infinite depth model is strongly indicative of the breakdown of the effective mass approximation for small QD radii and the finiteness of the potential barrier at QD-matrix boundary [14, 19]. It is anticipated that the lowest energy states of small QDs at higher k wave vectors will deviate from the simple parabolic band theory. In fact, at higher k vectors, the non-ideal energy dispersion should be less than quadratic. This inherently caused the incoherent mathematical description of the experimental observations that is based on the effective mass approximation. For better elucidation, the parabolic energy dispersion curve extrapolated from $k = 0$ is shown in comparison with the non-ideal energy band structure in Figure 6.7.

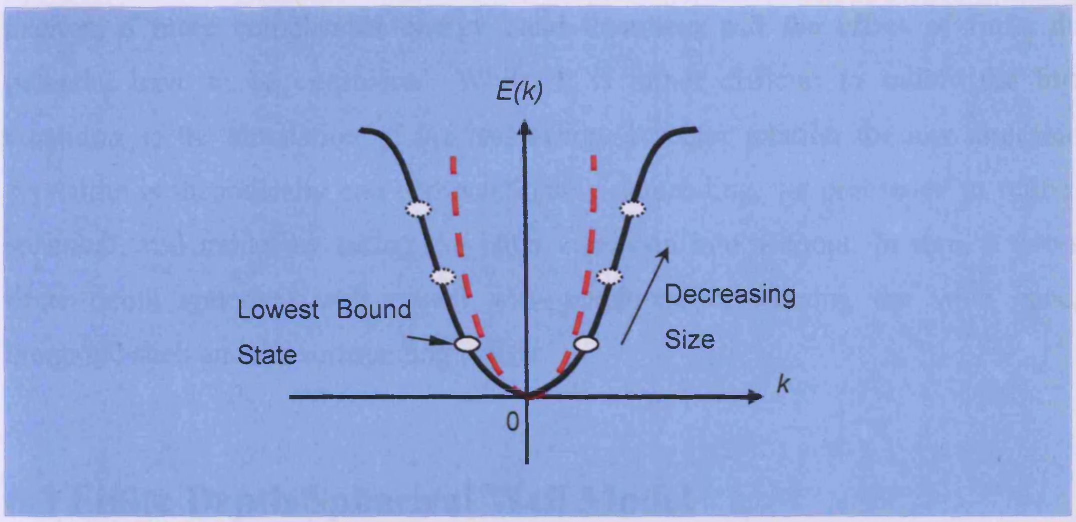

Figure 6.7: Variation of energy with wave vector k for non-ideal (—) and ideal (—) crystallites. The solid circle represents the discrete lowest excited state of QD which is systematically shifted upward at decreasing dot size (shown by dotted circles). The diagram is adapted from [19].

Following Figure 6.7, as QD becomes increasing smaller, the exciton energy progressively departs from the ideal quadratic dependence upon the wave vector. As a result, there will be a marked difference between the calculated and the real energy shifts. Hereby, it shows that the extrapolation of the energy shift that based on the effective mass model only works over a small range of k values that are essentially near the band minimum. This is apparent in Figure 6.6 where, for larger QD radii (where k vector approaches 0), the calculated and the experimental absorption peaks begin to converge.

Besides the non-parabolic energy-k dependence in the real solid, the infinite potential condition that imposed on electron (hole) in solving the Schrödinger equation can also lead to the overestimation of the blue shift of QD bandgap. The matrix surrounding the bare QD or the inorganic shell of passivated QD cannot be treated as the rigid wall in the 'particle-in-a-sphere' model since the band offsets at heterojunctions are not infinite. In the non-ideal finite barriers, the spatial distribution of the electron-hole wavefunctions is allowed outside the QD core. Therein, it is intuitive that the spread of carrier wavefunction over wider space will effectively lower the exciton energy.

To acquire a better mathematical description of the real quantum size effect on QD exciton, a more complicated energy band treatment and the effect of finite depth potential have to be considered. Whilst it is rather difficult to satisfy the former condition as the simulation of the real energy-*k* vector relation for low dimensional crystallite is theoretically and computationally demanding, we proceeded to refine the spherical well model by taking the latter condition into account. In turn, a two-step finite depth spherical well model was developed considering the wide bandgap inorganic shell and the surrounding matrix.

6.3 Finite Depth Spherical Well Model

High quality core-shell QDs with different compositions of core and shell materials i.e. CdSe/ZnS and CdTe/CdS have been successful synthesised since the last decade with the ensemble quantum yield reaching over 50 %, depending on the shell thickness [5, 20]. Therefore, on account of the significant enhancement in the photoluminescence relative to the uncapped QDs, the core-shell QDs are presently marketed as the new class of fluorescent labels for various bio-applications. This enables us to purchase the bio-functionalised core-shell QDs, namely Qdot585-STV and Qdot705-STV, from Invitrogen in order to carry out the pre-emptive FRET studies of QD-fluorophore self-assemblies for the future development of nano-sensing bioassays. In that both Qdot585-STV and Qdot705-STV are capped with wide bandgap ZnS semiconductor, the band offsets at the heterojunction cannot be quantitatively perceived as infinitude. Hereby, we improved the current 'particle-in-a-sphere' model by incorporating finite potentials at core/shell and shell/polymer (or matrix) interfaces into the mathematical treatment of the size dependent quantum confinement effect. Following that, a two-step finite depth spherical well model was established. In this model, the amphiphilic polymer layer is mathematically dismissible since the conduction and valence band offsets at ZnS/polymer interface are literally unfound. The outermost layer can be replaced by any matrix of arbitrary band offsets. The fundamental band lineup of core-shell QD is shown in Figure 6.8.

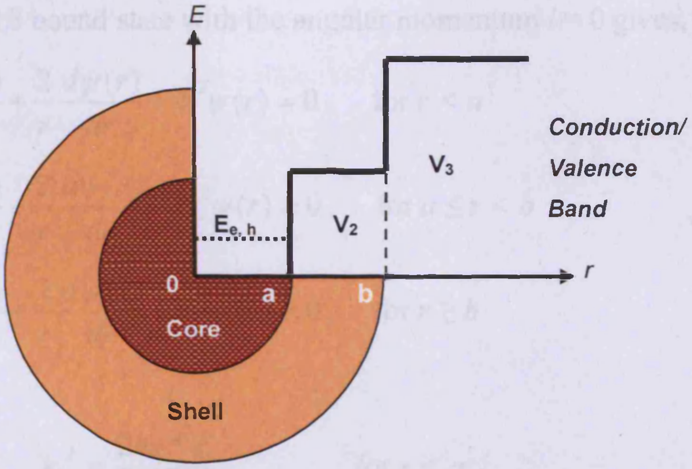

Figure 6.8: Schematic diagram of core-shell QD heterostructure accompanied by the depiction of spherically symmetric potentials, i.e. V_2 and V_3, at core/shell and shell/matrix interfaces and the energy level of spatially bound electron (hole), $E_{e,\,h}$, within the framework of finite depth spherical well model.

To evaluate the size dependent effective bandgap of QD, the generic time independent Schrödinger equation (see Equation 6.4) was employed at the different regions i.e. core, shell and matrix.

For,

$$\begin{aligned}\frac{d^2}{dr^2}(r\psi(r)) &= \frac{d}{dr}\left(r\frac{d}{dr}\psi(r)+\psi(r)\right)\\ &= r\frac{d^2}{dr^2}\psi(r)+2\frac{d}{dr}\psi(r)\end{aligned} \qquad (6.10)$$

Equation 6.4 becomes,

$$-\frac{\hbar^2}{2m^*}\left[r\frac{d^2}{dr^2}+2\frac{d}{dr}\right](\psi(r))+V(r)(r\psi(r))=E(r\psi(r)) \qquad (6.11)$$

The two-step spherical well model is a centro-symmetric barrier system composed of several constant potentials such that,

$$\begin{aligned}&V(r)=0, \quad r<a\\ &V(r)=V_2, \quad a\le r<b\\ &V(r)=V_3, \quad r\ge b\end{aligned} \qquad (6.12)$$

where a, b and c are the distances from the centre of the core.

Hence, rearranging the wave equations at the inner core, the intermediate shell and the outermost matrix for 1S bound state with the angular momentum $l = 0$ gives,

$$\frac{d^2\psi(r)}{dr^2}+\frac{2}{r}\frac{d\psi(r)}{dr}+k_1^{\,2}\psi(r)=0\,, \quad \text{for } r < a \tag{6.13}$$

$$\frac{d^2\psi(r)}{dr^2}+\frac{2}{r}\frac{d\psi(r)}{dr}-k_2^{\,2}\psi(r)=0\,, \quad \text{for } a \le r < b \tag{6.14}$$

$$\frac{d^2\psi(r)}{dr^2}+\frac{2}{r}\frac{d\psi(r)}{dr}-k_3^{\,2}\psi(r)=0\,, \quad \text{for } r \ge b \tag{6.15}$$

with,

$$k_1^{\,2}=\frac{2m_1{}^*E}{\hbar^2}\,, \quad \text{for } r < a \tag{6.16}$$

$$k_2^{\,2}=\frac{2m_2{}^*\left|E-V_2\right|}{\hbar^2}\,, \quad \text{for } a \le r < b \tag{6.17}$$

$$k_3^{\,2}=\frac{2m_3{}^*\left|E-V_3\right|}{\hbar^2}\,, \quad \text{for } r \ge b \tag{6.18}$$

where the subscripts *1*, *2*, *3* denote the core, the shell and the matrix regions and m_1*, m_2*, m_3* are the bulk effective masses of electron (hole).

The solutions of Equation 6.13, 6.14 and 6.15 are the 1S radial wavefunctions that can be expressed in terms of spherical Bessel functions of the first and the third kinds of zeroth order [9, 10, 21].

$$\psi_1(r)=\frac{A\sin(k_1r)}{r}\,, \quad \text{for } r < a \tag{6.19}$$

$$\psi_2(r)=\frac{B\exp(-k_2r)}{r}+\frac{C\exp(k_2r)}{r}\,, \quad \text{for } a \le r < b \tag{6.20}$$

$$\psi_3(r)=\frac{D\exp(-k_3r)}{r}\,, \quad \text{for } r \ge b \tag{6.21}$$

with A, B, C and D as the amplitudes of the wavefunctions. The extra rising exponential term, $\exp(k_2r)$, in $\psi_2(r)$ accounts for the reflection of the forward moving wavefunction due to the discontinuity of the potential energy at $r = b$. This is valid as the exponential rise is bound by the finite width in the region $a \le r < b$. Besides that, $r.\psi(r)$ should approach zero at $r = 0$ if the wavefunction is to be finite everywhere [6]. The condition is satisfied by the sine function in the region $r < a$.

In the conformity with the one dimensional well model, the radial wavefunctions in the spherical well model are also required to satisfy the matching conditions at the interfaces in order to solve for the energy eigenvalue of the lowest excited state. This is done by preserving the continuity of the wavefunction and its derivative at the discontinuity of the potential. Hence, both conditions are contained in the logarithmic derivative with the conservation of probability current intact [6, 10, 22, 23]. The boundary continuity relation is

$$\left.\frac{1}{m_1{}^*\psi_1(r)}\frac{d\psi_1(r)}{dr}\right|_{r\to a}=\left.\frac{1}{m_2{}^*\psi_2(r)}\frac{d\psi_2(r)}{dr}\right|_{r\to a} \tag{6.22}$$

at the core/shell junction with $r = a$. The same expression also applies to the shell/matrix boundary where $r = b$,

$$\left.\frac{1}{m_2{}^*\psi_2(r)}\frac{d\psi_2(r)}{dr}\right|_{r\to b}=\left.\frac{1}{m_3{}^*\psi_3(r)}\frac{d\psi_3(r)}{dr}\right|_{r\to b} \tag{6.23}$$

so that the continuity of wavefunction and its derivative are retained throughout the whole system. Following Equation 6.22 and 6.23, the derivative of the wavefunction for each region is defined as,

$$\left.\frac{d}{dr}\left(\frac{A\sin(k_1r)}{r}\right)\right|_{r\to a}=\left.\frac{A(k_1r\cos(k_1r)-\sin(k_1r))}{r^2}\right|_{r=a} \tag{6.24}$$

$$\left.\frac{d}{dr}\left(\frac{B\exp(-k_2r)}{r}+\frac{C\exp(k_2r)}{r}\right)\right|_{r\to a,\,r\to b}=\left.\begin{matrix}\dfrac{-B(k_2r\exp(-k_2r)+\exp(-k_2r))}{r^2}+\\ \dfrac{C(k_2r\exp(k_2r)-\exp(k_2r))}{r^2}\end{matrix}\right|_{r=a,\,r=b} \tag{6.25}$$

$$\left.\frac{d}{dr}\left(\frac{D\exp(-k_3r)}{r}\right)\right|_{r\to b}=\left.\frac{-D(k_3r\exp(-k_3r)+\exp(-k_3r))}{r^2}\right|_{r=b} \tag{6.26}$$

By the substitution of Equation 6.19, 6.20, 6.24 and 6.25 with the core radius $r = a$, Equation 6.22 takes the form of

$$\frac{A(k_1a\cos(k_1a)-\sin(k_1a))}{m_1{}^*A\sin(k_1a)}=\frac{-B(k_2a\exp(-k_2a)+\exp(-k_2a))+C(k_2a\exp(k_2a)-\exp(k_2a))}{m_2{}^*(B\exp(-k_2a)+C\exp(k_2a))} \tag{6.27}$$

Similarly to Equation 6.23 for the shell/matrix boundary $r = b$, the substitution of Equation 6.20, 6.21, 6.25 and 6.26 results in

$$\frac{-B(k_2 b\exp(-k_2 b)+\exp(-k_2 b))+C(k_2 b\exp(k_2 b)-\exp(k_2 b))}{m_2{}^*(B\exp(-k_2 b)+C\exp(k_2 b))}=\frac{-D(k_3 b\exp(-k_3 b)+\exp(-k_3 b))}{m_3{}^*D\exp(-k_3 b)} \tag{6.28}$$

To solve for the lowest bound state energy, the eigenvalue of the stationary Schrödinger equation must satisfy both conditions set in Equation 6.27 and 6.28. This will require some computational work as the solution to the answer is embedded inside the functions. Hence, the mathematical derivation of $E_{e,h}$ is more rigorous than the former infinite depth model. In the 'particle-in-a-sphere' treatment, the energy shift of electron (hole) can be directly related to the core radius (see Equation 6.8). Conversely, in the present model, the matching conditions have to be satisfied prior to solving for the right eigenvalue, E. As the principle idea for solving the eigenenergy in the two-step spherically square well model has been outlined in an orderly manner, further thorough numeration of E will be dealt in Appendix A.

The improved two-step finite depth model was used to evaluate the size dependent energy shift in CdSe/ZnS and CdTe/ZnS core-shell QDs. It is anticipated that the incomplete confinement by the finiteness of band offset will help to red shift the energy predicted by the infinite depth well model further in the direction towards the experimental values. However, the influence of band bending, strain deformation and alloying on the subject of non-ideal heterojunction were not considered within the modelling of the electronic confinement in QD. We proceeded with the simple abrupt band offsets for ideal flat hetero-boundaries. The material parameters used in the calculations are tabulated in Table 6.2. The lack of real empirical conduction and valance band offsets for CdSe/ZnS and CdTe/ZnS heterostructures has rendered us relying on the theoretical values found in the literature.

QD Material	Effective Masses		Bulk Bandgap (300 K)	Band Offsets	
	m_e^*/m_e	m_h^*/m_e	E_g (eV)	ΔE_c(CdX/ZnS)* (eV)	ΔE_v(CdX/ZnS) (eV)
CdSe[a]	0.13	0.45	1.74	1.46	0.60
CdTe[b]	0.11	0.35	1.56	1.07	1.17
ZnS[c]	0.28	0.49	3.80	0	0
Matrix	1.00	1.00	n/a	n/a	n/a

[a] m_e^*, m_h^* from Ref. [11], E_g from Ref. [12], ΔE_v from Ref. [24].

[b] m_e^*, m_h^* from Ref. [10], E_g from Ref. [13], ΔE_v from Ref. [24].

[c] m_e^*, m_h^* from Ref. [11], E_g from Ref. [12], ΔE_v from Ref. [24].

*$\Delta E_c = E_g(\text{ZnS}) - E_g(\text{CdX}) - \Delta E_v$ [25].

Table 6.2: Material parameters utilised in the computation of the two-step spherical well model.

Because of the absence of pertinent organic material parameters, we assumed free electron and hole outside the core-shell QD as indicated in Table 6.2. Besides that, for the outermost matrix (polymer) layer, the height of potential barrier was assigned to 3.0 eV in both electron and hole cases since the bandgap of insulating material is roughly 7 eV [11] and the real band alignments for the inorganic-organic hybrid structure are largely unclear. Henceforth, with the predetermination of the matrix barrier, the postulated band alignments for CdSe/ZnS and CdTe/ZnS heterostructures are illustrated in Figure 6.9.

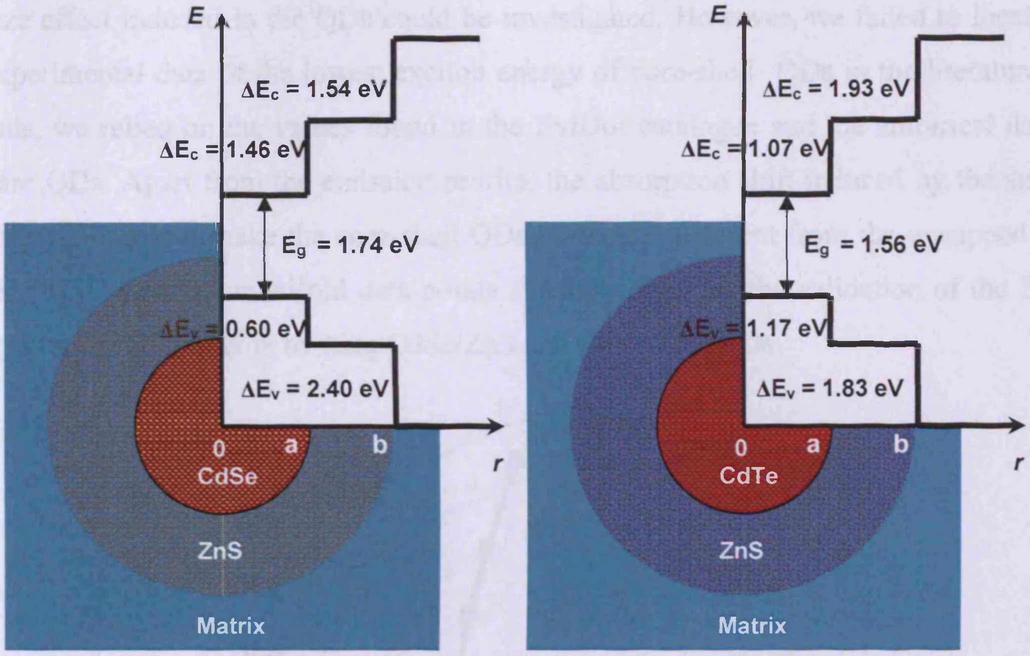

Figure 6.9: Schematic diagrams of CdSe/ZnS and CdTe/ZnS core-shell QD structures superimposed on the conduction and valence band lineups.

Based on the postulated barrier setting in Figure 6.9 and the effective masses compiled in Table 6.2, the energy shifts of electron and hole in response to the variation in the core size can be analysed quantitatively using the two-step finite depth spherical well model while retaining the shell thickness at 5 Å. It is worthy to note that in the computation of E values, the potential in the core was assignable to the zero reference potential energy. Therefore, the energy of electron (hole) in the core was essentially kinetic. With the lowest excited state energies of electron and hole successfully deduced from the finite well model, the effective bandgap (total exciton energy) of QD can be determined by the expression below,

$$E_{eff}(QD) = E_g(bulk) + E_e + E_h \tag{6.29}$$

where E_g is the bulk bandgap of QD core material, E_e and E_h are the energies of electron and hole corresponding to the lowest bound state in the finite spherical well. Out of practical interest, the calculated energy gap of QD was converted to wavelength primarily for direct correlating the absorption band edge with the core radius. The calculated excitonic band edge was later compared with the empirical values acquired from the literature in order that the closeness of the theoretical fit to the real quantum size effect induced in the QDs could be investigated. However, we failed to locate the experimental data of the lowest exciton energy of core-shell QDs in the literature and thus, we relied on the values found in the EviDot catalogue and the empirical data of bare QDs. Apart from the emission profile, the absorption shift induced by the surface capping does not make the core-shell QDs markedly different from the uncapped QDs [5, 20]. Hence, the manifold data points should suffice for the validation of the 2-step spherical well model in treating CdSe/ZnS and CdTe/ZnS QDs.

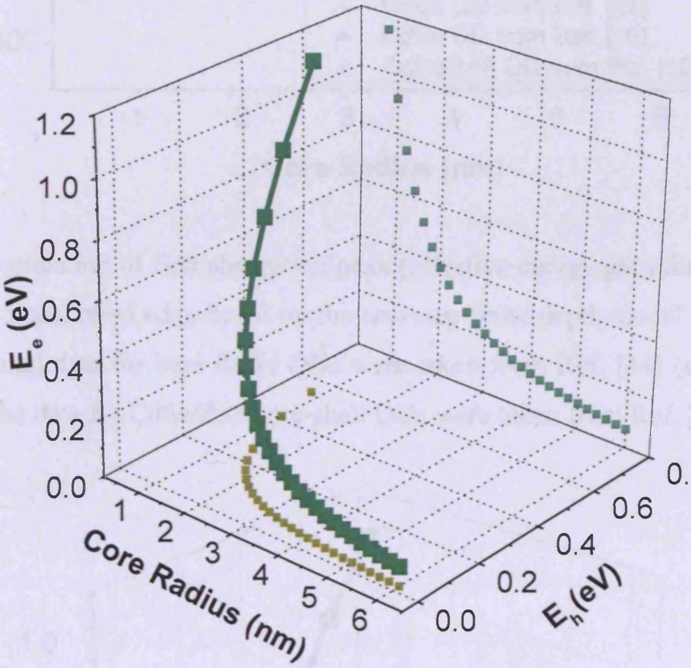

Figure 6.10: Plots of calculated energy eigenvalues of electron and hole i.e. E_e and E_h versus core radius of CdSe/ZnS QD.

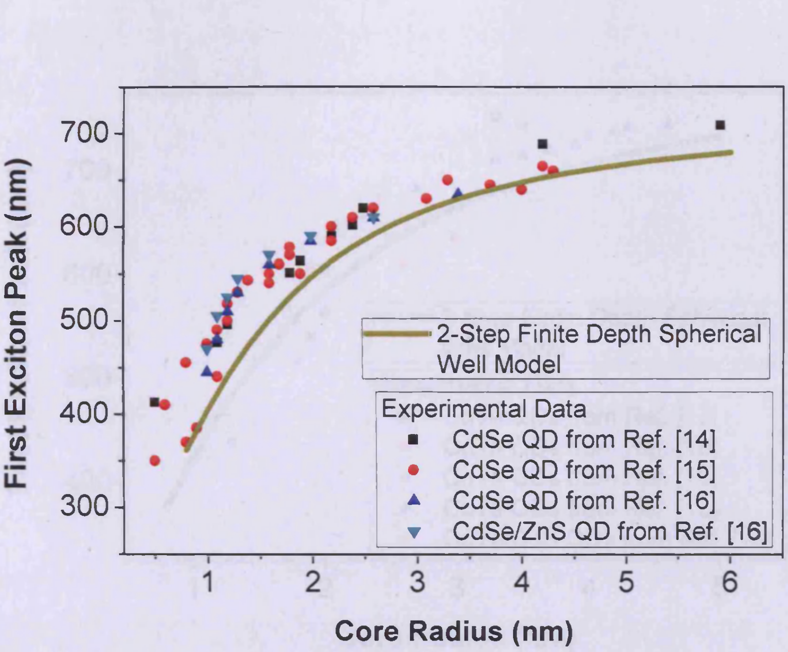

Figure 6.11: Size correlation of first absorption peak (effective energy gap) for CdSe/ZnS core-shell QDs. The predicted band edge based on the two-step finite depth model is shown in solid line. The experimental data for bare CdSe QDs were taken from Ref. [14] (■), Ref. [15] (●), Ref. [16] (▲) and the data for CdSe/ZnS core-shell QDs were taken from Ref. [16] (▼).

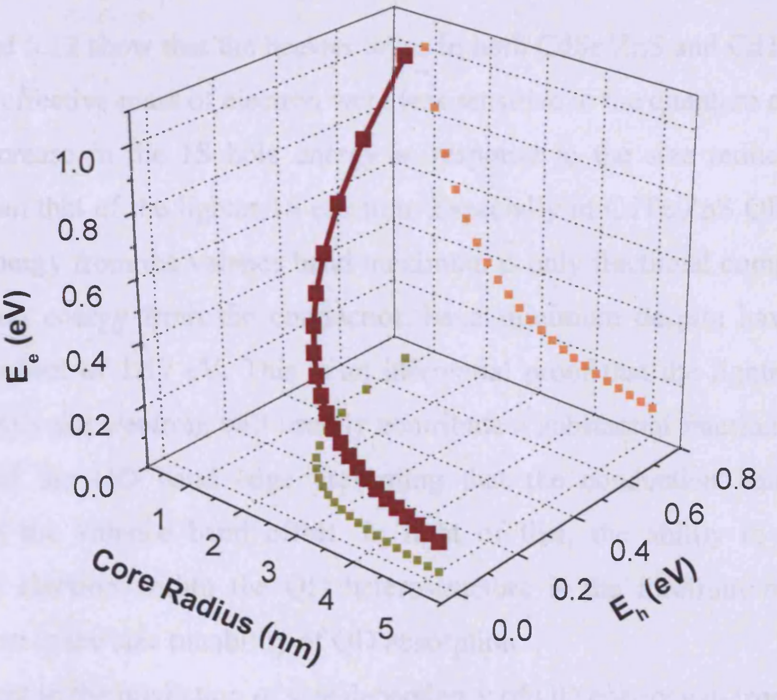

Figure 6.12: Plots of predicted energy shifts of 1S electron and 1S hole i.e. E_e and E_h versus core radius of CdTe/ZnS QD.

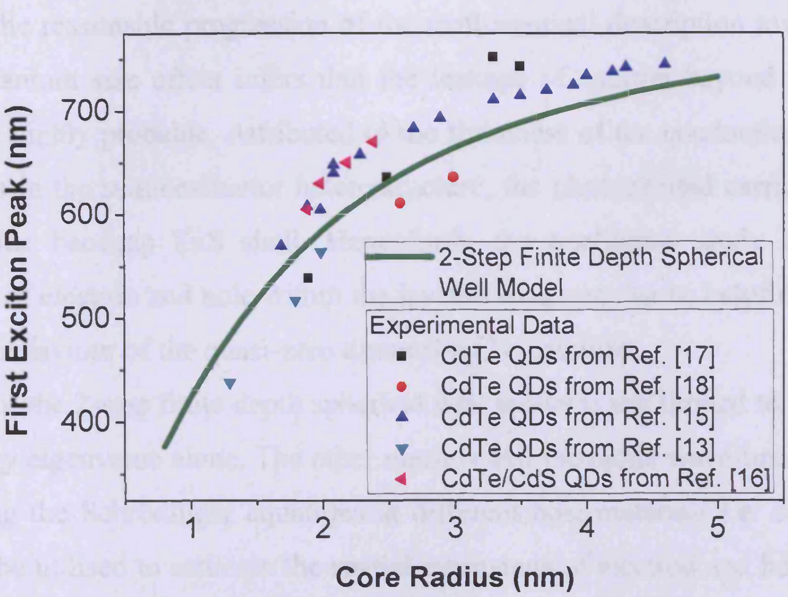

Figure 6.13: Correlation between first absorption peak (bandgap of QD) and core radius for CdTe/ZnS core-shell QDs. The prediction is shown in solid line. The empirical data for bare CdTe QDs were obtained from Ref. [17] (■), Ref. [18] (●), Ref. [15] (▲), Ref. [13] (▼) and the experimental values for CdTe/CdS were obtained from Ref. [16] (◀).

Figure 6.10 and 6.12 show that the heavier holes in both CdSe/ZnS and CdTe/ZnS QDs with threefold effective mass of electron were less sensitive to the quantum confinement effect. The increase in the 1S hole energy in response to the size reduction is less pronounced than that of the lighter 1S electron. Especially in CdTe/ZnS QD where the shift of hole energy from the valence band maximum is only fractional compared to the shift of electron energy from the conduction band minimum despite having greater valence band offset of 1.17 eV. This is an inferential proof that the lighter carrier of exciton, generally the electron, will usually contribute a substantial fraction to the total energy shift of the QD band edge presuming that the conduction band offset is comparable to the valence band offset. In light of that, the ability to control the localisation of electron within the QD heterostructure is the forefront of achieving greater precision in the size tunability of QD absorption.

An improvement in the prediction of size dependency of QD energy gap from the 2-step finite barrier model is apparent in Figure 6.11 and 6.13. Relative to the rigid 'particle-in-a-sphere' model, the blue shift of the absorption band edge predicted by the finite well is concordant with the experimental observations, albeit a close match is yet to be procured. The reasonable progression of the mathematical description towards the real physical quantum size effect infers that the leakage of exciton beyond the core/shell boundary is highly probable. Attributed to the finiteness of the conduction and valence band offsets in the semiconductor heterostructure, the photoexcited carriers can tunnel into the wide bandgap ZnS shell. Henceforth, the qualitative study of the spatial distribution of electron and hole within the layered structure can be helpful in relating to the optical behaviour of the quasi-zero dimensional crystallite.

The utility of the 2-step finite depth spherical well model is not limited to the derivation of the energy eigenvalue alone. The other merit is that the radial wavefunctions deduced from solving the Schrödinger equations at different host materials i.e. core, shell and matrix can be utilised to estimate the spatial extensions of electron and hole outside the core confinement. This is achieved by the normalisation of the probability densities of electron and hole to unity [6].

$$\int_0^\infty \left|\psi_{e,h}\right|^2 dV = 1 \tag{6.30}$$

with dV as the element of volume.

For the spherically symmetric radial function used in the finite well model, the element of volume is the product of the area of the shell, $4\pi r^2$ and its infinitesimal thickness, dr. As a result of that, the integral can be expanded to,

$$\int_0^\infty \left|\psi_{e,h}(r)\right|^2 4\pi r^2 dr = 1 \tag{6.31}$$

$$4\pi\left(\int_0^a \left|\psi_{1e,h}(r)\right|^2 r^2 dr + \int_a^b \left|\psi_{2e,h}(r)\right|^2 r^2 dr + \int_b^\infty \left|\psi_{3e,h}(r)\right|^2 r^2 dr\right) = 1 \tag{6.32}$$

With the above normalisation condition such that the probability density integrated over large distance is unity, we can now deduce the amplitude of the radial wavefunction at the respective region of host material constituting the core-shell QD. The normalised constants have the unit of $m^{-1/2}$. Thereafter, a complete descriptive representation of electron (hole) wavefunction can finally be realised by matching the radial functions at the core/shell and shell/matrix boundaries. The detailed account of the normalisation work can be referred to Appendix A. As the radial probability density function, $r^2.|\psi(r)|^2$ is linked to the spatial distributions of electron-hole wavefunctions, we investigated the influence of the finite potential barriers upon the tunnelling of charge carriers inside the QD.

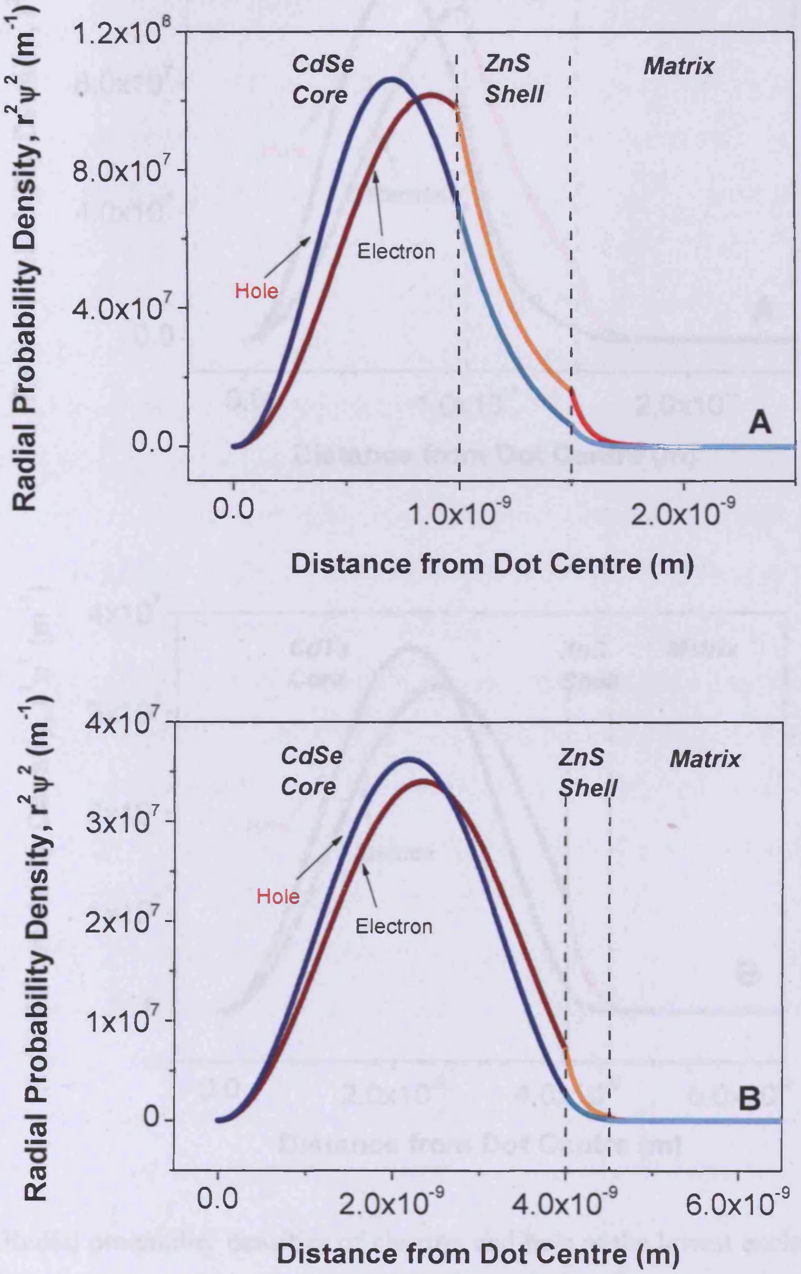

Figure 6.14: Radial probability densities of electron and hole in the lowest excited state plotted as a function of distance from the centre of QD. Diagram A describes the radial probabilities of carriers in CdSe/ZnS QD with a 1 nm core radius and a 0.5 nm shell thickness. Diagram B describes the radial probabilities of carriers in CdSe/ZnS QD with a 4 nm core radius and a 0.5 nm shell thickness.

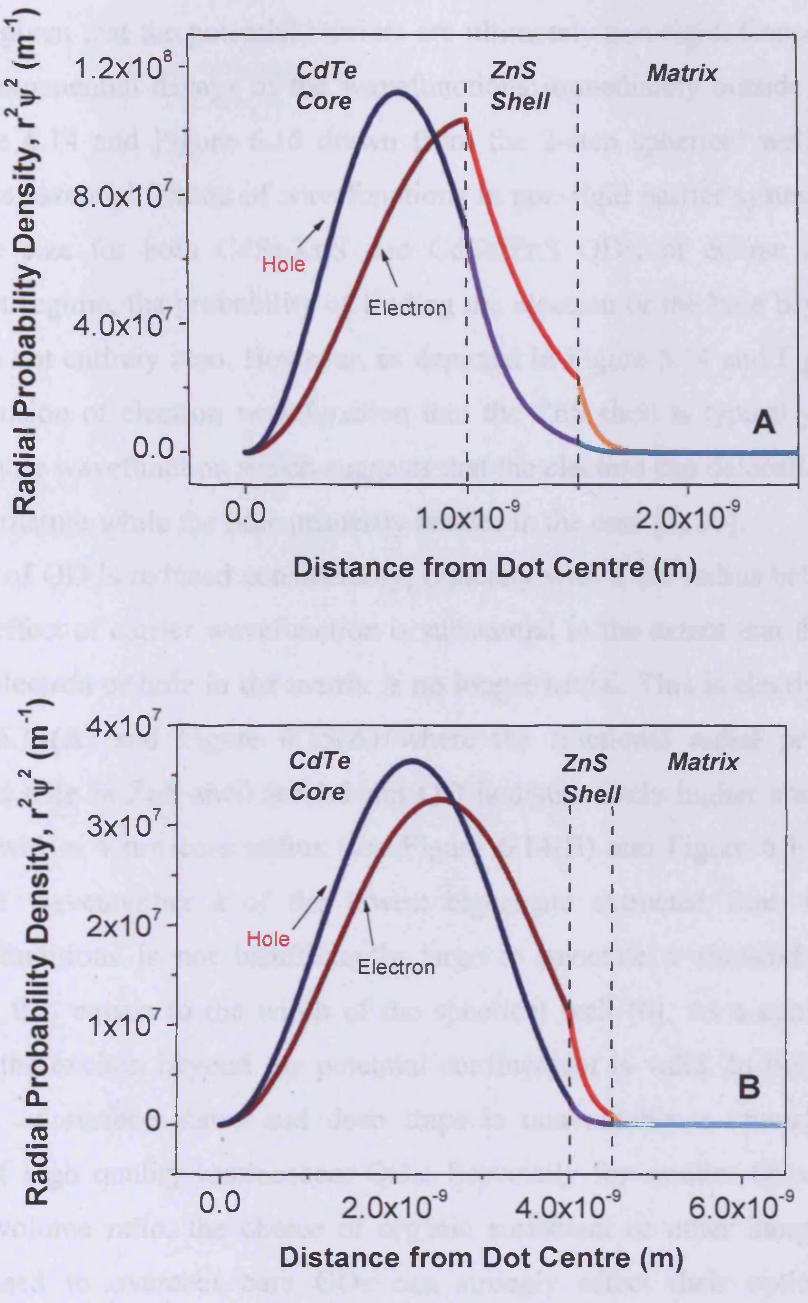

Figure 6.15: Radial probability densities of electron and hole at the lowest excited state plotted against the distance from the centre of QD. Diagram A depicts the radial probabilities of carriers in CdTe/ZnS QD with a 1 nm core radius and a 0.5 nm shell thickness. Diagram B depicts the radial probabilities of carriers in CdTe/ZnS QD with a 4 nm core radius and a 0.5 nm shell thickness.

Infinite band discontinuities do not exist in real semiconductor hetero-system. Likewise in the pseudo-atomic core-shell QD, the wavefunctions of electron and hole cannot be pinned against zero energy level when approaching the core/shell and the shell/matrix boundaries given that the potential barriers are ultimately non-rigid. Consequently, this yields the exponential decays of the wavefunctions immediately outside the potential well. Figure 6.14 and Figure 6.15 drawn from the 2-step spherical well model have revealed this essential feature of wavefunctions in non-rigid barrier system. Regardless of the core size for both CdSe/ZnS and CdTe/ZnS QDs, of course in the strong confinement regime, the probability of finding the electron or the hole beyond the core boundary is not entirely zero. However, as depicted in Figure 6.14 and Figure 6.15, the spatial extension of electron wavefunction into the ZnS shell is typically greater than that of the hole wavefunction which suggests that the electron can delocalise throughout the heterostructure while the hole primarily resides in the core [5, 20].

As the size of QD is reduced considerably, typically with a dot radius below 1 nm, the tunnelling effect of carrier wavefunction is substantial to the extent that the probability of finding electron or hole in the matrix is no longer trivial. This is clearly exemplified in Figure 6.14(A) and Figure 6.15(A) where the fractional radial probabilities of electron and hole in ZnS shell for 1.5 nm QD is distinctively higher compared to the larger QD with a 4 nm core radius (see Figure 6.14(B) and Figure 6.15(B)). This is because the wavenumber k of the lowest eigenstate extracted from the boundary matching conditions is not insufficiently large to generate a sinusoid with a half-wavelength that equals to the width of the spherical well [6]. As a consequence, the leakage of the exciton beyond the potential confinement is valid. In light of that, the suppression of surface states and deep traps is unavoidably a crucial step in the synthesis of high quality luminescent QDs. Especially for smaller QDs with greater surface to volume ratio, the choice of organic surfactant or other inorganic capping materials used to overcoat bare QDs can strongly affect their optical properties particularly the quantum yield [5, 20, 26-28]. To highlight the extent of electron-hole tunnelling, we calculated the fractional probabilities of these charge carriers in the respective regions as the core radius is varied.

Core-Shell QD	Core* Radius (nm)	Fractional Radial Probabilities					
		Core		Shell		Matrix	
		electron	hole	electron	hole	electron	hole
CdSe/ZnS	1.0	0.709	0.812	0.277	0.183	0.014	0.005
	2.0	0.924	0.963	0.074	0.036	0.002	0.001
	3.0	0.970	0.987	0.029	0.012	0.001	0.001
	4.0	0.986	0.994	0.014	0.006	0.000	0.000
CdTe/ZnS	1.0	0.638	0.857	0.342	0.140	0.020	0.003
	2.0	0.883	0.973	0.113	0.026	0.004	0.001
	3.0	0.949	0.991	0.049	0.009	0.002	0.000
	4.0	0.974	0.996	0.026	0.004	0.000	0.000

*Shell thickness is fixed at 0.5 nm.

Table 6.3: Tabulation of fractional radial probabilities of electron and hole in different host materials.

On the basis of 2-step finite spherical well model, further quantitative analysis of the spatial distribution has revealed that the electron and the hole of large QD is mainly confined in the inner core with the radial probabilities above 0.9. By contrast, for smaller QD with a core radius of 1 nm, there are notable fractions of electron-hole in the shell layer which have substantially contributed to the radial probabilities above 0.1 as reported in Table 6.3. Hence, depending on the extent of carrier wavefunctions, QDs are not totally inert to the local environment [29]. The dynamics of QDs may vary when dissolved in different solvents.

As the QD size decreases, the further the spread of electron wavefunction means the weaker the overlap integral of electron and hole in the core. For both the oscillator strength and the radiative decay rate have quadratic dependence on the overlap factor, it is intuitive that the variation of the intrinsic optical characteristics of QD could be mediated by the change in the core size if QD is presumable as an electric dipole. With reference to the mathematically modelled wavefunctions as seen in Figure 6.13 and 6.14, we calculated the fractions of the spatial overlaps of electron-hole at the core and the shell. To calculate the electron-hole overlap integral, the following expression was applied,

$$U = \int \psi_e(r)\psi_h(r)dV \tag{6.33}$$

with $dV = 4\pi r^2 dr$.

For the core radius of CdSe/ZnS and CdTe/ZnS QDs ranging from 1 nm to 4 nm, the relevant spatial overlap of electron and hole in the lowest excited state is numerically noted in Table 6.4 and also graphically represented in Figure 6.15 and 6.16.

Core-Shell QD	Core* Radius (nm)	Electron-Hole Overlap Integral	Fractional Electron-Hole Overlap Integral		
			Core	Shell	Matrix
CdSe/ZnS	1.0	0.987	0.755	0.224	0.001
	2.0	0.989	0.947	0.052	0.001
	3.0	0.993	0.981	0.019	0.000
	4.0	0.995	0.991	0.009	0.000
CdTe/ZnS	1.0	0.952	0.767	0.226	0.007
	2.0	0.965	0.943	0.056	0.001
	3.0	0.975	0.978	0.021	0.001
	4.0	0.982	0.990	0.010	0.000

*Constant shell thickness of 0.5 nm.

Table 6.4: Tabular form of the electron-hole wavefunction overlap and the corresponding fractional overlap in the core, the shell and the matrix.

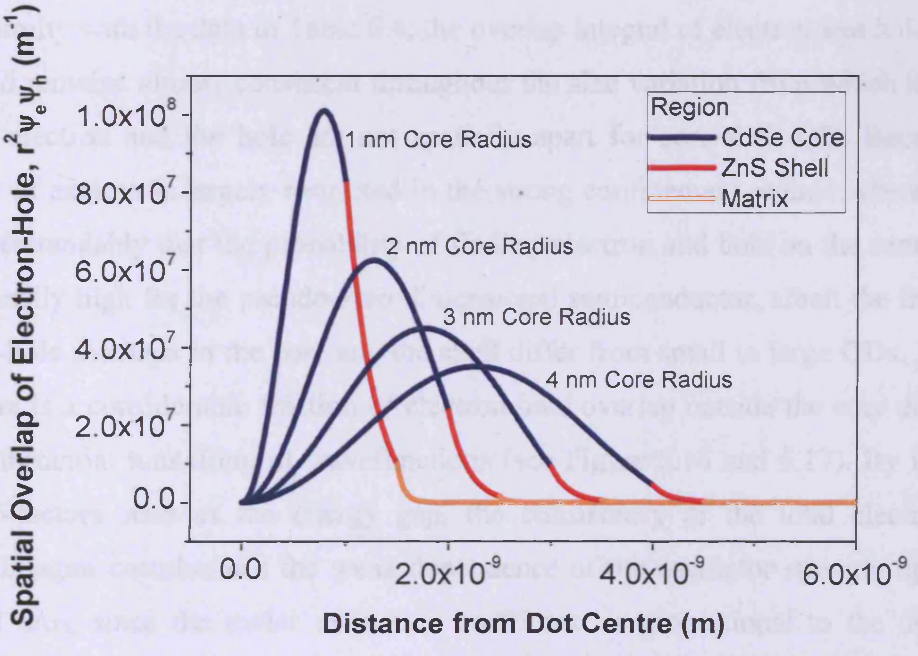

Figure 6.16: Plot of the spatial overlap of the electron-hole wavefunctions against distance for CdSe/ZnS QD with variable core radius. The shell is 0.5 nm thick.

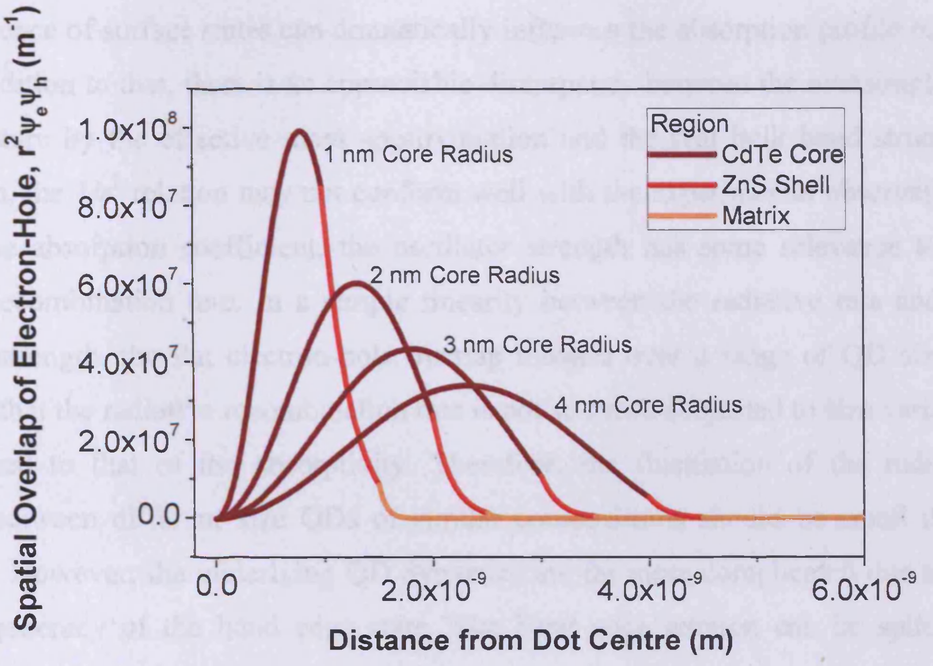

Figure 6.17: Depiction of the spatial overlap of the lowest excited state electron-hole wavefunctions for CdTe/ZnS QD with variable core radius. The shell thickness of 0.5 nm is constant throughout the calculations.

In conformity with the data in Table 6.4, the overlap integral of electron and hole is near unity and remains almost consistent throughout the size variation from which indicates that the electron and the hole are not spatially apart for core-shell QD. Because the mobility of exciton is largely restricted in the strong confinement regime where $r < a_B$, it is understandably that the probability of finding electron and hole on the same site is exceptionally high for the pseudo-zero dimensional semiconductor, albeit the fractional electron-hole overlaps in the core and the shell differ from small to large QDs. In small QD, there is a considerable fraction of electron-hole overlap outside the core attributed to the substantial tunnelling of wavefunctions (see Figure 6.16 and 6.17). By ignoring other co-factors such as the energy gap, the consistency of the total electron-hole overlap integral corroborates the weak dependence of the oscillator strength upon QD size and thus, since the molar extinction coefficient is proportional to the oscillator strength per unit volume, the intensity of band edge absorption should follow a simple $1/r^3$ relation [19]. This elucidates the appearance of discrete band edge feature in the absorption of QD ensemble with decreasing dot size [14]. Nonetheless, the $1/r^3$

dependence of the excitonic absorption peak should be treated as an approximation only as the presence of surface states can dramatically influence the absorption profile of QD [30]. In addition to that, there is an appreciable discrepancy between the oversimplified band structure by the effective mass approximation and the real bulk band structure. Henceforth, the $1/r^3$ relation may not conform well with the experimental observations. Besides the absorption coefficient, the oscillator strength has some relevance to the radiative recombination rate. In a simple linearity between the radiative rate and the oscillator strength, the flat electron-hole overlap integral over a range of QD sizes is indicative that the radiative recombination rate is not so much subjected to size variation as compared to that of the absorptivity. Therefore, the fluctuation of the radiative lifetimes between different size QDs of similar compositions should be small if not negligible. However, the underlying QD dynamics are far more complicated due to the strong degeneracy of the band edge state. The band edge exciton can be split into optically active 'bright' exciton and optically passive 'dark' exciton which contributes to the observation of the long radiative lifetime at low temperatures [31]. This phenomenal behaviour is not supported by the two level system implemented in the 2-step finite spherical well model. Also, the nonradiative component is always present in the fluorescence decay rate since the quantum yield of QD ensemble is rarely 1.0. This invariably obviates the acquisition of convincing time-response data in order to justify the dependence of the radiative rate upon dot size.

6.4 Finite Depth Spherical Well Modelling of Type-II Quantum Dots

Wide bandgap capped QDs like CdSe/ZnS and CdTe/ZnS in the foregoing discussions are customarily classified as type-I QDs with the conduction and valence band extrema centre round the QD core. The kind of band alignments mediates the localisation of carriers in the core, in turn, induces the strong spatial overlap of electron-hole wavefunctions. Whilst we have taken the finite barrier into account, our theoretical model, with reference to the spatial overlap of electron-hole wavefunctions, fails to afford a rational explanation to the unusual long lifetime (over 100 ns) of Qdot705-STV fluorescence that is highly contradictory to the typical radiative lifetimes of bare CdSe and CdTe QDs, reported so far, in the order of 20 ns [32, 33]. This makes us to speculate that there could be alloying at the CdTe/ZnS interface of Qdot705-STV due to the 17 % difference in the bond length between CdTe and ZnS. The interfacial layer sandwiched between CdTe and ZnS could render Qdot705-STV type-II from which band lineups QD has the conduction and valence band extrema at different host materials as illustrated in Figure 6.18 [34].

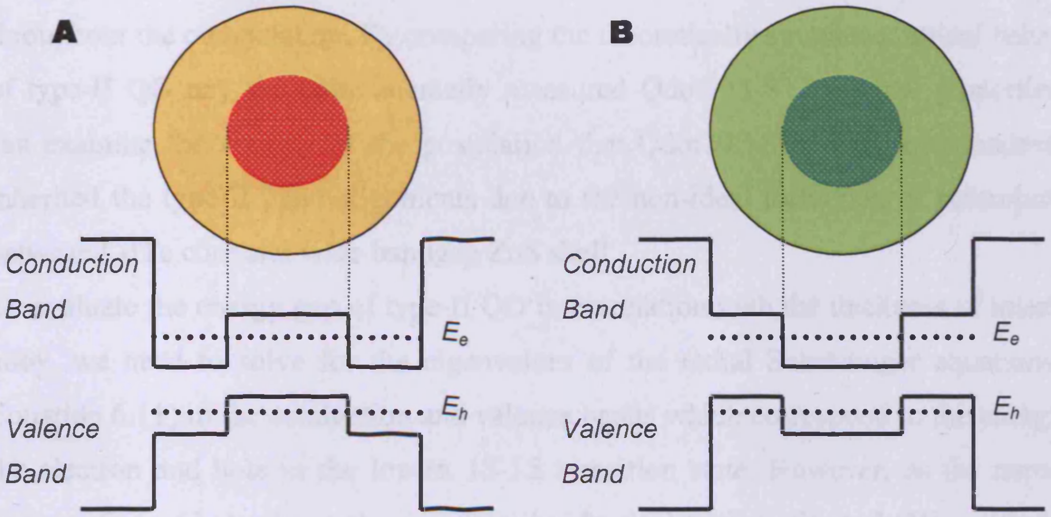

Figure 6.18: Band diagrams of type-II QDs. Diagram A represents the type-II QD with the conduction band minimum at the shell and the valence band maximum at the core. Diagram B represents the type-II QD with the conduction band minimum at the core and the valence band maximum at the shell.

With the kind of band alignments as depicted in Figure 6.18, the carriers can be spatially separated and this reduces the overall overlap of electron-hole wavefunctions. In turn, the decreased electron-hole overlap results in the weak oscillator strength of QD dipole due to its quadratic dependence on the overlap integral. Therein, this accounts for the indecipherable band edge feature in the absorption profile and the reduced radiative rate for the type-II QDs [34, 35]. Seemingly, they conform very well with what we have observed in Qdot705-STV. Qdot705-STV does not have the structured absorption lineshape and the fast exciton recombination rate close to that of Qdot585-STV, irrespective of the difference in the core composition. Henceforth, based on the type-II conception, we incorporated the band lineups similar to Figure 6.18(A) into the 2-step finite depth spherical well model. Using the modified 2-step finite depth spherical well model, we explored the possibility of type-II band structure in Qdot705-STV, even though it should be ideally type-I QD. The tunable trait in the emission/absorption of type-II QDs is not only highly influenced by the core radius but also the shell thickness [35]. Therefore, in the context of type-II potential confinement (see Figure 6.18(A)), we simulated the trend in the effective bandgap of QD and the overlap integral of electron-hole wavefunctions for a range of shell thickness using the 2-step finite depth spherical well model. It is important to address that the core radius was set at a constant value throughout the computation. By comparing the theoretically simulated optical behaviour of type-II QD and the experimentally measured Qdot705-STV optical properties, we can examine the validity of the postulation that Qdot705-STV may have undesirably inherited the type-II band alignments due to the non-ideal formation of heterojunction between CdTe core and wide bandgap ZnS shell.

To evaluate the energy gap of type-II QD in correlation with the thickness of interfacial alloy, we need to solve for the eigenvalues of the radial Schrödinger equations (see Equation 6.11) in the conduction and valence bands which correspond to the energies of the electron and hole in the lowest 1S-1S transition state. However, as the numerical computation of hole eigenvalue is primarily identical to that of type-I QD as previously dealt in Section 6.2, we emphasise on the derivation of energy eigenvalue of electron alone. Prior to the quantitative analysis of radial wave equation, the potential in the conduction band of the centro-symmetric multi-layer system is first defined as follows,

$$\begin{aligned} &V(r) = V_1, \quad \text{for } r < a \\ &V(r) = 0, \quad \text{for } a \leq r < b \\ &V(r) = V_3, \quad \text{for } r \geq b \end{aligned} \tag{6.34}$$

with a, b and c are the distances from the centre of the dot. Unlike type-I QD modelling, the potential in the intermediate shell is used as the zero reference potential. Since the number of layers in the 2-step finite well model is restricted, the ZnS shell has to be extended to the third layer that was previously ascribed to the matrix in order to incorporate the alloy layer, thereby, neglecting the confinement effect exerted by the matrix potential. In other words, this also implies that the ZnS shell at the outermost layer of the mathematical model will be infinitely thick. This compromise does not inflict too much complication on the simulation of type-II behaviour in Qdot705-STV as the spatial extension of electron-hole wavefunctions beyond alloy/ZnS boundary is trivial for large QD like Qdot705-STV. The depiction of 2-step spherical well model in the association with type-II QD is shown in Figure 6.19.

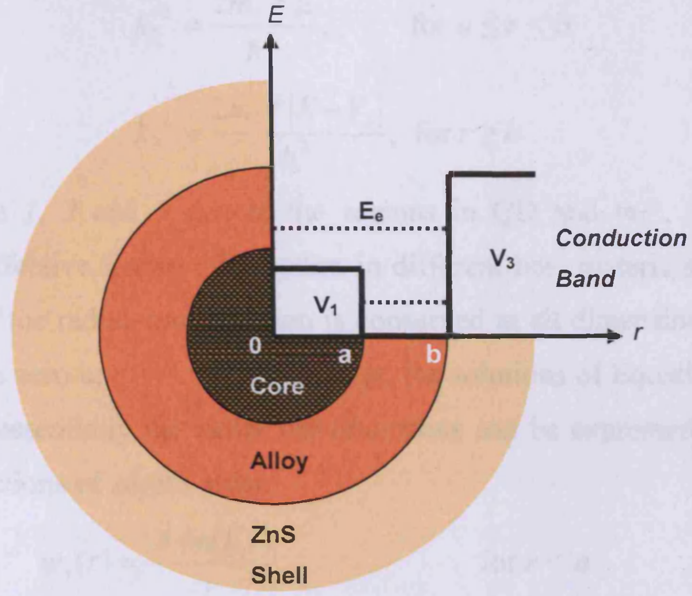

Figure 6.19: Sketch of type-II QD cross-section in concert with the finite potential steps, i.e. V_1 and V_3, at the respective conduction heterojunctions utilised in the calculation of 1S electron energy eigenvalue, E_e.

In finding the right solution for the stationary Schrödinger equation at each region, the extent of the energy shift in response to the thickness of the alloy layer has to be identified first. The lowest state of electron wavefunction can either lie above the core potential or bound inside the spherical well sandwiched between the core and the ZnS shell. Henceforth, the analysis is divided into two categories depending on whether $E > V_1$ or $E < V_1$.

If $E > V_1$, the radial Schrödinger equations in the core, the intermediate alloy and the outermost ZnS shell for 1S electronic state with the angular momentum $l = 0$ become,

$$\frac{d^2\psi(r)}{dr^2} + \frac{2}{r}\frac{d\psi(r)}{dr} + k_1^{\,2}\psi(r) = 0\,, \quad \text{for } r < a \tag{6.35}$$

$$\frac{d^2\psi(r)}{dr^2} + \frac{2}{r}\frac{d\psi(r)}{dr} + k_2^{\,2}\psi(r) = 0\,, \quad \text{for } a \le r < b \tag{6.36}$$

$$\frac{d^2\psi(r)}{dr^2} + \frac{2}{r}\frac{d\psi(r)}{dr} - k_3^{\,2}\psi(r) = 0\,, \quad \text{for } r \ge b \tag{6.37}$$

with

$$k_1^2 = \frac{2m_1^* |E - V_1|}{\hbar^2}, \quad \text{for } r < a \tag{6.38}$$

$$k_2^2 = \frac{2m_2^* E}{\hbar^2}, \quad \text{for } a \leq r < b \tag{6.39}$$

$$k_3^2 = \frac{2m_3^* |E - V_3|}{\hbar^2}, \quad \text{for } r \geq b \tag{6.40}$$

where the subscripts *1*, *2* and *3* denote the regions in QD and m_1*, m_2* and m_3* represent the bulk effective masses of electron in different host materials. It is crucial that the finiteness of the radial wavefunction is conserved in all dimensions and hence, $r.\psi(r)$ must approach zero at $r = 0$. Following that, the solutions of Equation 6.35, 6.36 and 6.37 which are essentially the radial wavefunctions can be expressed explicitly as spherical Bessel functions of zeroth order,

$$\psi_1(r) = \frac{A\sin(k_1 r)}{r}, \quad \text{for } r < a \tag{6.41}$$

$$\psi_2(r) = \frac{B\sin(k_2 r)}{r} + \frac{C\cos(k_2 r)}{r}, \quad \text{for } a \leq r < b \tag{6.42}$$

$$\psi_3(r) = \frac{D\exp(-k_3 r)}{r}, \quad \text{for } r \geq b \tag{6.43}$$

where A, B, C and D are the amplitudes of wavefunctions. Since $E > V_1$, the radial wavefunctions in the core and the alloy regions must be sinusoidal as shown in Equation 6.41 and 6.42. However, in contrast with the single odd solution in the core region, the wavefunction for $a \leq r < b$ is composed of odd and even solutions as it is not subjected to the condition $r.\psi(0) = 0$. Therefore, besides the sine term, the radial wavefunction in the intermediate layer may also include the additional cosine term. As for the outermost ZnS region where $E < V_3$, the tunnelling of electron can be represented by the exponential decay term in Equation 6.43. It should be highlighted that all deduced radial wavefunctions in Equation 6.41, 6.42 and 6.43 are only valid if $E > V_1$.

For $E < V_1$, alternative solutions are necessary to solve the time independent radial Schrödinger equations as defined below,

$$\frac{d^2\psi(r)}{dr^2} + \frac{2}{r}\frac{d\psi(r)}{dr} - k_1^2\psi(r) = 0, \quad \text{for } r < a \tag{6.44}$$

$$\frac{d^2\psi(r)}{dr^2}+\frac{2}{r}\frac{d\psi(r)}{dr}+k_2{}^2\psi(r)=0\,,\ \text{for } a\leq r<b \tag{6.45}$$

$$\frac{d^2\psi(r)}{dr^2}+\frac{2}{r}\frac{d\psi(r)}{dr}-k_3{}^2\psi(r)=0\,,\ \text{for } r\geq b \tag{6.46}$$

with

$$k_1{}^2=\frac{2m_1{}^*\left|E-V_1\right|}{\hbar^2}\,,\ \text{for } r<a \tag{6.47}$$

$$k_2{}^2=\frac{2m_2{}^*E}{\hbar^2}\,,\qquad \text{for } a\leq r<b \tag{6.48}$$

$$k_3{}^2=\frac{2m_3{}^*\left|E-V_3\right|}{\hbar^2}\,,\ \text{for } r\geq b \tag{6.49}$$

where the subscripts *1*, *2* and *3* denote the distinct regions in QD and $m_1{}^*$, $m_2{}^*$ and $m_3{}^*$ stand for the effective masses of electron at different host materials. The solutions of Equation 6.44, 6.45 and 6.46 can again be expressed in terms of spherical Bessel functions of zeroth order. However, the 1S radial wavefunction in the core region is not as straightforward as previously assumed. Since $E < V_1$, the core wavefunction is no longer sinusoidal. Instead, it should decay away from the well towards the origin. Due to the abrupt potential step at $r = a$, besides the forward propagating transmission, we have to consider the reflection of the incident wave back into the core. Thus, the final outcome of the radial wavefunction in the core will include both the exponential decrease and the exponential increase terms. The anticipated wavefunction for $r < a$ may take the form as follows,

$$\psi_1(r)=\frac{A\exp(k_1r)}{r}+\frac{A^*\exp(-k_1r)}{r}\,,\ \text{for } r<a \tag{6.50}$$

where A and A^* are the coefficients of the exponential terms. The rising exponential is valid as long as it is bound by the finite core radius.

But, given that

$$r\psi_1(0)=0$$

$$A\exp(0)+A^*\exp(0)=0 \tag{6.51}$$

$$A=-A^*$$

Equation 6.50 reduces to,

$$\begin{aligned}\psi_1(r) &= \frac{A\exp(k_1 r)}{r} - \frac{A\exp(-k_1 r)}{r} \\ &= A\left(\frac{\exp(k_1 r)}{r} - \frac{\exp(-k_1 r)}{r}\right), \text{ for } r < a \\ &= A\left(\frac{\sinh(k_1 r)}{r}\right)\end{aligned} \tag{6.52}$$

with the factor 2 being absorbed into the last coefficient A.

With the radial wavefunction successfully derived for the core region, the remaining solutions of the Schrödinger equations in the intermediate alloy layer and the outermost ZnS shell are,

$$\psi_2(r) = \frac{B\sin(k_2 r)}{r} + \frac{C\cos(k_2 r)}{r}, \quad \text{for } a \le r < b \tag{6.53}$$

$$\psi_3(r) = \frac{D\exp(-k_3 r)}{r}, \quad \text{for } r \ge b \tag{6.54}$$

with B, C and D being the amplitudes of wavefunctions. As shown above, the wavefunctions described by Equation 6.53 and 6.54 are no different from Equation 6.42 and 6.43 for $E > V_1$. This is because, for $E < V_1$, the assumed lowest state energy of electron remains above the zero potential level in the $a \le r < b$ regime and below the potential step in the $r \ge b$ regime. Hereby, irrespective of $E > V_1$ or $E < V_1$, the solutions in the intermediate and the outermost layers will take the same form. All characterised electron-hole radial wavefunctions in three distinct regions are summarised in Table 6.5 for reference.

Charged Carrier	Lowest State Energy	Regions		
		r < a	a ≤ r < b	r ≥ b
Electron	E > V$_1$	$\psi_1(r) = \frac{A\sin(k_1 r)}{r}$	$\psi_2(r) = \frac{B\sin(k_2 r)}{r} + \frac{C\cos(k_2 r)}{r}$	$\psi_3(r) = \frac{D\exp(-k_3 r)}{r}$
	E < V$_1$	$\psi_1(r) = \frac{A\sinh(k_1 r)}{r}$	$\psi_2(r) = \frac{B\sin(k_2 r)}{r} + \frac{C\cos(k_2 r)}{r}$	$\psi_3(r) = \frac{D\exp(-k_3 r)}{r}$
Hole	n/a	$\psi_1(r) = \frac{A\sin(k_1 r)}{r}$	$\psi_2(r) = \frac{B\exp(-k_2 r)}{r} + \frac{C\exp(k_2 r)}{r}$	$\psi_3(r) = \frac{D\exp(-k_3 r)}{r}$

Table 6.5: Electron and hole radial wavefunctions in three distinct regions.

In analogy with the one dimensional finite well problem, the eigenvalue of the lowest state energy can be resolved by satisfying the matching conditions at the boundaries $r = a$ and $r = b$. In turn, the continuity of wavefunction and its derivative at potential discontinuity must be preserved. This can be achieved by simultaneously solving the logarithmic derivative weighted for the carrier effective masses at $r = a$ and $r = b$ boundaries [10].

$$\left.\frac{1}{m_1{}^*\psi_1(r)}\frac{d\psi_1(r)}{dr}\right|_{r\to a} = \left.\frac{1}{m_2{}^*\psi_2(r)}\frac{d\psi_2(r)}{dr}\right|_{r\to a}, \text{ for } r = a \qquad (6.55)$$

$$\left.\frac{1}{m_2{}^*\psi_2(r)}\frac{d\psi_2(r)}{dr}\right|_{r\to b} = \left.\frac{1}{m_3{}^*\psi_3(r)}\frac{d\psi_3(r)}{dr}\right|_{r\to b}, \text{ for } r = b \qquad (6.56)$$

The conservation of probability current has been taken into account by the above continuity expressions [23]. Again, I only outline the principal steps in the procurement of the eigenvalue E of the lowest excited state as regards the electron alone.

For $E > V_1$, the derivatives of electron wavefunctions with respect to the distance in separate media are

$$\frac{d\psi_1(r)}{dr} = \frac{A(k_1 r\cos(k_1 r) - \sin(k_1 r))}{r^2}, \qquad \text{for } r < a \qquad (6.57)$$

$$\frac{d\psi_2(r)}{dr} = \frac{B(k_2 r\cos(k_2 r) - \sin(k_2 r))}{r^2} - \frac{C(k_2 r\sin(k_2 r) + \cos(k_2 r))}{r^2}, \text{ for } a \le r < b \qquad (6.58)$$

$$\frac{d\psi_3(r)}{dr} = \frac{-D(k_3 r\exp(-k_3 r) + \exp(-k_3 r))}{r^2}, \qquad \text{for } r \ge b \qquad (6.59)$$

Conversely, for $E < V_1$, the derivatives of the radial wavefunctions with respect to the distance in three distinct regions are

$$\frac{d\psi_1(r)}{dr} = \frac{A(k_1 r\cosh(k_1 r) - \sinh(k_1 r))}{r^2}, \qquad \text{for } r < a \qquad (6.60)$$

$$\frac{d\psi_2(r)}{dr} = \frac{B(k_2 r\cos(k_2 r) - \sin(k_2 r))}{r^2} - \frac{C(k_2 r\sin(k_2 r) + \cos(k_2 r))}{r^2}, \text{ for } a \le r < b \qquad (6.61)$$

$$\frac{d\psi_3(r)}{dr} = \frac{-D(k_3 r\exp(-k_3 r) + \exp(-k_3 r))}{r^2}, \qquad \text{for } r \ge b \qquad (6.62)$$

By substituting the correct derivatives into Equation 6.55 and 6.56 and sequentially followed by some rearrangements, the energies of electron in the lowest bound states for $E > V_1$ and $E < V_1$ can be explicitly determined. As the fundamental idea of solving for the electron energy eigenvalue on the basis of 2-step finite depth spherical well model is concisely presented, further details of the derivation will be dealt in Appendix B and Appendix C. With the complete set of radial wavefunctions, the energy shifts of electron and hole i.e. E_e and E_h depending on the thickness of interfacial alloy can be predicted from which we estimate the effective bandgap of type-II QD based on the expression

$$E_{eff}(QD) = E_g(bulk) + E_e + E_h \tag{6.63}$$

where E_g is the bulk bandgap of core material and E_e, E_h are the energy eigenvalues of 1S electron and 1S hole acquired from the calculations. To perform the mathematical simulation of the speculated type-II behaviour in Qdot705-STV, the material parameters for CdTe and ZnS as supplied in Table 6.6 are incorporated in the modified 2-step finite depth spherical well model. Since the notion of the intermediate alloy layer is purely conjectural without the basis of real crystallographic information, the material parameters of the alloy are fabricated to ensure the smooth execution of computational type-II QD modelling.

QD Material	Effective Masses		Bulk Bandgap (300 K)	Band Offsets	
	m_e^*/m_e	m_h^*/m_e	E_g (eV)	ΔE_c(CdX/ZnS)* (eV)	ΔE_v(CdX/ZnS) (eV)
CdTe[a]	0.11	0.35	1.56	1.07	1.17
ZnS[b]	0.28	0.49	3.80	0	0
Alloy	0.10	0.40	n/a	n/a	n/a

[a] m_e^*, m_h^* from Ref. [10], E_g from Ref. [13], ΔE_v from Ref. [24].

[b] m_e^*, m_h^* from Ref. [11], E_g from Ref. [12], ΔE_v from Ref. [24].

*$\Delta E_c = E_g(ZnS) - E_g(CdX) - \Delta E_v$ [25].

Table 6.6: Tabular record of the material parameters in the computation of E_e and E_h using the 2-step finite depth spherical well model.

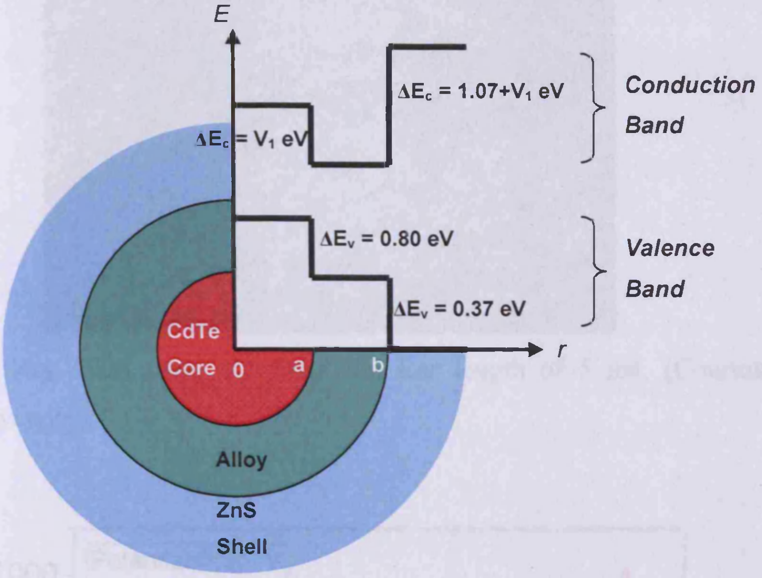

Figure 6.20: Sketch of the postulated conduction and valence band alignments and the cross-section of type-II core-shell QD resembling Qdot705-STV structure with the exception of the intermediate alloy layer.

As exemplified in Figure 6.20, the conduction band offsets at CdTe/alloy and alloy/ZnS heterojunctions were treated as the variable parameters while the valence band offsets were predominantly fixed. By adjusting the conduction band offsets, in essence the depth of well, we are able to control the spatial distribution of electron wavefunction. On the contrary, the hole wavefunction is largely confined in the core. In the mathematical modelling, several combinations of conduction band offsets and alloy thicknesses were adopted. Henceforth, our objectives of the finite spherical well computation encompass the investigations of the effective bandgap of type-II QD and the spatial overlap of electron-hole wavefunctions at variable conduction band offsets and alloy thickness in effort to provide a logical explanation to the long lived Qdot705-STV fluorescence. Regardless of the shape anisotropy of Qdot705, the spatial confinement of electron-hole is expected to be more profound along the minor axis of the crystallite as justified by the comparison between Figure 2.15 and Figure 2.16. Therefore, in the type-II QD modelling, the central core radius was kept at 2 nm despite the fact that Qdot705 nanoparticles are generally elongated in shape with a ~5 nm radius along the major axis as shown in Figure 6.21.

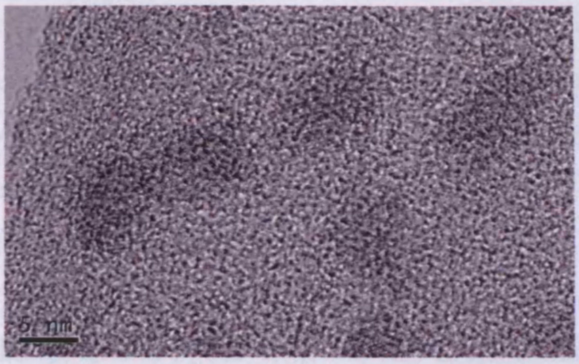

Figure 6.21: Exemplary TEM image of Qdot705. Bar length of 5 nm. (Courtesy of Chris Cooper, Purdue University)

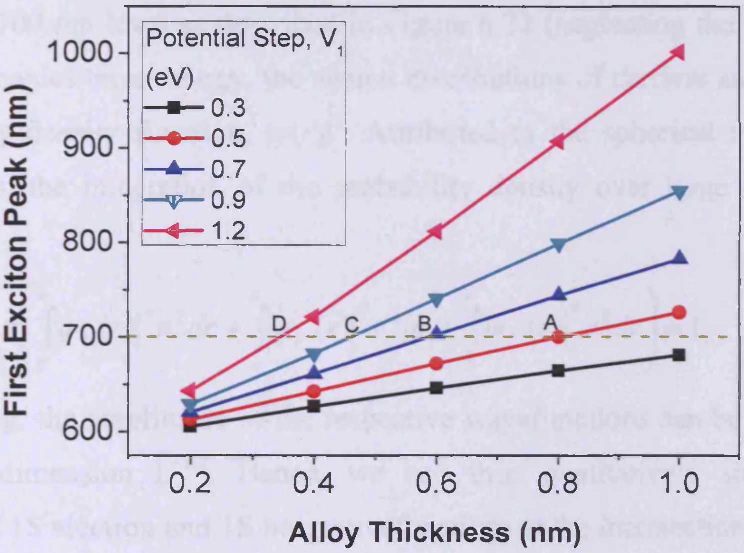

Figure 6.22: First exciton peak of type-II QD with increasing thickness of interfacial alloy. A, B, C, and D are points of intersection with 700 nm dashed line.

As highlighted in Figure 6.22, the band edge absorption of type-II core-shell QD can red shift to longer wavelengths with increasing thickness of the alloy shell, even though the inner core radius remains constant. In a systematic broadening of the shell thickness (essentially the width of the well) from 0.2 nm to 1.0 nm, the energy eigenvalue of electron began to decline from $E > V_1$ to $E < V_1$ while no pronounced change in the hole energy. This can be rationalised by the understanding that the spatial extension of the electron wavefunction can be elevated with the increased well width in the conduction band and the hole wavefunction is remotely affected due to the considerable potential confinement. As a result, the progressive reduction in the energy of 1S electron will imperatively decrease the overall bandgap of type-II core-shell QD which accounts for the red shift in the absorption [36]. The inherent dependence of the bandgap on the shell thickness makes type-II QD very distinctive from the conventional type-I core-shell QD like CdSe/ZnS. Nevertheless, the proportionality of type-II QD energy gap with the shell thickness is highly influenced by the conduction band offset at core/shell heterojunction i.e. V_1 in this case. The greater the potential step V_1, the steeper the slope is. This is understandable, as analogous with the one dimensional box model, that the energy shift of electron wavefunction can increase by the escalation of the barrier height. Since Qdot705-STV emits at ~700 nm, we restricted our analysis to the spatial distribution of electron-hole at the points of intersection between the predicted exciton peak and the 700 nm level as described in Figure 6.22 (neglecting the Stokes shift). In quantum mechanics terminology, the spatial distributions of carriers are determined by the probability density function, $|\psi(r)|^2$. Attributed to the spherical symmetry of the wavefunctions, the integration of the probability density over large distance can be written as

$$4\pi\left(\int_0^a|\psi_1(r)|^2r^2dr+\int_a^b|\psi_2(r)|^2r^2dr+\int_b^\infty|\psi_3(r)|^2r^2dr\right)=1 \tag{6.64}$$

By normalising, the amplitudes of the respective wavefunctions can be determined and they are of dimension $L^{-1/2}$. Hence, we can then qualitatively study the spatial distribution of 1S electron and 1S hole wavefunctions at the intersections A, B, C and D (refer to Figure 6.22).

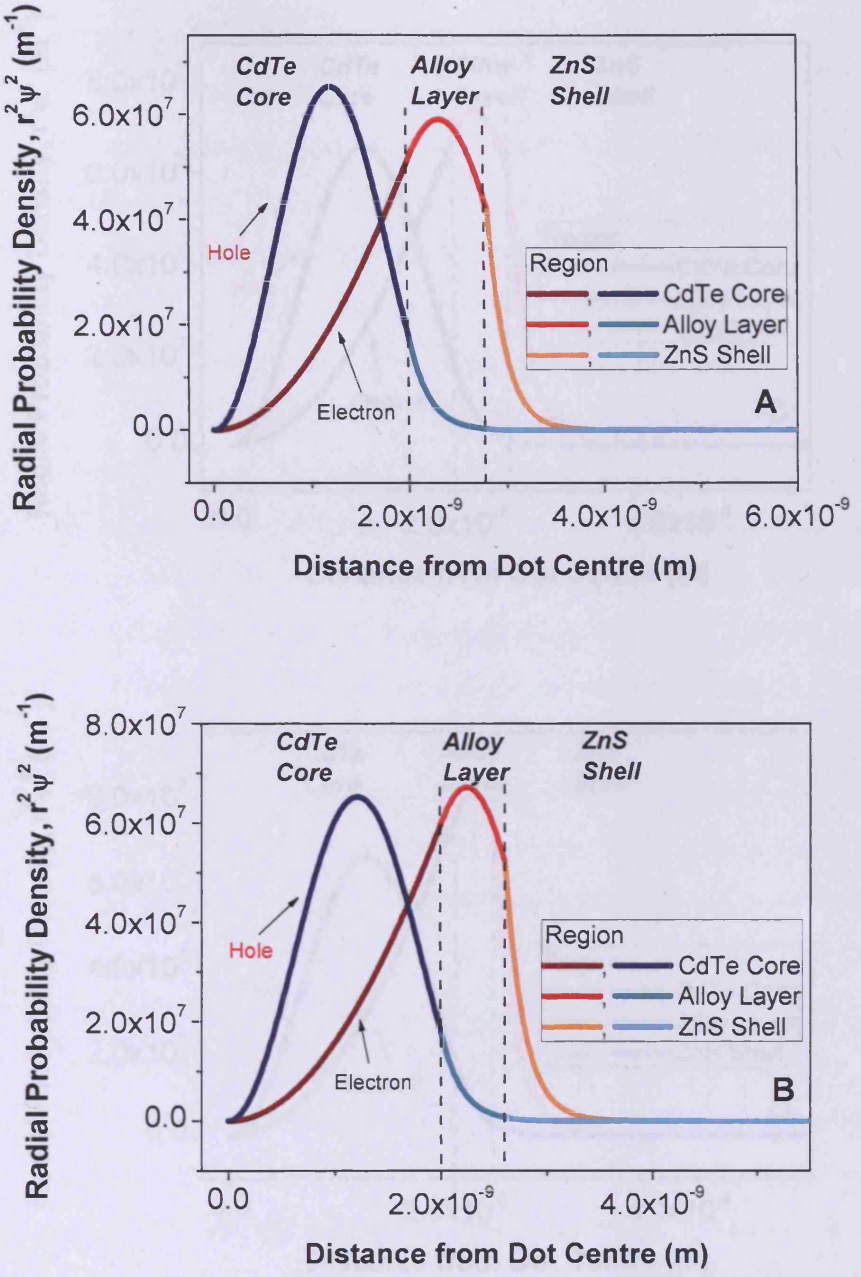
Radial Probability Density, $r^2\psi^2$ (m^{-1})
CdTe Core
Alloy Layer
ZnS Shell
$6.0x10^7$
$4.0x10^7$
$2.0x10^7$
0.0
Hole
Electron
Region
CdTe Core
Alloy Layer
ZnS Shell
A
0.0
$2.0x10^{-9}$
$4.0x10^{-9}$
$6.0x10^{-9}$
Distance from Dot Centre (m)
Radial Probability Density, $r^2\psi^2$ (m^{-1})
$8.0x10^7$
$6.0x10^7$
$4.0x10^7$
$2.0x10^7$
0.0
CdTe Core
Alloy Layer
ZnS Shell
Hole
Electron
Region
CdTe Core
Alloy Layer
ZnS Shell
B
0.0
$2.0x10^{-9}$
$4.0x10^{-9}$
Distance from Dot Centre (m)

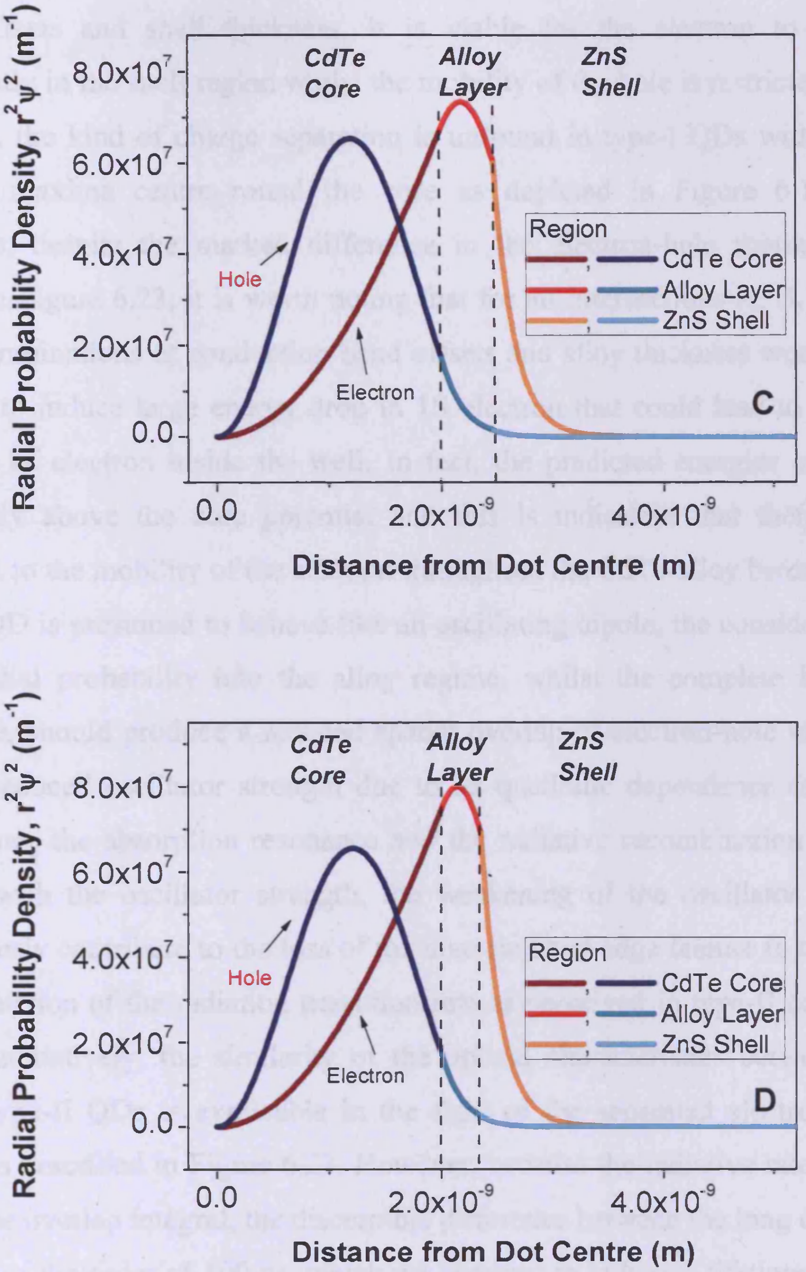

Figure 6.23: Plots of radial probability densities of electron and hole for the intersections A, B, C and D shown in Figure 6.22. The alloy thickness and the potential V_l used: 0.80 nm and 0.5 eV for (A); 0.60 nm and 0.7 eV for (B); 0.47 nm and 0.9 eV for (C); 0.35 nm and 1.2 eV for (D).

Figure 6.23 demonstrates that, with the type-II band alignments, the radial probability maxima of 1S electron and 1S hole can appear at different host materials evoked by the variations of conduction band offsets and the alloy shell thickness. In this case, the electron is loosely confined in the core which infers that, at the optimum configuration of band offsets and shell thickness, it is viable for the electron to be localised predominantly in the shell region whilst the mobility of the hole is restricted to the core. Conversely, the kind of charge separation is unfound in type-I QDs with both carrier probability maxima centre round the core as depicted in Figure 6.14 and 6.15. Nonetheless, despite the marked difference in the electron-hole spatial distribution displayed in Figure 6.23, it is worth noting that for all intersections A, B, C and D, the assessed combinations of conduction band offsets and alloy thickness were found to be inadequate to induce large energy drop in 1S electron that could lead to the complete localisation of electron inside the well. In fact, the predicted energies of 1S electron were slightly above the core potential and this is indicative that there will be no impediment to the mobility of the electron throughout the CdTe-alloy heterostructure.

If excited QD is presumed to behave like an oscillating dipole, the considerable shift of electron radial probability into the alloy regime, whilst the complete localisation is unattainable, should produce a reduced spatial overlap of electron-hole wavefunctions, in turn, a reduced oscillator strength due to its quadratic dependence on the overlap integral. Since the absorption resonance and the radiative recombination rate are both correlated with the oscillator strength, the weakening of the oscillator strength will unambiguously contribute to the loss of the discrete band edge feature in the absorption and the reduction of the radiation transition rate as perceived in type-II core-shell QDs [34-36]. Qualitatively, the similarity of the optical characteristics between Qdot705-STV and type-II QDs is explicable in the light of the separated electron-hole radial probabilities described in Figure 6.23. However, because the radiative rate scales as the square of the overlap integral, the discernible difference between the long decay lifetime component of the order of 100 ns, which we ascribed to radiative lifetime, of Qdot705-STV as compared to ~20 ns radiative lifetime of bare CdTe QDs reported in the literature means that the spatial overlap of electron and hole must be at most ~50 % if not less assuming that the overlap integral in the latter QDs is near unity. To justify the coherence between the experimental decay lifetime of Qdot705-STV and the predicted spatial distribution of electron-hole based on the 2-step finite depth spherical well model, we explicitly calculated the electron-hole overlap integral of Figure 6.23 in accordance to

$$U = 4\pi \int r^2 \psi_e(r)\psi_h(r)dr \tag{6.65}$$

where the subscripts e and h denote the electron and hole.

Diagram of Figure 6.23	Alloy* Thickness (nm)	Potential Height, V_1 (eV)	Electron-Hole Overlap Integral	Fractional Electron-Hole Overlap Integral		
				CdTe Core	Intermediate Alloy	ZnS Shell
A	0.80	0.5	0.745	0.814	0.177	0.009
B	0.60	0.7	0.791	0.824	0.161	0.015
C	0.47	0.9	0.826	0.835	0.143	0.022
D	0.35	1.2	0.864	0.848	0.121	0.031

*CdTe core radius is maintained at 2.0 nm.

Table 6.7: Compilation of electron-hole overlap integral for type-II QD based on 2-step finite depth spherical well model at various combinations of potential height and alloy thickness.

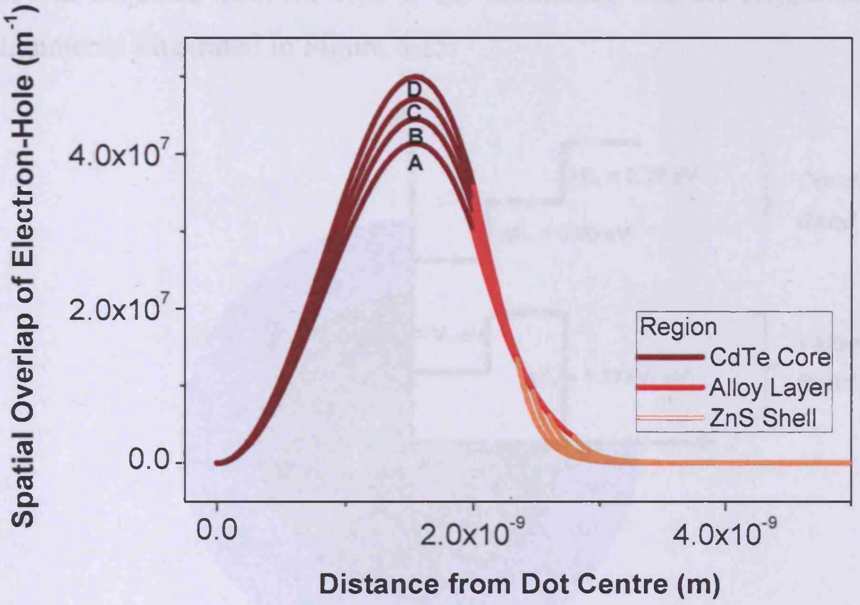

Figure 6.24: Spatial overlap of electron and hole radial wavefunctions as a function of distance.

While we have extended the width and the depth of the well to 0.8 nm and 1.2 eV respectively, the spatial overlap of electron and hole was largely centred on the inner CdTe core as depicted in Figure 6.24. The substantial overlap in the core is ameliorated by the delocalisation of electron over the CdTe-alloy heterostructure since no electronic state is bound inside the well at the band edge absorption. In view of the spatial extension of electron wavefunction over the entire heterostructure and the localisation of hole within the core regime, the inner core invariably contributes to the major fraction of the overall overlap integral.

With reference to Table 6.7, the electron-hole spatial overlap integral in our type-II QD model are effectively above 0.5, albeit a pronounced separation between the electron-hole radial probability density maxima can be clearly seen in Figure 6.23. Even for the lowest calculated overlap integral of 0.7, the corresponding shell thickness is still unrealistic for the formation of few angstrom thick alloy at any non-ideal heterojunctions. Furthermore, the overlap factor is not succinctly small to justify the slow transient of Qdot705-STV fluorescence upon femtosecond excitation. Hypothetically speaking, say the bare CdTe QDs with the typical radiative lifetime of 20 ns has the overlap integral of 1, the overlap of 0.7 predicted from our model can only afford a lifetime of ~40 ns. The similar outcome, in terms of electron-hole overlap integral, was acquired from the type-II QD modelling with the conduction and valence band alignments illustrated in Figure 6.25.

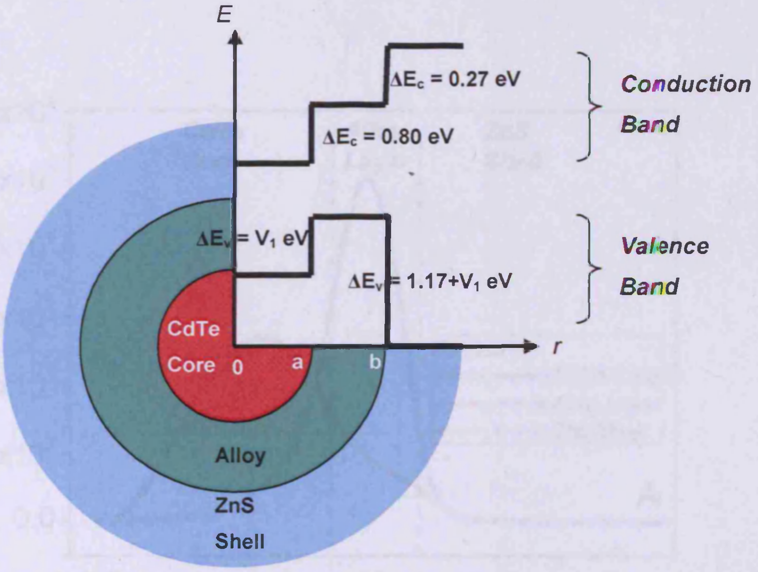

Figure 6.25: Sketch of the postulated conduction and valence band alignments alongside the cross-section of type-II QD.

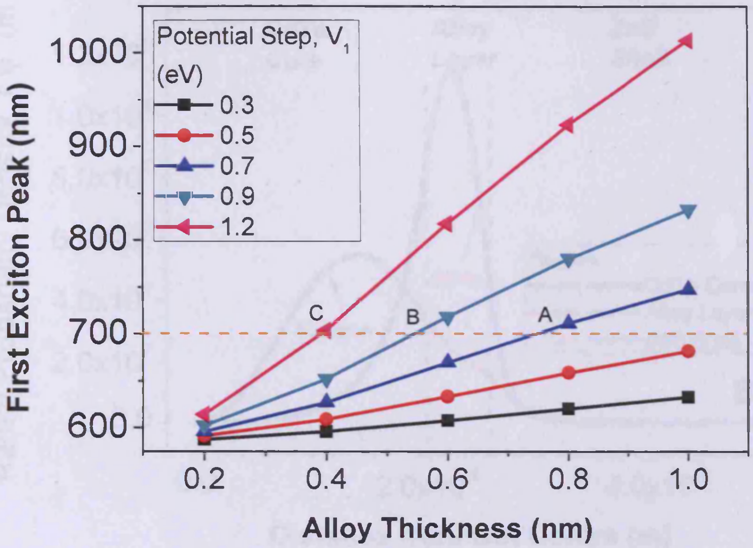

Figure 6.26: First exciton peak of type-II QD versus alloy thickness for a range of V_1 values. A, B and C are points of intersection with 700 nm dashed line.

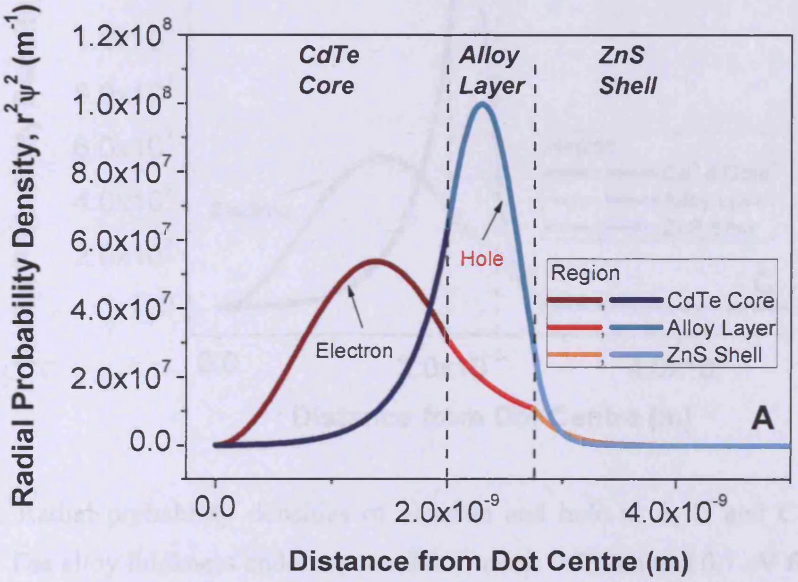

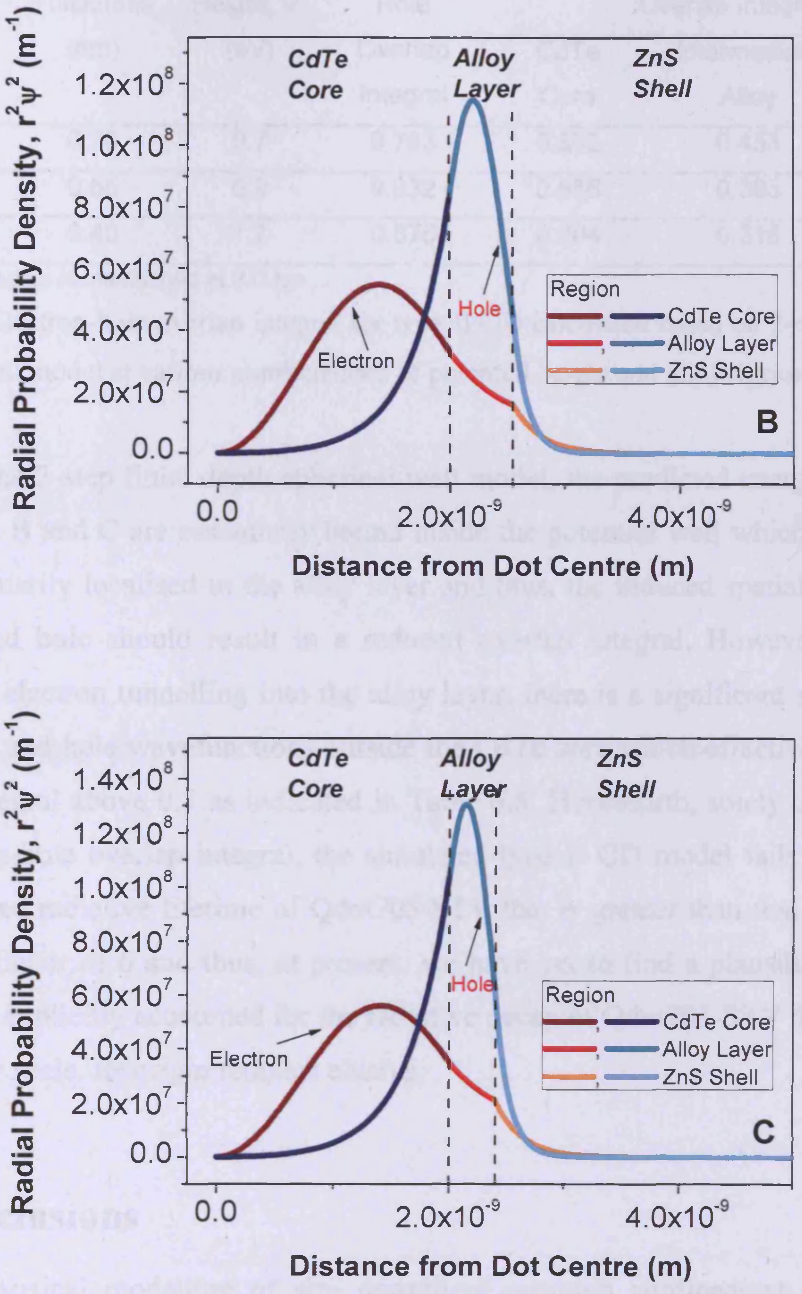

Figure 6.27: Radial probability densities of electron and hole at A, B and C as depicted in Figure 6.26. The alloy thickness and the potential V_l used: 0.75 nm and 0.7 eV for (A); 0.55 nm and 0.9 eV for (B); 0.40 nm and 1.2 eV for (C).

Diagram of Figure 6.27	Alloy* Thickness (nm)	Potential Height, V_1 (eV)	Electron-Hole Overlap Integral	Fractional Electron-Hole Overlap Integral		
				CdTe Core	Intermediate Alloy	ZnS Shell
A	0.75	0.7	0.783	0.502	0.453	0.045
B	0.55	0.9	0.832	0.556	0.383	0.061
C	0.40	1.2	0.875	0.604	0.315	0.081

*CdTe core radius is maintained at 2.0 nm.

Table 6.8: Electron-hole overlap integral for type-II QD calculated based on 2-step finite depth spherical well model at various combinations of potential height and alloy thickness.

Based on the 2-step finite depth spherical well model, the predicted energy states of 1S hole for A, B and C are essentially bound inside the potential well which infer that the hole is primarily localised in the alloy layer and thus, the induced spatial separation of electron and hole should result in a reduced overlap integral. However, due to the substantial electron tunnelling into the alloy layer, there is a significant spatial overlap of electron and hole wavefunctions outside the CdTe core which effectively retains the overlap integral above 0.7 as indicated in Table 6.8. Henceforth, solely on the basis of the electron-hole overlap integral, the simulated type-II QD model fails to agree with the measured radiative lifetime of Qdot705-STV that is greater than that of bare CdTe QDs by a factor of 6 and thus, at present, we have yet to find a plausible explanation that can be explicitly accounted for the radiative decay of Qdot705-STV that spans over 100 ns time scale. Its origin remains elusive.

6.5 Conclusions

In the theoretical modelling of size dependent quantum confinement energies with respect to CdSe/ZnS and CdTe/ZnS core-shell QDs, I have shown that the 'particle-in-a-sphere' model, when the tunnelling of carrier is not considered outside the core, fails to agree with the experimental data over wide range of core radii. This, however, was improved with the developed 2-step finite depth spherical well model by taking the band offsets at the CdSe/ZnS and CdTe/ZnS heterojunctions into account. A pronounced red shift in the predicted bandgap energies was procured, yet it was not an exact match of the real confinement effect perceived in those dots as the nonparabolic nature of the real band structure, aside from the core radius, could also play an important role in the determination of carrier energy which was overlooked by our theoretical model. By the incorporation of finite band offsets, it seems apparent that the leakage of carriers, particularly the electron with the lighter mass, into the shell region is possible. Apart from type-I QD modelling, I have shown that, with the slight modification of the 2-step finite well model, that the energy gaps for QDs of type-II band lineups are dependent on the thickness of the overcoating shell which to a certain extent could results in the localisation of electron outside the core, in turn, the concomitant spatial separation of charges. However, our computational approach fails to afford a substantive elucidation to the long lived fluorescence of Qdot705-STV based on the spatial overlap integral of electron and hole wavefunctions. The reduced overlap integral predicted from our type-II model is not fully accountable for the radiative lifetime of Qdot705-STV that is almost sixfold greater than that of bare CdTe QDs.

6.6 References

1. Nirmal M, Brus L. Luminescence Photophysics in Semiconductor Nanocrystals. *Accounts Chem Res* 1999, **32**(5):407-414.

2. Kapitonov AM, Stupak AP, Gaponenko SV, Petrov EP, Rogach AL, Eychmuller A. Luminescence Properties of Thiol-Stabilized CdTe Nanocrystals. *Journal of Physical Chemistry B* 1999, **103**(46):10109-10113.

3. http://probes.invitrogen.com/servlets/spectra/

4. Brus L. Electronic Wave-Functions in Semiconductor Clusters - Experiment and Theory. *J Phys Chem* 1986, **90**(12):2555-2560.

5. Dabbousi BO, RodriguezViejo J, Mikulec FV, Heine JR, Mattoussi H, Ober R, Jensen KF, Bawendi MG. (CdSe)ZnS Core-Shell Quantum Dots: Synthesis and Characterization of a Size Series of Highly Luminescent Nanocrystallites. *Journal of Physical Chemistry B* 1997, **101**(46):9463-9475.

6. French AP, Taylor EF. An Introduction to Quantum Physics. Stanley Thornes, 1998.

7. Brus LE. A Simple-Model for the Ionization-Potential, Electron-Affinity, and Aqueous Redox Potentials of Small Semiconductor Crystallites. *J Chem Phys* 1983, **79**(11):5566-5571.

8. Brus LE. Electron-Electron and Electron-Hole Interactions in Small Semiconductor Crystallites - The Size Dependence of the Lowest Excited Electronic State. *J Chem Phys* 1984, **80**(9):4403-4409.

9. Nanda KK, Kruis FE, Fissan H. Energy Levels in Embedded Semiconductor Nanoparticles and Nanowires. *Nano Letters* 2001, **1**(11):605-611.

10. Pellegrini G, Mattei G, Mazzoldi P. Finite Depth Square Well Model: Applicability and Limitations. *J Appl Phys* 2005, **97**(7).

11. Haus JW, Zhou HS, Honma I, Komiyama H. Quantum Confinement in Semiconductor Heterostructure Nanometer-Size Particles. *Phys Rev B* 1993, **47**(3):1359-1365.

12. Bhargava R. Structural, Thermal and Miscellaneous Properties of Wide II-VIs. *Properties of Wide Bandgap II-VI Semiconductors*. Edited by Bhargava R. INSPEC, 1997.

13. Rajh T, Micic OI, Nozik AJ. Synthesis and Characterization of Surface-Modified Colloidal CdTe Quantum Dots. *J Phys Chem* 1993, **97**(46):11999-12003.

14. Murray CB, Norris DJ, Bawendi MG. Synthesis and Characterization of Nearly Monodisperse CdE (E = S, Se, Te) Semiconductor Nanocrystallites. *J Am Chem Soc* 1993, **115**(19):8706-8715.

15. Yu WW, Qu LH, Guo WZ, Peng XG. Experimental Determination of the Extinction Coefficient of CdTe, CdSe, and CdS Nanocrystals. *Chemistry of Materials* 2003, **15**(14):2854-2860.

16. EviDots and EviComposites: Commercially Available Quantum Dots for Wide Range of Novel Semiconductor Applications. Evident Technologies, 2005.

17. Mastai Y, Hodes G. Size Quantization in Electrodeposited CdTe Nanocrystalline Films. *Journal of Physical Chemistry B* 1997, **101**(14):2685-2690.

18. Masumoto Y, Sonobe K. Size-Dependent Energy Levels of CdTe Quantum Dots. *Phys Rev B* 1997, **56**(15):9734-9737.

19. Wang Y, Herron N. Nanometer-Sized Semiconductor Clusters - Materials Synthesis, Quantum Size Effects, and Photophysical Properties. *J Phys Chem* 1991, **95**(2):525-532.

20. Peng XG, Schlamp MC, Kadavanich AV, Alivisatos AP. Epitaxial Growth of Highly Luminescent CdSe/CdS Core/Shell Nanocrystals with Photostability and Electronic Accessibility. *J Am Chem Soc* 1997, **119**(30):7019-7029.

21. Nosaka Y. Finite Depth Spherical Well Model for Excited-States of Ultrasmall Semiconductor Particles - An Application. *J Phys Chem* 1991, **95**(13):5054-5058.

22. Merzbacher E. Quantum Mechanics. 3rd edn. John Wiley and Sons, 1998.

23. Horiguchi S. Validity of Effective Mass Theory for Energy Levels in Si Quantum Wires. *Physica B* 1996, **227**(1-4):336-338.

24. Wei SH, Zunger A. Calculated Natural Band Offsets of all II-VI and III-V Semiconductors: Chemical Trends and the Role of Cation d Orbitals. *Applied Physics Letters* 1998, **72**(16):2011-2013.

25. Wei SH, Zhang SB, Zunger A. First-Principles Calculation of Band Offsets, Optical Bowings, and Defects in CdS, CdSe, CdTe, and their Alloys. *J Appl Phys* 2000, **87**(3):1304-1311.

26. Hines MA, Guyot-Sionnest P. Synthesis and Charaterization of Strongly Luminescencing ZnS-Capped CdSe Nanocrystals. *J Phys Chem* 1996, **100**(2):468-471.

27. Li JJ, Wang YA, Guo WZ, Keay JC, Mishima TD, Johnson MB, Peng XG. Large-Scale Synthesis of Nearly Monodisperse CdSe/CdS Core/Shell Nanocrystals Using Air-Stable Reagents via Successive Ion Layer Adsorption and Reaction. *J Am Chem Soc* 2003, **125**(41):12567-12575.

28. Kalyuzhny G, Murray RW. Ligand Effects on Optical Properties of CdSe Nanocrystals. *Journal of Physical Chemistry B* 2005, **109**(15):7012-7021.

29. Kloepfer JA, Bradforth SE, Nadeau JL. Photophysical Properties of Biologically Compatible CdSe Quantum Dot Structures. *Journal of Physical Chemistry B* 2005, **109**(20):9996-10003.

30. Wang Y, Suna A, McHugh J, Hilinski EF, Lucas PA, Johnson RD. Optical Transient Bleaching of Quantum-Confined CdS Clusters - The Effects of Surface-Trapped Electron-Hole Pairs. *J Chem Phys* 1990, **92**(11):6927-6939.

31. Nirmal M, Norris DJ, Kuno M, Bawendi MG, Efros AL, Rosen M. Observation of the Dark Exciton in CdSe Quantum Dots. *Phys Rev Lett* 1995, **75**(20):3728-3731.

32. Crooker SA, Hollingsworth JA, Tretiak S, Klimov VI. Spectrally Resolved Dynamics of Energy Transfer in Quantum-Dot Assemblies: Towards Engineered Energy Flows in Artificial Materials. *Phys Rev Lett* 2002, **89**(18).

33. Wuister SF, Donega CD, Meijerink A. Influence of Thiol Capping on the Exciton Luminescence and Decay Kinetics of CdTe and CdSe Quantum Dots. *Journal of Physical Chemistry B* 2004, **108**(45):17393-17397.

34. Kim S, Fisher B, Eisler HJ, Bawendi M. Type-II Quantum Dots: CdTe/CdSe(Core/Shell) and CdSe/ZnTe(Core/Shell) Heterostructures. *J Am Chem Soc* 2003, **125**(38):11466-11467.

35. Balet LP, Ivanov SA, Piryatinski A, Achermann M, Klimov VI. Inverted Core/Shell Nanocrystals Continuously Tunable between Type-I and Type-II Localization Regimes. *Nano Letters* 2004, **4**(8):1485-1488.

36. Ivanov SA, Nanda J, Piryatinski A, Achermann M, Balet LP, Bezel IV, Anikeeva PO, Tretiak S, Klimov VI. Light Amplification Using Inverted Core/Shell Nanocrystals: Towards Lasing in the Single-Exciton Regime. *Journal of Physical Chemistry B* 2004, **108**(30):10625-10630.

CHAPTER 7:

SUMMARY AND FUTURE WORK

CONTENTS:

Abstract: In the last chapter, I provide a brief summary of the work done above all the FRET experiments on Qdot585-STV-AF594-Bio and Qdot705-STV-DY731-Bio self-assemblies and the theoretical modelling of core-shell QDs in the parabolic band approximation. In addition, I also highlight the intricate yet important issues encountered in the analyses of FRET in a multivalent QD-dye configuration. Finally, I end this thesis with a few suggestions for the continuance of exciting QD FRET research in which the concept is still new to the semiconductor world.

CHAPTER 7:

SUMMARY AND FUTURE WORK

7.1 Summary

- The highest valency of Qdot585-STV is ~10.
- FRET efficiency achievable by Qdot585-STV-AF594-Bio at the maximum valency is ~30 % from time-resolved measurements.
- The highest valency of Qdot705-STV is ~20.
- FRET efficiency achievable by Qdot705-STV-DY731-Bio at the maximum valency is ~50 % from time-resolved measurements.
- From type-I QD modelling, lighter electron can delocalise over the core-shell heterostructure while heavier hole is primarily confined within the inner core.

In our pursuit to investigate the efficacies of II-VI semiconductor QDs as the energy donors in FRET based self-assemblies, streptavidin functionalised Qdot nanoparticles of different core compositions were carefully selected to conjugate with biotinylated organic dyes via streptavidin-biotin binding scheme. Hydrophilic Qdot585-STV constituted of CdSe core that emits in the visible spectrum was paired with AF594-Bio, whilst hydrophilic Qdot705-STV composed of CdTe core that emits in the far-red spectrum was paired with DY731-Bio such that the spectral cross-talk between QD and dye emissions was minimal but the spectral overlap between the QD emission and dye absorption was maximal. In this thesis, I have shown that the steady state and the temporal measurements both have produced unequivocal evidence corroborating the effectiveness of QDs as energy donors in the proximity-induced resonance interactions, however, subjected to the vital criterion that multivalent donor-acceptor conjugation is feasible. This is essentially attributed to the physical dimensions of Qdot nanoparticles which can reach up to several orders of magnitude larger than the conventional luminescent biomolecules after solubilisation to afford water solubility and followed by bio-functionalisation to provide labelling specificity.

From the time-resolved fluorescence measurements on Qdot585-STV-AF594-Bio assays attained after the ultrafiltration, I revealed that the quenching efficiency achievable by Qdot585-STV is strongly dependent on its loading capacity. Based on our findings, on average, the highest number of biotinylated biomolecules that can actually be appended to the surface of Qdot585-STV is ~10. Unfortunately, at such labelling ratio, only a modest FRET efficiency of 0.3 was calculated from the lifetime data in which the time constant of Qdot585-STV luminescence decay in the absence of AF594-Bio was assigned to the radiative recombination process. By contrast, further loss of QD luminescence was observed beyond that valency in the course of titration of Qdot585-STV with AF594-Bio in which a quenching efficiency as high as 0.7 was obtained at the acceptor-to-donor stoichiometry of 20:1. We attributed the enhanced quenching effect to the FRET mediated by fast diffusing unbound acceptors. Due to the large surface area of Qdot585-STV, greater number of energetically resonant acceptors, irrespective of their bound/unbound states, can be in the vicinity of Qdot585-STV to compete for the dipolar interactions. Henceforth, it is intuitive that the efficacy of the excitation energy transfer from Qdot585-STV to AF594-Bio can be rectified if only the existing valency of Qdot585-STV-AF594-Bio conjugate can be elevated. The same notion could be applied to Qdot705-STV with limited bio-targeting functionality.

Only by the size exclusion filtration, I unveiled that, on average, a maximum of ~20 acceptors can pack around a single Qdot705-STV via ligand-receptor binding. The underlying factor for the higher number labelled DY731-Bio per Qdot705-STV in contradistinction to the number of bound AF594-Bio per Qdot585-STV is imperatively related to the geometrical structure of Qdot705-STV with the major diameter that can be twofold the size of Qdot585-STV if not more. The high specificity of Qdot705-STV can compensate for the loss of its sensitivity to FRET interactions due to its considerable large size, which can be deleterious if it is utilised in a single donor-acceptor configuration. At the acceptor-to-donor labelling ratio of 20:1, we procured a substantial FRET efficiency of ~0.5 from the time-resolved measurements. In the steady state fluorescence measurements, a similar effect of the diffusion enhanced FRET as observed in the foregoing Qdot585-STV titration was also perceived in Qdot705-STV whereby successive titrations with DY731-Bio beyond the limitation of Qdot705-STV targeting ability resulted in a reduced donor fluorescence. Due to the feasible dipole-dipole interactions between Qdot705-STV and unbound DY731-Bio molecules in the unfiltered mixture, further donor quenching was detected and thus producing a net increase in the FRET efficiency. For example, at 40 acceptor/donor ratio, a 60 % of quenching efficiency was predicated on the steady state measurements.

In this thesis, I also showcased the practical usage of FRET theory in providing the structural information about the QD-dye self-assemblies. The donor-acceptor separations in Qdot585-AF594-Bio and Qdot705-DY731-Bio multiplexes were estimated from the theoretical fitting of the measured efficiency data at varied loading ratios. From the steady state fluorescence quenching, the best fit produced a distance of 10 nm for Qdot585-STV-AF594-Bio complex while a slightly larger distance, 11.6 nm, was predicated on the temporal measurements. The subtle difference can be attributed to the trivial inner filter effect during the course of steady state fluorescence measurements and also the possible overestimation of the conjugation ratios for Qdot585-STV-AF594-Bio self-assemblies. Nonetheless, the distances derived from two independent spectroscopic techniques are remarkably close to the speculated diameter of near spherical Qdot585-STV i.e. ~20-21 nm assuming a centro-symmetric array of streptavidin proteins of size ~5 nm.

Contrary to Qdot585-STV-AF594-Bio self-assemblies, the FRET analysis of Qdot705-STV-DY731-Bio bioassays based on the time-resolved measurements was not entirely straightforward. The confusion in the evaluation of FRET efficiency was elevated by the profound non-exponential dynamics of Qdot705-STV in which the measured fluorescence decays were statistically fitted with a two-lifetime decay function giving rise to short lifetime components ranging from 20 to 40 ns and long lifetime components ranging from 90 to 130 ns. With reference to the two-lifetime luminescence decay of Qdot705-STV in the absence of DY731-Bio, I presented a hypothetical model in association with the dynamics of Qdot705-STV in which the short lifetime component was assignable to the carrier trapping by the surface states and the long lifetime component was assignable to the predominant radiative relaxation process on the basis of the fractional contribution of each decay time to the steady state intensity.

From that angle of perception, I quantified the efficiency of the excitation energy transfer with respect to each lifetime component as a function of acceptor-to-donor labelling ratio and thus, generating two distinct efficiencies of ~0.5 for the short lifetime and ~0.3 for the long lifetime at the maximum acceptor-to-donor labelling ratio of 20:1. Whilst the theoretical fit of the steady state quenching efficiencies produced a reasonable donor-acceptor distance of 12.6 nm considering the polydisperse Qdot705-STV dot system, the distances estimated from the two-lifetime approach did not converge at the same value i.e. 11.6 nm for the short lifetime and 16.4 nm for the long lifetime, even though the fluctuation of the quantum efficiency has been taken into consideration. This moves us to speculate that the shape anisotropy of Qdot705-STV and the charging of inner core upon carrier capture by the surface states could have instigated Qdot705-STV to deviate from the point dipole approximation used in the FRET formulation, however, the extent of the deviation and the underlying mechanisms are not fully understood. This requires the extensive theoretical and experimental studies of Qdot705-STV photophysics prior to further detailed FRET analysis as regards Qdot705-STV-DY731-Bio multiplexes. Seemingly, the discrepancy of the distances derived from two lifetimes is indicative that the manifold processes of Qdot705-STV have been overlooked by the steady state measurements but are resolvable in the decay measurements, thus, rendering the donor-acceptor distance deduced from the steady state approach less reliable above all for those QDs exhibiting pronounced non-exponential decays. Having said that, the steady state and the time-resolved measurements both unequivocally produced substantive evidence confirming that Qdot705-STV can be an efficient energy donor in a multivalent system.

All in all, it is worth mentioning that there is no simple approach to FRET analysis of QD-dye system taking account of several vital issues in which some could be more intricate than the other. i) multivalency, which is paramount for effective FRET interactions between QDs and immobilised dyes, can elevate the distribution of donor-acceptor distances caused by the heterogeneity of QD system, ii) the number of immobilised acceptors, in turn, the FRET efficiency can vary from dot to dot in ensemble solution iii) organic binding moieties used as donor-acceptor linkers are generally non-rigid and their local motions can affect the radial distances of the bound acceptors, iv) the exact transition processes underpinning the non-exponential time- and ensemble-averaged QD fluorescence decays can be difficult to unravel and this imperatively evokes some confusion in the use of the correct decay expression to extract the pertinent lifetimes, v) point dipole approximation may no longer work for QDs exhibiting inherent shape anisotropy and non-exponential kinetics, to the extent that the idealised FRET efficiency formula may probably have to be modified.

Apart from the QD FRET investigations, some theoretical modelling of size dependent quantum confinement effect of QD within the parabolic band approximation was performed in order to better understand the underlying physics behind the phenomenological QD behaviours. By considering the layered structures of Qdot585-STV and Qdot705-STV and the finite band offsets at interfaces, I developed a 2-step finite depth spherical well model to provide an alternative theoretical treatment of CdSe/ZnS and CdTe/ZnS QDs. In comparison with the 'particle-in-a-sphere' model in which the potential is unrealistically taken to infinity, the energy gaps computed using the present finite well model have shown a pronounced red shift. However, we do not expect the energy eigenvalues derived from the model to be quantitatively correct. The deviation of real energy bands from parabolic relationship accounts for the discrepancy (overestimation) at small QD radii.

Besides the theoretical simulation of the size effect on the QD bandgap, the spatial distributions of 1S carriers for CdSe/ZnS and CdTe/ZnS QDs were studied qualitatively. The wavefunctions derived from the finite well model suggested that the electron is capable of delocalisation over the core-shell heterostructure which by contrast, the mobility of the hole is primarily restricted to the inner core with negligible leakage into the shell layer. Other than the typical type-I QD, the 2-step finite well model was modified to treat QD of type-II band profile in attempt to assess the likelihood that Qdot705-STV could be type-II underpinned by the observation of long fluorescence decay over 100 ns time scale. In type-II QDs, whilst the tunnelling of hole is indecipherable, the radial probability of electron in the shell regime is no longer trivial. However, the reduced overlap calculated from the theoretical model was not enough to elucidate the long radiative lifetime of Qdot705-STV which is sixfold greater than that of bare CdTe QDs. Henceforth, the detailed analyses of the crystalline morphology and the elemental composition of Qdot705-STV are vital to uncover the underlying mechanisms responsible for its long lived fluorescence decay.

7.2 Future Work

The evidence from the steady state and the time-resolved measurements unequivocally confirms that QDs, even for those with an overall size of ~30 nm, can serve as efficient energy donors if given the specificity to target multiple liganded acceptors. However, the conformational information of individual QD-dye FRET system in bulk solution is basically lost in the ensemble measurements. To have better understanding of FRET process involving inhomogeneous semiconductor QDs, further experimental work on QD FRET is necessary and it can be ramified into several directions. One, the fact that the single dot emission is several-fold narrower than ensemble emission and the efficiency of FRET is determined by the spectral overlap integral, $J(\lambda)$, it will be useful to investigate the effect of dot-to-dot spectral variation on the FRET efficiencies of QD-dye subpopulations by spectrally and temporally resolving the donor fluorescence. Alternatively, in order to eliminate the problem of size heterogeneity and to restrict the motions of bio-linkers, it is also possible to embed the QD-dye assays in solid matrices and monitor the resonance interactions with the utility of single molecule spectroscopy. Besides that, some knowledge of the radial distribution of acceptors can be beneficial to the modification of the present FRET efficiency model and this can be done by the structural analysis of biofunctionalised QD with atomic force microscopy which has the capability to reveal the overall shape of QD including the binding moieties. Whilst the structural information of QDs is important, the understanding of the charge distribution in non-spherical QDs and the effect of surface charge on that by theoretical simulation can also help to advance the current FRET efficiency formula.

Appendix A

2-Step Finite Depth Spherical Well Model for CdSe/ZnS Type-I Quantum Dots

1. 1S Electron Radial Wavefunction and Its Radial Probability Function

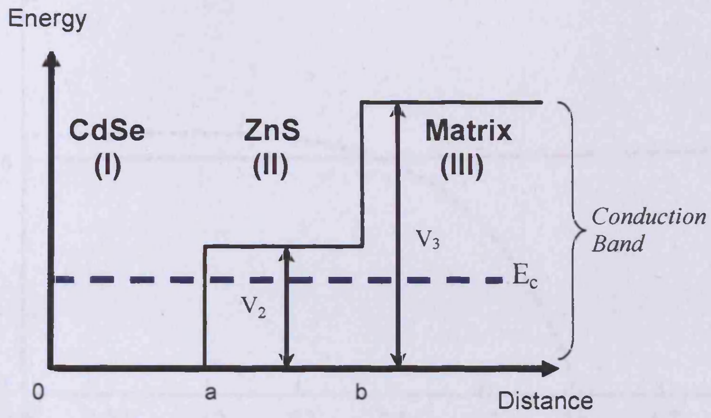

1.1 Defining Constants:

$me := 9.109 \cdot 10^{-31}$ kg

$me1 := 0.13 \cdot me$ $\quad$ $me2 := 0.28 \cdot me$ $\quad$ $me3 := me$

$hbar := 1.055 \cdot 10^{-34}$ Js $\quad$ $e := 1.602 \cdot 10^{-19}$ C

$V2 := 1.46 \cdot e$ potential barrier at CdSe/ZnS in J $\quad$ $V3 := 3.0 \cdot e$ potential barrier at ZnS/Matrix in J

$a := 2.0 \cdot 10^{-9}$ $\quad$ $b := 2.5 \cdot 10^{-9}$ $\quad$ distance from the centre of QD in m

1.2 Finding the Energy Eigenvalue E_c of Electron at the Lowest Excited State:

$$k1(E) := \frac{(2 \cdot me1 \cdot E)^{\frac{1}{2}}}{hbar} \qquad k2(E) := \frac{[2 \cdot me2 \cdot (|V2 - E|)]^{\frac{1}{2}}}{hbar} \qquad k3(E) := \frac{[2 \cdot me3 \cdot (|V3 - E|)]^{\frac{1}{2}}}{hbar}$$

Solve the equations below simultaneously to find E such that it satisfies g(E) - h(E) = 0,

$$q(E) := me2 \cdot k3(E) \cdot b \cdot \exp(-2 \cdot k2(E) \cdot b) + me2 \cdot \exp(-2 \cdot k2(E) \cdot b)$$

$$g(E) := \frac{-me3 \cdot k2(E) \cdot b \cdot \exp(-2 \cdot k2(E) \cdot b) - me3 \cdot \exp(-2 \cdot k2(E) \cdot b) + q(E)}{-me2 \cdot k3(E) \cdot b - me2 + me3 - me3 \cdot k2(E) \cdot b}$$

$$h(E) := \frac{\exp(-2\,k2(E)\cdot a)(-me1\cdot k2(E)\cdot a - me1 - me2\cdot k1(E)\cdot a\cdot \cot(k1(E)\cdot a) + me2)}{me2\cdot k1(E)\cdot a\cdot \cot(k1(E)\cdot a) - me2 - me1\cdot k2(E)\cdot a + me1}$$

$E := 0.0001\cdot e, 0.0002\cdot e .. 0.8\cdot e$

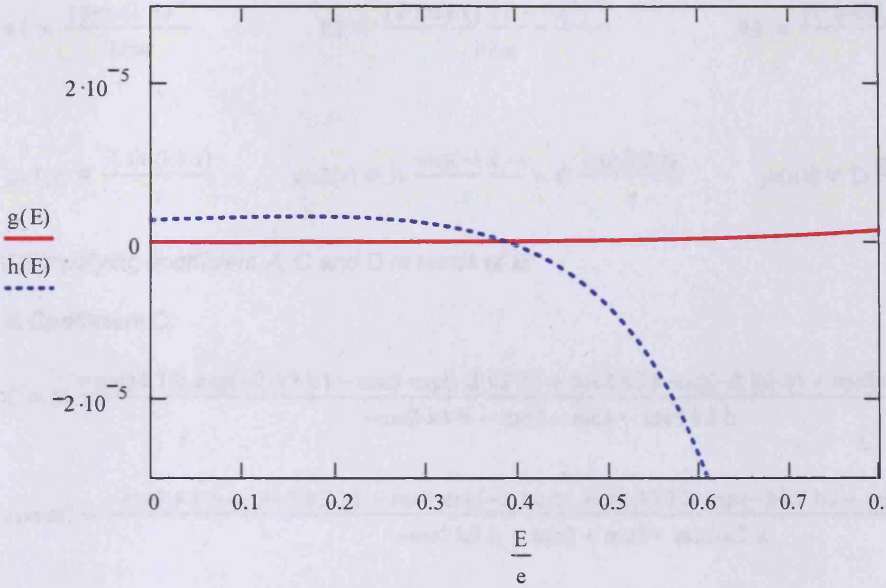

$E := 0.3\cdot e$

$TOL := 1\cdot 10^{-9}$ To improve the accuracy of *root* function.

$p(E) := (g(E) - h(E))\cdot 10^{5}$

$soln := root(p(E), E)$

$\frac{soln}{e} = 3.8574 \times 10^{-1}$

$E := soln$

$p(E) = -4.2087 \times 10^{-16}$

Therefore, E_c is:

$\frac{E}{e} = 3.8574 \times 10^{-1}$ in eV

1.3 Plotting Electron Radial Wavefunction and its Radial Probability Function:

Region I: *Region II:* *Region III:*

$$k1 := \frac{(2\cdot me1\cdot E)^{\frac{1}{2}}}{hbar} \qquad k2 := \frac{[2\cdot me2\cdot(|V2 - E|)]^{\frac{1}{2}}}{hbar} \qquad k3 := \frac{[2\cdot me3\cdot(|V3 - E|)]^{\frac{1}{2}}}{hbar}$$

$$\psi e1(r) = \frac{A\sin(k1\cdot r)}{r} \qquad \psi e2(r) = B\cdot\frac{\exp(-k2\cdot r)}{r} + C\cdot\frac{\exp(k2\cdot r)}{r} \qquad \psi e3(r) = D\cdot\frac{\exp(-k3\cdot r)}{r}$$

i) Simplifying coefficient A, C and D in terms of B:

a) Coefficient C:

$$C = B\cdot\frac{-me3\cdot k2\cdot b\cdot\exp(-2\cdot k2\cdot b) - me3\cdot\exp(-2\cdot k2\cdot b) + me2\cdot k3\cdot b\cdot\exp(-2\cdot k2\cdot b) + me2\cdot\exp(-2\cdot k2\cdot b)}{-me2\cdot k3\cdot b - me2 + me3 - me3\cdot k2\cdot b}$$

.... $C = B\cdot constC$

$$constC := \frac{-me3\cdot k2\cdot b\cdot\exp(-2\cdot k2\cdot b) - me3\cdot\exp(-2\cdot k2\cdot b) + me2\cdot k3\cdot b\cdot\exp(-2\cdot k2\cdot b) + me2\cdot\exp(-2\cdot k2\cdot b)}{-me2\cdot k3\cdot b - me2 + me3 - me3\cdot k2\cdot b}$$

$constC = 1.2821 \times 10^{-7}$

b) Coefficient A:

$$A = \frac{B\cdot\exp(-k2\cdot a) + C\cdot\exp(k2\cdot a)}{\sin(k1\cdot a)}$$

.... $A = B\cdot constA$

$$constA := \frac{\exp(-k2\cdot a) + constC\cdot\exp(k2\cdot a)}{\sin(k1\cdot a)}$$

$constA = 4.8945 \times 10^{-3}$

c) Coefficient D:

$$D = \frac{B\cdot\exp(-k2\cdot b) + C\cdot\exp(k2\cdot b)}{\exp(-k3\cdot b)}$$

.... $D = B\cdot constD$

$$constD := \frac{\exp(-k2\cdot b) + constC\cdot\exp(k2\cdot b)}{\exp(-k3\cdot b)}$$

$constD = 1.0113 \times 10^{6}$

ii) Normalising $r^2\psi^*\psi$ to find B:

$c := 1\cdot10^{-8}$ This defines the upper limit for integration in Region III.

$$R1 := \int_0^a \left[r\cdot\left(\text{constA}\cdot\frac{\sin(k1\cdot r)}{r}\right)\right]^2 dr$$

$$R2 := \int_a^b \left[r\cdot\left(\frac{\exp(-k2\cdot r)}{r} + \text{constC}\cdot\frac{\exp(k2\cdot r)}{r}\right)\right]^2 dr$$

$$R3 := \int_b^{b+c} \left[r\cdot\left(\text{constD}\cdot\frac{\exp(-k3\cdot r)}{r}\right)\right]^2 dr$$

$R1 + R2 + R3 = 3.1546\times10^{-14}$

$p(Y) := 1 - Y\cdot\left[4\pi(R1 + R2 + R3)\right]$

$Y := 0.00001$

$\text{soln2} := \text{root}(p(Y), Y)$

$\text{soln2} = 2.5225\times10^{12}$

$B := \text{soln2}^{\frac{1}{2}}$

$B = 1.5883\times10^{6}$ Substitute B into the equations below to find the values of A, C and D.

$$C(B) := B\cdot\frac{-me3\cdot k2\cdot b\cdot\exp(-2\cdot k2\cdot b) - me3\cdot\exp(-2\cdot k2\cdot b) + me2\cdot k3\cdot b\cdot\exp(-2\cdot k2\cdot b) + me2\cdot\exp(-2\cdot k2\cdot b)}{-me2\cdot k3\cdot b - me2 + me3 - me3\cdot k2\cdot b}$$

$$A(B) := \frac{B\cdot(\exp(-k2\cdot a) + \text{constC}\cdot\exp(k2\cdot a))}{\sin(k1\cdot a)}$$

$$D(B) := \frac{B\cdot(\exp(-k2\cdot b) + \text{constC}\cdot\exp(k2\cdot b))}{\exp(-k3\cdot b)}$$

Therefore,

$A(B) = 7.7737\times10^{3}$

$A := A(B)$

$C(B) = 2.0363\times10^{-1}$

$C := C(B)$

$D(B) = 1.6063 \times 10^{12}$

$D := D(B)$

Wavefunctions for 3 Separate Regions (I, II and III):

$$\psi e1(r1) := \frac{A \cdot \sin(k1 \cdot r1)}{r1}$$ ________ Wavefunction in Region I

$$\psi e2(r2) := B \cdot \frac{\exp(-k2 \cdot r2)}{r2} + C \cdot \frac{\exp(k2 \cdot r2)}{r2}$$ ___________ Wavefunction in Region II

$$\psi e3(r3) := D \cdot \frac{\exp(-k3 \cdot r3)}{r3}$$ ____________ Wavefunction in Region III

iii) To check the matching conditions:

a) At boundary r = a,

$r1 := a \qquad r2 := a$

$$\frac{\frac{d}{dr1}\psi e1(r1)}{\frac{d}{dr2}\psi e2(r2)} = 4.6429 \times 10^{-1} \qquad \frac{me1}{me2} = 4.6429 \times 10^{-1}$$

b) At boundary r = b,

$r2 := b \qquad r3 := b$

$$\frac{\frac{d}{dr2}\psi e2(r2)}{\frac{d}{dr3}\psi e3(r3)} = 2.8 \times 10^{-1} \qquad \frac{me2}{me3} = 2.8 \times 10^{-1}$$

iv) Plot of electron radial wavefunction and its corresponding radial probability function:

Defining the r1, r2 and r3 intervals:

$r1 := 0\cdot10^{-9}, 0.01\cdot10^{-9} .. a \qquad r2 := a, a + 0.01\cdot10^{-9} .. b \qquad r3 := b, b + 0.01\cdot10^{-9} .. 8\cdot10^{-9}$

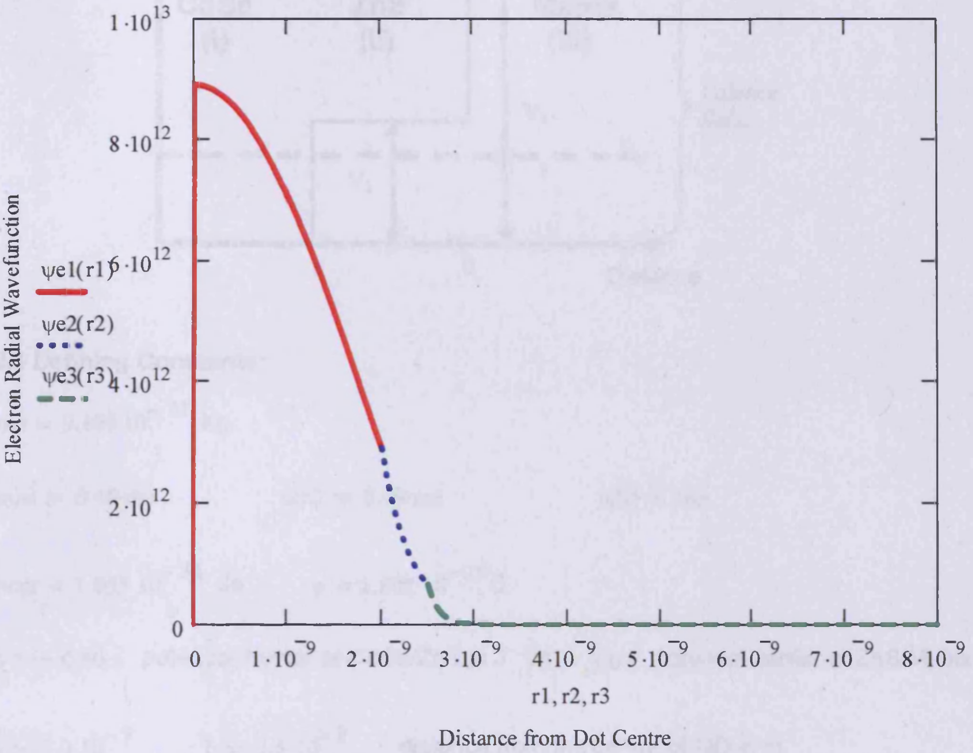

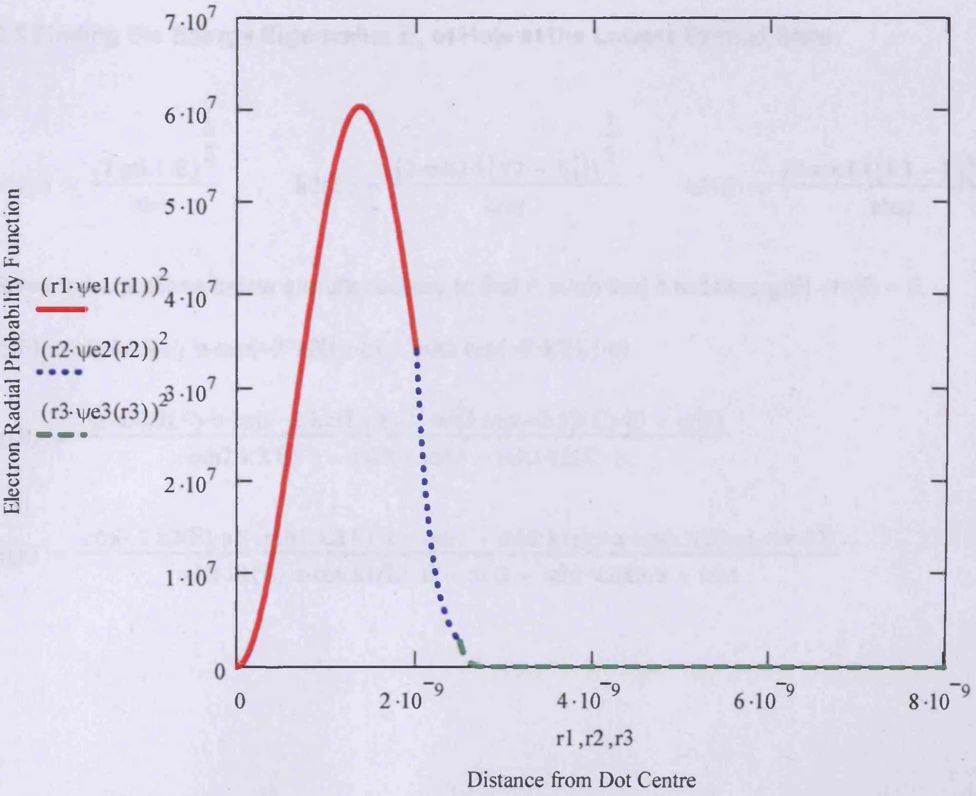

2. 1S Hole Radial Wavefunction and Its Radial Probability Function

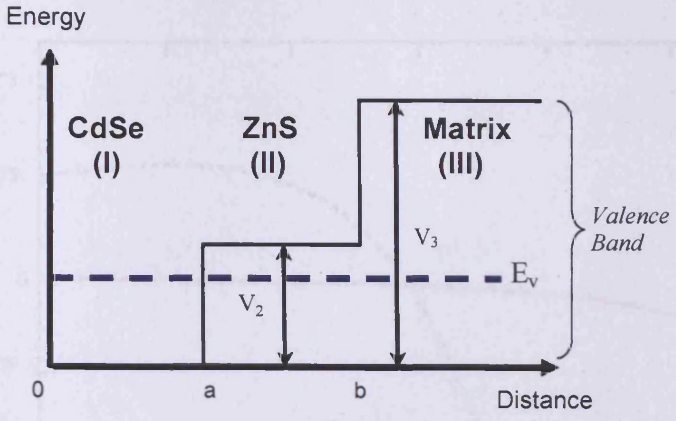

2.1 Defining Constants:

$me := 9.109 \cdot 10^{-31}$ kg

$mh1 := 0.45 \cdot me$ $\quad$ $mh2 := 0.49 \cdot me$ $\quad$ $mh3 := me$

$hbar := 1.055 \cdot 10^{-34}$ Js $\quad$ $e := 1.602 \cdot 10^{-19}$C

$V2 := 0.60 \cdot e$ potential barrier at CdSe/ZnS in J $\quad$ $V3 := 3.0 \cdot e$ potential barrier at ZnS/Matrix in J

$a := 2.0 \cdot 10^{-9}$ $\quad$ $b := 2.5 \cdot 10^{-9}$ $\quad$ distance from the centre of QD in m

2.2 Finding the Energy Eigenvalue E_v of Hole at the Lowest Excited State:

$$k1(E) := \frac{(2 \cdot mh1 \cdot E)^{\frac{1}{2}}}{hbar} \qquad k2(E) := \frac{[2 \cdot mh2 \cdot (|V2 - E|)]^{\frac{1}{2}}}{hbar} \qquad k3(E) := \frac{[2 \cdot mh3 \cdot (|V3 - E|)]^{\frac{1}{2}}}{hbar}$$

Solve the equations below simultaneously to find E such that it satisfies g(E) - h(E) = 0,

$$q(E) := mh2 \cdot k3(E) \cdot b \cdot \exp(-2 \cdot k2(E) \cdot b) + mh2 \cdot \exp(-2 \cdot k2(E) \cdot b)$$

$$g(E) := \frac{-mh3 \cdot k2(E) \cdot b \cdot \exp(-2 \cdot k2(E) \cdot b) - mh3 \cdot \exp(-2 \cdot k2(E) \cdot b) + q(E)}{-mh2 \cdot k3(E) \cdot b - mh2 + mh3 - mh3 \cdot k2(E) \cdot b}$$

$$h(E) := \frac{\exp(-2\, k2(E) \cdot a)(-mh1 \cdot k2(E) \cdot a - mh1 - mh2 \cdot k1(E) \cdot a \cdot \cot(k1(E) \cdot a) + mh2)}{mh2 \cdot k1(E) \cdot a \cdot \cot(k1(E) \cdot a) - mh2 - mh1 \cdot k2(E) \cdot a + mh1}$$

$E := 0.0001 \cdot e, 0.0002 \cdot e .. 0.3 \cdot e$

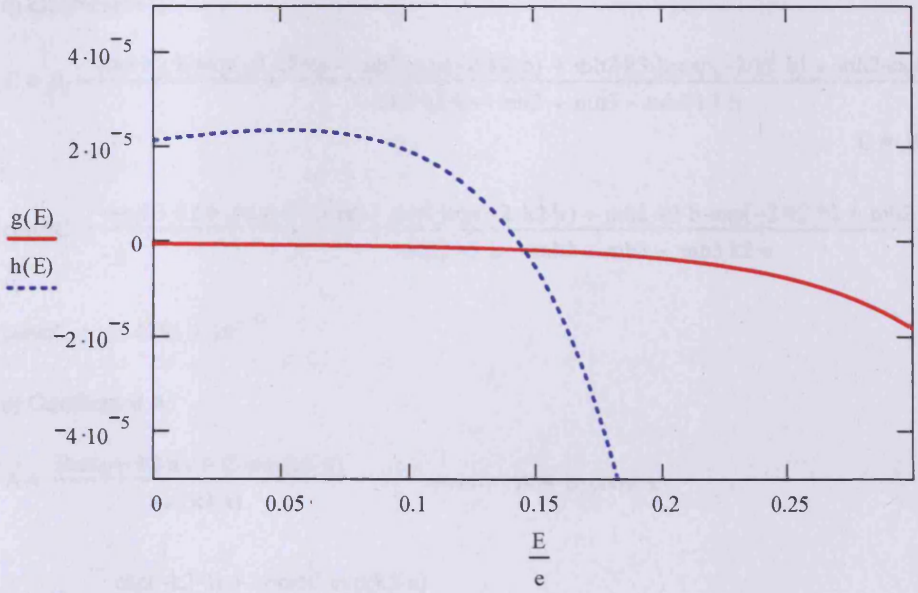

$E := 0.15 \cdot e$

$p(E) := (g(E) - h(E)) \cdot 10^{5}$

$\text{soln} := \text{root}(p(E), E)$

$\frac{\text{soln}}{e} = 1.4545 \times 10^{-1}$

$E := \text{soln}$

$p(E) = -3.0917 \times 10^{-15}$

Therefore, ΔE_V is:

$\frac{E}{e} = 1.4545 \times 10^{-1}$ in eV

2.3 Plotting Hole Radial Wavefunction and its Radial Probability Function:

Region I: *Region II:* *Region III:*

$k1 := \frac{(2 \cdot mh1 \cdot E)^{\frac{1}{2}}}{hbar}$ $k2 := \frac{[2 \cdot mh2 \cdot (|V2 - E|)]^{\frac{1}{2}}}{hbar}$ $k3 := \frac{[2 \cdot mh3 \cdot (|V3 - E|)]^{\frac{1}{2}}}{hbar}$

$\psi h1(r) = \frac{A \sin(k1 \cdot r)}{r}$ $\psi h2(r) = B \cdot \frac{\exp(-k2 \cdot r)}{r} + C \cdot \frac{\exp(k2 \cdot r)}{r}$ $\psi h3(r) = D \cdot \frac{\exp(-k3 \cdot r)}{r}$

i) Simplifying coefficient A, C and D in terms of B:

a) Coefficient C:

$$C = B\cdot\frac{-mh3\cdot k2\cdot b\cdot \exp(-2\cdot k2\cdot b) - mh3\cdot \exp(-2\cdot k2\cdot b) + mh2\cdot k3\cdot b\cdot \exp(-2\cdot k2\cdot b) + mh2\cdot \exp(-2\cdot k2\cdot b)}{-mh2\cdot k3\cdot b - mh2 + mh3 - mh3\cdot k2\cdot b}$$

.... $C = B\cdot constC$

$$constC := \frac{-mh3\cdot k2\cdot b\cdot \exp(-2\cdot k2\cdot b) - mh3\cdot \exp(-2\cdot k2\cdot b) + mh2\cdot k3\cdot b\cdot \exp(-2\cdot k2\cdot b) + mh2\cdot \exp(-2\cdot k2\cdot b)}{-mh2\cdot k3\cdot b - mh2 + mh3 - mh3\cdot k2\cdot b}$$

$constC = -1.4181\times 10^{-6}$

b) Coefficient A:

$$A = \frac{B\cdot \exp(-k2\cdot a) + C\cdot \exp(k2\cdot a)}{\sin(k1\cdot a)}$$ .... $A = B\cdot constA$

$$constA := \frac{\exp(-k2\cdot a) + constC\cdot \exp(k2\cdot a)}{\sin(k1\cdot a)}$$

$constA = 1.562\times 10^{-2}$

c) Coefficient D:

$$D = \frac{B\cdot \exp(-k2\cdot b) + C\cdot \exp(k2\cdot b)}{\exp(-k3\cdot b)}$$ .... $D = B\cdot constD$

$$constD := \frac{\exp(-k2\cdot b) + constC\cdot \exp(k2\cdot b)}{\exp(-k3\cdot b)}$$

$constD = 4.4063\times 10^{6}$

ii) Normalising $r^2\psi^*\psi$ to find B:

$c := 1\cdot 10^{-8}$ This defines the upper limit for integration in Region III.

$$R1 := \int_0^a \left[r\cdot\left(constA\cdot\frac{\sin(k1\cdot r)}{r}\right)\right]^2 dr$$

$$R2 := \int_a^b \left[r\cdot\left(\frac{\exp(-k2\cdot r)}{r} + constC\cdot\frac{\exp(k2\cdot r)}{r}\right)\right]^2 dr$$

$$R3 := \int_b^{b+c} \left[r\cdot\left(constD\cdot\frac{\exp(-k3\cdot r)}{r}\right)\right]^2 dr$$

$R1 + R2 + R3 = 2.95 \times 10^{-13}$

$p(Y) := 1 - Y \cdot \left[4\pi(R1 + R2 + R3)\right]$

$Y := 0.00001$

$soln2 := root(p(Y), Y)$

$soln2 = 2.6976 \times 10^{11}$

$B := soln2^{\frac{1}{2}}$

$B = 5.1938 \times 10^{5}$ Substitute B into the equations below to find the values of A, C and D.

$$C(B) := B \cdot \frac{-mh3 \cdot k2 \cdot b \cdot \exp(-2 \cdot k2 \cdot b) - mh3 \cdot \exp(-2 \cdot k2 \cdot b) + mh2 \cdot k3 \cdot b \cdot \exp(-2 \cdot k2 \cdot b) + mh2 \cdot \exp(-2 \cdot k2 \cdot b)}{-mh2 \cdot k3 \cdot b - mh2 + mh3 - mh3 \cdot k2 \cdot b}$$

$$A(B) := \frac{B \cdot (\exp(-k2 \cdot a) + constC \cdot \exp(k2 \cdot a))}{\sin(k1 \cdot a)}$$

$$D(B) := \frac{B \cdot (\exp(-k2 \cdot b) + constC \cdot \exp(k2 \cdot b))}{\exp(-k3 \cdot b)}$$

Therefore,

$A(B) = 8.113 \times 10^{3}$

$A := A(B)$

$C(B) = -7.3653 \times 10^{-1}$

$C := C(B)$

$D(B) = 2.2885 \times 10^{12}$

$D := D(B)$

Wavefunctions for 3 Separate Regions (I, II and III):

$\psi h1(r1) := \frac{A \cdot \sin(k1 \cdot r1)}{r1}$ ________ Wavefunction in Region I

$\psi h2(r2) := B \cdot \frac{\exp(-k2 \cdot r2)}{r2} + C \cdot \frac{\exp(k2 \cdot r2)}{r2}$ __________ Wavefunction in Region II

$\psi h3(r3) := D \cdot \frac{\exp(-k3 \cdot r3)}{r3}$ ____________ Wavefunction in Region III

iii) To check the matching conditions:

a) At boundary r = a,

$$r1 := a \qquad r2 := a$$

$$\frac{\frac{d}{dr1}\psi h1(r1)}{\frac{d}{dr2}\psi h2(r2)} = 9.1837\times 10^{-1} \qquad \frac{mh1}{mh2} = 9.1837\times 10^{-1}$$

b) At boundary r = b,

$$r2 := b \qquad r3 := b$$

$$\frac{\frac{d}{dr2}\psi h2(r2)}{\frac{d}{dr3}\psi h3(r3)} = 4.9\times 10^{-1} \qquad \frac{mh2}{mh3} = 4.9\times 10^{-1}$$

iv) Plotting hole radial wavefunction and its corresponding radial probability function:

Defining the r1, r2 and r3 intervals:

$$r1 := 0\cdot 10^{-9}, 0.01\cdot 10^{-9} .. a \qquad r2 := a, a + 0.01\cdot 10^{-9} .. b \qquad r3 := b, b + 0.01\cdot 10^{-9} .. 8\cdot 10^{-9}$$

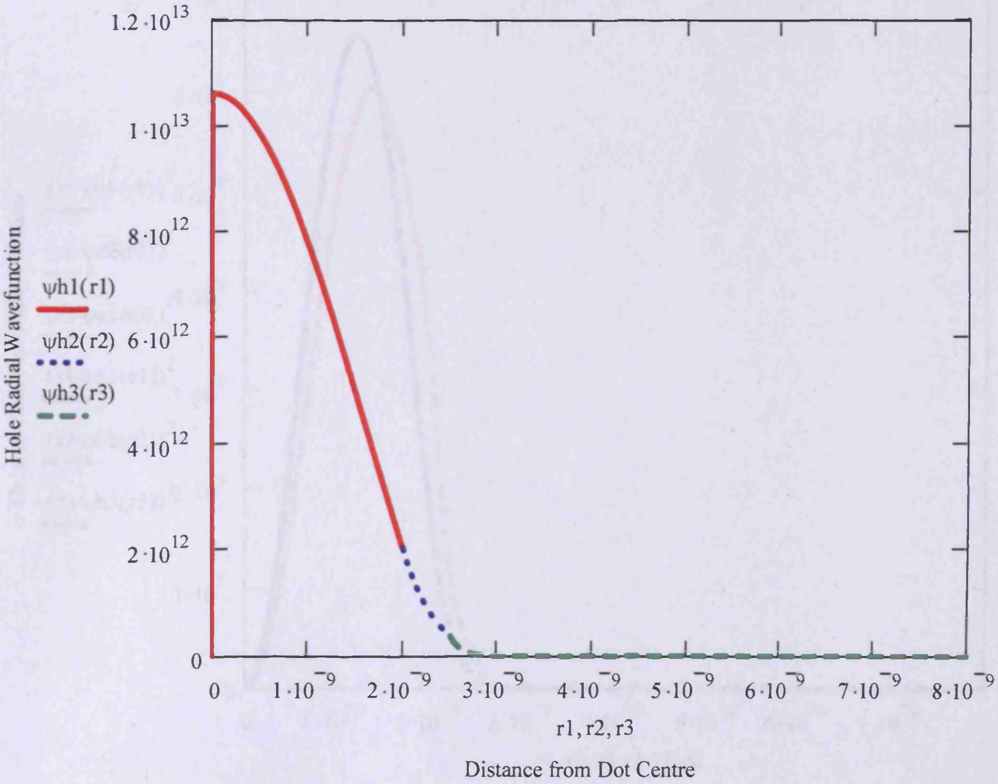

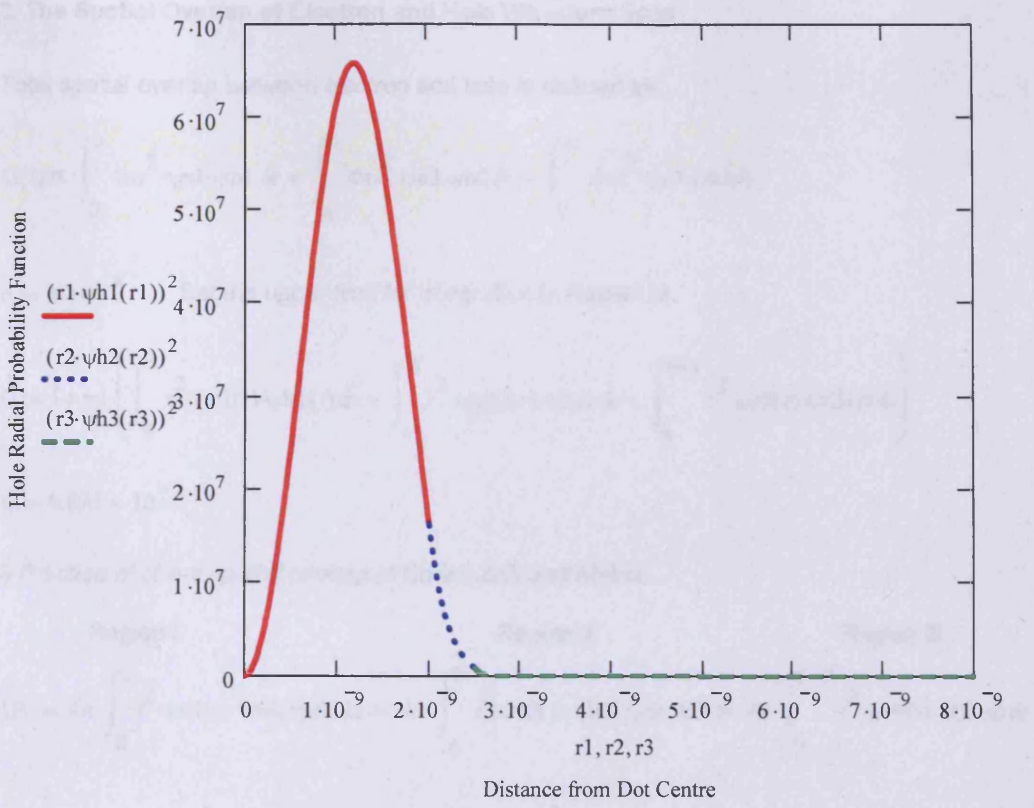
Hole Radial Probability Function
$(r1\cdot\psi h1(r1))^2$
$(r2\cdot\psi h2(r2))^2$
$(r3\cdot\psi h3(r3))^2$
$7\cdot10^7$
$6\cdot10^7$
$5\cdot10^7$
$4\cdot10^7$
$3\cdot10^7$
$2\cdot10^7$
$1\cdot10^7$
0
0
$1\cdot10^{-9}$
$2\cdot10^{-9}$
$3\cdot10^{-9}$
$4\cdot10^{-9}$
$5\cdot10^{-9}$
$6\cdot10^{-9}$
$7\cdot10^{-9}$
$8\cdot10^{-9}$
r1, r2, r3
Distance from Dot Centre

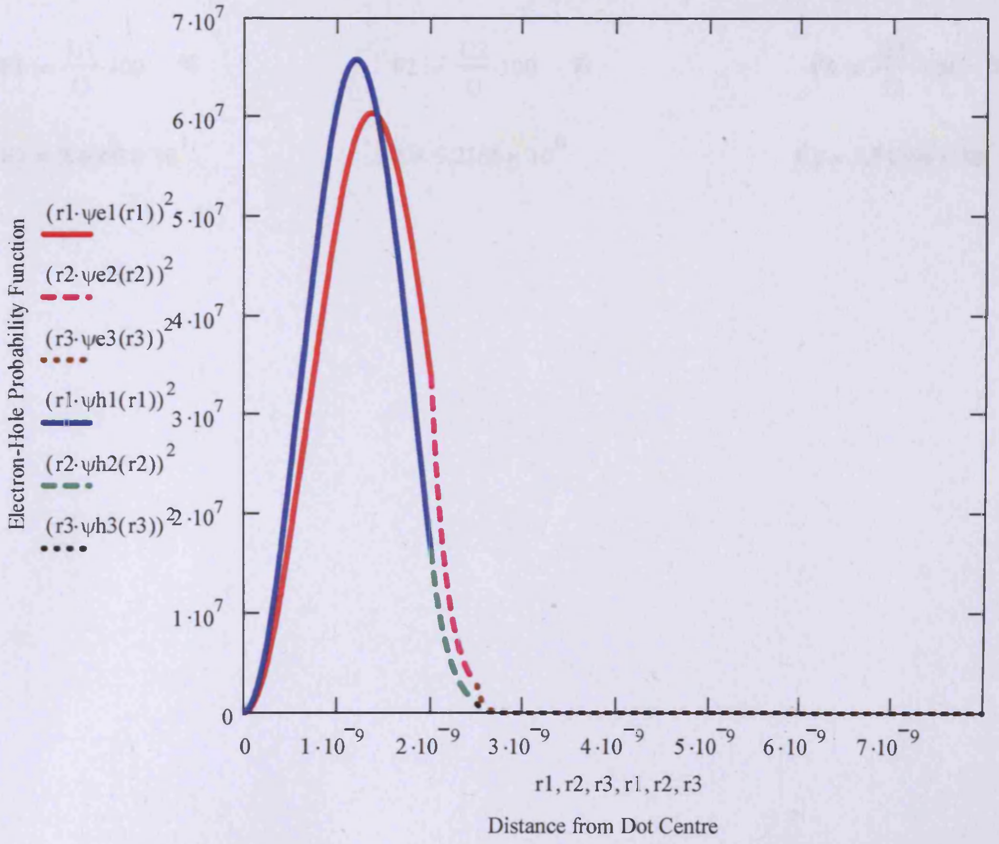
Electron-Hole Probability Function
$(r1\cdot\psi e1(r1))^2$
$(r2\cdot\psi e2(r2))^2$
$(r3\cdot\psi e3(r3))^2$
$(r1\cdot\psi h1(r1))^2$
$(r2\cdot\psi h2(r2))^2$
$(r3\cdot\psi h3(r3))^2$
$7\cdot10^7$
$6\cdot10^7$
$5\cdot10^7$
$4\cdot10^7$
$3\cdot10^7$
$2\cdot10^7$
$1\cdot10^7$
0
0
$1\cdot10^{-9}$
$2\cdot10^{-9}$
$3\cdot10^{-9}$
$4\cdot10^{-9}$
$5\cdot10^{-9}$
$6\cdot10^{-9}$
$7\cdot10^{-9}$
r1, r2, r3, r1, r2, r3
Distance from Dot Centre

3. The Spatial Overlap of Electron and Hole Wavefunctions

Total spatial overlap between electron and hole is defined as,

$$U(r) = \int_0^a 4\pi r^2 \cdot \psi e1 \cdot \psi h1 \, dr + \int_a^b 4\pi r^2 \cdot \psi e2 \cdot \psi h2 \, dr + \int_b^\infty 4\pi r^2 \cdot \psi e3 \cdot \psi h3 \, dr$$

$c := 1 \cdot 10^{-8}$ Set the upper limit for integration in Region III.

$$U := (4 \cdot \pi) \cdot \left(\int_0^a r^2 \cdot \psi e1(r) \cdot \psi h1(r) \, dr + \int_a^b r^2 \cdot \psi e2(r) \cdot \psi h2(r) \, dr + \int_b^{b+c} r^2 \cdot \psi e3(r) \cdot \psi h3(r) \, dr \right)$$

$U = 9.893 \times 10^{-1}$

i) Fraction of of e-h spatial overlap in CdSe, ZnS and Matrix:

Region I:	Region II:	Region III:
$U1 := 4\pi \cdot \int_0^a r^2 \cdot \psi e1(r) \cdot \psi h1(r) \, d$	$U2 := 4\pi \cdot \int_a^b r^2 \cdot \psi e2(r) \cdot \psi h2(r) \, dr$	$U3 := 4\pi \cdot \int_b^{b+c} r^2 \cdot \psi e3(r) \cdot \psi h3(r) \, dr$
$U1 = 9.3656 \times 10^{-1}$	$U2 = 5.1608 \times 10^{-2}$	$U3 = 1.1302 \times 10^{-3}$
$F1 := \frac{U1}{U} \cdot 100$ %	$F2 := \frac{U2}{U} \cdot 100$ %	$F3 := \frac{U3}{U} \cdot 100$ %
$F1 = 9.4669 \times 10^{1}$	$F2 = 5.2166 \times 10^{0}$	$F3 = 1.14246 \times 10^{-1}$

ii) Plot of of e-h overlap:

$U1(r1) := r1^2 \cdot \psi e1(r1) \cdot \psi h1(r1) \qquad U2(r2) := r2^2 \cdot \psi e2(r2) \cdot \psi h2(r2) \qquad U3(r3) := r3^2 \cdot \psi e3(r3) \cdot \psi h3(r3)$

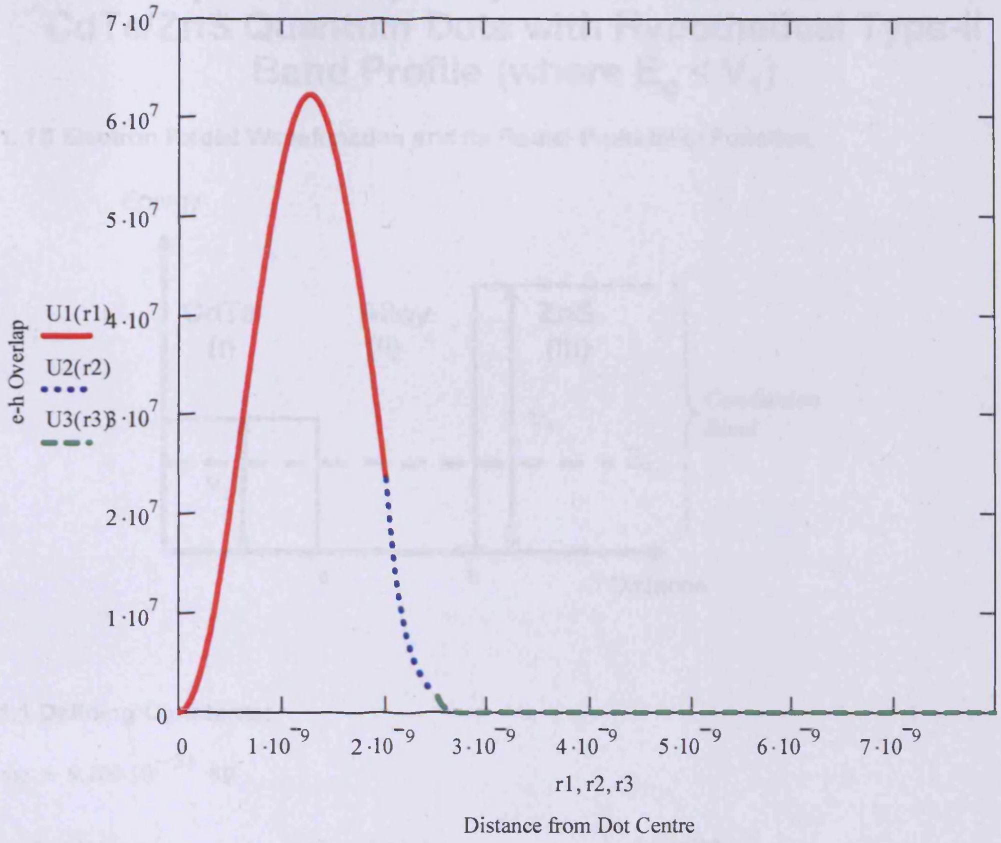

Appendix B

2-Step Finite Depth Spherical Well Model for CdTe/ZnS Quantum Dots with Hypothetical Type-II Band Profile (where $E_c < V_1$)

1. 1S Electron Radial Wavefunction and Its Radial Probability Function

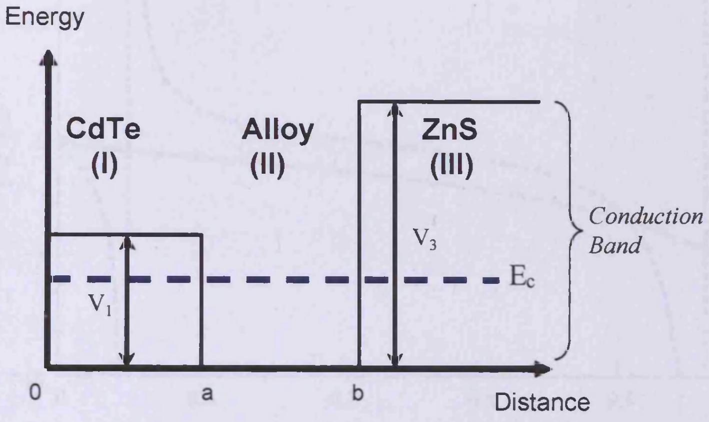

1.1 Defining Constants:

$me := 9.109\cdot10^{-31}$ kg

$me1 := 0.11\cdot me$ $me2 := 0.10\cdot me$ $me3 := 0.28\cdot me$

$hbar := 1.055\cdot10^{-34}$ Js $e := 1.602\cdot10^{-19}$C

$V1 := 0.8\cdot e$ potential barrier at CdTe/Alloy in J $V3 := 1.87\cdot e$ potential barrier at Alloy/ZnS in J

$a := 2.0\cdot10^{-9}$ $b := 3.5\cdot10^{-9}$ distance from the centre of QD in m

1.2 Finding the Energy Eigenvalue E_c of Electron at the Lowest Excited State:

$$k1(E) := \frac{(2\cdot me1\cdot|E - V1|)^{\frac{1}{2}}}{hbar} \qquad k2(E) := \frac{[2\cdot me2\cdot(E)]^{\frac{1}{2}}}{hbar} \qquad k3(E) := \frac{[2\cdot me3\cdot(|V3 - E|)]^{\frac{1}{2}}}{hbar}$$

Solve the equations below simultaneously to find E such that it satisfies g(E) - h(E) = 0,

$$g(E) := \frac{me2\cdot(k1(E)\cdot a\cdot \coth(k1(E)\cdot a) - 1)\cdot \sin(k2(E)a) - me1\cdot(k2(E)\cdot a\cdot \cos(k2(E)\cdot a) - \sin(k2(E)\cdot a))}{me1\cdot(-k2(E)\cdot a\cdot \sin(k2(E)\cdot a) - \cos(k2(E)\cdot a)) - me2\cdot(k1(E)\cdot a\cdot \coth(k1(E)\cdot a) - 1)\cdot \cos(k2(E)\cdot a)}$$

$$h(E) := \frac{me3\cdot(k2(E)\cdot b\cdot\cos(k2(E)\cdot b) - \sin(k2(E)\cdot b)) - me2\cdot(-k3(E)\cdot b - 1)\cdot\sin(k2(E)\cdot b)}{me2\cdot(-k3(E)\cdot b - 1)\cdot\cos(k2(E)\cdot b) - me3\cdot(-k2(E)\cdot b\cdot\sin(k2(E)\cdot b) - \cos(k2(E)\cdot b))}$$

$E := 0.001\cdot e, 0.002\cdot e .. 0.5\cdot e$

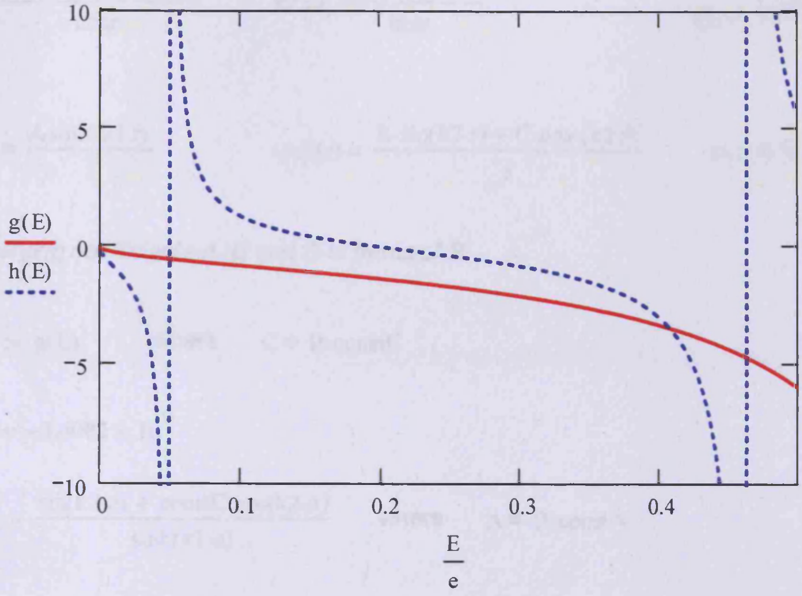

$E := 0.4\cdot e$

$TOL := 1\cdot 10^{-9}$ To improve the accuracy of *root* function.

$p(E) := (g(E) - h(E))\cdot 10^{5}$

$p(E) = -3.1517 \times 10^{4}$

$soln := root(p(E), E)$

$\frac{soln}{e} = 4.0757 \times 10^{-1}$

$E := soln$

$p(E) = -6.2172 \times 10^{-10}$

Therefore, E_c is:

$\frac{E}{e} = 4.0757 \times 10^{-1}$ in eV

1.3 Plotting Electron Radial Wavefunction and its Radial Probability Function:

Region I: *Region II:* *Region III:*

$$k1 := \frac{(2\cdot me1\cdot |E - V1|)^{\frac{1}{2}}}{hbar} \qquad k2 := \frac{(2\cdot me2\cdot |E|)^{\frac{1}{2}}}{hbar} \qquad k3 := \frac{(2\cdot me3\cdot |V3 - E|)^{\frac{1}{2}}}{hbar}$$

$$\psi e1(r) = \frac{A\,\sinh(k1\cdot r)}{r} \qquad \psi e2(r) = \frac{B\cdot \sin(k2\cdot r) + C\cdot \cos\cdot(k2\cdot r)}{r} \qquad \psi e3(r) = D\cdot\frac{\exp(-k3\cdot r)}{r}$$

i) Simplifying coefficients A, C and D in terms of B:

$constC := g(E)$ where $C = B\cdot constC$

$constC = -3.4082\times 10^{0}$

$constA := \dfrac{\sin(k2\cdot a) + constC\cdot\cos(k2\cdot a)}{\sinh(k1\cdot a)}$ where $A = B\cdot constA$

$constA = 6.0488\times 10^{-1}$

$constD := \dfrac{\sin(k2\cdot b) + constC\cdot\cos(k2\cdot b)}{\exp(-k3\cdot b)}$ where $D = B\cdot constD$

ii) Normalising $r^2\psi^*\psi$ to find B:

$c := 1\cdot 10^{-6}$ This defines the upper limit for integration in Region III.

$$R1 := \int_0^a \left[r\cdot\left(\frac{constA\,\sinh(k1\cdot r)}{r}\right)\right]^2 dr$$

$$R2 := \int_a^b \left[r\cdot\left(\frac{\sin(k2\cdot r)}{r} + \frac{constC\cdot\cos(k2\cdot r)}{r}\right)\right]^2 dr$$

$$R3 := \int_b^{b+c} \left[r\cdot\left(\frac{constD\cdot\exp(-k3\cdot r)}{r}\right)\right]^2 dr$$

$R1 + R2 + R3 = 1.824 \times 10^{-8}$

$p(B) := 1 - B \cdot \left[4\pi (R1 + R2 + R3) \right]$

$B := 0.1$

$p(B) = 10 \times 10^{-1}$

$soln2 := \mathrm{root}(p(B), B)$

$soln2 = 4.3627 \times 10^{6}$

$B := soln2^{\frac{1}{2}}$

$B = 2.0887 \times 10^{3}$ Substitute B into the equations below to find the values of A, C and D.

$A := constA \cdot B$

$C := constC \cdot B$

$D := constD \cdot B$

$A = 1.2634 \times 10^{3}$

$B = 2.0887 \times 10^{3}$

$C = -7.1188 \times 10^{3}$

$D = 5.1348 \times 10^{8}$

Wavefunctions for 3 Separate Regions (I, II and III):

$\psi e1(r1) := \dfrac{A \cdot \sinh(k1 \cdot r1)}{r1}$ _________ Wavefunction in Region I

$\psi e2(r2) := \dfrac{B \cdot \sin(k2 \cdot r2)}{r2} + \dfrac{C \cdot \cos(k2 \cdot r2)}{r2}$ ___________ Wavefunction in Region II

$\psi e3(r3) := \dfrac{D \exp(-k3 \cdot r3)}{r3}$ ____________ Wavefunction in Region III

iii) To check the matching conditions:

a) At boundary r = a,

$r1 := a \qquad r2 := a$

$$\frac{\psi e1(r1)}{\psi e2(r2)} = 10 \times 10^{-1}$$

$$\frac{\frac{d}{dr1}\psi e1(r1)}{\frac{d}{dr2}\psi e2(r2)} = 1.1 \times 10^{0} \qquad \frac{me1}{me2} = 1.1 \times 10^{0}$$

b) At boundary r = b,

$r2 := b \qquad r3 := b$

$$\frac{\psi e2(r2)}{\psi e3(r3)} = 1 \times 10^{0}$$

$$\frac{\frac{d}{dr2}\psi e2(r2)}{\frac{d}{dr3}\psi e3(r3)} = 3.5714 \times 10^{-1} \qquad \frac{me2}{me3} = 3.5714 \times 10^{-1}$$

iv) Plot of electron radial wavefunction and its corresponding radial probability function:

Defining the r1, r2 and r3 intervals:

$r1 := 0 \cdot 10^{-9}, 0.01 \cdot 10^{-9} .. a \qquad r2 := a, a + 0.01 \cdot 10^{-9} .. b \qquad r3 := b, b + 0.01 \cdot 10^{-9} .. 8 \cdot 10^{-9}$

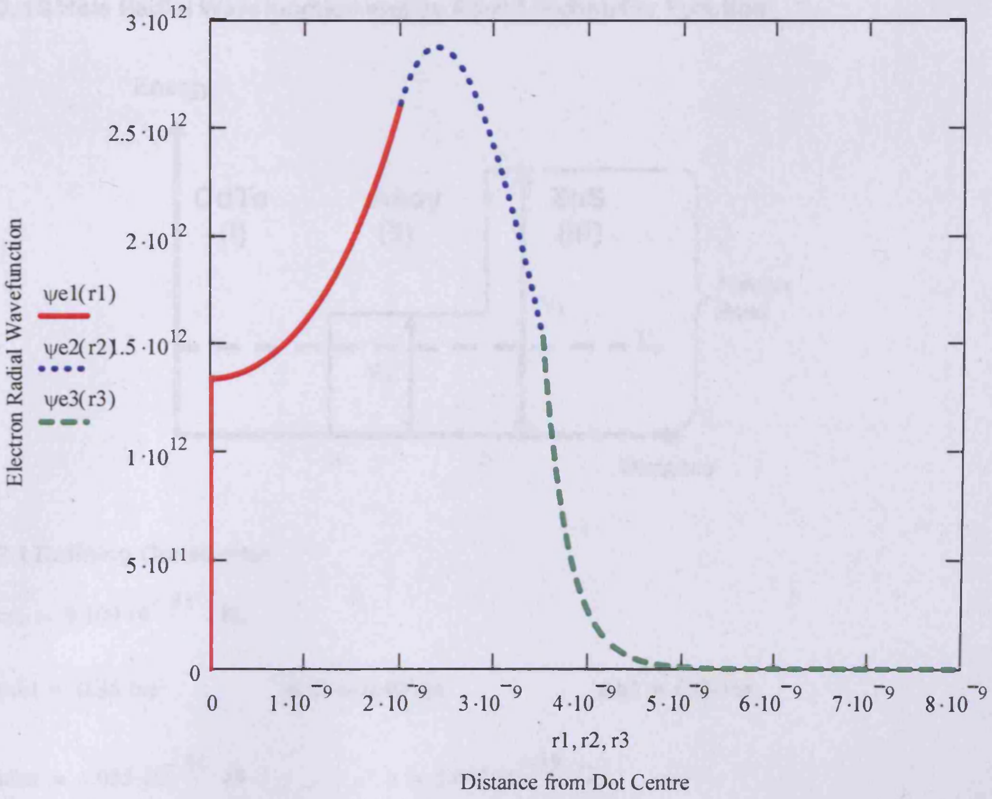

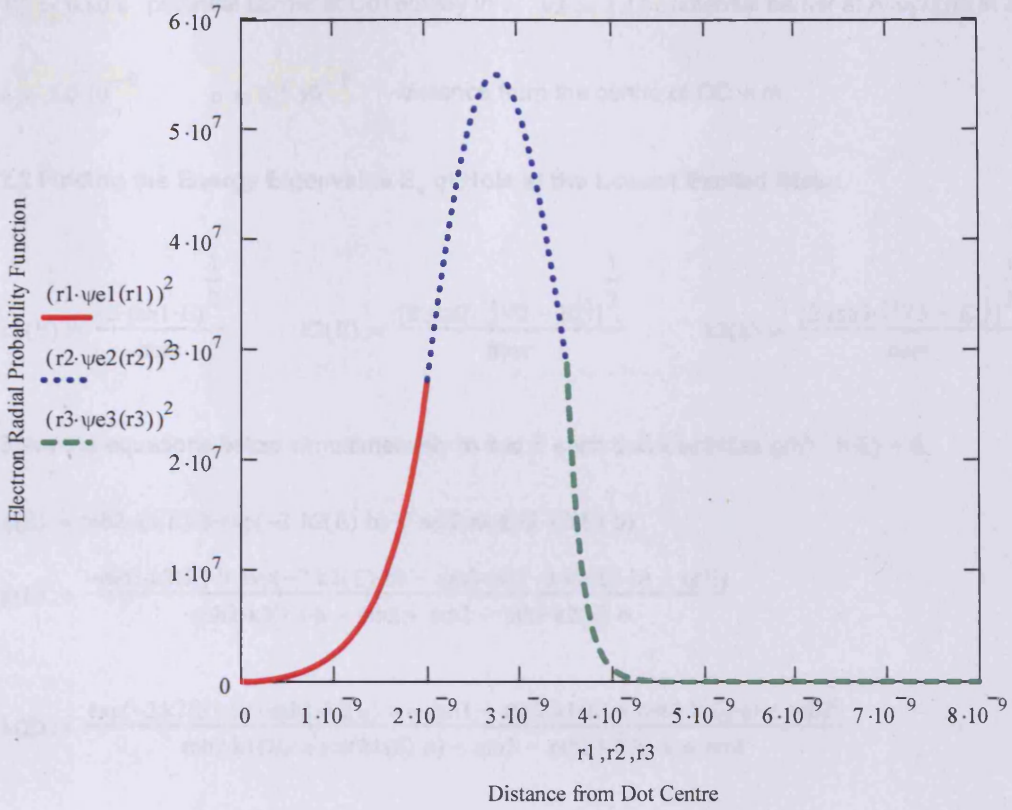

2. 1S Hole Radial Wavefunction and Its Radial Probability Function

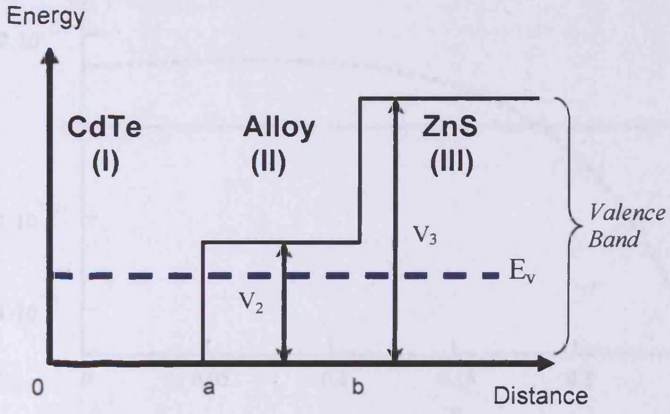

2.1 Defining Constants:

$me := 9.109 \cdot 10^{-31}$ kg

$mh1 := 0.35 \cdot me$ $mh2 := 0.40 \cdot me$ $mh3 := 0.49 \cdot me$

$hbar := 1.055 \cdot 10^{-34}$ Js $e := 1.602 \cdot 10^{-19}$ C

$V2 := 0.80 \cdot e$ potential barrier at CdTe/Alloy in J $V3 := 1.17 \cdot e$ potential barrier at Alloy/ZnS in J

$a := 2.0 \cdot 10^{-9}$ $b := 3.5 \cdot 10^{-9}$ distance from the centre of QD in m

2.2 Finding the Energy Eigenvalue E_v of Hole at the Lowest Excited State:

$$k1(E) := \frac{(2 \cdot mh1 \cdot E)^{\frac{1}{2}}}{hbar} \qquad k2(E) := \frac{[2 \cdot mh2 \cdot (|V2 - E|)]^{\frac{1}{2}}}{hbar} \qquad k3(E) := \frac{[2 \cdot mh3 \cdot (|V3 - E|)]^{\frac{1}{2}}}{hbar}$$

Solve the equations below simultaneously to find E such that it satisfies g(E) - h(E) = 0,

$$q(E) := mh2 \cdot k3(E) \cdot b \cdot \exp(-2 \cdot k2(E) \cdot b) + mh2 \cdot \exp(-2 \cdot k2(E) \cdot b)$$

$$g(E) := \frac{-mh3 \cdot k2(E) \cdot b \cdot \exp(-2 \cdot k2(E) \cdot b) - mh3 \cdot \exp(-2 \cdot k2(E) \cdot b) + q(E)}{-mh2 \cdot k3(E) \cdot b - mh2 + mh3 - mh3 \cdot k2(E) \cdot b}$$

$$h(E) := \frac{\exp(-2\, k2(E) \cdot a)(-mh1 \cdot k2(E) \cdot a - mh1 - mh2 \cdot k1(E) \cdot a \cdot \cot(k1(E) \cdot a) + mh2)}{mh2 \cdot k1(E) \cdot a \cdot \cot(k1(E) \cdot a) - mh2 - mh1 \cdot k2(E) \cdot a + mh1}$$

$E := 0.0001 \cdot e, 0.0002 \cdot e .. 0.5 \cdot e$

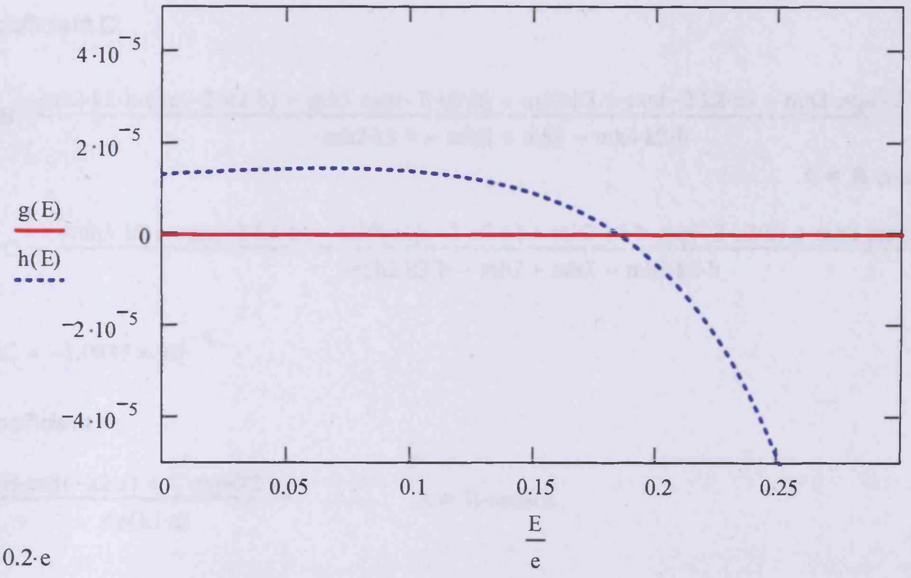

$E := 0.2 \cdot e$

$p(E) := (g(E) - h(E)) \cdot 10^{5}$

$soln := root(p(E), E)$

$\frac{soln}{e} = 1.8416 \times 10^{-1}$

$E := \mathrm{soln}$

$p(E) = 5.1444 \times 10^{-16}$

Therefore, E_v is:

$\frac{E}{e} = 1.8416 \times 10^{-1}$ in eV

2.3 Plotting Hole Radial Wavefunction and its Radial Probability Function:

Region I:

$$k1 := \frac{(2 \cdot mh1 \cdot E)^{\frac{1}{2}}}{hbar}$$

$$\psi h1(r) = \frac{A \sin(k1 \cdot r)}{r}$$

Region II:

$$k2 := \frac{[2 \cdot mh2 \cdot (|V2 - E|)]^{\frac{1}{2}}}{hbar}$$

$$\psi h2(r) = B \cdot \frac{\exp(-k2 \cdot r)}{r} + C \cdot \frac{\exp(k2 \cdot r)}{r}$$

Region III:

$$k3 := \frac{[2 \cdot mh3 \cdot (|V3 - E|)]^{\frac{1}{2}}}{hbar}$$

$$\psi h3(r) = D \cdot \frac{\exp(-k3 \cdot r)}{r}$$

i) Simplifying coefficient A, C and D in terms of B:

a) Coefficient C:

$$C = B \cdot \frac{-mh3 \cdot k2 \cdot b \cdot \exp(-2 \cdot k2 \cdot b) - mh3 \cdot \exp(-2 \cdot k2 \cdot b) + mh2 \cdot k3 \cdot b \cdot \exp(-2 \cdot k2 \cdot b) + mh2 \cdot \exp(-2 \cdot k2 \cdot b)}{-mh2 \cdot k3 \cdot b - mh2 + mh3 - mh3 \cdot k2 \cdot b}$$

.... $C = B \cdot \mathrm{constC}$

$$\mathrm{constC} := \frac{-mh3 \cdot k2 \cdot b \cdot \exp(-2 \cdot k2 \cdot b) - mh3 \cdot \exp(-2 \cdot k2 \cdot b) + mh2 \cdot k3 \cdot b \cdot \exp(-2 \cdot k2 \cdot b) + mh2 \cdot \exp(-2 \cdot k2 \cdot b)}{-mh2 \cdot k3 \cdot b - mh2 + mh3 - mh3 \cdot k2 \cdot b}$$

$\mathrm{constC} = -1.0837 \times 10^{-9}$

b) Coefficient A:

$$A = \frac{B \cdot \exp(-k2 \cdot a) + C \cdot \exp(k2 \cdot a)}{\sin(k1 \cdot a)}$$

.... $A = B \cdot \mathrm{constA}$

$$\mathrm{constA} := \frac{\exp(-k2 \cdot a) + \mathrm{constC} \cdot \exp(k2 \cdot a)}{\sin(k1 \cdot a)}$$

$\mathrm{constA} = 1.2031 \times 10^{-2}$

c) Coefficient D:

$$D = \frac{B\cdot \exp(-k2\cdot b) + C\cdot \exp(k2\cdot b)}{\exp(-k3\cdot b)} \quad \ldots\ldots\ldots \quad D = B\cdot constD$$

$$constD := \frac{\exp(-k2\cdot b) + constC\cdot \exp(k2\cdot b)}{\exp(-k3\cdot b)}$$

$constD = 3.3175 \times 10^{1}$

ii) Normalising $r^2\psi^*\psi$ to find B:

$c := 1\cdot 10^{-6}$ This defines the upper limit for integration in Region III.

$$R1 := \int_0^a \left[r\cdot\left(constA\cdot\frac{\sin(k1\cdot r)}{r}\right)\right]^2 dr$$

$$R2 := \int_a^b \left[r\cdot\left(\frac{\exp(-k2\cdot r)}{r} + constC\cdot\frac{\exp(k2\cdot r)}{r}\right)\right]^2 dr$$

$$R3 := \int_b^{b+c} \left[r\cdot\left(constD\cdot\frac{\exp(-k3\cdot r)}{r}\right)\right]^2 dr$$

$R1 + R2 + R3 = 1.7688 \times 10^{-13}$

$p(Y) := 1 - Y\cdot\left[4\pi(R1 + R2 + R3)\right]$

$Y := 0.00001$

$soln2 := root(p(Y), Y)$

$soln2 = 4.4989 \times 10^{11}$

$B := soln2^{\frac{1}{2}}$

$B = 6.7074 \times 10^{5}$ Substitute B into the equations below to find the values of A, C and D.

$$C(B) := B\cdot\frac{-mh3\cdot k2\cdot b\cdot \exp(-2\cdot k2\cdot b) - mh3\cdot \exp(-2\cdot k2\cdot b) + mh2\cdot k3\cdot b\cdot \exp(-2\cdot k2\cdot b) + mh2\cdot \exp(-2\cdot k2\cdot b)}{-mh2\cdot k3\cdot b - mh2 + mh3 - mh3\cdot k2\cdot b}$$

$$A(B) := \frac{B\cdot(\exp(-k2\cdot a) + constC\cdot \exp(k2\cdot a))}{\sin(k1\cdot a)}$$

$$D(B) := \frac{B\cdot(\exp(-k2\cdot b) + constC\cdot \exp(k2\cdot b))}{\exp(-k3\cdot b)}$$

Therefore,

$$A(B) = 8.0694 \times 10^{3}$$

$$A := A(B)$$

$$C(B) = -7.2686 \times 10^{-4}$$

$$C := C(B)$$

$$D(B) = 2.2252 \times 10^{7}$$

$$D := D(B)$$

Wavefunctions for 3 Separate Regions (I, II and III):

$$\psi h1(r1) := \frac{A \cdot \sin(k1 \cdot r1)}{r1}$$ ________ Wavefunction in Region I

$$\psi h2(r2) := B \cdot \frac{\exp(-k2 \cdot r2)}{r2} + C \cdot \frac{\exp(k2 \cdot r2)}{r2}$$ ___________ Wavefunction in Region II

$$\psi h3(r3) := D \cdot \frac{\exp(-k3 \cdot r3)}{r3}$$ ____________ Wavefunction in Region III

iii) To check the matching conditions:

a) At boundary r = a,

$$r1 := a \qquad r2 := a$$

$$\frac{\frac{d}{dr1}\psi h1(r1)}{\frac{d}{dr2}\psi h2(r2)} = 8.75 \times 10^{-1} \qquad \frac{mh1}{mh2} = 8.75 \times 10^{-1}$$

b) At boundary r = b,

$$r2 := b \qquad r3 := b$$

$$\frac{\frac{d}{dr2}\psi h2(r2)}{\frac{d}{dr3}\psi h3(r3)} = 8.1633 \times 10^{-1} \qquad \frac{mh2}{mh3} = 8.1633 \times 10^{-1}$$

iv) Plotting hole radial wavefunction and its corresponding radial probability function:

Defining the r1, r2 and r3 intervals:

$$r1 := 0 \cdot 10^{-9}, 0.01 \cdot 10^{-9} .. a \qquad r2 := a, a + 0.01 \cdot 10^{-9} .. b \qquad r3 := b, b + 0.01 \cdot 10^{-9} .. 8 \cdot 10^{-9}$$

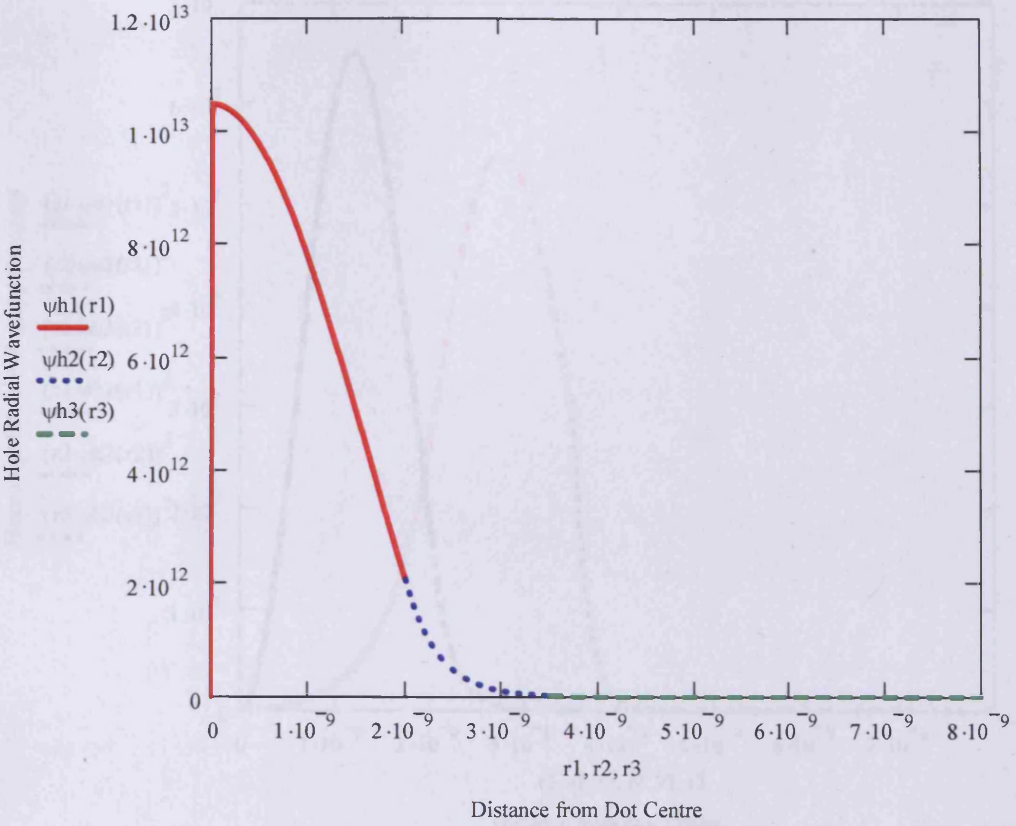
Hole Radial Wavefunction
ψh1(r1)
ψh2(r2)
ψh3(r3)
1.2·10^13
1·10^13
8·10^12
6·10^12
4·10^12
2·10^12
0
0
1·10^−9
2·10^−9
3·10^−9
4·10^−9
5·10^−9
6·10^−9
7·10^−9
8·10^−9
r1, r2, r3
Distance from Dot Centre

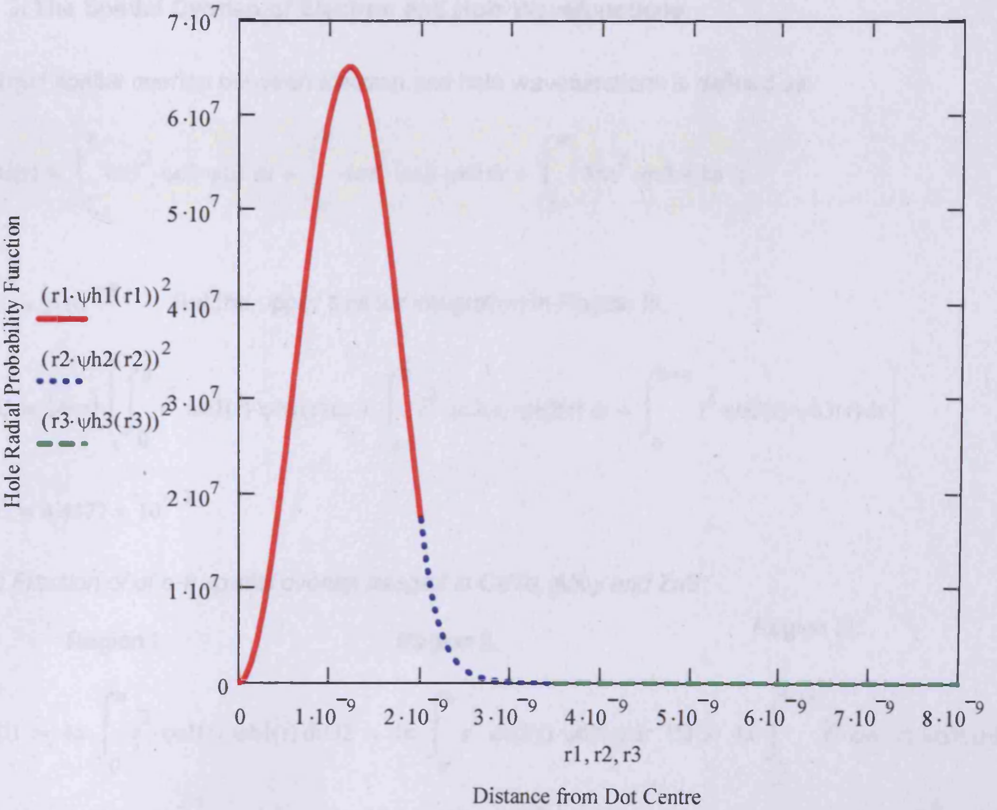
Hole Radial Probability Function
(r1·ψh1(r1))^2
(r2·ψh2(r2))^2
(r3·ψh3(r3))^2
7·10^7
6·10^7
5·10^7
4·10^7
3·10^7
2·10^7
1·10^7
0
0
1·10^−9
2·10^−9
3·10^−9
4·10^−9
5·10^−9
6·10^−9
7·10^−9
8·10^−9
r1, r2, r3
Distance from Dot Centre

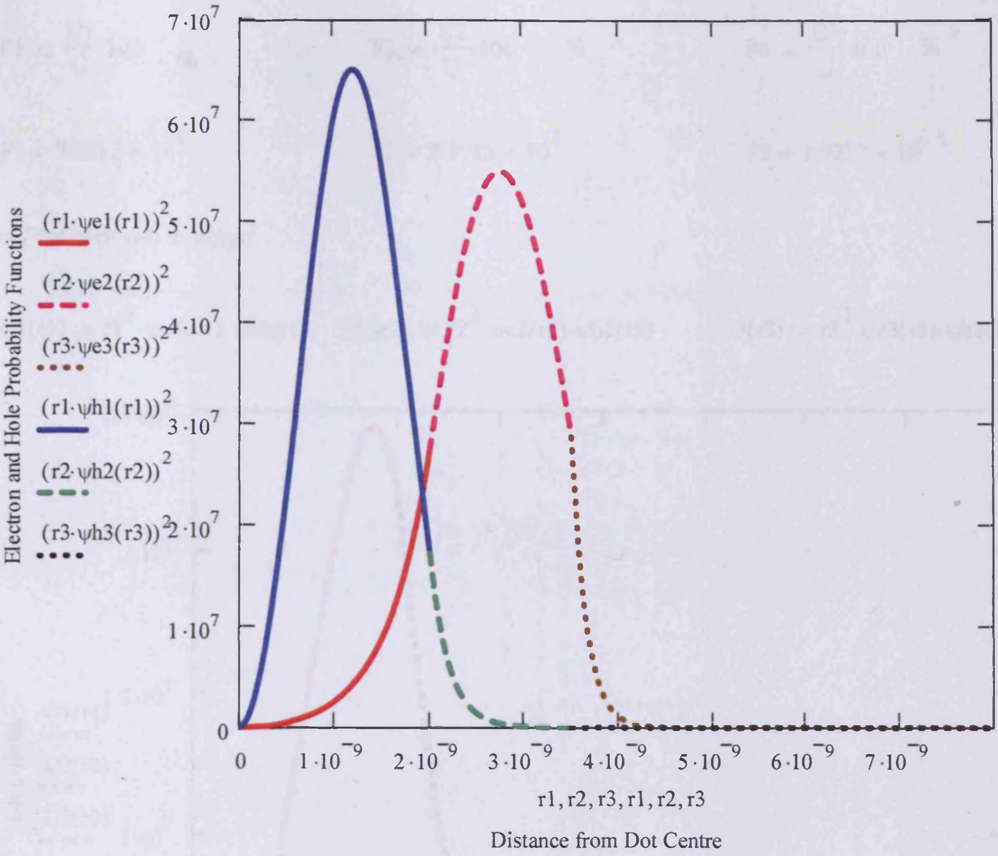

3. The Spatial Overlap of Electron and Hole Wavefunctions

Total spatial overlap between electron and hole wavefunctions is defined as,

$$U(r) = \int_0^a 4\pi r^2 \cdot \psi e1 \cdot \psi h1 \, dr + \int_a^b 4\pi r^2 \cdot \psi e2 \cdot \psi h2 \, dr + \int_b^\infty 4\pi r^2 \cdot \psi e3 \cdot \psi h3 \, dr$$

$c := 1 \cdot 10^{-8}$ Set the upper limit for integration in Region III.

$$U := (4 \cdot \pi) \cdot \left(\int_0^a r^2 \cdot \psi e1(r) \cdot \psi h1(r) \, dr + \int_a^b r^2 \cdot \psi e2(r) \cdot \psi h2(r) \, dr + \int_b^{b+c} r^2 \cdot \psi e3(r) \cdot \psi h3(r) \, dr \right)$$

$U = 4.4477 \times 10^{-1}$

i) Fraction of of e-h spatial overlap integral in CdTe, Alloy and ZnS:

Region I: Region II: Region III:

$$U1 := 4\pi \cdot \int_0^a r^2 \cdot \psi e1(r) \cdot \psi h1(r) \, d \quad U2 := 4\pi \cdot \int_a^b r^2 \cdot \psi e2(r) \cdot \psi h2(r) \, dr \quad U3 := 4\pi \cdot \int_b^{b+c} r^2 \cdot \psi e3(r) \cdot \psi h3(r) \, dr$$

$U1 = 3.1532 \times 10^{-1}$ $U2 = 1.286 \times 10^{-1}$ $U3 = 8.5448 \times 10^{-4}$

$F1 := \frac{U1}{U}\cdot 100$ % $F2 := \frac{U2}{U}\cdot 100$ % $F3 := \frac{U3}{U}\cdot 100$ %

$F1 = 7.0895 \times 10^{1}$ $F2 = 2.8913 \times 10^{1}$ $F3 = 1.9212 \times 10^{-1}$

ii) Plot of of e-h overlap:

$U1(r1) := r1^{2}\cdot \psi e1(r1)\cdot \psi h1(r1)$ $U2(r2) := r2^{2}\cdot \psi e2(r2)\cdot \psi h2(r2)$ $U3(r3) := r3^{2}\cdot \psi e3(r3)\cdot \psi h3(r3)$

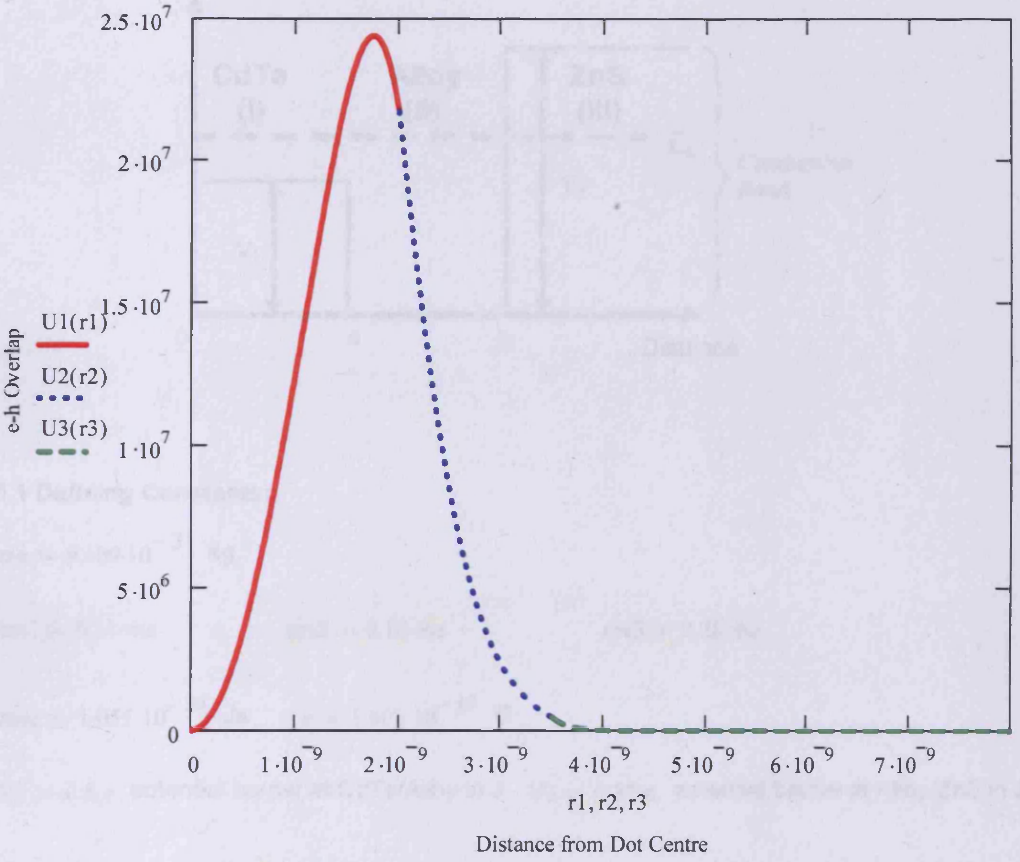

Appendix C

2-Step Finite Depth Spherical Well Model for CdTe/ZnS Quantum Dots with Hypothetical Type-II Band Profile (where $E_c > V_1$)

1. 1S Electron Radial Wavefunction and Its Radial Probability Function

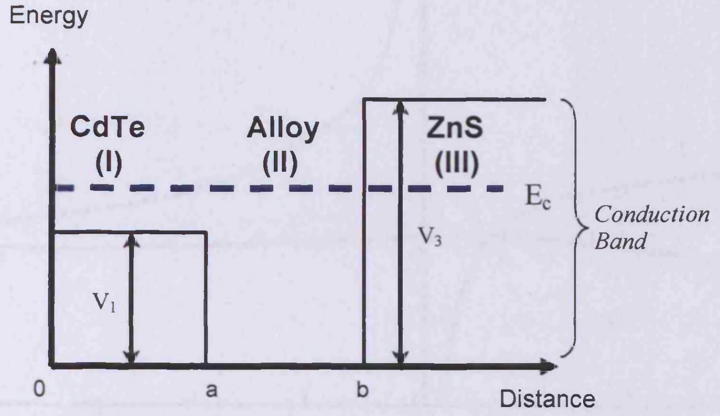

1.1 Defining Constants:

$me := 9.109 \cdot 10^{-31}$ kg

$me1 := 0.11 \cdot me$ $\quad$ $me2 := 0.10 \cdot me$ $\quad$ $me3 := 0.28 \cdot me$

$hbar := 1.055 \cdot 10^{-34}$ Js $\quad$ $e := 1.602 \cdot 10^{-19}$ C

$V1 := 0.8 \cdot e$ potential barrier at CdTe/Alloy in J $\quad$ $V3 := 1.87 \cdot e$ potential barrier at Alloy/ZnS in J

$a := 2.0 \cdot 10^{-9}$ $\quad$ $b := 2.3 \cdot 10^{-9}$ distance from the centre of QD in m

1.2 Finding the Energy Eigenvalue E_c of Electron at the Lowest Excited State:

$$k1(E) := \frac{(2 \cdot me1 \cdot |E - V1|)^{\frac{1}{2}}}{hbar} \qquad k2(E) := \frac{[2 \cdot me2 \cdot (E)]^{\frac{1}{2}}}{hbar} \qquad k3(E) := \frac{[2 \cdot me3 \cdot (|V3 - E|)]^{\frac{1}{2}}}{hbar}$$

Solve the equations below simultaneously to find E such that it satisfies g(E) - h(E) = 0,

$$g(E) := \frac{me2 \cdot \sin(k2(E) \cdot a) \cdot (k1(E) \cdot a \cdot \cot(k1(E) \cdot a) - 1) - me1 \cdot (k2(E) \cdot a \cdot \cos(k2(E) \cdot a) - \sin(k2(E) \cdot a))}{me3 \cdot (k2(E) \cdot b \cdot \cos(k2(E) \cdot b) - \sin(k2(E) \cdot b)) - me2 \cdot (-k3(E) \cdot b - 1) \cdot (\sin(k2(E) \cdot b))}$$

$$h(E) := \frac{me1\cdot(-k2(E)\cdot a\cdot \sin(k2(E)\cdot a) - \cos(k2(E)\cdot a)) - me2\cdot \cos(k2(E)\cdot a)\cdot(k1(E)\cdot a\cdot \cot(k1(E)\cdot a) - 1)}{me2\cdot(-k3(E)\cdot b - 1)\cdot \cos(k2(E)\cdot b) - me3\cdot(-k2(E)\cdot b\cdot \sin(k2(E)\cdot b) - \cos(k2(E)\cdot b))}$$

$E := 0.001\cdot e, 0.002\cdot e .. 1.2\cdot e$

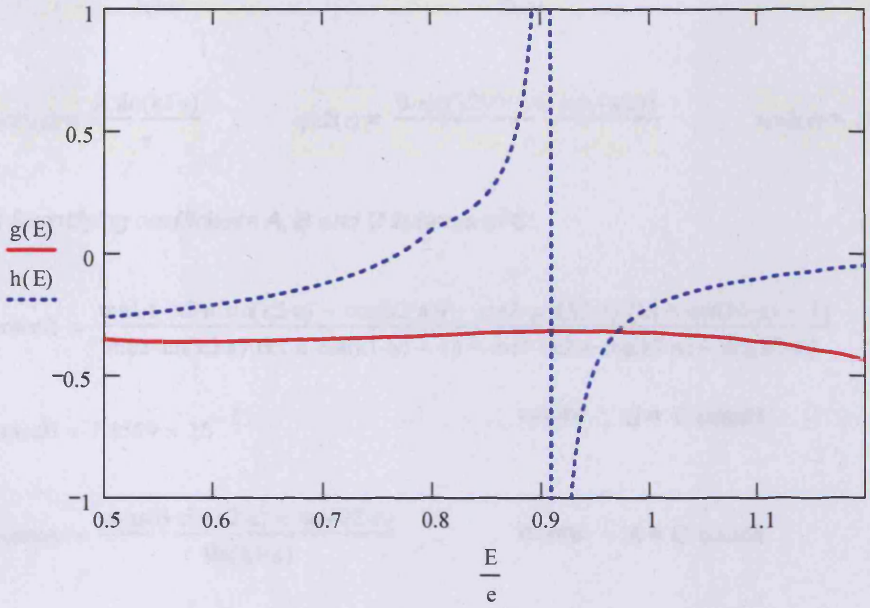

$E := 0.95\cdot e$

$TOL := 1\cdot 10^{-9}$ To improve the accuracy of *root* function.

$p(E) := (g(E) - h(E))\cdot 10^{5}$

$p(E) = 1.4132 \times 10^{4}$

$soln := root(p(E), E)$

$\frac{soln}{e} = 9.6966 \times 10^{-1}$

$E := soln$

$p(E) = 2.2204 \times 10^{-11}$

Therefore, E_c is:

$\frac{E}{e} = 9.6966 \times 10^{-1}$ in eV

1.3 Plotting Electron Radial Wavefunction and its Radial Probability Function:

Region I:

$$k1 := \frac{(2\cdot me1\cdot|E - V1|)^{\frac{1}{2}}}{hbar}$$

Region II:

$$k2 := \frac{(2\cdot me2\cdot|E|)^{\frac{1}{2}}}{hbar}$$

Region III:

$$k3 := \frac{(2\cdot me3\cdot|V3 - E|)^{\frac{1}{2}}}{hbar}$$

$$\psi e1(r) = \frac{A \sin(k1\cdot r)}{r}$$

$$\psi e2(r) = \frac{B\cdot\sin(k2\cdot r) + C\cdot\cos\cdot(k2\cdot r)}{r}$$

$$\psi e3(r) = D\cdot\frac{\exp(-k3\cdot r)}{r}$$

i) Simplifying coefficients A, B and D in terms of C:

$$constB := \frac{me1\cdot(-k2\cdot a\cdot\sin(k2\cdot a) - \cos(k2\cdot a)) - me2\cdot\cos(k2\cdot a)\cdot(k1\cdot a\cdot\cot(k1\cdot a) - 1)}{me2\cdot\sin(k2\cdot a)\cdot(k1\cdot a\cdot\cot(k1\cdot a) - 1) - me1\cdot(k2\cdot a\cdot\cos(k2\cdot a) - \sin(k2\cdot a))}$$

$constB = 1.4589 \times 10^{-1}$ where $B = C\cdot constB$

$$constA := \frac{constB\cdot\sin(k2\cdot a) + \cos(k2\cdot a)}{\sin(k1\cdot a)}$$ where $A = C\cdot constA$

$constA = -1.0208 \times 10^{0}$

$$constD := \frac{constB\cdot\sin(k2\cdot b) + \cos(k2\cdot b)}{\exp(-k3\cdot b)}$$ where $D = C\cdot constD$

$constD = -3.4708 \times 10^{2}$

ii) Normalising $r^2\psi^*\psi$ to find B:

$c := 1\cdot 10^{-6}$ This defines the upper limit for integration in Region III.

$$R1 := \int_0^a \left[r\cdot\left(\frac{constA \sin(k1\cdot r)}{r}\right)\right]^2 dr$$

$$R2 := \int_a^b \left[r\cdot\left(\frac{constB\cdot\sin(k2\cdot r)}{r} + \frac{\cos(k2\cdot r)}{r}\right)\right]^2 dr$$

$$R3 := \int_b^{b+c} \left[r\cdot\left(\frac{constD\cdot\exp(-k3\cdot r)}{r}\right)\right]^2 dr$$

$R1 + R2 + R3 = 1.2211 \times 10^{-9}$

$p(C) := 1 - C \cdot \left[4\pi(R1 + R2 + R3)\right]$

$C := 0.1$

$p(C) = 10 \times 10^{-1}$

$soln2 := root(p(C), C)$

$soln2 = 6.5171 \times 10^{7}$

$p(soln2) = 0 \times 10^{0}$

$C := soln2^{\frac{1}{2}}$

$C = 8.0729 \times 10^{3}$ Substitute C into the equations below to find the values of A, B and D.

$A := constA \cdot C$

$B := constB \cdot C$

$D := constD \cdot C$

$A = -8.2409 \times 10^{3}$

$B = 1.1778 \times 10^{3}$

$C = 8.0729 \times 10^{3}$

$D = -2.8019 \times 10^{6}$

Wavefunctions for 3 Separate Regions (I, II and III):

$\psi e1(r1) := \left|\frac{A \cdot \sin(k1 \cdot r1)}{r1}\right|$ ________ Wavefunction in Region I

$\psi e2(r2) := \left|\frac{B \cdot \sin(k2 \cdot r2)}{r2} + \frac{C \cdot \cos(k2 \cdot r2)}{r2}\right|$ __________ Wavefunction in Region II

$\psi e3(r3) := \left|\frac{D \cdot \exp(-k3 \cdot r3)}{r3}\right|$ ____________ Wavefunction in Region III

iii) To check the matching conditions:

a) At boundary r = a,

$r1 := a \qquad r2 := a$

$$\frac{\psi e1(r1)}{\psi e2(r2)} = 10 \times 10^{-1}$$

$$\frac{\frac{d}{dr1}\psi e1(r1)}{\frac{d}{dr2}\psi e2(r2)} = 1.1 \times 10^{0} \qquad \frac{me1}{me2} = 1.1 \times 10^{0}$$

b) At boundary r = b,

$r2 := b \qquad r3 := b$

$$\frac{\psi e2(r2)}{\psi e3(r3)} = 1 \times 10^{0}$$

$$\frac{\frac{d}{dr2}\psi e2(r2)}{\frac{d}{dr3}\psi e3(r3)} = 3.5714 \times 10^{-1} \qquad \frac{me2}{me3} = 3.5714 \times 10^{-1}$$

iv) Plot of electron radial wavefunction and its corresponding radial probability function:

Defining the r1, r2 and r3 intervals:

$r1 := 0 \cdot 10^{-9}, 0.01 \cdot 10^{-9} .. a \qquad r2 := a, a + 0.01 \cdot 10^{-9} .. b \qquad r3 := b, b + 0.01 \cdot 10^{-9} .. 8 \cdot 10^{-9}$

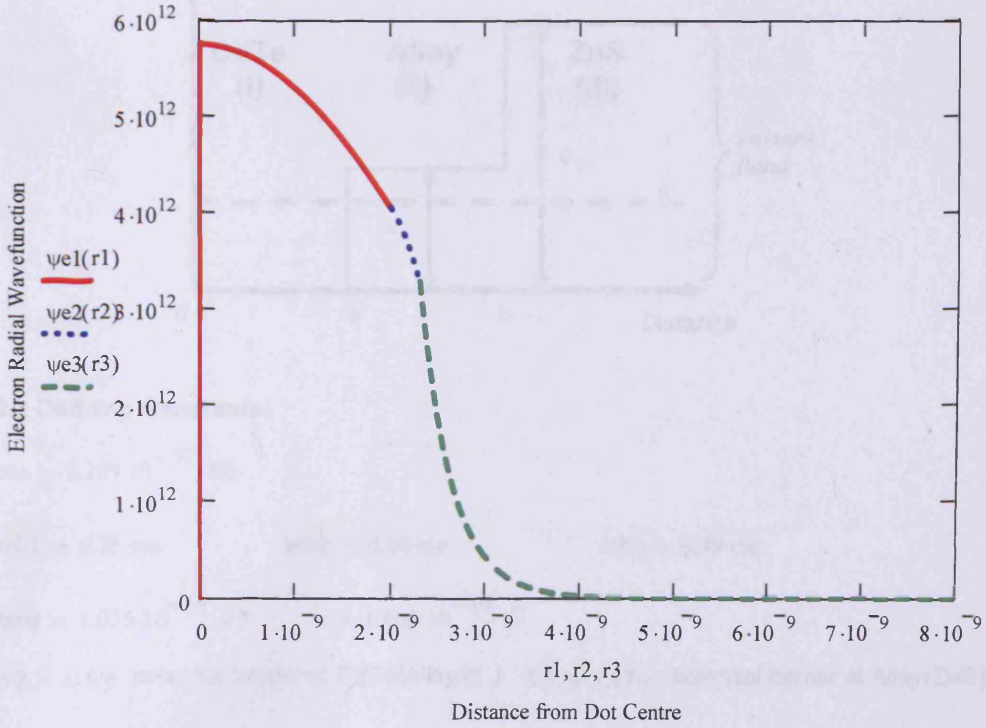

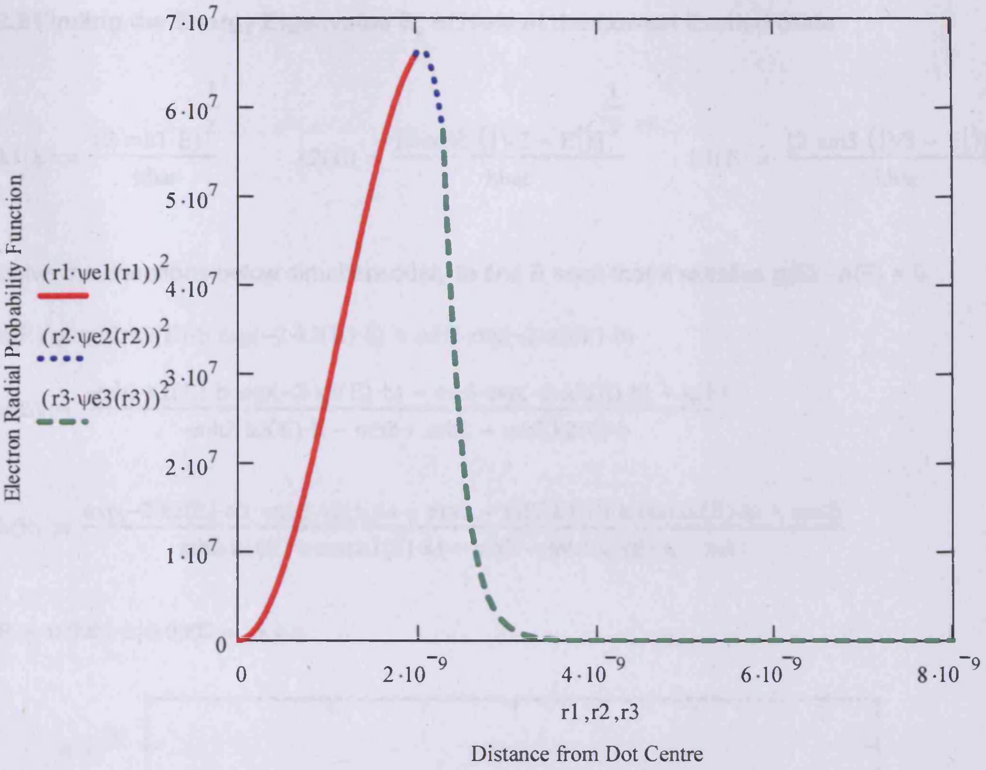

2. Hole Radial Wavefunction and Its Radial Probability Function

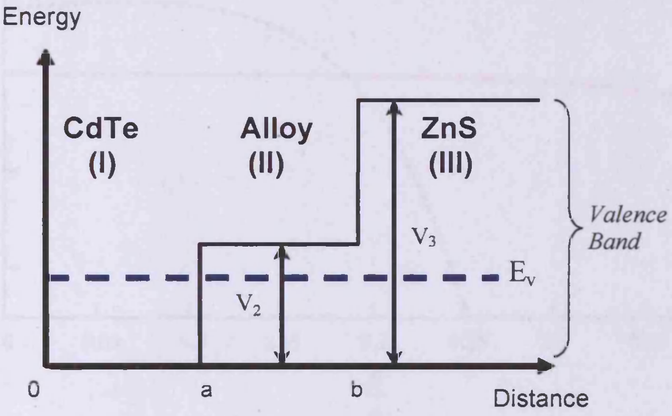

2.1 Defining Constants:

$me := 9.109\cdot 10^{-31}$ kg

$mh1 := 0.35\cdot me$ $mh2 := 0.40\cdot me$ $mh3 := 0.49\cdot me$

$hbar := 1.055\cdot 10^{-34}$ Js $e := 1.602\cdot 10^{-19}$ C

$V2 := 0.8\cdot e$ potential barrier at CdTe/Alloy in J $V3 := 1.17\cdot e$ potential barrier at Alloy/ZnS in J

$a := 2.0\cdot 10^{-9}$ $b := 2.3\cdot 10^{-9}$ distance from the centre of QD in m

2.2 Finding the Energy Eigenvalue E_v of Hole at the Lowest Excited State:

$$k1(E) := \frac{(2\cdot mh1\cdot E)^{\frac{1}{2}}}{hbar} \qquad k2(E) := \frac{[2\cdot mh2\cdot(|V2 - E|)]^{\frac{1}{2}}}{hbar} \qquad k3(E) := \frac{[2\cdot mh3\cdot(|V3 - E|)]^{\frac{1}{2}}}{hbar}$$

Solve the equations below simultaneously to find E such that it satisfies g(E) - h(E) = 0,

$$q(E) := mh2\cdot k3(E)\cdot b\cdot \exp(-2\cdot k2(E)\cdot b) + mh2\cdot \exp(-2\cdot k2(E)\cdot b)$$

$$g(E) := \frac{-mh3\cdot k2(E)\cdot b\cdot \exp(-2\cdot k2(E)\cdot b) - mh3\cdot \exp(-2\cdot k2(E)\cdot b) + q(E)}{-mh2\cdot k3(E)\cdot b - mh2 + mh3 - mh3\cdot k2(E)\cdot b}$$

$$h(E) := \frac{\exp(-2\,k2(E)\cdot a)(-mh1\cdot k2(E)\cdot a - mh1 - mh2\cdot k1(E)\cdot a\cdot \cot(k1(E)\cdot a) + mh2)}{mh2\cdot k1(E)\cdot a\cdot \cot(k1(E)\cdot a) - mh2 - mh1\cdot k2(E)\cdot a + mh1}$$

$$E := 0.0001\cdot e, 0.0002\cdot e .. 0.4\cdot e$$

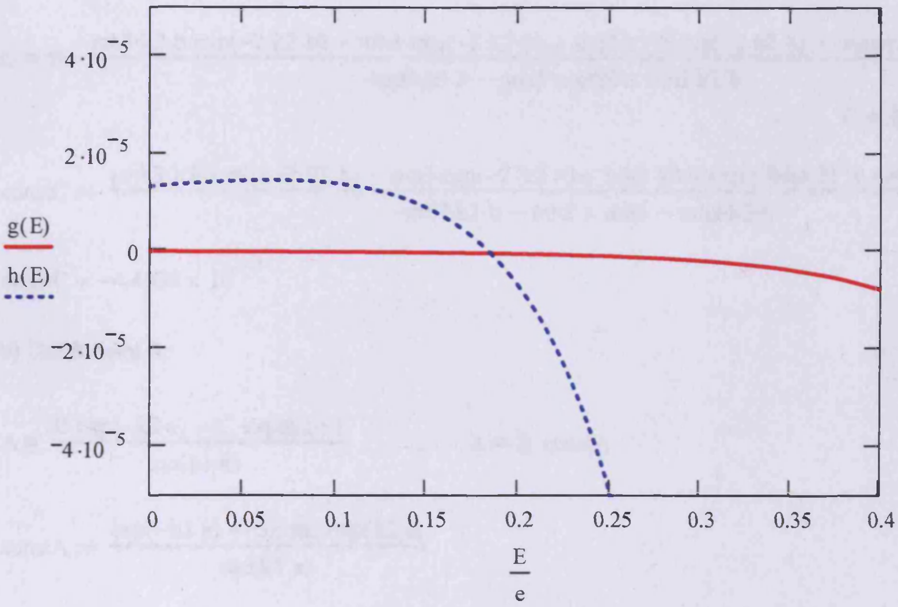

$$E := 0.2\cdot e$$

$$p(E) := (g(E) - h(E))\cdot 10^{5}$$

$$soln := root(p(E), E)$$

$$\frac{soln}{e} = 1.8537 \times 10^{-1}$$

$$E := soln$$

$$p(E) = -8.0468 \times 10^{-16}$$

Therefore, E_v is:

$\frac{E}{e} = 1.8537 \times 10^{-1}$ in eV

2.3 Plotting Hole Radial Wavefunction and its Radial Probability Function:

Region I:

$$k1 := \frac{(2 \cdot mh1 \cdot E)^{\frac{1}{2}}}{hbar}$$

Region II:

$$k2 := \frac{[2 \cdot mh2 \cdot (|V2 - E|)]^{\frac{1}{2}}}{hbar}$$

Region III:

$$k3 := \frac{[2 \cdot mh3 \cdot (|V3 - E|)]^{\frac{1}{2}}}{hbar}$$

$$\psi h1(r) = \frac{A \sin(k1 \cdot r)}{r}$$

$$\psi h2(r) = B \cdot \frac{\exp(-k2 \cdot r)}{r} + C \cdot \frac{\exp(k2 \cdot r)}{r}$$

$$\psi h3(r) = D \cdot \frac{\exp(-k3 \cdot r)}{r}$$

i) Simplifying coefficient A, C and D in terms of B:

a) Coefficient C:

$$C = B \cdot \frac{-mh3 \cdot k2 \cdot b \cdot \exp(-2 \cdot k2 \cdot b) - mh3 \cdot \exp(-2 \cdot k2 \cdot b) + mh2 \cdot k3 \cdot b \cdot \exp(-2 \cdot k2 \cdot b) + mh2 \cdot \exp(-2 \cdot k2 \cdot b)}{-mh2 \cdot k3 \cdot b - mh2 + mh3 - mh3 \cdot k2 \cdot b}$$

.... $C = B \cdot constC$

$$constC := \frac{-mh3 \cdot k2 \cdot b \cdot \exp(-2 \cdot k2 \cdot b) - mh3 \cdot \exp(-2 \cdot k2 \cdot b) + mh2 \cdot k3 \cdot b \cdot \exp(-2 \cdot k2 \cdot b) + mh2 \cdot \exp(-2 \cdot k2 \cdot b)}{-mh2 \cdot k3 \cdot b - mh2 + mh3 - mh3 \cdot k2 \cdot b}$$

$constC = -4.4938 \times 10^{-7}$

b) Coefficient A:

$$A = \frac{B \cdot \exp(-k2 \cdot a) + C \cdot \exp(k2 \cdot a)}{\sin(k1 \cdot a)}$$

.... $A = B \cdot constA$

$$constA := \frac{\exp(-k2 \cdot a) + constC \cdot \exp(k2 \cdot a)}{\sin(k1 \cdot a)}$$

$constA = 1.2124 \times 10^{-2}$

c) Coefficient D:

$$D = \frac{B \cdot \exp(-k2 \cdot b) + C \cdot \exp(k2 \cdot b)}{\exp(-k3 \cdot b)}$$

.... $D = B \cdot constD$

$$constD := \frac{\exp(-k2 \cdot b) + constC \cdot \exp(k2 \cdot b)}{\exp(-k3 \cdot b)}$$

$constD = 9.8398 \times 10^{0}$

ii) Normalising $r^2\psi^*\psi$ to find B:

$c := 1\cdot10^{-8}$ This defines the upper limit for integration in Region III.

$$R1 := \int_0^a \left[r\cdot\left(constA\cdot\frac{\sin(k1\cdot r)}{r}\right)\right]^2 dr$$

$$R2 := \int_a^b \left[r\cdot\left(\frac{\exp(-k2\cdot r)}{r} + constC\cdot\frac{\exp(k2\cdot r)}{r}\right)\right]^2 dr$$

$$R3 := \int_b^{b+c} \left[r\cdot\left(constD\cdot\frac{\exp(-k3\cdot r)}{r}\right)\right]^2 dr$$

$R1 + R2 + R3 = 1.7844\times10^{-13}$

$p(Y) := 1 - Y\cdot[4\pi(R1 + R2 + R3)]$

$Y := 0.0001$

$soln2 := root(p(Y), Y)$

$soln2 = 4.4596\times10^{11}$

$B := soln2^{\frac{1}{2}}$

$B = 6.678\times10^{5}$ Substitute B into the equations below to find the values of A, C and D.

$$C(B) := B\cdot\frac{-mh3\cdot k2\cdot b\cdot\exp(-2\cdot k2\cdot b) - mh3\cdot\exp(-2\cdot k2\cdot b) + mh2\cdot k3\cdot b\cdot\exp(-2\cdot k2\cdot b) + mh2\cdot\exp(-2\cdot k2\cdot b)}{-mh2\cdot k3\cdot b - mh2 + mh3 - mh3\cdot k2\cdot b}$$

$$A(B) := \frac{B\cdot(\exp(-k2\cdot a) + constC\cdot\exp(k2\cdot a))}{\sin(k1\cdot a)}$$

$$D(B) := \frac{B\cdot(\exp(-k2\cdot b) + constC\cdot\exp(k2\cdot b))}{\exp(-k3\cdot b)}$$

Therefore,

$A(B) = 8.0966\times10^{3}$

$A := A(B)$

$C(B) = -3.001\times10^{-1}$

$C := C(B)$

$D(B) = 6.571\times10^{6}$

$D := D(B)$

Wavefunctions for 3 Separate Regions (I, II and III):

$$\psi h1(r1) := \frac{A \cdot \sin(k1 \cdot r1)}{r1}$$

________ Wavefunction in Region I

$$\psi h2(r2) := B \cdot \frac{\exp(-k2 \cdot r2)}{r2} + C \cdot \frac{\exp(k2 \cdot r2)}{r2}$$

__________ Wavefunction in Region II

$$\psi h3(r3) := D \cdot \frac{\exp(-k3 \cdot r3)}{r3}$$

___________ Wavefunction in Region III

iii) To check the matching conditions:

a) At boundary r = a,

$r1 := a \qquad r2 := a$

$$\frac{\frac{d}{dr1}\psi h1(r1)}{\frac{d}{dr2}\psi h2(r2)} = 8.75 \times 10^{-1} \qquad \frac{mh1}{mh2} = 8.75 \times 10^{-1}$$

b) At boundary r = b,

$r2 := b \qquad r3 := b$

$$\frac{\frac{d}{dr2}\psi h2(r2)}{\frac{d}{dr3}\psi h3(r3)} = 8.1633 \times 10^{-1} \qquad \frac{mh2}{mh3} = 8.1633 \times 10^{-1}$$

iv) Plotting hole radial wavefunction and its corresponding radial probability function:

Defining the r1, r2 and r3 intervals:

$r1 := 0\cdot 10^{-9}, 0.01\cdot 10^{-9} .. a \qquad r2 := a, a + 0.01\cdot 10^{-9} .. b \qquad r3 := b, b + 0.01\cdot 10^{-9} .. 8\cdot 10^{-9}$

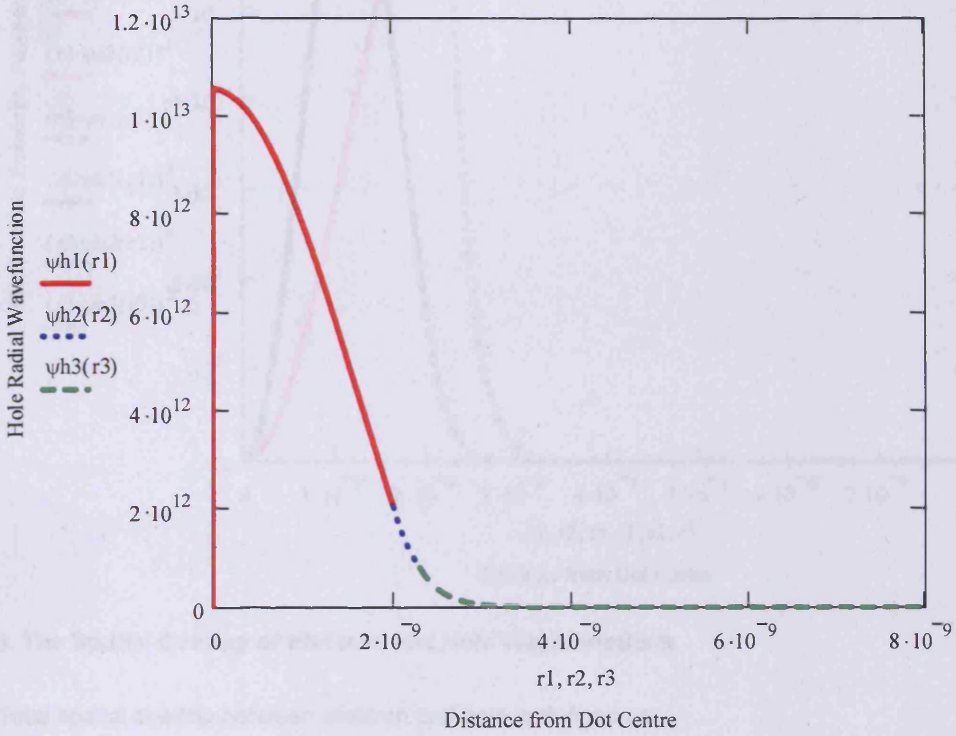

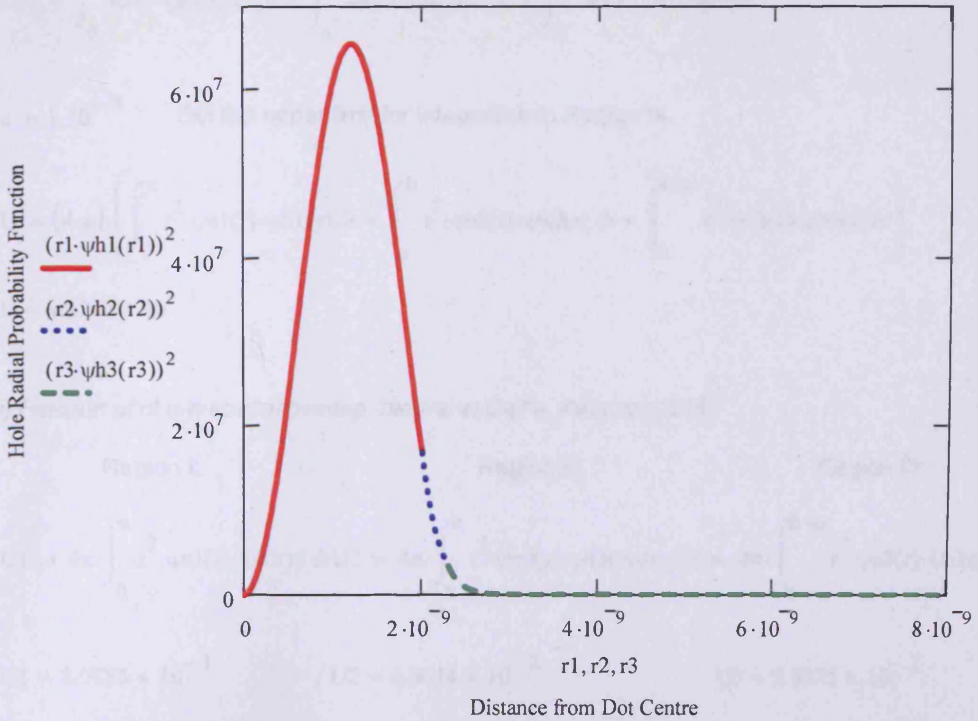

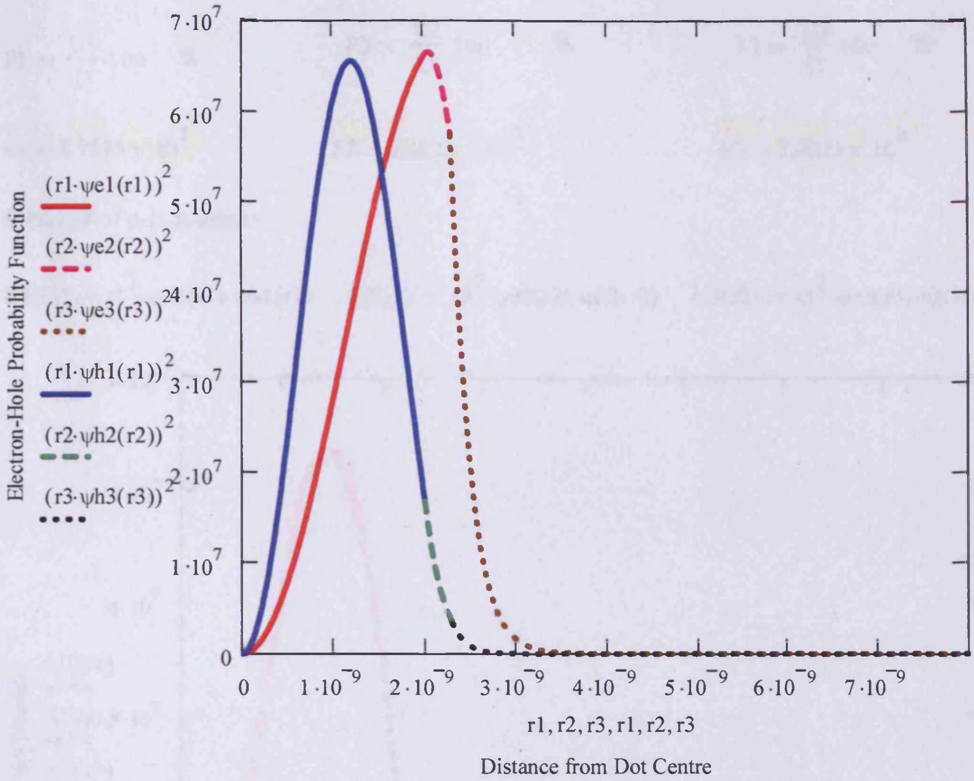

3. The Spatial Overlap of Electron and Hole Wavefunctions

Total spatial overlap between electron and hole is defined as,

$$U(r) = \int_0^a 4\pi r^2\cdot\psi e1\cdot\psi h1\,dr + \int_a^b 4\pi r^2\cdot\psi e2\cdot\psi h2\,dr + \int_b^\infty 4\pi r^2\cdot\psi e3\cdot\psi h3\,dr$$

$c := 1\cdot 10^{-8}$ Set the upper limit for integration in Region III.

$$U := (4\cdot\pi)\cdot\left(\int_0^a r^2\cdot\psi e1(r)\cdot\psi h1(r)\,dr + \int_a^b r^2\cdot\psi e2(r)\cdot\psi h2(r)\,dr + \int_b^{b+c} r^2\cdot\psi e3(r)\cdot\psi h3(r)\,dr\right)$$

$U = 9.2246\times 10^{-1}$

i) Fraction of of e-h spatial overlap integral in CdTe, Alloy and ZnS:

Region I: Region II: Region III:

$U1 := 4\pi\cdot\int_0^a r^2\cdot\psi e1(r)\cdot\psi h1(r)\,d$ $U2 := 4\pi\cdot\int_a^b r^2\cdot\psi e2(r)\cdot\psi h2(r)\,dr$ $U3 := 4\pi\cdot\int_b^{b+c} r^2\cdot\psi e3(r)\cdot\psi h3(r)\,dr$

$U1 = 8.0785\times 10^{-1}$ $U2 = 8.6044\times 10^{-2}$ $U3 = 2.8575\times 10^{-2}$

$F1 := \frac{U1}{U}\cdot 100$ %

$F2 := \frac{U2}{U}\cdot 100$ %

$F3 := \frac{U3}{U}\cdot 100$ %

$F1 = 8.7575 \times 10^{1}$

$F2 = 9.3276 \times 10^{0}$

$F3 = 3.0976 \times 10^{0}$

ii) Plot of of e-h overlap:

$U1(r1) := r1^{2}\cdot \psi e1(r1)\cdot \psi h1(r1)$

$U2(r2) := r2^{2}\cdot \psi e2(r2)\cdot \psi h2(r2)$

$U3(r3) := r3^{2}\cdot \psi e3(r3)\cdot \psi h3(r3)$